Adaptive Equalization and Capacity Analysis for Amplify-and-Forward Relays

Abdulla Firag

A thesis submitted in fulfillment
of the requirements for the degree of

Doctor of Philosophy

in

Electrical and Electronic Engineering

University of Canterbury
Christchurch, New Zealand

December 2008

Abstract

Recent research has shown that multiple-input multiple-output (MIMO) systems provide high spectral efficiencies and error performance gains. However, the use of multiple antennas in mobile terminals may not be very practical. Certainly there is limited space and other implementation issues which make this a challenging problem. Therefore, to harness the diversity gains afforded by MIMO transmitter diversity techniques, while maintaining a minimal number of antennas on each handset, *cooperative diversity* techniques have been proposed. In addition, attention has also been given to combining wireless relaying systems with MIMO techniques to improve capacity, coverage, and obtain better diversity at the expense of increased node complexity.

This thesis considers the design and analysis of cooperative diversity systems and MIMO amplify-and-forward relaying systems. In particular, we investigate adaptive time- and frequency-domain equalization techniques for cooperative diversity systems using space-time block codes (STBC). For MIMO relaying systems, we analyze the ergodic capacity of various systems and compare different amplify-and-forward methods in terms of system capacity performance.

We propose a new block time-domain adaptive equalization structure for time reversal-space time block coding (TR-STBC) systems, which eliminates the separate decoder and also the need for explicit channel state information (CSI) estimation at the receiver. Our simulation results show that the time-domain adaptive block equalizer performs better than the frequency-domain counterpart but at the cost of increased complexity. Then, we extend this time-domain adaptive equalization scheme to distributed TR-STBC systems. We also develop a frequency-domain

counterpart for the distributed systems. Our simulation results show that the adaptive algorithms work well for Protocols I and III proposed by Nabar *et al.* The time-domain adaptive algorithms perform better than the frequency-domain algorithms, and overall the Protocol I receivers outperform the Protocol III receivers. We also show that, if only the Protocol III receiver is used, it can be susceptible to noise amplification due to a weaker source-to-relay link compared to the relay-to-destination link. This problem can be mitigated by using the Protocol I receivers with some extra complexity but much superior diversity performance.

We also present an ergodic capacity analysis of an amplify-and-forward (AF) MIMO two-hop system including the direct link and validate the analysis with simulations. We show that having the direct link improves the capacity due to diversity and quantify this improvement. We also present an ergodic capacity analysis of an AF MIMO two-hop, two relay system. Our results verify the capacity gain of relaying systems with two relays due to the extra diversity compared to a single relaying system. However, the results also show that when one of the source-to-relay links has a markedly higher SNR compared to the other, a single relay system has better capacity than a two relay system.

Finally, we compare three types of relay amplification methods: a) average amplification, b) instantaneous channel amplification, and c) instantaneous power amplification. The instantaneous power amplification method has a higher mean capacity but with a higher variance. Also, it requires additional information at the destination and would create enormous overheads compared to the other methods. We also find that the instantaneous channel amplification method has almost no advantage in terms of the mean capacity but its capacity is less variable than the average amplification method. On the other hand, the average amplification method is simpler to implement as it does not require channel estimation at the relaying terminal.

Acknowledgements

I am thankful to God for giving me patience, guidance and opportunities through all the people who have helped me during this research. I would like to express my gratitude to everyone who supported me. First of all, I would like to acknowledge the University of Canterbury for giving me this opportunity through the Doctoral Scholarship. I would like to express my utmost gratitude to both my supervisors, Dr. Lee Garth and Assoc. Prof. Peter Smith for their excellent guidance. This research project progressed smoothly with the help of their invaluable comments, suggestions and directions. I would also like to thank Assist. Prof. Matthew McKay (Hong Kong University of Science and Technology, Hong Kong) for his knowledge and expertise provided in the later stage of this research.

I would also like to acknowledge my colleagues at the Communications Research Group for their company and sharing updated information from different areas of wireless communication.

I want to thank my wife, Mizna, and my son, Yoosuf, for their patience and understanding throughout my work. Especially, I would like to thank my wife for reading, over and over again, this thesis and also the papers I have written. Finally, I want to thank my extended family, specially my parents. I would have never be able to accomplish this research without their love, sacrifice, support and encouragement.

I dedicate this thesis to my brother, Ahmed Mohamed, for the sacrifice he made and support he has given for the education of me and my other siblings. He is the one taking care of the whole family, including my responsibilities while I have been away from home. I would not be able to come this far, if I did not have a brother like him.

Contents

List of Figures

List of Tables

Chapter 1

Introduction

This thesis considers the design and analysis of cooperative diversity systems and multiple-input multiple-output relaying systems. Cooperative diversity systems are designed which include space-time block codes with adaptive equalization in either the time or the frequency domains. In multiple-input multiple-output relaying systems, the capacity of the various systems are analyzed and also different amplify-and-forward methods are explored.

In the last decade, we have seen a vast growth in wireless technologies like cellular telephony, personal/portable devices and mobile internet. With this growth has come a mandate for reliable higher-speed data transmission over wireless channels. Unfortunately, reliable wireless transmission is difficult due to the limited radio spectrum and the time-varying multipath fading of the wireless channel. In multipath fading the received signal is made up of components traveling over multiple propagation paths of differing length, often with no line-of-sight component, hence introducing inter-symbol interference (ISI). In addition, the signal components do not arrive at the receiver in phase with one another so the strength of the received signal varies with time, and as a result the signal fades. Hence, one of the main tasks of wireless communication system designers is to explore new techniques in order to achieve high spectral efficiencies and error performance gains.

The error performance of single antenna systems can be increased using coding techniques, such as low density parity check [2, 3] and turbo codes [4]. Furthermore,

considerable gains in spectral efficiency and error performance are attainable by increasing the number of antennas at both the transmitter and the receiver [5, 6]. This type of multiple antenna system is usually called a multiple-input multiple-output (MIMO) system. MIMO systems can operate either as spatial diversity systems and/or spatial multiplexing systems.

Spatial diversity systems, using multiple antennas at the transmitter and/or receiver, have been proven to be effective at mitigating multipath fading effects, and hence, provide better system error performance. The basic aim of diversity techniques is to provide multiple replicas of the transmitted signals at the receiver, all carrying the same information but with small correlation in the fading statistics [7]. A classical approach to achieving spatial diversity is to use multiple antennas at the receiver. More recently, transmitter diversity techniques using space-time codes (STC), which use multiple transmit antennas, have been proposed [8, 6]. The two most well-known STC are Space-Time Trellis Codes (STTC) [9], and Space-Time Block Codes (STBC) [10]. The implementation of STTC can become very complicated as the number of antennas increases. However, STBC are relatively simple to implement.

In contrast to diversity systems, the aim of spatial multiplexing systems is to improve the spectral efficiency or throughput of the system [5, 11, 12, 13]. A multiplexing system divides the incoming data into sub-streams and transmits them on different antennas. As a result, the overall throughput of the system improves as multiple data streams are sent simultaneously.

MIMO systems can provide reliable higher-speed data transmission over wireless channels using these spatial diversity and multiplexing techniques. However, these systems also have challenges and constraints. It is usually not very practical to have multiple antennas at mobile terminals. This is due to terminal constraints such as size, cost and power. Small antennas for MIMO mobile terminals, such as planar inverted-F antennas, have recently been proposed [14, 15, 16]. Furthermore, cross polarized antennas for MIMO systems are now receiving considerable attention, because they are able to double the antenna number within half the spacing need

of co-polarized antennas [17]. Using these new antenna design technologies, it may be possible to overcome the size issue. However, research into these technologies is still in progress. In addition to these constraints on MIMO systems, wireless communication systems also need to increase the communication range. To extend the range and decrease the mobile terminal requirements, wireless relaying networks have recently been given considerable attention.

1.1 Wireless Relaying Systems

Relaying systems have been studied since the 1970s [18, 19]. The main objectives of relaying systems are to increase coverage and reduce the need to use high power at the transmitter or source terminal. Basically, in relaying systems the source terminal uses other terminals or relays to forward its information to the destination terminal. In general, there are two types of relaying systems, non-regenerative and regenerative systems [20], depending on the nature and the complexity of the relays used. In regenerative systems, also called decode-and-forward (DF) relaying systems, the relay fully decodes the received signal and retransmits the decoded symbol to the destination. Non-regenerative systems, also called amplify-and-forward (AF) systems, on the other hand use less complex relays that do not perform any sort of decoding, but simply amplify the received signal and forward it to the destination. Recently, with a better understanding of the advantages of MIMO systems, researchers have proposed alternative techniques that could achieve the advantages of both MIMO and/or wireless relaying systems.

Although MIMO systems provide high spectral efficiencies and error performance gains, having multiple antennas at mobile terminals may not be very practical. However, to harness the diversity gains afforded by the MIMO transmitter diversity techniques, while maintaining a minimal number of antennas on each handset, *cooperative diversity* techniques have recently been proposed [21, 1, 22]. These techniques allow a source terminal to leverage the spatial diversity offered by other terminals' antennas to form a virtual multiple-antenna array.

Cooperative diversity systems utilize the spatial diversity gains of MIMO systems by using single antenna based relaying systems. Recently, attention has been given to combining wireless relaying systems with MIMO techniques [23, 24]. In this hybrid technique, each terminal, source, relay(s) and destination has multiple antennas as in MIMO systems, and the relay(s) helps to forward the source terminal information to the destination. Using this approach, the system gets better capacity, coverage, and better diversity at the expense of increased node complexity.

1.2 Thesis Contributions

Transmit diversity techniques have proven to be effective at mitigating multipath fading. In [10], Alamouti proposed a transmit diversity scheme for flat fading channels that achieves the same diversity benefits as can be achieved by receive diversity, while requiring only linear decoding complexity. In [25], Lindskog and Paulraj extended Alamouti's method to frequency selective fading channels. Their time reversal-space time block coding (TR-STBC) scheme combines time-domain filtering, conjugation and time reversal operations. The outputs of the TR-STBC decoder are decoupled but contain residual inter-symbol interference (ISI) which must be mitigated using equalizers. Unfortunately, to perform this equalization, the optimal maximum likelihood sequence estimation techniques have exponentially increasing complexity with the signal constellation size and channel impulse response length.

Several block STBC structures for frequency selective fading channels, including single carrier-frequency domain equalizers (SC-FDE) [26] and orthogonal frequency division multiplexing (OFDM) transcievers [27], have been proposed. In these schemes, the decoding and equalization of the STBC transmissions require explicit estimation of the channel impulse response (CIR) at the receiver.

However, an improved approach is a combined decoder/adaptive equalizer structure that does not require separate CIR estimation, thereby reducing the system overhead and at the same time providing a tracking mechanism for time-varying channels. In [28], such a decoding/adaptive equalization scheme has been proposed

for SC FDE-STBC systems. One advantage of this particular scheme is that it delivers recursive least-squares (RLS) performance using least-mean-square (LMS) order complexity. However, as the scheme is based on frequency domain block equalization, the equalizer is constrained to have the same length as the data block length. This means that the complexity of the equalizer grows as the block length increases, even when the CIR is very short. Therefore, the scheme is advantageous primarily for channels with very long delay spreads.

Exploiting the efficiency of processing the received data in the time-domain, the first part of this thesis presents an adaptive block decoding/equalization scheme for TR-STBC systems with a decoder/equalizer length that is independent of the block length, making it suitable for channels with short CIRs.

In cellular systems, transmitter diversity techniques have generally been considered only for the *downlink* to minimize the number of power-hungry and expensive antennas in the mobile handset. However, to harness the diversity gains afforded by these transmitter techniques in the *uplink* as well, while maintaining a minimal number of antennas on each handset, *cooperative diversity* techniques have recently been proposed. Most researchers working on cooperative diversity assume a flat fading channel. However, Mheidat *et al.* [29, 22] have studied the performance of equalization techniques for distributed STBC systems in frequency selective fading channels. Their decoding and equalization techniques for the distributed STBC transmissions require explicit estimation of the CIR at the receiver. Using the results given in the first part of the thesis, we also develop both time- and frequency-domain adaptive combined decoding/equalization schemes for relay-assisted TR-STBC transmission systems. This method does not require explicit estimation of the CIR at the receiver.

As mentioned before, using relays can have a number of advantages. In addition to increasing the range, cooperative transmission can also provide increases in diversity. Furthermore, extending MIMO techniques to relaying systems [30] can increase the capacity of the relaying system compared to single antenna based relaying systems by providing additional diversity gains. Hence, it is important to analyze MIMO relaying systems to study the effects of various system parameters on the

performance of these systems. Many papers have been written on MIMO system analysis [31, 32, 33, 34, 35]. However, relatively few consider the analysis of MIMO relaying systems. Therefore, in this area we analyze the capacity of various MIMO relaying systems using an eigenvalue based analysis and compare and explain the performance of different AF methods in wireless relaying systems.

To summarize, the main contributions of the thesis are:

1. **Adaptive equalization for STBC systems**:
   A time domain adaptive block equalizer for TR-STBC systems is proposed and its performance is compared with a frequency domain counterpart.

2. **Adaptive equalization for STBC based cooperative diversity systems**:
   Time and frequency domain adaptive block equalizers for TR-STBC based cooperative diversity systems are given. Adaptive equalizers are developed and compared for two different relaying protocols.

3. **Capacity analysis of MIMO two-hop relaying systems**:
   Capacity analysis is performed for a MIMO two-hop one-relay relaying system with a source to destination link and also for a MIMO two-hop two-relay relaying system. Expressions for the probability density functions of an arbitrary eigenvalue of the systems are first derived. Then closed-form expressions for the ergodic capacity of the systems are derived.

4. **Amplify-and-Forward amplification methods for relaying systems**:
   Three different amplification methods for MIMO two-hop relaying systems are compared in terms of their capacity using simulation. Then the capacity behavior of these systems is explained using the cumulative distribution functions of the signal-to-noise ratios of the systems.

1.3 Thesis Outline

The rest of this thesis is organized as follows:

In Chapter 2 we introduce the required background information for the thesis. First, we describe the wireless channel and the fading environment, including the models used in the thesis, followed by an outline of space-time block codes and adaptive block equalization. Finally, wireless relaying systems and MIMO relay capacity analysis are explained.

In Chapter 3 we present a time-domain block equalizer for TR-STBC transceivers, which eliminates the need for a separate decoding block requiring explicit channel estimation. We first describe the TR-STBC encoding and decoding used in the system followed by the Minimum Mean Square Error (MMSE) equalizer derivation. Then, from the MMSE equalizer, we derive the adaptive receiver scheme. Finally, the performance of the time-domain RLS based adaptive receiver is presented using simulation and compared with the frequency domain adaptive receiver given in [28].

In Chapter 4 we develop both time- and frequency-domain adaptive combined decoding/equalization schemes for relay-assisted TR-STBC transmission systems. We derive both time- and frequency-domain adaptive combined decoding/equalization schemes from MMSE solutions for an amplify-and-forward relay network based on Protocols I and III proposed by Nabar *et al.* [1]. The chapter also includes an extensive Monte Carlo simulation study and complexity analysis of both the time- and frequency-domain adaptive combined decoding/equalization schemes.

In Chapter 5 we derive an exact expression for the capacity of an AF MIMO two-hop system including a source to destination link. The expression derived in this chapter can be used for arbitrary numbers of antennas at the source, relay and destination. We also present simulation results to validate the analysis, and use the results to quantify the capacity improvement due to the direct link. Further, we also show that the ergodic capacity for a single relaying system without the direct link can be derived from these results as a special case.

In Chapter 6 we derive an exact expression for the capacity of an AF MIMO two-hop two relay system. We first develop an expression for the probability density function of an arbitrary eigenvalue of the system. Then, using this result, we derive a closed-form expression for the ergodic capacity of the system. We also present

simulation results to validate the analysis. Further, we also show that the ergodic capacity for a single relaying system without the direct link can be derived from these results as a special case.

In Chapter 7 we compare three types of relay amplification methods in AF MIMO relaying systems in terms of system capacity performance. Furthermore, we also explain the capacity behavior using the cumulative distribution functions of the signal-to-noise ratios of the amplification methods.

Finally, in Chapter 8 we present our conclusions for the thesis and future research directions.

1.4 Publications

The majority of the material presented in this thesis is based on the following original papers:

- A. Firag and L. M. Garth, "Joint time-domain decoding and equalization for time reversal-space time block coded systems," in *Proc. IEEE Vehicular Technology Conf.*, Baltimore, MD, USA, Sep. 2007. pp. 506-510.

- A. Firag and L. M. Garth, "Adaptive decoding and equalization for time reversal-space time block-coded cooperative diversity systems," in *Proc. IEEE Int'l. Conf. on Communications*, Beijing, China, May 19-23, 2008. pp. 531-537.

- A. Firag and L. M. Garth, "Adaptive joint decoding and equalization for space-time block-coded amplify-and-forward relaying systems," accepted for publication in *IEEE Trans. Signal Processing.*

- A. Firag and P. J. Smith, "Capacity analysis for MIMO two-hop amplify-and-forward relaying systems," to appear in *Int'l. Symposium on Information Theory and its Applications (ISITA)*, Auckland, New Zealand, 2008.

- A. Firag, P. J. Smith, and M. R. McKay, "Capacity analysis for MIMO two-hop amplify-and-forward relaying systems with the source to destination link,"

submitted to *IEEE Int'l. Conf. on Communications*, 2009.

Chapter 2

Background and Assumptions

In this chapter we present the required background information for the thesis. First, the wireless channel and the fading environment, including the models used in the thesis, are described. This is followed by background information used in Chapters 3 and 4 on space time block codes (STBC) and adaptive block equalization. Finally, wireless relaying systems and MIMO relay capacity analysis are explained.

2.1 Wireless Channel

The characteristics of a wireless channel impose fundamental limitations on the performance of wireless communication systems. The wireless channel can be studied by decomposing it into two parts. Large-scale (long-term) impairments, including path loss and shadowing, and a small-scale (short-term) impairments which are commonly referred to as fading. The large-scale impairments are used to predict the average signal power at the receiver side and the transmission coverage area. Fading is due to the time-varying multipath propagation of the wireless channel. This affects the instantaneous signal-to-noise ratio (SNR). Fading is the major problem encountered in wireless transmission, hence, we focus more on it here.

In wireless signal propagation, the received signal is made up of different components traveling over multiple propagation paths of differing lengths, often with no line-of-sight component. In addition, the signal components do not arrive at the

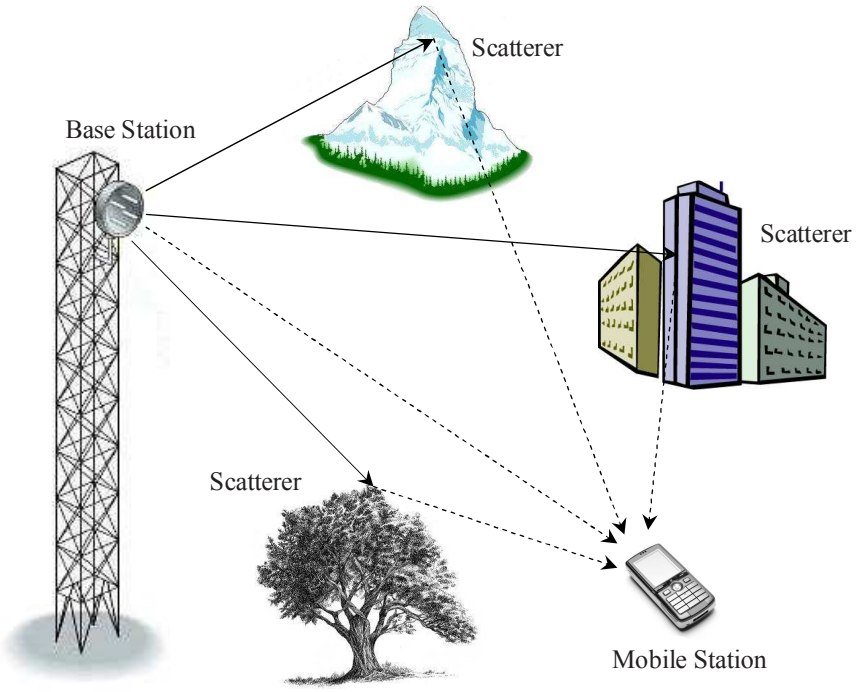

Figure 2.1: Multipath phenomenon in a wireless propagation environment.

receiver in phase with one another, so the strength of the received signal varies with time, and as a result the signal fades. This phenomenon is called *multipath fading* and is illustrated in Fig. 2.1.

In fading, two critical measures of the wireless channel characteristics are the *coherence bandwidth* and *coherence time*. The coherence bandwidth is the frequency range over which the fading process is correlated [7]. If the transmitted signal bandwidth is smaller than the channel coherence bandwidth, then the fading is referred to as *frequency flat*, otherwise it is *frequency selective*. In frequency selective fading, inter-symbol interference (ISI) occurs due to the arrival times of the multipath components being significantly different (large *delay spread*). The coherence time determines how quickly or slowly the channel is changing. Channels with large coherence times change slowly. This thesis includes both frequency flat and selective fading environments. Chapters 3 and 4 deal with frequency selective fading environments whereas Chapters 5, 6 and 7 consider frequency flat scenarios. The channel models used in the thesis are introduced in the following subsection.

2.1.1 Fading SISO Channel

The techniques discussed in Chapters 3 and 4 use multiple-input single-output (MISO) and relay based transmission schemes[1]. Examples of such schemes are shown in Fig. 2.2. Each separate link in Fig. 2.2 can be modeled as a SISO channel. Consider the link between the source and destination nodes in Fig. 2.2.(b). Let the channel between the source and destination be frequency selective with channel impulse response (CIR),

$$\boldsymbol{h} = [h(0), h(1), \ldots, h(V)]^T, \tag{2.1}$$

where V is the channel memory and $[.]^T$ represents the transpose. When $V = 0$, the channel is frequency flat. In the transmission, it is assumed that the nodes use block based transmission with zero-padding (ZP) [22], as shown in Fig. 2.3. ZP is used to eliminate the inter-block interference by placing V zero symbols between each data block. During each block interval, the source transmits N symbols,

$$\boldsymbol{x} = [x(0), \ldots, x(N-1)]^T. \tag{2.2}$$

Then, using a tapped-delay-line channel model [36], the discrete baseband received signal at the destination during the t-th symbol period of the k-th block can be given as

$$y^{(k)}(t) = \sqrt{E_{SD}} \sum_{l=0}^{V} h^{(k,t)}(l) x^{(k)}(t-l) + n^{(k)}(t). \tag{2.3}$$

In (2.3), E_{SD} is the average energy available at the destination, taking into account the path loss and shadowing effects over the source to destination link, $n^{(k)}(t)$ is an additive white complex Gaussian noise with zero-mean and variance σ_D^2, and $h^{(k,t)}(l)$ is the channel coefficient (fade coefficient) of the l-th path.

In the techniques discussed in Chapters 3 and 4, it is assumed that the channels are slowly fading (*quasi-static fading* [9]) so that the channels remain constant for a specified period of time. In this scenario, if the channel remains constant for a

[1]This subsection discusses fading single-input single-output (SISO) channels. These channels are considered only in Chapters 3 and 4, and are not relevant to the other chapters of the thesis.

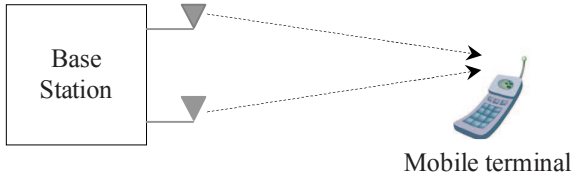

a) MISO transmission.

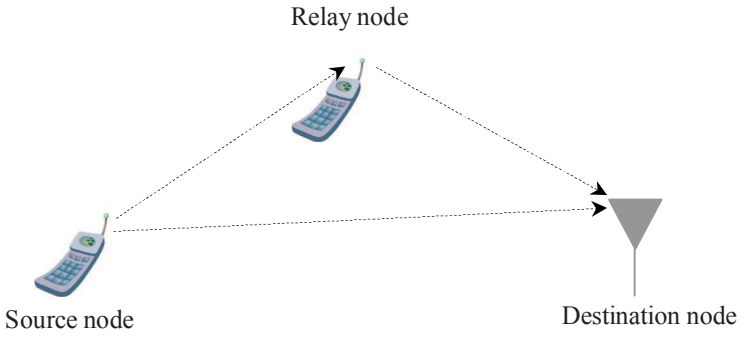

b) Relay assisted transmission.

Figure 2.2: (a) MISO transmission. (b) Relay assisted transmission.

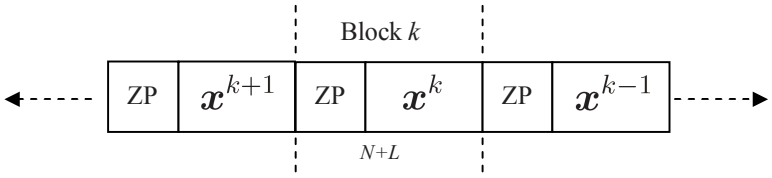

Figure 2.3: Zero-padded transmission.

block period, then $h^{(k,t)}(l) = h^{(k)}(l)$. Now, stacking all of the observations of the block, the received signal during the k-th block can be given as

$$\begin{aligned} \boldsymbol{y}^{(k)} &= \left[y^{(k)}(0), y^{(k)}(1), \ldots, y^{(k)}(N+V-1)\right]^T \\ &= \sqrt{E_{SR}}\, \boldsymbol{H}^{(k)}\, \boldsymbol{x}^{(k)} + \boldsymbol{n}^{(k)}, \end{aligned} \tag{2.4}$$

where

$$\begin{aligned} \boldsymbol{n}^{(k)} &= \left[n^{(k)}(0), n^{(k)}(1), \ldots, n^{(k)}(N+V-1)\right]^T, \\ \boldsymbol{x}^{(k)} &= \left[x^{(k)}(0), x^{(k)}(1), \ldots, x^{(k)}(N-1)\right]^T, \end{aligned} \tag{2.5}$$

and $\boldsymbol{H}^{(k)}$ is the channel convolution matrix. The matrix $\boldsymbol{H}^{(k)}$ has dimension $(N+V) \times N$ and the form

$$\boldsymbol{H}^{(k)} = \begin{bmatrix} \boldsymbol{h}^{(k)} & 0 & \ldots & 0 \\ 0 & \boldsymbol{h}^{(k)} & \ldots & 0 \\ \vdots & \vdots & \ddots & \vdots \\ 0 & 0 & \ldots & \boldsymbol{h}^{(k)} \end{bmatrix}, \tag{2.6}$$

where $\boldsymbol{h}^{(k)} = \left[h^{(k)}(0), h^{(k)}(1), \ldots, h^{(k)}(V)\right]^T$.

The channel coefficients, $h^{(k,t)}(l)$ in (2.3), are time-varying complex random variables. How quickly the channel coefficients vary as a function of t is an important channel parameter, and it depends on the statistical characteristics of the channel. Details about the statistical characteristics of the channels considered in this thesis are presented in the next section.

2.1.2 Statistical Channel Models

In addition to ray-tracing models and spatial geometric models, fading channels are also commonly modeled using a range of different statistical models. The most commonly used models are Ricean and Rayleigh [37]. The former is suitable for an environment where there are many small scatterers or reflectors and also in which a line-of-sight (LOS) path is present. Likewise, the Rayleigh fading channel model is suitable for an environment where there are many small reflectors or scatterers but

no LOS path. In addition, the Rayleigh fading channel model is simple, physically based, reasonable for urban environments and is sometimes considered as a worst case scenario. Hence, we use the Rayleigh fading channel model.

In Rayleigh fading, the channel coefficients, $h^{(k,t)}(l)$, are zero mean circularly symmetric complex Gaussian (ZMCSCG) random variables of variance σ_l^2, denoted by $h^{(k,t)}(l) \sim \mathcal{CN}(0, \sigma_l^2)$. Therefore, the envelope or the magnitude of each channel coefficient, $|h^{(k,t)}(l)|$, is Rayleigh distributed. In most cases the channels are normalized so that the sum of the powers from all paths is equal to one, i.e. $\sum_{l=0}^{V} \sigma_l^2 = 1$.

How quickly a wireless channel or the channel coefficients change with time is an important property in the performance analysis of wireless communication systems. The rate of channel variation has a significant impact on several aspects of the communication problem. A statistical quantity that models this relationship is the *auto-correlation function* of the channel coefficients. There are different models for the auto-correlation function of the channel coefficients, such as the classical Jakes model and the mobile-to-mobile model. We use the classical Jakes model which assumes an omni-directional antenna has waves arriving in the horizontal plane, there are a large number of reflected waves and a uniform received power over the incident angles. The auto-correlation function of the channel coefficients in this case is given as [38],

$$\begin{aligned} R(\tau) &= E\left\{h^{(k,t)}(l)\left[h^{(k,t+\tau)}(l)\right]^*\right\} \\ &= J_0(2\pi f_D \tau), \end{aligned} \tag{2.7}$$

where $E\{.\}$ denotes expectation, $(.)^*$ denotes complex conjugation, $J_0(.)$ represents the zero order Bessel function of the first kind, f_D is the Doppler frequency (maximum Doppler shift), and τ is the time displacement. The Doppler frequency represents the maximum shift in frequency of a multipath wave due to relative motion between the transmitter and the receiver. This can be given as,

$$f_D = \frac{v f_c}{c_0}, \tag{2.8}$$

where v, f_c, and c_0 are the relative speeds of the transmitter and the receiver, the carrier frequency, and the speed of light, respectively.

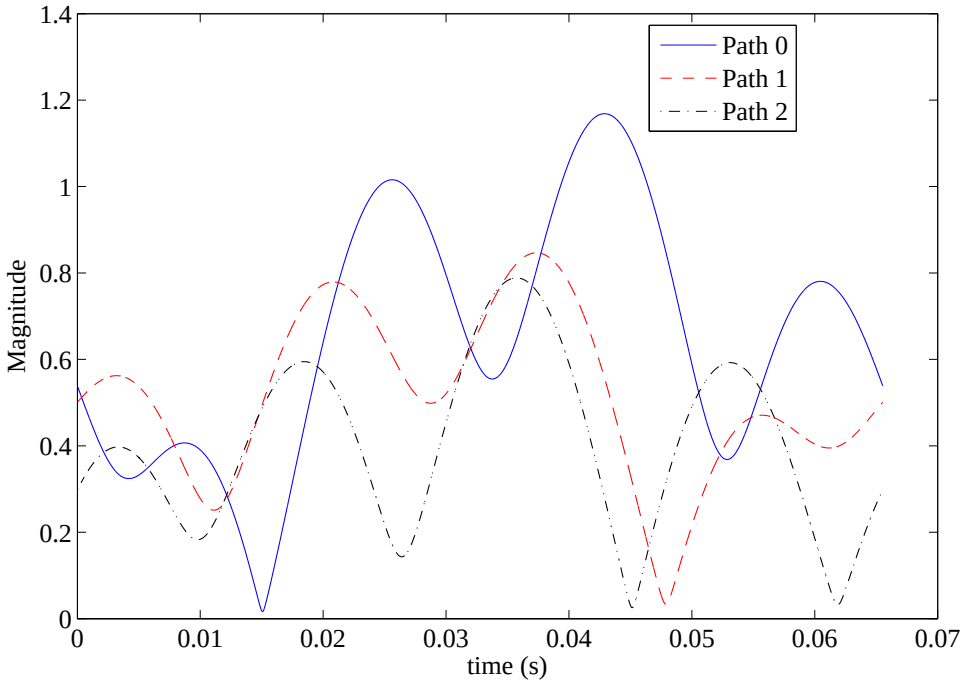

Figure 2.4: Channel coefficient variation with time in a Rayleigh fading channel at 40Hz Doppler.

An example of how a wireless channel changes with time is included here. Consider a frequency selective Rayleigh fading channel with channel memory $V = 2$. The channel is normalized such that $\sigma_0^2 = 0.5$, $\sigma_1^2 = 0.3$ and $\sigma_2^2 = 0.2$. Figure 2.4 shows the channel coefficients' magnitude variation with time at a Doppler frequency of 40Hz. As seen in Fig. 2.4, the channel coefficients vary with time. This variation is dependent on the Doppler frequency. If the Doppler frequency is high the channel variation will be higher within a given time period. Hence, the validity of the assumption that the channel remains constant for a block period will depend on the block period and the rate of channel variation. Thus, if the channel variation is higher, then the block size has to be decreased accordingly to make the assumption valid.

The fading models given in this section are mainly for SISO channels. However, these models can be applied to the MIMO scenario as shown in the next section.

2.1.3 Fading MIMO Channel

Chapters 5, 6 and 7 of the thesis focus on mainly MIMO relaying systems. Any link in a MIMO relaying system can be modeled as a normal MIMO link as shown in Fig. 2.5. The MIMO system shown has n_s transmit and n_d receive antennas, and each antenna of the source station sends a symbol from a complex symbol alphabet within each symbol period. The transmit symbol is encoded, modulated, up-converted and launched into the radio link. At the destination, the signals are down-converted to baseband, sampled, and passed on to the decoder to extract the message. For the sake of convenience, the work considered in this thesis on MIMO relaying assumes that the channels are frequency-flat so that there is no ISI. Also the source and the destination stations are assumed to be perfectly synchronized. In this condition, the received signal at the destination can be given by [37],

$$\boldsymbol{y} = \boldsymbol{H}\boldsymbol{x} + \boldsymbol{n}, \tag{2.9}$$

where $\boldsymbol{x}$ is a vector of n_s transmitted symbols, $\boldsymbol{y}$ is a vector of n_d received observations, $\boldsymbol{n}$ is a circularly symmetrical complex Gaussian noise vector with variance σ_n^2 and $\boldsymbol{H}$ is a $n_d \times n_s$ channel matrix defined by:

$$\boldsymbol{H} = \begin{bmatrix} h_{1,1} & h_{1,2} & \dots & h_{1,n_s} \\ h_{2,1} & h_{2,2} & \dots & h_{2,n_s} \\ \vdots & \vdots & \ddots & \vdots \\ h_{n_d,1} & h_{n_d,2} & \dots & h_{n_d,n_s} \end{bmatrix}. \tag{2.10}$$

The entries of $\boldsymbol{H}$, $h_{i,j}$, are the complex baseband equivalents of the channel coefficients between the jth transmit antenna and the ith receive antenna. In this work it is assumed that the entries of $\boldsymbol{H}$ are independent, identically distributed (i.i.d.) circular symmetric complex Gaussian with zero mean and unit magnitude variance. Hence, $h_{i,j} \sim \mathcal{CN}(0,1)$ and the envelopes of the channel entries are Rayleigh distributed and can be modeled as in Sec. 2.1.2.

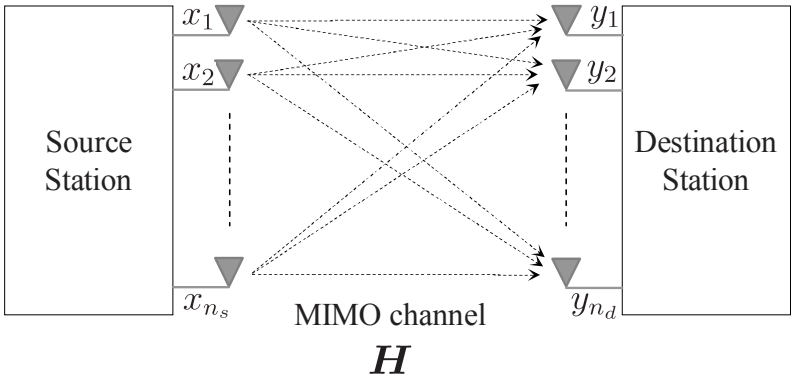

Figure 2.5: Block diagram of a MIMO system.

2.2 Space-Time Block Codes

In wireless communications, diversity techniques are widely used to reduce the the effects of multipath fading as they improve the reliability of transmission without increasing the transmission power or sacrificing the bandwidth [39, 40]. Diversity techniques require multiple copies of the transmitted signals at the receiver, all carrying the same information and not too highly correlated. As a result, the probability of all copies experiencing a simultaneous deep fade will be low compared to the probability that a single copy of the signal is in a deep fade. A number of different methods are used to achieve diversity. These include diversity in time, frequency and space. Space diversity, also called *antenna diversity*, is perhaps the most popular technique. This is implemented by using multiple antennas, usually at the receiver, and is hence known as *receiver diversity*. Receiver diversity can easily be achieved in an uplink (from mobile to base station) scenario by implementing multiple antennas at the base station. However, receiver diversity is more difficult to implement in a down link scenario due to many reasons, such as the size, cost and power requirements of implementing multiple antennas in the mobile terminals. Because of these requirements, it is more practical to use *transmit diversity* for the downlink. In transmit diversity, messages to be transmitted are usually processed at the transmitter and then sent from multiple antennas.

It has been shown that in transmit diversity systems, error performance can be further improved by using error control coding [41, 42]. Codes designed for multiple

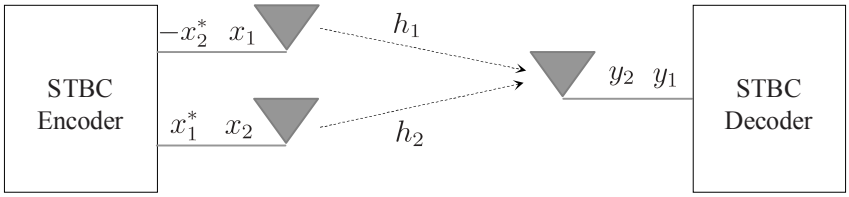

Figure 2.6: Block diagram of an Alamouti scheme.

antenna transmission or transmit diversity are called *space-time codes* (STCs) [9]. There are several different types of coding techniques available today, each with a unique performance and complexity. These codes include, space-time block codes (STBCs), space-time trellis codes (STTCs) and layered space-time codes. In this research, STBCs are used in Chapters 3 and 4 due to their simplicity compared to other STCs. Further, STBC systems specially designed to have orthogonality between the sequences generated by the two transmit antennas can lead to a much simpler receiver structure. Hence, some background STBCs is included here.

2.2.1 Alamouti Space-Time Block Code

The Alamouti STBC [10] is a STBC that provides full transmit diversity for systems with two transmit antennas. In addition, the Alamouti code achieves full transmit diversity gain with a simple decoding algorithm. Figure 2.6 shows a block diagram of an Alamouti scheme.

The STBC encoder outputs are transmitted in two consecutive signal periods from two transmit antennas. During the first signal period, two symbols, x_1 and x_2, are transmitted simultaneously from antennas one and two, respectively. In the second signal period, $-x_2^*$ (x_2 complex conjugated and negated) is transmitted from antenna one and x_1^* from antenna two. Assuming the channels are frequency-flat and the channels' coefficients remain constant for two consecutive signal periods, the received signals during two consecutive signal periods can be given as:

$$y_1 = h_1 x_1 + h_2 x_2 + n_1, \tag{2.11}$$

$$y_2 = -h_1 x_2^* + h_2 x_1^* + n_2. \tag{2.12}$$

In (2.11) - (2.12), h_1 and h_2 are the channel coefficients for channels one and two, respectively, and n_1 and n_2 are additive white complex Gaussian noise terms with zero-mean and variance σ_n^2 for signal periods one and two, respectively. Assuming the channels are known at the receiver, the transmitted symbols can be decoupled using combining as follows. First, we complex conjugate the received signal during the second signal period and stack the signals to give

$$\begin{bmatrix} y_1 \\ y_2^* \end{bmatrix} = \begin{bmatrix} h_1 & h_2 \\ h_2^* & -h_1^* \end{bmatrix} \begin{bmatrix} x_1 \\ x_2 \end{bmatrix} + \begin{bmatrix} n_1 \\ n_2^* \end{bmatrix}. \tag{2.13}$$

Then, the decoder decouples the message symbols using the combining matrix as

$$\begin{aligned} \begin{bmatrix} z_1 \\ z_2 \end{bmatrix} &\triangleq \begin{bmatrix} h_1 & h_2 \\ h_2^* & -h_1^* \end{bmatrix}^{\dagger} \begin{bmatrix} y_1 \\ y_2^* \end{bmatrix} \\ &= \begin{bmatrix} |h_1|^2 + |h_2|^2 & 0 \\ 0 & |h_1|^2 + |h_2|^2 \end{bmatrix} \begin{bmatrix} x_1 \\ x_2 \end{bmatrix} + \begin{bmatrix} h_1^* n_1 + h_2 n_2^* \\ -h_1 n_2^* + h_2^* n_1 \end{bmatrix}, \end{aligned} \tag{2.14}$$

where z_1 and z_2 are the decoder outputs. Note that z_1 is only a function of x_1 and z_2 is only a function of x_2. Hence, a simple estimation rule can be used to estimate the message symbols, x_1 and x_2. As mentioned before, the advantage of the Alamouti code is that it achieves full diversity gain with a simple decoding algorithm. The Alamouti code is designed for frequency-flat fading environments and is not suitable for frequency-selective channels. Hence, Lindskog and Paulraj developed a modified Alamouti code, called the time-reversal space-time block code (TR-STBC), that is suitable for frequency-selective channels [25].

2.2.2 Time-Reversal Space-Time Block Code

Again consider the scenario in which the transmitter has two transmitting antennas and the receiver has one antenna. The TR-STBC encoding is performed in the following manner [25]. Data symbols are transmitted from the antennas in blocks of length N. During the k-th block interval, where k is even, antenna 1 transmits the symbol block,

$$\boldsymbol{x}_1^{(k)} = \left[x_1^{(k)}(0), \ldots, x_1^{(k)}(N-1) \right]^T, \tag{2.15}$$

and antenna 2 transmits the symbol block,

$$\boldsymbol{x}_2^{(k)} = \left[x_2^{(k)}(0), \ldots, x_2^{(k)}(N-1)\right]^T. \tag{2.16}$$

During the $k+1$-th block interval, $\boldsymbol{x}_2^{(k)}$ is time reversed, complex conjugated and negated to create

$$\boldsymbol{x}_1^{(k+1)} = -\widetilde{\boldsymbol{x}}_2^{*(k)} = \left[-x_2^{*(k)}(N-1), \ldots, -x_2^{*(k)}(0)\right]^T. \tag{2.17}$$

This is transmitted by antenna 1. Also, $\boldsymbol{x}_1^{(k)}$ is time reversed and complex conjugated to create

$$\boldsymbol{x}_2^{(k+1)} = \widetilde{\boldsymbol{x}}_1^{*(k)} = \left[x_1^{*(k)}(N-1), \ldots, x_1^{*(k)}(0)\right]^T, \tag{2.18}$$

which is transmitted by antenna 2. After each data block, zero-padding (ZP) consisting of V zero symbols is inserted to prevent inter-block interference, where V is the channel memory.

In TR-STBC, it is assumed that the CIRs of the two channels are fixed over two consecutive blocks. Then, the received blocks

$$\begin{aligned}\boldsymbol{y}^{(k)} &= \left[y^{(k)}(0), \ldots, y^{(k)}(N+V-1)\right]^T,\\ \boldsymbol{y}^{(k+1)} &= \left[y^{(k+1)}(0), \ldots, y^{(k+1)}(N+V-1)\right]^T,\end{aligned}$$

in the presence of additive white noise are given by

$$\begin{aligned}\boldsymbol{y}^{(k)} &= \boldsymbol{H}_1^{(k)}\boldsymbol{x}_1^{(k)} + \boldsymbol{H}_2^{(k)}\boldsymbol{x}_2^{(k)} + \boldsymbol{n}^{(k)},\\ \boldsymbol{y}^{(k+1)} &= \boldsymbol{H}_1^{(k)}\boldsymbol{x}_1^{(k+1)} + \boldsymbol{H}_2^{(k)}\boldsymbol{x}_2^{(k+1)} + \boldsymbol{n}^{(k+1)}.\end{aligned} \tag{2.19}$$

In (2.19) $\boldsymbol{n}^{(k)}$ and $\boldsymbol{n}^{(k+1)}$ are noise vectors with covariance matrix $\sigma_D^2\boldsymbol{I}_{(N+V)}$, and $\boldsymbol{H}_1^{(k)}$ and $\boldsymbol{H}_2^{(k)}$ are the channel convolution matrices for channels 1 and 2, respectively. The noise samples and data symbols are assumed to be i.i.d. with zero means and variances σ_D^2 and σ_x^2, respectively. The matrix $\boldsymbol{H}_i^{(k)}$ has dimension $(N+V)\times N$ and the form

$$\boldsymbol{H}_i^{(k)} = \begin{bmatrix} \boldsymbol{h}_i^{(k)} & 0 & \ldots & 0 \\ 0 & \boldsymbol{h}_i^{(k)} & \ldots & 0 \\ \vdots & \vdots & \ddots & \vdots \\ 0 & 0 & \ldots & \boldsymbol{h}_i^{(k)} \end{bmatrix}, \tag{2.20}$$

where $\boldsymbol{h}_i^{(k)} = \left[h_i^{(k)}(0), h_i^{(k)}(1), \ldots, h_i^{(k)}(V)\right]^T$ is the CIR of the link between the i-th transmitting antenna and the receiver. Using encoding rules (2.17) and (2.18) and stacking the observation vectors, we obtain

$$\begin{aligned}\boldsymbol{y} &= \begin{bmatrix} \boldsymbol{y}^{(k)} \\ \widetilde{\boldsymbol{y}}^{*(k+1)} \end{bmatrix} = \boldsymbol{H}\boldsymbol{x} + \boldsymbol{n} \\ &\triangleq \begin{bmatrix} \boldsymbol{H}_1^{(k)} & \boldsymbol{H}_2^{(k)} \\ \widetilde{\boldsymbol{H}}_2^{*(k)} & -\widetilde{\boldsymbol{H}}_1^{*(k)} \end{bmatrix} \begin{bmatrix} \boldsymbol{x}_1^{(k)} \\ \boldsymbol{x}_2^{(k)} \end{bmatrix} + \begin{bmatrix} \boldsymbol{n}^{(k)} \\ \widetilde{\boldsymbol{n}}^{*(k+1)} \end{bmatrix}, \end{aligned} \tag{2.21}$$

where the matrix $\widetilde{\boldsymbol{H}}_i^{*(k)}$ has the same form as (2.20) with $\boldsymbol{h}_i^{(k)}$ replaced by $\widetilde{\boldsymbol{h}}_i^{*(k)}$ (time-reversed and complex conjugated $\boldsymbol{h}_i^{(k)}$). The matrix $\boldsymbol{H}$ has the property that the transmitted blocks, $\boldsymbol{x}_1^{(k)}$ and $\boldsymbol{x}_2^{(k)}$, become decoupled by multiplying both sides of (2.21) by the matrix

$$\boldsymbol{H}_{\mathrm{d}} = \begin{bmatrix} \widetilde{\boldsymbol{H}}_{1\mathrm{d}}^{*(k)} & \boldsymbol{H}_{2\mathrm{d}}^{(k)} \\ \widetilde{\boldsymbol{H}}_{2\mathrm{d}}^{*(k)} & -\boldsymbol{H}_{1\mathrm{d}}^{(k)} \end{bmatrix} \tag{2.22}$$

where matrices $\boldsymbol{H}_{i\mathrm{d}}^{(k)}$ and $\widetilde{\boldsymbol{H}}_{i\mathrm{d}}^{*(k)}$ have the same form as (2.20) but with dimensions $(N+2V)\times(N+V)$. Thus, the resulting output from the TR-STBC decoder is

$$\begin{aligned}\boldsymbol{z} &= \begin{bmatrix} \boldsymbol{z}_1^{(k)} \\ \boldsymbol{z}_2^{(k)} \end{bmatrix} = \boldsymbol{H}_{\mathrm{d}}\,\boldsymbol{y} \\ &= \begin{bmatrix} \boldsymbol{G}^{(k)} & \boldsymbol{0} \\ \boldsymbol{0} & \boldsymbol{G}^{(k)} \end{bmatrix} \begin{bmatrix} \boldsymbol{x}_1^{(k)} \\ \boldsymbol{x}_2^{(k)} \end{bmatrix} + \boldsymbol{H}_{\mathrm{d}} \begin{bmatrix} \boldsymbol{n}^{(k)} \\ \widetilde{\boldsymbol{n}}^{*(k+1)} \end{bmatrix}, \end{aligned} \tag{2.23}$$

where

$$\begin{aligned}\boldsymbol{G}^{(k)} &= \widetilde{\boldsymbol{H}}_{1\mathrm{d}}^{*(k)}\boldsymbol{H}_1^{(k)} + \boldsymbol{H}_{2\mathrm{d}}^{(k)}\widetilde{\boldsymbol{H}}_2^{*(k)} \\ &= \widetilde{\boldsymbol{H}}_{2\mathrm{d}}^{*(k)}\boldsymbol{H}_2^{(k)} + \boldsymbol{H}_{1\mathrm{d}}^{(k)}\widetilde{\boldsymbol{H}}_1^{*(k)}. \end{aligned}$$

As with the Alamouti code, the TR-STBC decoder output has the property that $\boldsymbol{z}_1^{(k)}$ is only a function of $\boldsymbol{x}_1^{(k)}$ and $\boldsymbol{z}_2^{(k)}$ is only a function of $\boldsymbol{x}_2^{(k)}$. Hence, in TR-STBC systems, the message symbol blocks, $\boldsymbol{x}_1^{(k)}$ and $\boldsymbol{x}_2^{(k)}$, can be estimated separately with a simple equalizer while still achieving the full diversity gain.

2.3 Adaptive Block Equalization

In this section we give a brief review of adaptive block equalization. Adaptive equalization is used in Chapters 3 and 4 in combination with STBC.

Communication systems involving frequency selective channels have delay spread, which causes ISI. *Equalization* is a method that is used in receivers to alleviate the effects of ISI [43]. Equalization techniques fall into two broad categories: *linear* and *nonlinear* methods. Linear techniques, such as zero-forcing (ZF) and minimum mean square error (MMSE) equalization, are generally the simplest to implement. However, nonlinear techniques, such as decision-feedback equalization (DFE) and maximum likelihood sequence estimation (MLSE), have better system performance with higher complexity. The optimal equalization technique is MLSE. Unfortunately, the complexity of this technique grows exponentially with memory length, and is therefore impractical for most channels of interest. Hence, to reduce the complexity of the equalizer and also to achieve reasonable system performance, MMSE equalization methods and their derivatives are used in this research.

Most wireless channels change over time, and hence the CIRs at a given time are not known when the receivers are designed. Therefore, practical receivers must learn the channels and adapt to any channel variation. To do this, the receivers often contain an *adaptive equalizer*. This adaptive equalizer periodically estimates the CIR and updates the equalizer taps accordingly. This process is called *equalizer training*. During training, the equalizer taps are updated based on a known training sequence or block that has been sent over the channel. How often the training block needs to be sent depends on the number of equalizer taps, the convergence speed of the training algorithm and also the rate of the channel variation. There are several types of training algorithms with different complexity and performance levels. The most commonly used algorithms are the LMS and RLS algorithms. The LMS algorithm has lower complexity compared to the RLS algorithm. However, the RLS algorithm has better performance than the LMS algorithm due to faster convergence. In Chapter 3 and 4 the block RLS adaptive algorithm is used instead

of other low complexity adaptive algorithms like LMS. This is because the system involves block equalization so the taps are updated only after each block, and hence very fast channel tracking is required to bring down the training overhead. The RLS method provides the extra convergence speed required. Preliminary simulations showed that the LMS approach did not converge quickly enough. Hence, the block version of the RLS algorithm is described below.

Consider the transmission scenario given in Sec. 2.1.1. The received signal during the k-th block is

$$\boldsymbol{y}^{(k)} = \sqrt{E_{SR}}\, \boldsymbol{H}^{(k)}\, \boldsymbol{x}^{(k)} + \boldsymbol{n}^{(k)}. \tag{2.24}$$

We assume that the block RLS adaptive equalizer has tap weight vector, $\boldsymbol{w}$, with q-taps. Then, the equalizer output is written as $\widehat{\boldsymbol{x}} = \boldsymbol{Y}^{(k)}\, \boldsymbol{w}^{(k)}$, where $\boldsymbol{Y}^{(k)}$ has dimensions $(N + V + q - 1) \times q$ and the form

$$\boldsymbol{Y}^{(k)} = \begin{bmatrix} \boldsymbol{y}^{(k)} & 0 & \dots & 0 \\ 0 & \boldsymbol{y}^{(k)} & \dots & 0 \\ \vdots & \vdots & \ddots & \vdots \\ 0 & 0 & \dots & \boldsymbol{y}^{(k)} \end{bmatrix}. \tag{2.25}$$

Assuming $V + q - 1$ is an even integer, for convenience, the estimation error at the output of the equalizer is $\boldsymbol{e}^{(k)} = \boldsymbol{x}_{\text{ext}}^{(k)} - \boldsymbol{Y}^{(k)}\, \boldsymbol{w}^{(k)}$ where

$$\boldsymbol{x}_{\text{ext}}^{(k)} = \left[\boldsymbol{0}_{1\times[(V+q-1)/2]}, (\boldsymbol{x}^{(k)})^T, \boldsymbol{0}_{1\times[(V+q-1)/2]}\right]^T. \tag{2.26}$$

The cost function to be minimized in the block RLS algorithm can be expressed as [44],

$$J^{(k)} = \sum_{i=1}^{k} \lambda^{k-i} \|\boldsymbol{e}^{(k)}\|^2 + \delta\lambda^k \|\boldsymbol{w}^{(k)}\|^2, \tag{2.27}$$

where λ is a *forgetting factor* which ensures that observations in the distant past are *forgotten* (λ is a positive constant close to but less than unity). The first component of (2.27) is the exponentially-weighted *sum of squared errors*, whereas the second component is a *regularizing term* which smoothes or regularizes the solution to the

otherwise ill-posed recursive least-squares problem [44]. The parameter δ is called the regularizing parameter, which is a small positive constant for high SNR and a large positive constant for low SNR.

It can be shown that the optimum tap-weight vector, $\boldsymbol{w}^{(k)}$, for which the cost function of (2.27) attains its minimum value, satisfies the normal equation

$$\boldsymbol{\Phi}^{(k)}\boldsymbol{w}^{(k)} = \boldsymbol{\kappa}^{(k)}. \tag{2.28}$$

In (2.28), the time-averaged autocorrelation matrix $\boldsymbol{\Phi}^{(k)}$ of the tap-input $\boldsymbol{Y}^{(k)}$ has the form

$$\boldsymbol{\Phi}^{(k)} = \sum_{i=1}^{k} \lambda^{k-i} (\boldsymbol{Y}^{(k)})^{\dagger} \boldsymbol{Y}^{(k)} + \delta\lambda^{k}\boldsymbol{I}_{q}, \tag{2.29}$$

where $\boldsymbol{I}_q$ is the $q \times q$ identity matrix and the $q \times 1$ time-averaged cross-correlation vector, $\boldsymbol{\kappa}^{(k)}$, between the tap inputs and the the desired response is

$$\boldsymbol{\kappa}^{(k)} = \sum_{i=1}^{k} \lambda^{k-i} (\boldsymbol{Y}^{(k)})^{\dagger} \boldsymbol{x}_{\text{ext}}^{(k)}. \tag{2.30}$$

To compute the solution to (2.28) in a recursive manner, it can be shown that $\boldsymbol{\Phi}^{(k)}$ and $\boldsymbol{\kappa}^{(k)}$ can be recursively calculated as

$$\boldsymbol{\Phi}^{(k)} = \lambda\boldsymbol{\Phi}^{(k-1)} + (\boldsymbol{Y}^{(k)})^{\dagger}\boldsymbol{Y}^{(k)}, \tag{2.31}$$

and

$$\boldsymbol{\kappa}^{(k)} = \lambda\boldsymbol{\kappa}^{(k-1)} + (\boldsymbol{Y}^{(k)})^{\dagger}\boldsymbol{x}_{\text{ext}}^{(k)}. \tag{2.32}$$

Table 2.1: Summary of the Block RLS Algorithm

Block RLS Algorithm
Initial conditions: $\boldsymbol{w}^{(0)} = \mathbf{0}_{q\times 1}$ $\boldsymbol{\Phi}^{(0)} = \delta^{-1}\boldsymbol{I}_q$
Update taps at each iteration using: $\boldsymbol{\Phi}^{(k)} = \lambda\boldsymbol{\Phi}^{(k-1)} + (\boldsymbol{Y}^{(k)})^{\dagger}\boldsymbol{Y}^{(k)}$ $\boldsymbol{\epsilon}^{(k)} = \boldsymbol{x}_{\text{ext}}^{(k)} - \boldsymbol{Y}^{(k)}\boldsymbol{w}^{(k-1)}$ $\boldsymbol{w}^{(k)} = \boldsymbol{w}^{(k-1)} + (\boldsymbol{\Phi}^{(k)})^{-1}(\boldsymbol{Y}^{(k)})^{\dagger}\boldsymbol{\epsilon}^{(k)}$ where λ is a small positive constant close to 1

Then, $\boldsymbol{w}^{(k)}$ in (2.28) can be recursively calculated as,

$$
\begin{aligned}
\boldsymbol{w}^{(k)} &= (\boldsymbol{\Phi}^{(k)})^{-1}\boldsymbol{\kappa}^{(k)} \\
&= \boldsymbol{w}^{(k-1)} + (\boldsymbol{\Phi}^{(k)})^{-1}\boldsymbol{\kappa}^{(k)} - \boldsymbol{w}^{(k-1)} \\
&= \boldsymbol{w}^{(k-1)} + (\boldsymbol{\Phi}^{(k)})^{-1}\left[\lambda\boldsymbol{\kappa}^{(k-1)} + (\boldsymbol{Y}^{(k)})^{\dagger}\boldsymbol{x}_{\text{ext}}^{(k)} - \boldsymbol{\Phi}^{(k)}\boldsymbol{w}^{(k-1)}\right] \\
&= \boldsymbol{w}^{(k-1)} \\
&\quad + (\boldsymbol{\Phi}^{(k)})^{-1}\left[\lambda\boldsymbol{\kappa}^{(k-1)} + (\boldsymbol{Y}^{(k)})^{\dagger}\boldsymbol{x}_{\text{ext}}^{(k)} - \lambda\boldsymbol{\Phi}^{(k-1)}\boldsymbol{w}^{(k-1)} - (\boldsymbol{Y}^{(k)})^{\dagger}\boldsymbol{Y}^{(k)}\boldsymbol{w}^{(k-1)}\right] \\
&= \boldsymbol{w}^{(k-1)} + (\boldsymbol{\Phi}^{(k)})^{-1}\left[(\boldsymbol{Y}^{(k)})^{\dagger}\boldsymbol{x}_{\text{ext}}^{(k)} - (\boldsymbol{Y}^{(k)})^{\dagger}\boldsymbol{Y}^{(k)}\boldsymbol{w}^{(k-1)}\right] \\
&= \boldsymbol{w}^{(k-1)} + (\boldsymbol{\Phi}^{(k)})^{-1}(\boldsymbol{Y}^{(k)})^{\dagger}\left[\boldsymbol{x}_{\text{ext}}^{(k)} - \boldsymbol{Y}^{(k)}\boldsymbol{w}^{(k-1)}\right] \\
&\triangleq \boldsymbol{w}^{(k-1)} + (\boldsymbol{\Phi}^{(k)})^{-1}(\boldsymbol{Y}^{(k)})^{\dagger}\boldsymbol{\epsilon}^{(k)}, \qquad (2.33)
\end{aligned}
$$

where $\boldsymbol{\epsilon}^{(k)} = \boldsymbol{x}_{\text{ext}}^{(k)} - \boldsymbol{Y}^{(k)}\boldsymbol{w}^{(k-1)}$ is the a priori estimation error. Note that in the block RLS algorithm, the Matrix Inversion Lemma is not applied, as it increases the dimensionality of the required matrix inversions. The block RLS algorithm is summarized in Table 2.1.

As mentioned before, the adaptive algorithms require training to estimate the channel. During the training period (block), the receiver knows the transmitted symbol block, $\boldsymbol{x}^{(k)}$. Hence, the a priori estimation error can be calculated as $\boldsymbol{\epsilon}^{(k)} = \boldsymbol{x}_{\text{ext}}^{(k)} - \boldsymbol{Y}^{(k)}\boldsymbol{w}^{(k-1)}$. However, when the training period is over, the algorithm operates in *decision directed* mode. In this mode the a priori estimation error is calculated

as $\boldsymbol{\epsilon}^{(k)} = \widetilde{\boldsymbol{x}}_{\text{ext}}^{(k)} - \boldsymbol{Y}^{(k)}\boldsymbol{w}^{(k-1)}$, where

$$\widetilde{\boldsymbol{x}}_{\text{ext}}^{(k)} = \left[\mathbf{0}_{1\times[(V+q-1)/2]}, (\widetilde{\boldsymbol{x}}^{(k)})^T, \mathbf{0}_{1\times[(V+q-1)/2]}\right]^T, \tag{2.34}$$

is the slicer output of the receiver. There are several factors that influence the performance of the adaptive algorithms, such as equalizer length and convergence rate. The adaptive equalizer parameters: training rate, equalizer length and data block length, mainly depend on the characteristics of the communication channel. Hence, once the channel characteristics are known, the adaptive equalizer can choose its parameters accordingly to achieve the optimum performance.

2.4 Wireless Relaying

In this section, cooperative diversity systems using relays with a single antenna per station are described. Then, the necessary background for MIMO techniques in relays is given.

In cellular systems, transmit diversity techniques have generally been considered only for the *downlink* to minimize the number of power-hungry and expensive antennas in the mobile handset. However, to harness the diversity gains afforded by these transmit techniques in the *uplink* as well, while maintaining a minimal number of antennas on each handset, *cooperative diversity* techniques have recently been proposed. These techniques allow a mobile terminal to leverage the spatial diversity offered by other terminals' antennas to form a virtual multiple-antenna array [21, 1, 22]. The basic idea is that the source terminal uses other terminals as relays to forward its information to the destination terminal. In general, there are two types of relaying systems, non-regenerative and regenerative systems [20], depending on the nature and the complexity of the relays used. In regenerative systems, also called decode-and-forward (DF) relaying systems, the relay fully decodes the received signal and retransmits the decoded symbol to the destination. Non-regenerative systems, also called amplify-and-forward (AF) systems, use less complex relays that do not perform any sort of decoding. The relay simply amplifies

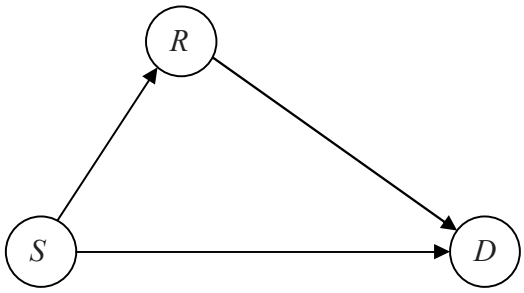

Figure 2.7: Relaying topology

the received signal and forwards it to the destination. The most basic amplification method used in wireless relaying is that the relay terminal amplifies the received signal from the source by using the second order statistics of the source to relay channel [1, 29]. In this method, the amplification factor, a, of the relay terminal is a constant and is calculated as:

$$a = \sqrt{\frac{P_r}{E\left\{\boldsymbol{y}_r^{\dagger}\,\boldsymbol{y}_r\right\}}}, \tag{2.35}$$

where $\boldsymbol{y}_r$ is the received signal at the relay, $a\,\boldsymbol{y}_r$ is the transmitted signal from the relay terminal and P_r is the average transmit power of the relay.

Nabar *et al.* [1] have proposed three different cooperative transmission protocols that can be used for three terminal based relaying systems, shown in Fig. 2.7. In *Protocol I*, the source (S) terminal communicates with both the relay (R) and the destination (D) terminals during the first time slot. During the second time slot of the block, both S and R transmit information to D. In *Protocol II*, S communicates with R and D over the first time slot. In the second time slot, only R communicates with D. *Protocol III* is identical to Protocol I except that D chooses not to receive during the first time slot. These protocols are summarized in Table 2.2. In the table, $A \rightarrow B$ represents communication between A and B.

A variety of cooperative diversity systems with a single relay terminal have been studied and analyzed in [45, 46, 47]. They have shown that cooperative diversity systems based on a single antenna per terminal can realize spatial diversity gains.

Relaying systems have been of interest since the 1970s [18, 19]. The main objective of such systems is to increase the coverage and reduce the need to use high

Table 2.2: Three Protocols Proposed by Nabar *et al.* [1].

Time Slot	Protocol I	Protocol II	Protocol III
1	$S \rightarrow R$, $S \rightarrow D$	$S \rightarrow R$, $S \rightarrow D$	$S \rightarrow R$
2	$S \rightarrow D$, $R \rightarrow D$	$R \rightarrow D$	$S \rightarrow D$, $R \rightarrow D$

power transmissions at the source terminal. The basic idea of a relaying system is that the source terminal uses other terminals or relays to forward its information to the destination terminal. Wireless relaying networks have recently been given considerable attention due to their many advantages. Apart from increasing the coverage, relaying networks can also achieve better diversity by using cooperative transmission from several relays as explained above. It is also well known that MIMO systems can provide better system capacity than single-input, SISO systems [5]. Hence, relaying has recently been extended to MIMO scenarios [23, 24] to obtain better system capacity, increases in range, and also to achieve better diversity. The only difference between the cooperative diversity systems described above and MIMO relaying systems is that in MIMO relaying, the terminals can have multiple antennas.

2.5 MIMO System Capacity

System capacity is defined as the maximum possible transmission rate such that the probability of error is arbitrarily small. Capacity analysis of a system is useful for gaining insights into the effects of various system parameters on its performance. Today, a wide range of results are available for the capacity analysis of various MIMO systems [48, 31, 5, 33]. This section presents an overview of the material required for such an analysis which is required in Chapters 5 and 6. Throughout the thesis it is assumed that the channel state information (CSI) is not known at the transmitter but is perfectly known at the receiver. Thus, we now derive the capacity of MIMO systems assuming that the CSI is not known at the transmitter

but perfectly known at the receiver.

2.5.1 Singular Value Decomposition

The Singular Value Decomposition (SVD) is a useful tool to analyze MIMO systems. Consider the received signal at the destination of the MIMO system described in Sec. 2.1.3,

$$\boldsymbol{y} = \boldsymbol{H}\boldsymbol{x} + \boldsymbol{n}. \tag{2.36}$$

Using the SVD, the channel matrix $\boldsymbol{H}$ can be written as

$$\boldsymbol{H} = \boldsymbol{U}\boldsymbol{D}\boldsymbol{V}^{\dagger}, \tag{2.37}$$

where $\boldsymbol{D}$ is an $n_d \times n_s$ non-negative diagonal matrix and $\boldsymbol{U} \in \mathcal{C}^{n_d \times n_d}$ and $\boldsymbol{V} \in \mathcal{C}^{n_s \times n_s}$ are unitary matrices. The notation $\mathcal{C}^{x \times y}$ denoted as a $x \times y$ matrix of complex numbers. The diagonal elements of $\boldsymbol{D}$, $\sqrt{\lambda_1} \geqslant \sqrt{\lambda_2} \geqslant \ldots \geqslant \sqrt{\lambda_m}$, are the positive singular values of the channel matrix $\boldsymbol{H}$, where $m = \min(n_s, n_d)$ is the rank of $\boldsymbol{H}$. Then, using the SVD, the channel correlation matrix can be decomposed using the standard eigenvalue decomposition as

$$\boldsymbol{H}\boldsymbol{H}^{\dagger} = \boldsymbol{U}\boldsymbol{D}\boldsymbol{D}^{\dagger}\boldsymbol{U}^{\dagger}. \tag{2.38}$$

Furthermore, the columns of $\boldsymbol{U}$ are the eigenvectors of $\boldsymbol{H}\boldsymbol{H}^{\dagger}$ and the columns of $\boldsymbol{V}$ are the eigenvectors of $\boldsymbol{H}^{\dagger}\boldsymbol{H}$.

Then, by substituting (2.37) into (2.36), the received signal can be written as

$$\boldsymbol{y} = \boldsymbol{U}\boldsymbol{D}\boldsymbol{V}^{\dagger}\boldsymbol{x} + \boldsymbol{n}. \tag{2.39}$$

Premultiplying $\boldsymbol{y}$ by $\boldsymbol{U}^{\dagger}$, results in

$$\begin{aligned} \boldsymbol{y}' \triangleq \boldsymbol{U}^{\dagger}\boldsymbol{y} &= \boldsymbol{D}\underbrace{\boldsymbol{V}^{\dagger}\boldsymbol{x}}_{\boldsymbol{x}'} + \underbrace{\boldsymbol{U}^{\dagger}\boldsymbol{n}}_{\boldsymbol{n}'} \\ &= \boldsymbol{D}\boldsymbol{x}' + \boldsymbol{n}'. \end{aligned} \tag{2.40}$$

Note that a unitary transformation of an i.i.d. Gaussian vector (or matrix) does not change the statistical properties of the vector (or matrix). Hence, the vector $\boldsymbol{n}' = \boldsymbol{U}^{\dagger}\boldsymbol{n}$ is statistically independent to the vector $\boldsymbol{n}$. Rewriting (2.40) gives

$$\begin{aligned} y_i' &= \sqrt{\lambda_i} x_i' + n_i', \qquad i = 1, 2, \ldots, m \\ y_i' &= n_i', \qquad i = m+1, m+2, \ldots, n_d. \end{aligned} \tag{2.41}$$

From (2.41), only m received components depend on the transmitted signal and the equivalent system described in (2.41) has no interference . Thus, the MIMO channel can be considered as consisting of m uncoupled parallel sub-channels, each with a singular value of the channel matrix as the amplitude channel gain.

2.5.2 Capacity

Since the MIMO channel can be described as a set of m uncoupled sub-channels, the overall capacity is the sum of the individual capacities. Assuming that the transmit power from each antenna in the MIMO system is P/n_s, the ergodic channel capacity, denoted as C, can be given as [11],

$$C = E\left\{\sum_{i=1}^{m} \log_2\left(1 + \frac{\lambda_i P}{n_s \sigma_n^2}\right)\right\}, \tag{2.42}$$

where $E\{\cdot\}$ denotes expectation with respect to the random vector $\boldsymbol{\lambda} = (\lambda_1, \ldots, \lambda_m)^T$. Using results in [11], the ergodic channel capacity of the MIMO systems given in (2.42) can also be given in matrix form as

$$C = E\left\{\log_2\left|\boldsymbol{I}_m + \frac{P}{n_s \sigma_n^2}\boldsymbol{W}\right|\right\}, \tag{2.43}$$

where $|\cdot|$ denotes the determinant and $\boldsymbol{W}$ is a *Wishart matrix* defined as

$$\boldsymbol{W} = \begin{cases} \boldsymbol{H}\boldsymbol{H}^{\dagger} & n_d < n_s \\ \boldsymbol{H}^{\dagger}\boldsymbol{H} & n_d \geqslant n_s \end{cases}. \tag{2.44}$$

Then, rewriting (2.43) gives:

$$C = E\left\{\log_2\left|\boldsymbol{I}_m + \frac{P}{n_s \sigma_n^2}\boldsymbol{W}\right|\right\} = m\int_0^{\infty} \log_2\left(1 + \frac{P}{n_s \sigma_n^2}\lambda\right) f(\lambda)\, d\lambda, \tag{2.45}$$

where λ denotes an arbitrary eigenvalue of $\boldsymbol{W}$ and $f(\lambda)$ is the probability density function (PDF) of λ. Hence, to find the ergodic capacity of the MIMO system using this approach, the arbitrary eigenvalue distribution of the random matrix $\boldsymbol{W}$ is needed.

2.5.3 Statistics of Wishart Distributions

Here, the Wishart distribution is described and the joint eigenvalue density of the Wishart matrix is given. From this density, the PDF of an arbitrary eigenvalue of the Wishart matrix can be obtained.

The matrix $\boldsymbol{W}$, defined in Sec. 2.5.2, has a *Wishart distribution* with parameters, m and $n = \max(n_s, n_d)$. The joint density of the unordered eigenvalues of $\boldsymbol{W}$ is given as [11, 49]

$$f(\lambda_1, \ldots, \lambda_m) \triangleq f(\boldsymbol{\lambda}) = \frac{\pi^{m(m-1)}}{m!\,\mathcal{C}\Gamma_m(m)\,\mathcal{C}\Gamma_m(n)} \prod_{k=1}^{m} \lambda_k^{n-m} e^{-\lambda_k} \prod_{k<p}^{m} (\lambda_k - \lambda_p)^2, \quad (2.46)$$

where $\mathcal{C}\Gamma_m(n)$ denotes the complex multivariate gamma function,

$$\mathcal{C}\Gamma_m(n) = \pi^{m(m-1)/2} \prod_{k=1}^{m} \Gamma(n-k+1). \quad (2.47)$$

Then, the PDF of an arbitrary eigenvalue of $\boldsymbol{W}$, $f(\lambda)$, can be obtained as,

$$f(\lambda_1) = \int_0^\infty \ldots \int_0^\infty f(\boldsymbol{\lambda})\, d\lambda_2 \ldots\, d\lambda_m. \quad (2.48)$$

Using this result, the ergodic capacity of the MIMO system given in (2.45) can be evaluated.

2.5.4 Pseudo-Wishart Distribution

The pseudo-Wishart distribution [50], a form of Wishart distribution, plays an important role in the analysis of communication systems using diversity in Rayleigh fading. In MIMO systems, one situation where the pseudo-Wishart distribution arises is when the transmitted signals are independent but the received signals are correlated. Consider the MIMO channel matrix $\boldsymbol{H}$ given in (2.36) to explain the

pseudo-Wishart distribution. Let the columns of the matrix $\boldsymbol{H}$ be given by $\boldsymbol{h}_i$; i.e., $\boldsymbol{H} = [\boldsymbol{h}_1, \ldots, \boldsymbol{h}_{n_s}]$, where $i = 1, \ldots, n_s$. Assume that the transmitted signals are independent but the received signals are correlated in Rayleigh fading, then $\boldsymbol{h}_1, \ldots, \boldsymbol{h}_{n_s}$, are $n_d \times 1$ independent zero-mean complex circular Gaussian random vectors such that each $\boldsymbol{h}_i$ has a $\mathcal{CN}(\boldsymbol{0}, \boldsymbol{\Sigma})$ distribution, where

$$\boldsymbol{\Sigma} = E\left\{\boldsymbol{h}_i \boldsymbol{h}_i^{\dagger}\right\}. \tag{2.49}$$

Then, the matrix $\boldsymbol{H}\boldsymbol{H}^{\dagger}$ has a Wishart distribution when $n_s \geqslant n_d$ and a pseudo-Wishart distribution when $n_s < n_d$. The important point to note is that when $\boldsymbol{\Sigma}$ is not a scaled version of $\boldsymbol{I}_{n_d}$ and $n_s < n_d$, the Hermitian matrix $\boldsymbol{H}\boldsymbol{H}^{\dagger}$ has a pseudo-Wishart distribution. However, the matrix $\boldsymbol{H}^{\dagger}\boldsymbol{H}$ does not have a Wishart distribution. It is only when $\boldsymbol{\Sigma}$ is a scaled version of $\boldsymbol{I}_{n_d}$ and $n_s < n_d$, $\boldsymbol{H}\boldsymbol{H}^{\dagger}$ pseudo-Wishart and $\boldsymbol{H}^{\dagger}\boldsymbol{H}$ is Wishart. Therefore, there are situations where pseudo-Wishart and Wishart distributions cannot be exchanged. In such a situation, we have to use statistics of the pseudo-Wishart distribution for the analysis.

Chapter 3

Adaptive Time-Domain Block Equalization for TR-STBC Decoding

One of the main problems in wireless transmission is the time-varying multipath fading of the wireless channel. However, spatial diversity techniques have been proven to be effective at mitigating this multipath fading. In [10], Alamouti proposed a transmit diversity scheme for flat fading channels that achieve the same diversity benefits as can be achieved by receive diversity, while requiring only linear decoding complexity. In [25], Lindskog and Paulraj have extended Alamouti's method for frequency selective fading channels. Their time reversal-space time block coding (TR-STBC) scheme combines time-domain filtering, conjugation and time reversal operations. The outputs of the TR-STBC decoder are decoupled but contain residual inter-symbol interference (ISI) which must be mitigated using equalizers. Unfortunately, to perform this equalization, the optimal maximum likelihood sequence estimation (MLSE) techniques have exponentially increasing complexity with the signal constellation size and the channel impulse response length.

Several more practical block STBC structures for frequency selective fading channels, including single carrier-frequency domain equalizers (SC-FDE) [26] and orthog-

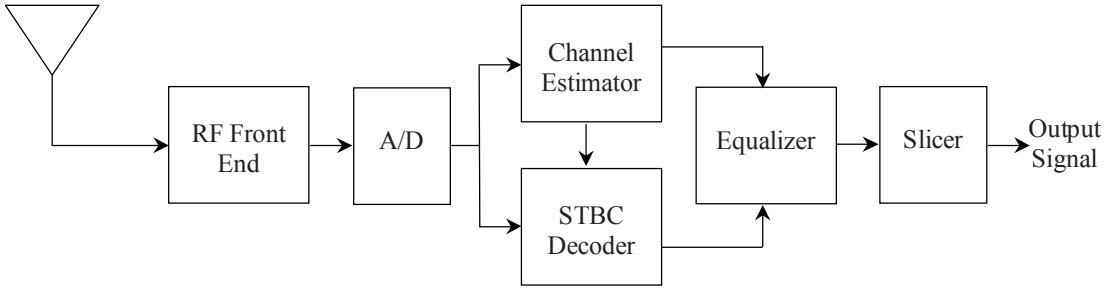

Figure 3.1: STBC receiver block diagram with channel estimation.

onal frequency division multiplexing (OFDM) transcievers [27], have been proposed. In these schemes, the decoding and equalization of the STBC transmissions require explicit estimation of the channel impulse response (CIR) at the receiver as shown in Fig. 3.1. Usually, channel estimation is done by adding a training sequence to each transmitted block and using it to estimate the channel, which tends to increase the system overhead. Reduction of the system overhead requires using longer blocks, which may not be viable for channels with fast variations.

An improved approach is an adaptive joint decoder and equalizer or *adaptive receiver* structure that does not require separate CIR estimation, reducing the system overhead and at the same time providing a tracking mechanism for time-varying channels. The main advantage of adaptive receivers is that they can eliminate the need for adding a training sequence to each data block. They use a few training blocks during initialization, and then they can track the channel variations in decision-directed mode. In this way, the system overhead can be reduced. One of the important performance parameters of the adaptive equalizers is how fast the equalizers track the channel variation. Usually, this depends on the type of adaptive algorithms used and also the length of the equalizers. If the length is short the equalizers converge faster, hence, adapting to the channel variation quickly. But, on the other hand, if the length is too short, the equalizer will not be able to remove the ISI completely. Hence, the performance will decreases. Therefore, to get better performance from the adaptive equalizers, a system designer must be be able to choose a suitable minimum equalizer length for the channel so that it can track the channel faster while not loosing too much performance due to the shorter equalizer

length.

In [28], such a adaptive receiver scheme has been proposed for SC FDE-STBC systems. One advantage of this particular scheme is that it delivers recursive least squares (RLS) performance using least mean square (LMS)-order complexity. However, as the scheme is based on frequency domain block equalization, the equalizer is constrained to have the same length as the data block length. This means that the length and hence, the complexity of the equalizer grows as the block length increases, even when the CIR is very short. Therefore, the scheme is advantageous primarily for channels with very long delay spreads.

Exploiting the efficiency of processing the received data in the time-domain, in this chapter we present an adaptive joint decoder and equalizer scheme for TR-STBC systems with an equalizer length that is independent of the block length, making it suitable for channels with short CIRs. Specifically, we propose a time-domain block equalizer for TR-STBC transceivers, which eliminates the need for a separate decoding block requiring explicit channel estimation. The block equalizer length is also independent of the data block length, making it particularly suitable for short delay spread channels. We first use the TR-STBC encoding and decoding process explained in Sec. 2.2.2 to derive the MMSE equalizer. Then, from the MMSE equalizer, our adaptive receiver scheme is derived. Finally, using simulations, the performance of the time-domain RLS based adaptive receiver is presented and compared with the frequency domain adaptive receiver given in [28].

3.1 MMSE Equalizer

Consider the TR-STBC encoding and decoding process given in Sec. 2.2.2, which is also depicted in Fig. 3.2. As seen in (2.23), the transmitted blocks $\boldsymbol{x}_1^{(k)}$ and $\boldsymbol{x}_2^{(k)}$ are decoupled by the decoder, but still the decoupled blocks have ISI within them. Hence, an equalizer needs to be used to remove the ISI.

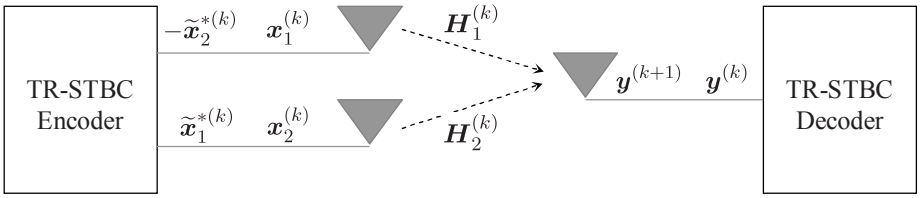

Figure 3.2: TR-STBC encoder and decoder.

The decoupled outputs from the TR-STBC decoder are given by

$$\begin{aligned}\boldsymbol{z}_1 &= \boldsymbol{G}\,\boldsymbol{x}_1 + \widetilde{\boldsymbol{H}}_{1\mathrm{d}}^{*}\,\boldsymbol{n} + \boldsymbol{H}_{2\mathrm{d}}\,\widetilde{\boldsymbol{n}}^{*} \\ \boldsymbol{z}_2 &= \boldsymbol{G}\,\boldsymbol{x}_2 + \widetilde{\boldsymbol{H}}_{2\mathrm{d}}^{*}\,\boldsymbol{n} - \boldsymbol{H}_{1\mathrm{d}}\,\widetilde{\boldsymbol{n}}^{*},\end{aligned} \tag{3.1}$$

where the superscripts, (k) and $(k+1)$, are dropped from the notation. We see that the decoupled signals have equal channel gain matrices and it can be shown that the noise statistics are the same. Therefore, the same MMSE tap weights can be applied to both blocks, $\boldsymbol{z}_1$ and $\boldsymbol{z}_2$, to remove the ISI. Hence, we only consider a block of one decoder's outputs, $\boldsymbol{z}_1 = [z_1(0), \ldots, z_1(N+2V-1)]^T$, when deriving the MMSE solution for the equalizer taps.

It is assumed that the q-tap equalizer is symbol spaced with a tap weight vector $\boldsymbol{w}$. For convenience, q is assumed to be an odd integer. The output of the block equalizer is written as, $\widehat{\boldsymbol{x}}_1 = \boldsymbol{Z}_1\,\boldsymbol{w}$, where $\boldsymbol{Z}_1$ has dimension $(N+2V+q-1)\times q$ and has the form

$$\boldsymbol{Z}_1 = \begin{bmatrix} \boldsymbol{z}_1 & 0 & \ldots & 0 \\ 0 & \boldsymbol{z}_1 & \ldots & 0 \\ \vdots & \vdots & \ddots & \vdots \\ 0 & 0 & \ldots & \boldsymbol{z}_1 \end{bmatrix}. \tag{3.2}$$

The estimation error at the output of the equalizer is

$$\boldsymbol{e}_1 = \boldsymbol{x}_{1\mathrm{ext}} - \boldsymbol{Z}_1\,\boldsymbol{w} \tag{3.3}$$

where $\boldsymbol{x}_{1\mathrm{ext}} = \left[\boldsymbol{0}_{1\times[(2V+q-1)/2]}, \boldsymbol{x}_1^T, \boldsymbol{0}_{1\times[(2V+q-1)/2]}\right]^T$.

To minimize the mean square error (MSE)

$$\boldsymbol{J}(\boldsymbol{w}) = E\left\{\left\|\boldsymbol{x}_{1\mathrm{ext}} - \boldsymbol{Z}_1\,\boldsymbol{w}\right\|^2\right\}, \tag{3.4}$$

with respect to the tap weight vector, $\boldsymbol{w}$, we take the gradient with respect to $\boldsymbol{w}^*$ and set the result equal to zero, yielding the optimum minimum mean square error (MMSE) equalizer tap weight vector

$$\boldsymbol{w}_o = \Big[E\{\boldsymbol{Z}_1^\dagger\,\boldsymbol{Z}_1\}\Big]^{-1}\,E\{\boldsymbol{Z}_1^\dagger\,\boldsymbol{x}_{1\text{ext}}\}\,. \tag{3.5}$$

It can be shown that the $(q \times q)$-dimensional autocorrelation matrix, $E\{\boldsymbol{Z}_1^\dagger\,\boldsymbol{Z}_1\}$, has the form

$$E\{\boldsymbol{Z}_1^\dagger\,\boldsymbol{Z}_1\} = \begin{bmatrix} \text{Tr}_0(\boldsymbol{R}_z) & \text{Tr}_1(\boldsymbol{R}_z) & \dots & \text{Tr}_{(q-1)}(\boldsymbol{R}_z) \\ \text{Tr}_{-1}(\boldsymbol{R}_z) & \text{Tr}_0(\boldsymbol{R}_z) & \dots & \text{Tr}_{(q-2)}(\boldsymbol{R}_z) \\ \vdots & \vdots & \ddots & \vdots \\ \text{Tr}_{-(q-1)}(\boldsymbol{R}_z) & \text{Tr}_{-(q-2)}(\boldsymbol{R}_z) & \dots & \text{Tr}_0(\boldsymbol{R}_z) \end{bmatrix}, \tag{3.6}$$

where

$$\boldsymbol{R}_z = E\{\boldsymbol{z}_1\,\boldsymbol{z}_1^\dagger\} = \sigma_x^2\boldsymbol{G}\,\boldsymbol{G}^\dagger + \sigma_n^2\widetilde{\boldsymbol{H}}_{1\text{d}}^{*}\,\widetilde{\boldsymbol{H}}_{1\text{d}}^{*\dagger} + \sigma_n^2\boldsymbol{H}_{2\text{d}}\,\boldsymbol{H}_{2\text{d}}^\dagger,$$

is the autocorrelation matrix of $\boldsymbol{z}_1$, and $\text{Tr}_k(\boldsymbol{R}_z)$ is the k-th off-diagonal trace of matrix $\boldsymbol{R}_z$. Similarly, defining the q-dimensional cross-correlation vector $\boldsymbol{p} \triangleq E\{\boldsymbol{Z}_1^\dagger\,\boldsymbol{x}_{1\text{ext}}\}$, it can be shown that its k-th row can be written

$$\begin{aligned} \boldsymbol{p}(k,1) = \text{Tr}_0\{[\boldsymbol{G}(&\max(1, V+1+p-k):\\ &\min(N+2V, V+N+p-k),\\ &\max(1, 1-V-p+k):\\ &\min(N, N+V-p+k))]^\dagger\}, \end{aligned} \tag{3.7}$$

where $p = (q+1)/2$ and we use MATLAB notation $\boldsymbol{G}(i:j,\, k:\ell)$ to represent the submatrix formed by taking the i-th through j-th rows of the k-th through ℓ-th columns of $\boldsymbol{G}$. The optimum MMSE equalizer tap weights can be obtained by substituting (3.6) and (3.7) into (3.5).

The TR-STBC decoder and the MMSE equalizer derived above require channel state information at the receiver. The aim of the next section is to design an adaptive receiver which does not require channel state information at the receiver.

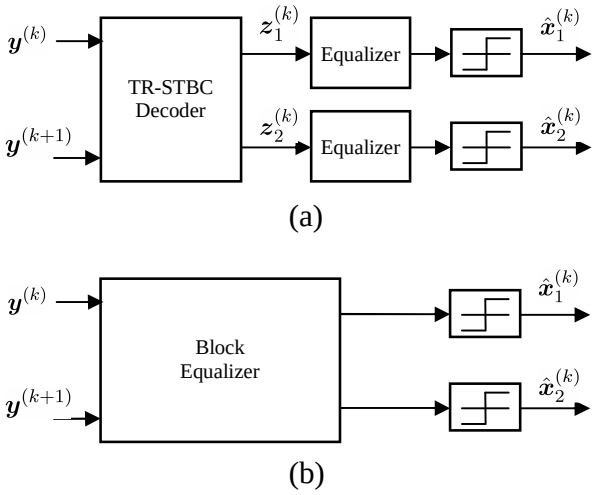

Figure 3.3: (a) Separate decoder and equalizer for TR-STBC receiver (b) Combined decoder and equalizer for TR-STBC receiver.

3.2 Adaptive Receiver Scheme

To design the adaptive receiver, the first step is to combine the TR-STBC decoding and equalization operations using a single time-domain block equalizer, moving from block diagram (a) to (b) in Fig. 3.3. Using the property that the Wiener tap weight vector $\boldsymbol{w}_o$ is the same for both outputs $\boldsymbol{z}_1$ and $\boldsymbol{z}_2$, from (2.21) – (2.23), the equalizer outputs for the two streams can be written as

$$\begin{aligned}\begin{bmatrix} \widehat{\boldsymbol{x}}_1 \\ \widehat{\boldsymbol{x}}_2 \end{bmatrix} &= \begin{bmatrix} \boldsymbol{W} & \boldsymbol{0} \\ \boldsymbol{0} & \boldsymbol{W} \end{bmatrix} \begin{bmatrix} \boldsymbol{z}_1 \\ \boldsymbol{z}_2 \end{bmatrix} \\ &= \begin{bmatrix} \boldsymbol{W}\,\widetilde{\boldsymbol{H}}_{1\mathrm{d}}^{*(k)} & \boldsymbol{W}\,\boldsymbol{H}_{2\mathrm{d}}^{(k)} \\ \boldsymbol{W}\,\widetilde{\boldsymbol{H}}_{2\mathrm{d}}^{*(k)} & -\boldsymbol{W}\,\boldsymbol{H}_{1\mathrm{d}}^{(k)} \end{bmatrix} \begin{bmatrix} \boldsymbol{y}^{(k)} \\ \widetilde{\boldsymbol{y}}^{*(k+1)} \end{bmatrix}, \end{aligned} \tag{3.8}$$

where equalizer matrix $\boldsymbol{W}$ has dimension $(N+2V+q-1)\times(N+2V)$ and has the form shown in (2.20) with $\boldsymbol{h}_i^{(k)}$ replaced by $\boldsymbol{w}$. Using the analysis of Sec. 3.1, it can be also shown that optimal tap weight vector $\boldsymbol{w}_o$ has the conjugate time-reversal symmetry property $\boldsymbol{w}_o = \widetilde{\boldsymbol{w}}_o^*$. Enforcing this property on the time-domain equalizer

(TDE), (3.8) can be rewritten as

$$\begin{aligned}\begin{bmatrix} \widehat{\boldsymbol{x}}_1 \\ \widehat{\boldsymbol{x}}_2 \end{bmatrix} &= \begin{bmatrix} \widetilde{\boldsymbol{W}}^* \widetilde{\boldsymbol{H}}_{1\mathrm{d}}^* & \boldsymbol{W}\boldsymbol{H}_{2\mathrm{d}} \\ \widetilde{\boldsymbol{W}}^* \widetilde{\boldsymbol{H}}_{2\mathrm{d}}^* & -\boldsymbol{W}\boldsymbol{H}_{1\mathrm{d}} \end{bmatrix} \begin{bmatrix} \boldsymbol{y}^{(k)} \\ \widetilde{\boldsymbol{y}}^{*(k+1)} \end{bmatrix} \\ &\triangleq \begin{bmatrix} \widetilde{\boldsymbol{A}}_1^* & \boldsymbol{A}_2 \\ \widetilde{\boldsymbol{A}}_2^* & -\boldsymbol{A}_1 \end{bmatrix} \begin{bmatrix} \boldsymbol{y}^{(k)} \\ \widetilde{\boldsymbol{y}}^{*(k+1)} \end{bmatrix}, \end{aligned} \tag{3.9}$$

where joint equalizer-channel matrices $\boldsymbol{A}_1 = \boldsymbol{W}\boldsymbol{H}_{1\mathrm{d}}$ and $\boldsymbol{A}_2 = \boldsymbol{W}\boldsymbol{H}_{2\mathrm{d}}$. Time reversing and conjugating $\widehat{\boldsymbol{x}}_2$, we have

$$\begin{bmatrix} \widehat{\boldsymbol{x}}_1 \\ \widetilde{\widehat{\boldsymbol{x}}}_2^* \end{bmatrix} = \begin{bmatrix} \widetilde{\boldsymbol{A}}_1^* \boldsymbol{y}^{(k)} + \boldsymbol{A}_2 \widetilde{\boldsymbol{y}}^{*(k+1)} \\ \boldsymbol{A}_2 \widetilde{\boldsymbol{y}}^{*(k)} - \widetilde{\boldsymbol{A}}_1^* \boldsymbol{y}^{(k+1)} \end{bmatrix}. \tag{3.10}$$

Defining the combined equalizer and decoder vectors, $\widetilde{\boldsymbol{w}}_1^* = \mathrm{conv}(\boldsymbol{w}, \boldsymbol{h}_1)$ and $\boldsymbol{w}_2 = \mathrm{conv}(\boldsymbol{w}, \boldsymbol{h}_2)$ of length $q_a = q + V$, the combined decoder and equalizer output can be written as

$$\begin{bmatrix} \widehat{\boldsymbol{x}}_1^{(k)} \\ \widetilde{\widehat{\boldsymbol{x}}}_2^{*(k)} \end{bmatrix} = \begin{bmatrix} \boldsymbol{Y}^{(k)} & \widetilde{\boldsymbol{Y}}^{*(k+1)} \\ -\boldsymbol{Y}^{(k+1)} & \widetilde{\boldsymbol{Y}}^{*(k)} \end{bmatrix} \begin{bmatrix} \boldsymbol{w}_1 \\ \boldsymbol{w}_2 \end{bmatrix} \triangleq \boldsymbol{U}\boldsymbol{w}^{(k)}, \tag{3.11}$$

where matrix $\boldsymbol{Y}^{(i)}$ has dimension $(N+2V+q-1)\times(q+V)$ and has the form shown in (2.20) with $\boldsymbol{h}_i^{(k)}$ replaced by $\boldsymbol{y}^{(i)}$ and $\widetilde{\boldsymbol{Y}}^{*(i)}$ is formed by replacing $\boldsymbol{y}^{(i)}$ by $\widetilde{\boldsymbol{y}}^{*(i)}$ in $\boldsymbol{Y}^{(i)}$.

The equalizer tap weights $\boldsymbol{w}^{(k)}$ in (3.11) are now isolated, and can be easily adapted using the block version of the RLS algorithm [44]. At the output of the block equalizer, the estimation error vector $\boldsymbol{e}^{(k)}$ is

$$\boldsymbol{e}^{(k)} \triangleq \begin{bmatrix} \boldsymbol{e}_1^{(k)} \\ \boldsymbol{e}_2^{(k)} \end{bmatrix} = \begin{bmatrix} \boldsymbol{x}_{1\mathrm{ext}}^{(k)} \\ \widetilde{\boldsymbol{x}}_{2\mathrm{ext}}^{*(k)} \end{bmatrix} - \begin{bmatrix} \widehat{\boldsymbol{x}}_1^{(k)} \\ \widetilde{\widehat{\boldsymbol{x}}}_2^{*(k)} \end{bmatrix} \tag{3.12}$$

where

$$\begin{aligned} \boldsymbol{x}_{1\mathrm{ext}}^{(k)} &= \left[\boldsymbol{0}_{1\times[(2V+q-1)/2]}, (\boldsymbol{x}_1^{(k)})^T, \boldsymbol{0}_{1\times[(2V+q-1)/2]}\right]^T \\ \widetilde{\boldsymbol{x}}_{2\mathrm{ext}}^{*(k)} &= \left[\boldsymbol{0}_{1\times[(2V+q-1)/2]}, (\widetilde{\boldsymbol{x}}_2^{*(k)})^T, \boldsymbol{0}_{1\times[(2V+q-1)/2]}\right]^T. \end{aligned}$$

Using a similar procedure to that described in Chapter 2, the RLS algorithm can be derived and is summarized in Table 3.1.

Table 3.1: Block RLS Algorithm for TR-STBC Systems

Block RLS Algorithm
Initial conditions: $\boldsymbol{w}^{(0)} = \mathbf{0}_{2q_a \times 1}$ $\boldsymbol{\Phi}^{(0)} = \boldsymbol{I}_{2q_a \times 2q_a}$
Update taps at each iteration using: $\boldsymbol{\Phi}^{(k+2)} = \lambda \boldsymbol{\Phi}^{(k)} + \boldsymbol{U}^{\dagger}\boldsymbol{U}$ $\boldsymbol{w}^{(k+2)} = \boldsymbol{w}^{(k)} + (\boldsymbol{\Phi}^{(k+2)})^{-1}\boldsymbol{U}^{\dagger}\boldsymbol{e}^{(k)}$ where λ is small positive close to 1

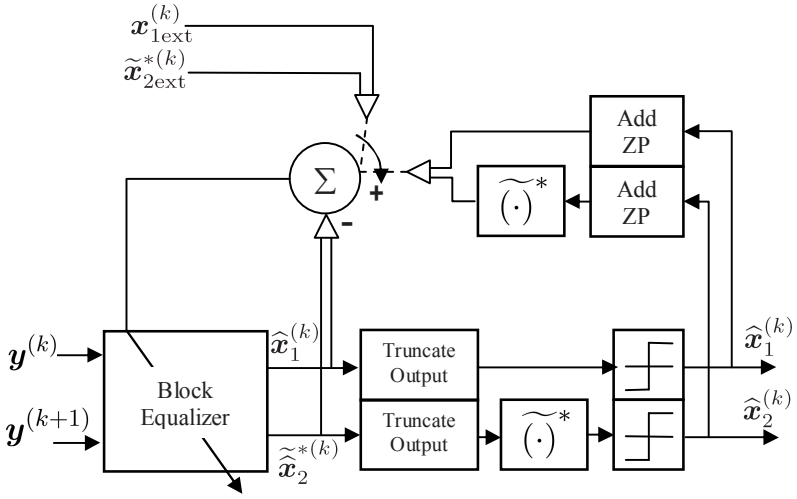

Figure 3.4: Adaptive receiver block diagram for TR-STBC system.

The block diagram of the adaptive receiver is depicted in Fig. 3.4. Because the matrix $\boldsymbol{U}$ contains four convolution sub-matrices and the convolution operation is commutative, an equivalent linear filter representation for the block equalizer is shown in Fig. 3.5. After stripping off the head and tail of the equalizer output block and a conjugate time-reversal operation, the slicer produces the symbol estimates. The output of the equalizer is compared with the desired response to generate the error vector, $\boldsymbol{e}^{(k)}$, which is then used to update the equalizer tap weights according to the adaptive algorithm. The equalizer operates in training mode for the training blocks within a frame and switches to decision directed mode for the data blocks.

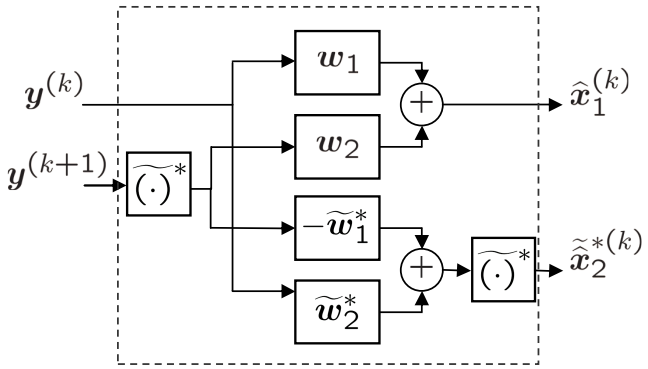

Figure 3.5: Equivalent time-domain filter representation of block equalizer.

3.3 Simulation Results and Discussions

To simulate the adaptive TDE for TR-STBC systems, a 4-QAM system is implemented with a symbol rate of 271 kSymbols/s. The typical urban (TU) channel [51] is used with a GMSK transmit pulse shape [36]. In this case, the overall length of the CIR memory plus pulse shaping is $V = 3$.

We also compared our adaptive scheme for TR-STBC systems with the adaptive scheme that was proposed for SC FDE-STBC systems in [28]. The TR-STBC system results are denoted as 'TDE' and the SC FDE-STBC system results are denoted as 'FDE'. Unless otherwise noted, a block size of $N = 256$ symbols is used with a ZP or cyclic-prefix (CP) length of 3 symbols. In the FDE case, CP is used instead of ZP.

As the number of taps in the TDE is independent of the data block size, an initial simulation is needed to find a suitable length for the TDE operating over the TU channel. Figure 3.6 shows the MMSE as a function of the number of TDE taps for different signal-to-noise ratio (SNR) values. The figure also shows the MMSE for the FDE. Because the FDE is forced to have as many equalizer taps as the block size, the length of the FDE is kept constant at 256. We see that the optimum length of the TDE increases with SNR but is much less than the length of the FDE. As a conservative value, which works well for all of the SNR values, we choose a TDE length of $q_a = 12$ for the remaining simulations in this chapter.

The faster an equalizer converges, the less training symbols are required and

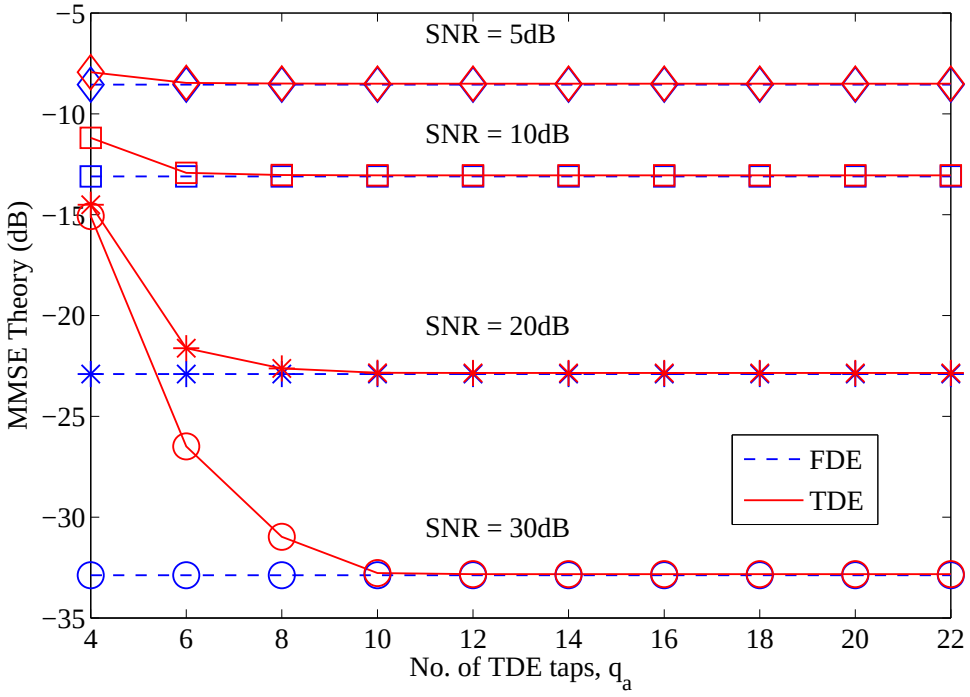

Figure 3.6: MMSE vs. TDE tap length.

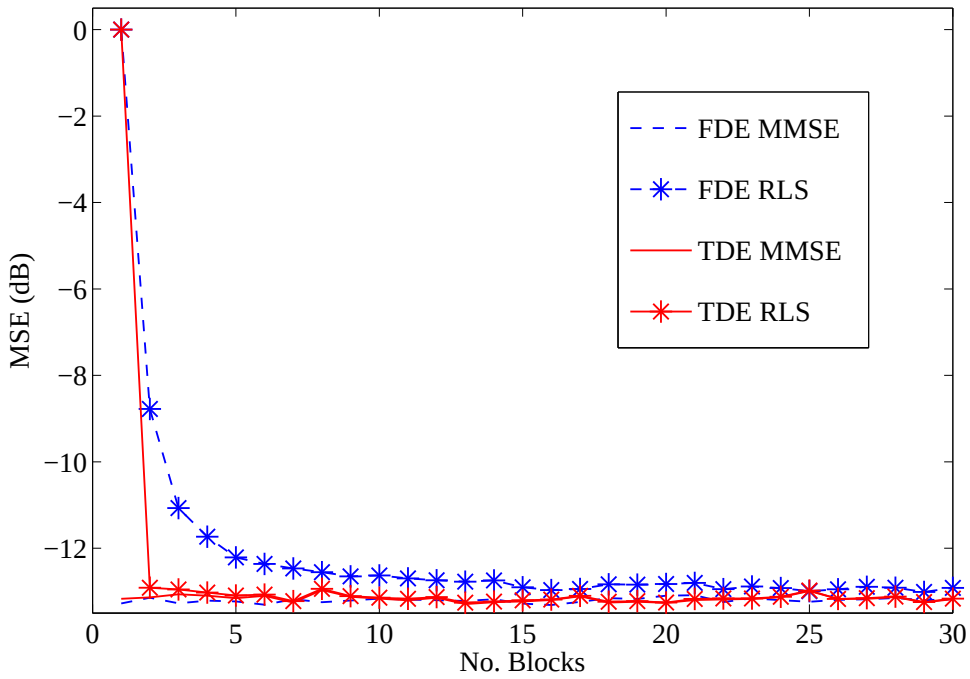

Figure 3.7: MSE convergence trajectories (SNR = 10dB).

the better the equalizer can track time-varying channels. Here, the MSE dynamic convergence of the TDE and FDE equalizers is compared. Figure 3.7 shows the convergence behaviors of the RLS TDE and FDE adaptive algorithm. Again, the theoretical MMSE solutions for the two equalizers are given as references. The step size parameters of the RLS adaptive algorithm for the TDE and FDE were set to $\lambda = 0.9$. Figure 3.7 shows that the TDE running the RLS algorithm converges the fastest (within one block) to the MMSE solution, whereas the FDE RLS adaptive algorithm takes several blocks to reach the MMSE solution. The main reason for the FDE to converge at a slower rate than the TDE might be due to the larger tap length of the FDE compared to the TDE.

The steady-state SER performances are also considered for the two equalizers, where each steady-state SER is measured during the data payload portions of the transmission frame. Although the analysis assumes that the channel is constant for two consecutive data blocks, in simulations, the TU channel varies from symbol to symbol with a Doppler frequency of 10Hz to more realistically model a real world fading environment. For this simulation, Frame Structure A (Fig. 3.8) is used, which has a total of 16 blocks of which 4 blocks are used for training. A ZP/CP of length 3 symbols is inserted after/before each block. The training and data blocks have the same size, $N = 256$. The step size parameter, λ, also plays an important role in the performance of the adaptive equalizers. By decreasing λ the system is more stable and the steady state value of MSE decreases, however the convergence of the adaptive algorithm will get slower [44]. Therefore, the basic rule should be that for a faster varying channel, λ has to be bigger to achieve faster convergence. In this simulation, simulation is performed for all possible values of λ in a grid on [0,1] and the value giving the minimum SER value is chosen. The results are shown in Fig. 3.9. The TDE RLS outperforms the FDE RLS algorithm. The main reason is that the TDE RLS requires far fewer equalizer taps than the FDE RLS for the considered channel. However, the tap length of the FDE RLS is fixed with the data block length ($N = 256$) even though the channel is very short. Therefore, the TDE RLS algorithm adapt much faster to the changing channel than the FDE RLS

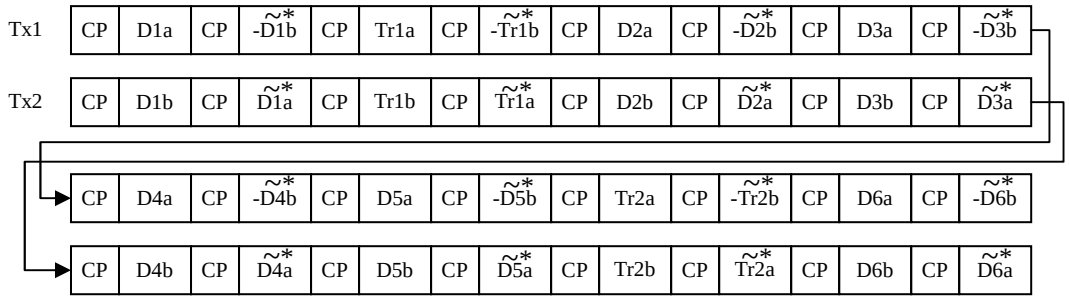

Figure 3.8: Frame Structure A.

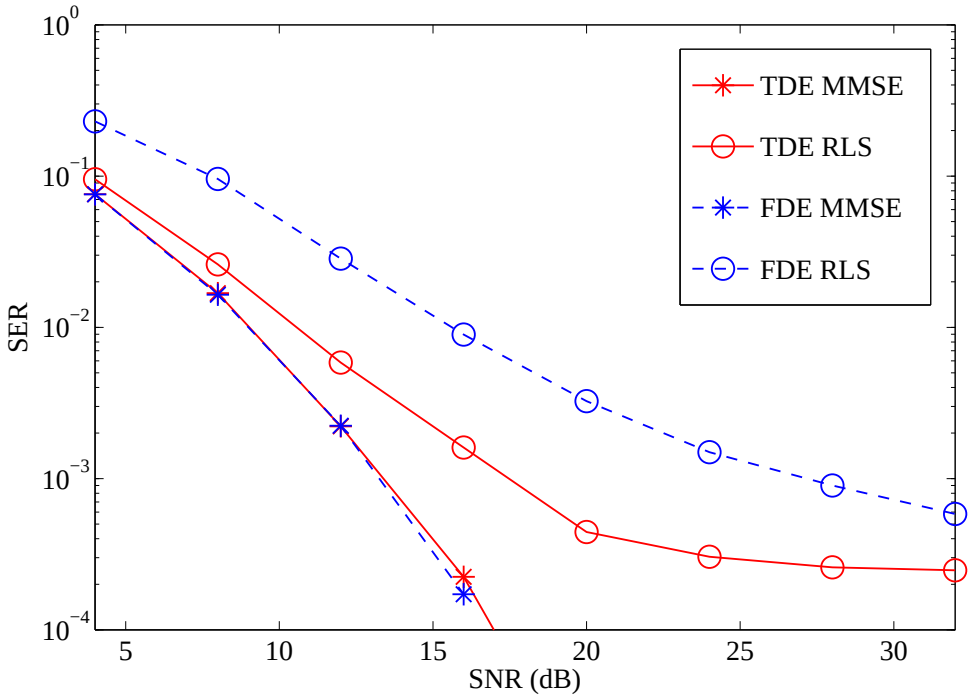

Figure 3.9: SER curves for TDE and FDE at 10Hz Doppler frequency.

algorithm. As a reference we also include the MMSE (non-adaptive) SER values where the receiver has perfect knowledge of the CIR at the middle of each individual transmission block. The MMSE SERs are almost the same for both FDE and TDE schemes. Figure 3.9 also shows an error floor for the higher SNR regions of both adaptive schemes. This floor is due to the fact that adaptive schemes require more time to converge to the optimum value at higher SNR values. One possible solution for this is to increase the rate of training or decrease the block size. However, both these options will increase the system overhead.

One of the advantages of our new TDE scheme over the existing FDE scheme

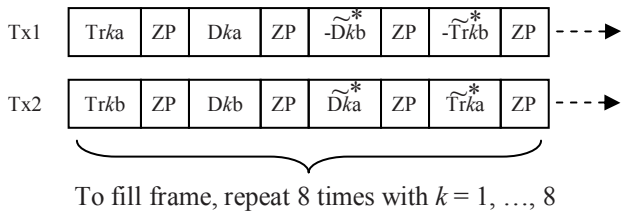

Figure 3.10: Frame Structure B.

is that we can use different length training and data blocks in the frame structure. This makes it easier to mix training and data evenly throughout the frame without affecting the bandwidth efficiency of the system. Such a mix allows the system to perform better in fast time-varying channels than frame structures that segregate the training and data into equal length blocks (e.g., Frame Structure A). On the other hand, the FDE system requires the same-length data and training blocks. Using this property of the TDE scheme, Frame Structure B (Fig. 3.10) is introduced in which data blocks are encapsulated by short training blocks, and at the same time keeping the total overhead equal to Frame Structure A. In Frame Structure B, each block is followed by a ZP of length 3 symbols, and each data block and training block has a length of 192 and 58 symbols, respectively. Using a 10Hz Doppler frequency, the results are shown in Fig. 3.11. In the figure 'TDE A' denotes the results for Frame Structure A and 'TDE B' denotes those for Frame Structure B. Clearly, TDE B outperforms TDE A, as the new frame structure allows the TDE to better track the fast time-varying channel conditions.

Overall, the adaptive TDE scheme proposed has better system performance compared to the existing adaptive FDE scheme. However, one of the advantages of the FDE scheme is that it has a lower complexity. Hence, to compare both schemes, it is also important to know the complexity of the schemes on a comparable basis. In the next section we analyze the complexity of the schemes.

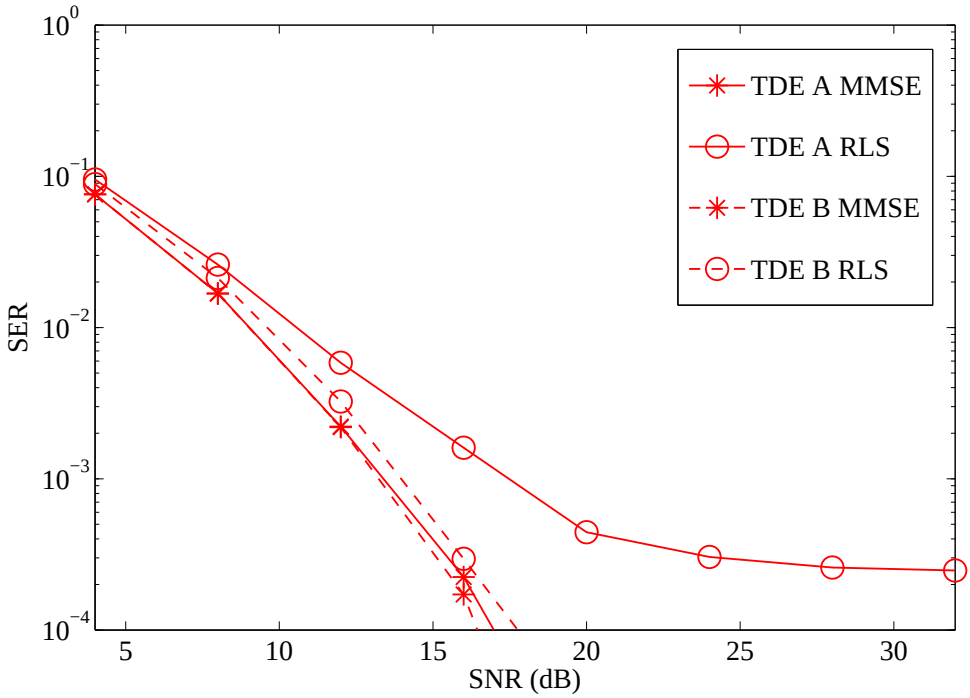

Figure 3.11: SER curves for TDE A and TDE B at 10Hz Doppler frequency.

3.4 Complexity of the Adaptive Algorithms

In this section, the complexities involved in computing the TDE and FDE RLS algorithms are considered. For the complexity analysis, we evaluate the total number of real multiplications, additions and divisions involved in computing the algorithms.

3.4.1 TDE RLS Algorithm

The TDE RLS algorithm is given in Table 3.1. The following steps explain the complexity involved in computing the TDE RLS equalizer output and the tap weight adaptation. These computations involve linear convolutions and correlations. Comparing research articles [52, 53, 54] on fast convolution and correlation for large samples, it seems that the fast fourier transform (FFT) algorithm is the best option. Hence, the FFT algorithm is used to compute the linear convolutions and correlations.

1. Equalizer output, $\boldsymbol{U}\boldsymbol{w}^{(k)}$ computation: the adaptive equalizer output consists of

four linear convolutions:

$$\begin{aligned}
&\boldsymbol{Y}^{(k)}\boldsymbol{w}_1 = \text{conv}(\boldsymbol{y}^{(k)}, \boldsymbol{w}_1),\\
&-\boldsymbol{Y}^{(k+1)}\boldsymbol{w}_1 = \text{conv}(-\boldsymbol{y}^{(k+1)}, \boldsymbol{w}_1),\\
&\widetilde{\boldsymbol{Y}}^{*(k+1)}\boldsymbol{w}_2 = \text{conv}(\widetilde{\boldsymbol{y}}^{*(k+1)}, \boldsymbol{w}_2), \text{ and}\\
&\widetilde{\boldsymbol{Y}}^{*(k)}\boldsymbol{w}_2 = \text{conv}(\widetilde{\boldsymbol{y}}^{*(k)}, \boldsymbol{w}_2).
\end{aligned}$$

Each of these convolutions can be implemented using the FFT algorithm as

$$\text{conv}(\boldsymbol{y}^{(l)}, \boldsymbol{w}_m) = \text{IFFT}(\text{diag}(\text{FFT}(\boldsymbol{y}^{(l)}))\text{FFT}(\boldsymbol{w}_m)) \tag{3.13}$$

where each FFT has $N + V + q_a - 1$ points. By using the FFT algorithm, the computation of the equalizer output is shown in the Fig. 3.12. From Fig. 3.12, the equalizer output computation requires 8 FFT operations, four $N+V+q_a-1$ complex multiplications and two $N + V + q_a - 1$ complex additions. Each N-point FFT operation requires $2N \log_2 N$ real multiplications and $3N \log_2 N$ real additions [52]. By defining $M = N+V+q_a-1$, the equalizer output computation requires $16M \log_2 M + 16M$ real multiplications and $24M \log_2 M + 12M$ real additions.

2. Estimation error vector, $\boldsymbol{e}^{(k)}$ computation: the estimation error vector, $\boldsymbol{e}^{(k)}$, is given in (3.12). Computing the error vector only requires $4N$ real additions, as $\boldsymbol{x}_{\ell\text{ext}}^{(k)}$ consists of zero padding before and after $\boldsymbol{x}_{\ell}^{(k)}$.

3. The $\boldsymbol{U}^{\dagger}\boldsymbol{U}$ computation: before trying to evaluate $\boldsymbol{U}^{\dagger}\boldsymbol{U}$, we define some important properties of time reversal matrices using the exchange matrix $\boldsymbol{E}_m$. The exchange matrix, $\boldsymbol{E}_m$, is a $m \times m$ square matrix with ones along the cross-diagonal and zeros elsewhere [55]. The inverse of $\boldsymbol{E}_m$ is $\boldsymbol{E}_m$ so that $\boldsymbol{E}_m\boldsymbol{E}_m = \boldsymbol{I}_m$, where $\boldsymbol{I}_m$ is an identity matrix of size $m \times m$. If $\boldsymbol{A}$ is a matrix of size $m \times n$, then the time reversal matrix of $\boldsymbol{A}$ is given by

$$\widetilde{\boldsymbol{A}} = \boldsymbol{E}_m\boldsymbol{A}\boldsymbol{E}_n \tag{3.14}$$

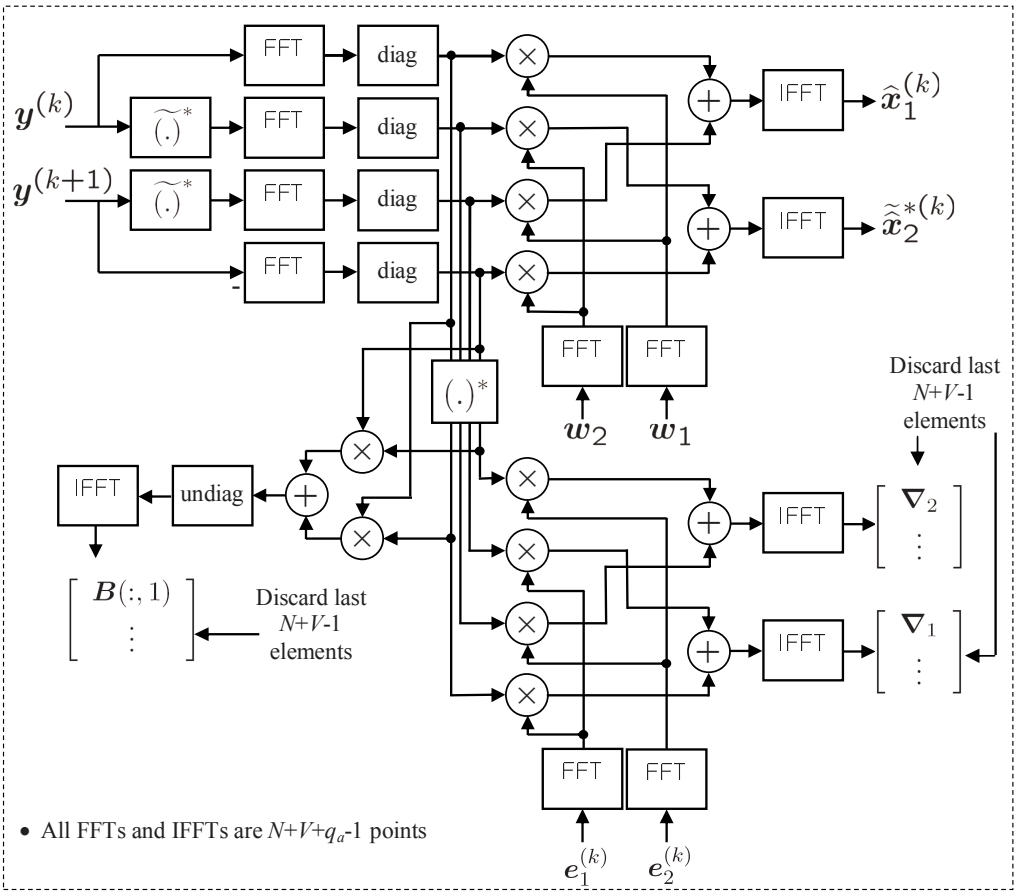

Figure 3.12: Equalizer output and tap weight adaptation of the TDE RLS algorithm.

and if $\boldsymbol{A}$ is a Toeplitz square matrix of size $m \times m$, then

$$\widetilde{\boldsymbol{A}} = \boldsymbol{A}^T = \boldsymbol{E}_m \boldsymbol{A} \boldsymbol{E}_m. \tag{3.15}$$

Using these matrix properties, $\boldsymbol{U}^\dagger \boldsymbol{U}$ can be computed. Defining $m = N + V + q_a - 1$ and $n = q_a$, then $\boldsymbol{U}$ can be written

$$\boldsymbol{U} = \begin{bmatrix} \boldsymbol{Y}^{(k)} & \boldsymbol{E}_m \boldsymbol{Y}^{*(k+1)} \boldsymbol{E}_n \\ -\boldsymbol{Y}^{(k+1)} & \boldsymbol{E}_m \boldsymbol{Y}^{*(k)} \boldsymbol{E}_n \end{bmatrix}. \tag{3.16}$$

Hence, the matrix $\boldsymbol{U}^\dagger \boldsymbol{U}$ can be evaluated as,

$$\begin{aligned} \boldsymbol{U}^\dagger \boldsymbol{U} &= \begin{bmatrix} (\boldsymbol{Y}^{(k)})^\dagger \boldsymbol{Y}^{(k)} + (\boldsymbol{Y}^{(k+1)})^\dagger \boldsymbol{Y}^{(k+1)} & \boldsymbol{0} \\ \boldsymbol{0} & (\boldsymbol{Y}^{(k)})^\dagger \boldsymbol{Y}^{(k)} + (\boldsymbol{Y}^{(k+1)})^\dagger \boldsymbol{Y}^{(k+1)} \end{bmatrix} \\ &\triangleq \begin{bmatrix} \boldsymbol{B} & \boldsymbol{0} \\ \boldsymbol{0} & \boldsymbol{B} \end{bmatrix}. \end{aligned} \tag{3.17}$$

The matrices $(\boldsymbol{Y}^{(k)})^\dagger \boldsymbol{Y}^{(k)}$, $(\boldsymbol{Y}^{(k+1)})^\dagger \boldsymbol{Y}^{(k+1)}$ and $\boldsymbol{B} = (\boldsymbol{Y}^{(k)})^\dagger \boldsymbol{Y}^{(k)} + (\boldsymbol{Y}^{(k+1)})^\dagger \boldsymbol{Y}^{(k+1)}$ are Hermitian Toeplitz. Therefore, to compute these matrices only the first column or first row of each matrix needs to be calculated. The first column of matrix $\boldsymbol{B}$ can be calculated using the FFT algorithm as shown in Fig. 3.12. This only requires 1 FFT operation, $2M$ complex multiplications and M complex additions. Therefore, the $\boldsymbol{U}^\dagger \boldsymbol{U}$ computation requires a total of $2M \log_2 M + 8M$ real multiplications and $3M \log_2 M + 6M$ real additions.

4. The $\boldsymbol{\Phi}^{(k+2)} = \lambda \boldsymbol{\Phi}^{(k)} + \boldsymbol{U}^\dagger \boldsymbol{U}$ computation: from the properties of the matrix, $\boldsymbol{U}^\dagger \boldsymbol{U}$, it can be shown that the matrix $\boldsymbol{\Phi}^{(k+2)}$ is a Hermitian matrix and has the following form,

$$\boldsymbol{\Phi}_{k+2} = \begin{bmatrix} \boldsymbol{A} & \boldsymbol{0} \\ \boldsymbol{0} & \boldsymbol{A} \end{bmatrix} \tag{3.18}$$

where $\boldsymbol{A}$ is Hermitian Toeplitz. Hence $\boldsymbol{\Phi}^{(k)}$ is also Hermitian and has the same form as $\boldsymbol{\Phi}^{(k+2)}$. Therefore, to calculate $\boldsymbol{\Phi}^{(k+2)}$, we only need to compute the first column or row of the Hermitian Toeplitz matrix, $\boldsymbol{A}$. First, the λ multiplication requires $2q_a$ real multiplications, and then the addition of $\lambda \boldsymbol{\Phi}^{(k)}$ and $\boldsymbol{U}^\dagger \boldsymbol{U}$ requires $2q_a$ real additions.

5. The $(\boldsymbol{\Phi}^{(k+2)})^{-1}$ computation: from matrix inversion properties, the inverse of $\boldsymbol{\Phi}^{(k+2)}$ has the form,

$$(\boldsymbol{\Phi}^{(k+2)})^{-1} = \begin{bmatrix} \boldsymbol{A} & \boldsymbol{0} \\ \boldsymbol{0} & \boldsymbol{A} \end{bmatrix}^{-1} = \begin{bmatrix} \boldsymbol{A}^{-1} & \boldsymbol{0} \\ \boldsymbol{0} & \boldsymbol{A}^{-1} \end{bmatrix}. \tag{3.19}$$

Therefore, computing $(\boldsymbol{\Phi}^{(k+2)})^{-1}$ only requires computing the inverse of the Hermitian Toeplitz matrix $\boldsymbol{A}$. Here the Trench algorithm given in [55] is used to calculate the inverse of the Hermitian Toeplitz matrix $\boldsymbol{A}$. Using this algorithm, the $(\boldsymbol{\Phi}^{(k+2)})^{-1}$ computation requires $10q_a^2 - 23q_a + 14$ real multiplications, $9q_a^2 - 17q_a + 10$ real additions, and q_a real divisions.

6. The $\boldsymbol{w}^{(k+2)} = \boldsymbol{w}^{(k)} + (\boldsymbol{\Phi}^{(k+2)})^{-1}\boldsymbol{U}^{\dagger}\boldsymbol{e}^{(k)}$ computation: defining,

$$\boldsymbol{e}^{(k)} = \begin{bmatrix} \boldsymbol{e}_1^{(k)} \\ \boldsymbol{e}_2^{(k)} \end{bmatrix}, \tag{3.20}$$

$$\boldsymbol{U}^{\dagger}\boldsymbol{e}^{(k)} = \begin{bmatrix} \boldsymbol{\nabla}_1 \\ \boldsymbol{\nabla}_2 \end{bmatrix} \tag{3.21}$$

and then using Fig. 3.12, the $\boldsymbol{U}^{\dagger}\boldsymbol{e}^{(k)}$ computation requires 4 FFT operations, $4M$ complex multiplications and $2M$ complex additions. The required real operations are $8M\log_2 M + 16M$ real multiplications and $12M\log_2 M + 12M$ real additions. The multiplication of $(\boldsymbol{\Phi}^{(k+2)})^{-1}$ and $\boldsymbol{U}^{\dagger}\boldsymbol{e}^{(k)}$ requires $8q_a^2$ real multiplications and $8q_a^2 - 4q_a$ real additions. Finally, the addition of $\boldsymbol{w}^{(k)}$ and $(\boldsymbol{\Phi}^{(k+2)})^{-1}\boldsymbol{U}^{\dagger}\boldsymbol{e}^{(k)}$ requires $4q_a$ real additions.

Table 3.2 summarizes the real multiplications, additions and divisions involved in computing the TDE RLS equalizer output and tap weight adaptation.

3.4.2 FDE RLS Algorithm

In this section, the complexity of the RLS FDE system given in [28] is analyzed. First, a summary of the FDE RLS scheme is given here for clarity. The received blocks after removing CP in two consecutive time periods are $\boldsymbol{y}^{(k)}$ and $\boldsymbol{y}^{(k+1)}$. Note

Table 3.2: TDE RLS Algorithm Complexity Summary

Operations	**Real '×'**	**Real '+'**	**Real '÷'**
$\boldsymbol{U}\boldsymbol{w}^{(k)}$	$16M\log_2 M + 16M$	$24M\log_2 M + 12M$	
$\boldsymbol{e}^{(k)}$		$4N$	
$\boldsymbol{U}^{\dagger}\boldsymbol{U}$	$2M\log_2 M + 8M$	$3M\log_2 M + 6M$	
$\boldsymbol{\Phi}^{(k+2)}$	$2q_a$	$2q_a$	
$(\boldsymbol{\Phi}^{(k+2)})^{-1}$	$10q_a^2 - 23q_a + 14$	$9q_a^2 - 17q_a + 10$	q_a
$\boldsymbol{U}^{\dagger}\boldsymbol{e}^{(k)}$	$8M\log_2 M + 16M$	$12M\log_2 M + 12M$	
$(\boldsymbol{\Phi}^{(k+2)})^{-1}\boldsymbol{U}^{\dagger}\boldsymbol{e}^{(k)}$	$8q_a^2$	$8q_a^2 - 4q_a$	
$\boldsymbol{w}^{(k+2)}$		$4q_a$	
Total	$26M\log_2 M + 40M + 18q_a^2 - 21q_a + 14$	$39M\log_2 M + 30M + 4N + 17q_a^2 - 15q_a + 10$	q_a

that the length of the data blocks after removing CP is N. The RLS FDE output is given as

$$\begin{bmatrix} \widehat{\underline{\boldsymbol{x}}}_1^{(k)} \\ (\widehat{\underline{\boldsymbol{x}}}_2^{(k)})^* \end{bmatrix} = \begin{bmatrix} \mathrm{diag}(\underline{\boldsymbol{y}}^{(k)}) & \mathrm{diag}((\underline{\boldsymbol{y}}^{(k+1)})^*) \\ \mathrm{diag}(-\underline{\boldsymbol{y}}^{(k+1)}) & \mathrm{diag}((\underline{\boldsymbol{y}}^{(k)})^*) \end{bmatrix} \begin{bmatrix} \boldsymbol{w}_{1f} \\ \boldsymbol{w}_{2f} \end{bmatrix} \triangleq \boldsymbol{U}_f \boldsymbol{w}_f^{(k)}, \quad (3.22)$$

where $\underline{\boldsymbol{z}}$ denotes the Fourier transform of $\boldsymbol{z}$, given as $\underline{\boldsymbol{z}} = \boldsymbol{Q}\,\boldsymbol{z}$, where $\boldsymbol{Q}$ is the orthonormal discrete Fourier transform (DFT) matrix. Then, the estimation error vector, $\boldsymbol{e}_f^{(k)}$, at the output of the equalizer is given as

$$\boldsymbol{e}_f^{(k)} = \begin{bmatrix} \underline{\boldsymbol{x}}_1^{(k)} \\ (\underline{\boldsymbol{x}}_2^{(k)})^* \end{bmatrix} - \begin{bmatrix} \widehat{\underline{\boldsymbol{x}}}_1^{(k)} \\ (\widehat{\underline{\boldsymbol{x}}}_2^{(k)})^* \end{bmatrix}. \quad (3.23)$$

The RLS FDE algorithm is summarized in Table 3.3.

The following steps explain the complexity involved in computing the FDE RLS equalizer output and tap weight adaptation.

1. The $\underline{\boldsymbol{y}}^{(k)}$ and $\underline{\boldsymbol{y}}^{(k+1)}$ computation: each $\underline{\boldsymbol{y}}$ is computed by using an N-point FFT operation. Again, each N-point FFT involves $2N\log_2 N$ real multiplications and $3N\log_2 N$ real additions [52]. Therefore, the $\underline{\boldsymbol{y}}^{(k)}$ and $\underline{\boldsymbol{y}}^{(k+1)}$ computations require $4N\log_2 N$ real multiplications and $6N\log_2 N$ real additions.

Table 3.3: Block RLS FDE Algorithm

FDE RLS Algorithm
Initial conditions: $\boldsymbol{w}_f^{(0)} = \mathbf{0}_{2N\times 1}$ $\boldsymbol{\Phi}_f^{(0)} = \delta \boldsymbol{I}_{2N\times 2N}$ where δ is small number
Update taps at each iteration using: $\boldsymbol{\Phi}_f^{(k+2)} = \lambda \boldsymbol{\Phi}_f^{(k)} + \boldsymbol{U}_f^{\dagger}\boldsymbol{U}_f$ $\boldsymbol{w}_f^{(k+2)} = \boldsymbol{w}_f^{(k)} + (\boldsymbol{\Phi}_f^{(k+2)})^{-1}\boldsymbol{U}_f^{\dagger}\boldsymbol{e}_f^{(k)}$ where λ is small positive close to 1

2. Equalizer output, $\boldsymbol{U}_f \boldsymbol{w}_f^{(k)}$, computation: the matrix $\boldsymbol{U}_f$ has only two non-zero elements in each of its rows. Using this property of $\boldsymbol{U}_f$, the equalizer output computation requires $16N$ real multiplications and $12N$ real additions.

3. Estimation error vector, $\boldsymbol{e}_f^{(k)}$, computation: the estimation error vector is given in (3.23). To compute the estimation error vector, first the equalizer output need to be converted to the time-domain by taking the inverse FFT (IFFT) and making a decision and then converting back to the frequency domain by taking the FFT. These computations require a total of $8N\log_2 N$ real multiplications and $12N\log_2 N$ real additions as well as a further $4N$ real additions to compute the error vector. Hence, the estimation error vector computation requires a total of $8N\log_2 N$ real multiplications and $12N\log_2 N + 4N$ real additions

4. The $\boldsymbol{U}_f^{\dagger}\boldsymbol{U}_f$ computation: the matrix $\boldsymbol{U}_f^{\dagger}\boldsymbol{U}_f$ can be evaluated as

$$\boldsymbol{U}_f^{\dagger}\boldsymbol{U}_f \triangleq \begin{bmatrix} \boldsymbol{B} & \mathbf{0} \\ \mathbf{0} & \boldsymbol{B} \end{bmatrix} \tag{3.24}$$

where

$$\boldsymbol{B} = \mathrm{diag}(\underline{\boldsymbol{y}}^{(k)})\mathrm{diag}((\underline{\boldsymbol{y}}^{(k)})^*) + \mathrm{diag}(-\underline{\boldsymbol{y}}^{(k+1)})\mathrm{diag}((\underline{\boldsymbol{y}}^{(k+1)})^*) \tag{3.25}$$

is a real diagonal matrix. Considering the fact that $\boldsymbol{B}$ involves multiplication of numbers with their conjugates, the computation of $\boldsymbol{B}$ requires $4N$ real multiplications and $3N$ real additions.

5. The $\boldsymbol{\Phi}_f^{(k+2)} = \lambda\boldsymbol{\Phi}_f^{(k)} + \boldsymbol{U}_f^{\dagger}\boldsymbol{U}_f$ computation: from the properties of the matrix $\boldsymbol{U}_f^{\dagger}\boldsymbol{U}_f$, it can be shown that the matrix $\boldsymbol{\Phi}_f^{(k+2)}$ is a real diagonal matrix and has the following form,

$$\boldsymbol{\Phi}_f^{(k+2)} = \begin{bmatrix} \boldsymbol{A} & \boldsymbol{0} \\ \boldsymbol{0} & \boldsymbol{A} \end{bmatrix} \tag{3.26}$$

where $\boldsymbol{A}$ is real diagonal matrix. Matrix $\boldsymbol{\Phi}_f^{(k)}$ is also a real diagonal matrix and has the same form as $\boldsymbol{\Phi}_f^{(k+2)}$. Therefore, to calculate $\boldsymbol{\Phi}_f^{(k+2)}$, we only need to compute $\boldsymbol{A}$. First, the λ multiplication requires N real multiplications, and then the addition of $\lambda\boldsymbol{\Phi}_f^{(k)}$ and $\boldsymbol{U}_f^{\dagger}\boldsymbol{U}_f$ requires N real additions.

6. The $(\boldsymbol{\Phi}_f^{(k+2)})^{-1}$ computation: from the matrix inversion properties, the inverse of $\boldsymbol{\Phi}_f^{(k+2)}$ has the form

$$\boldsymbol{\Phi}_{k+2}^{-1} = \begin{bmatrix} \boldsymbol{A} & \boldsymbol{0} \\ \boldsymbol{0} & \boldsymbol{A} \end{bmatrix}^{-1} = \begin{bmatrix} \boldsymbol{A}^{-1} & \boldsymbol{0} \\ \boldsymbol{0} & \boldsymbol{A}^{-1} \end{bmatrix}. \tag{3.27}$$

Therefore, computing $(\boldsymbol{\Phi}_f^{(k+2)})^{-1}$ only requires computing the inverse of the real diagonal matrix, $\boldsymbol{A}$. This only requires N real divisions.

7. The $\boldsymbol{w}_f^{(k+2)} = \boldsymbol{w}_f^{(k)} + (\boldsymbol{\Phi}_f^{(k+2)})^{-1}\boldsymbol{U}_f^{\dagger}\boldsymbol{e}_f^{(k)}$ computation: first the $\boldsymbol{U}_f^{\dagger}\boldsymbol{e}_f^{(k)}$ computation requires $16N$ real multiplications and $12N$ real additions. The multiplication of $(\boldsymbol{\Phi}_f^{(k+2)})^{-1}$ and $\boldsymbol{U}_f^{\dagger}\boldsymbol{e}_f^{(k)}$ requires $4N$ real multiplications, and finally, the addition of $\boldsymbol{w}_f^{(k)}$ and $(\boldsymbol{\Phi}_f^{(k+2)})^{-1}\boldsymbol{U}_f^{\dagger}\boldsymbol{e}_f^{(k)}$ requires $4N$ real additions.

Table 3.4 summarizes the real multiplications, additions and divisions involved in computing the FDE RLS equalizer output and tap weight adaptation. To make the complexity comparison clearer, Fig. 3.13 shows the number of real multiplications involved in computing the FDE and TDE RLS algorithms. The channel parameters are fixed to those used in the simulations, and we vary the data block length, N. We see that the TDE system has higher complexity than the FDE system with around twice the complexity at large values of N. Thus, the TDE adaptive algorithm has better system performance but at the cost of increased complexity compared to the FDE adaptive system.

Table 3.4: FDE RLS Algorithm Complexity Summary

Operations	**Real '×'**	**Real '+'**	**Real '÷'**
$\underline{\boldsymbol{y}}^{(k)}$, $\underline{\boldsymbol{y}}^{(k+1)}$	$4N\log_2 N$	$6N\log_2 N$	
$\boldsymbol{U}_f\boldsymbol{w}_f^{(k)}$	$16N$	$12N$	
$\boldsymbol{e}_f^{(k)}$	$8N\log_2 N$	$12N\log_2 N + 4N$	
$\boldsymbol{U}_f^{\dagger}\boldsymbol{U}_f$	$4N$	$3N$	
$\boldsymbol{\Phi}_f^{(k+2)}$	N	N	
$(\boldsymbol{\Phi}_f^{(k+2)})^{-1}$			N
$\boldsymbol{w}_f^{(k+2)}$	$20N$	$16N$	
Total	$12N\log_2 N + 41N$	$18N\log_2 N + 36N$	N

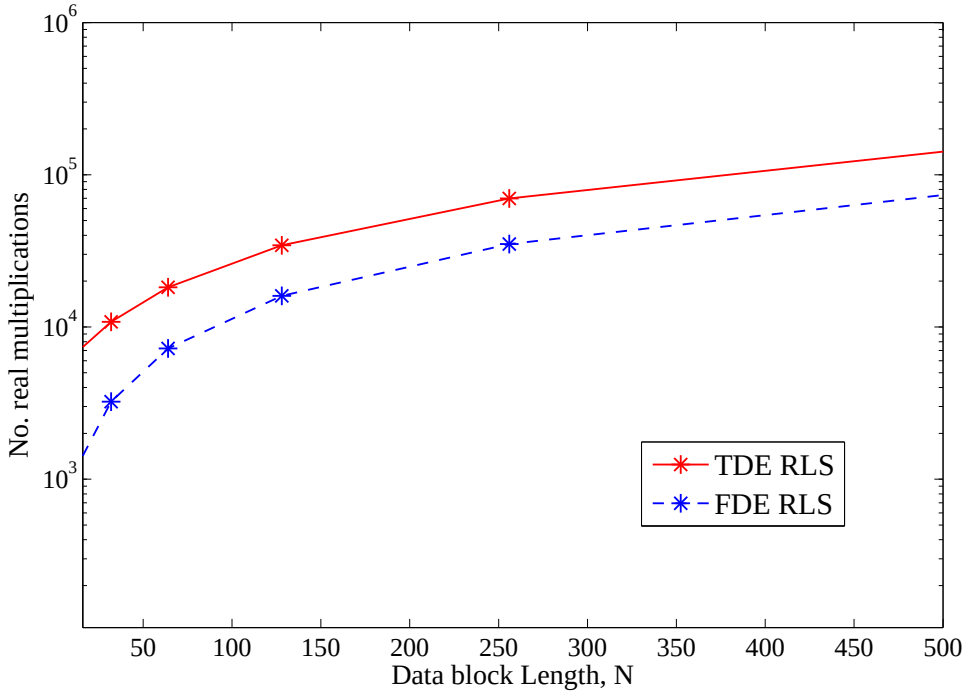

Figure 3.13: Number of real multiplications required for the TDE and FDE RLS algorithms.

3.5 Summary

In this chapter, we have developed a new block TDE structure for TR-STBC systems which eliminates the separate decoder and also the need for explicit CIR estimation at the receiver. Using simulation, we have shown that the block TDE requires significantly less equalizer taps than the analogous FDE for SC FDE-STBC systems for short delay spread channels. The results show that TDE RLS algorithm outperforms the analogous adaptive FDE algorithms in MSE dynamic convergence behavior and SER steady-state performance. Using the increased flexibility of the block TDE, we have also developed a new frame structure which allows the system to perform better in fast time-varying channels.

Finally, we also analyzed the computational complexity of the TDE and FDE RLS algorithms. We show that the TDE system has a higher complexity than the FDE system. In summary, the TDE adaptive algorithm has better system performance but at the cost of increased complexity compared to the FDE adaptive system.

Chapter 4

Adaptive Equalization in STBC-Based Relaying Systems

A time domain adaptive equalization scheme for a time-reversal space-time block-coding (TR-STBC) based transmitter diversity system was presented in the last chapter. As explained in Chapter 2, cooperative diversity systems have been proposed recently due to several potential advantages they may offer. In this chapter, we extend the adaptive equalization scheme given in Chapter 3 to cooperative diversity systems.

Several block STBC structures for frequency selective fading channels, including TR-STBC [25], single-carrier frequency-domain equalization for STBC (SC FDE-STBC) [26] and orthogonal frequency division multiplexing (OFDM) for STBC [27], have been proposed. In these schemes, the decoding and equalization of the STBC transmissions require explicit estimation of the CIR at the receiver. Comparisons of these non-adaptive equalization schemes for STBC systems can be found in [56, 57, 58] and [29, 59] for non-distributed and distributed STBC systems, respectively. These studies show that, due to their increased sensitivity to frequency errors as well as their inability to exploit the multipath diversity offered by the frequency selectivity of the channel, OFDM-STBC systems perform poorly compared to TR-STBC and SC FDE-STBC systems for both distributed and non-distributed

transceivers.[1]

Given the previous research results, the purpose of this chapter is to develop both time- and frequency-domain adaptive combined decoding/equalization schemes for relay-assisted TR-STBC transmission systems. In this chapter we derive both time- and frequency-domain adaptive combined decoding/equalization schemes for an amplify-and-forward relay network based on Protocols I and III proposed by Nabar *et al.* [1]. The chapter also includes an extensive Monte Carlo simulation study and complexity analysis of both the time- and frequency-domain adaptive combined decoding/equalization schemes.

4.1 Protocols and Transmission Procedures

Figure 4.1 shows the relay network topology used in this chapter. It is assumed that the source (S), relay (R), and destination (D) terminals are all equipped with a single antenna, and, to multiplex the various signals in the network, the well-known Protocols I and III proposed by Nabar *et al.* [1] are implemented. As a shorthand, these protocols are denoted by 'P1' and 'P3'. For P1, during the first time slot of each block, source S transmits information to relay R and destination D. During the second time slot of the block, both S and R transmit information to D. P3 is identical to P1 except that D chooses not to receive during the first time slot. These protocols are summarized in Table 4.1. Note that for sake of analysis it is assumed that the two signals arriving at D from S and R during the second time slot are perfectly synchronized, which can be difficult to achieve in practical systems.[2]

We also assume that the relay terminal assists in the communication with the destination terminal using amplify-and-forward (AF) mode. In this mode, with-

[1]Note that these studies assume perfect timing synchronization. If more realistic imperfect synchronization is considered, the performance advantages of TR-STBC and SC FDE-STBC systems over OFDM-STBC systems could decrease.

[2]In [60, 61] researchers have considered modifications of cooperative STBC decoding techniques for the case of imperfect synchronization, which could be applied to the techniques presented here.

Table 4.1: Protocols I and III

Time Slot	Protocol I	Protocol III
1	$S \rightarrow R$, $S \rightarrow D$	$S \rightarrow R$
2	$S \rightarrow D$, $R \rightarrow D$	$S \rightarrow D$, $R \rightarrow D$

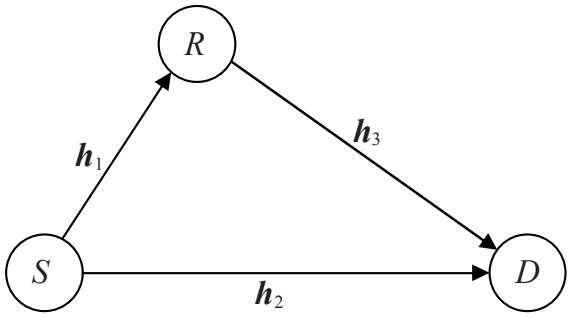

Figure 4.1: Relay network topology.

out decoding or demodulation the relay terminal buffers, amplifies and retransmits blocks of received observations corresponding to the signal from the source terminal. These operations can be implemented easily using a codec, some DRAM and an amplifier. Further it is assumed that the relay terminal has the capability of removing or adding zero-padding (ZP) or a cyclic prefix (CP), depending on the type of STBC method used in the transmission, which again requires synchronization between R and S.

Let the CIRs for the source-to-relay ($S \rightarrow R$), source-to-destination ($S \rightarrow D$), and relay-to-destination ($R \rightarrow D$) links for the k-th transmission block be given by

$$\begin{aligned} \boldsymbol{h}_1^{(k)} &= [h_1^{(k)}(0), ..., h_1^{(k)}(L_1)]^T, \\ \boldsymbol{h}_2^{(k)} &= [h_2^{(k)}(0), ..., h_2^{(k)}(L_2)]^T, \\ \boldsymbol{h}_3^{(k)} &= [h_3^{(k)}(0), ..., h_3^{(k)}(L_3)]^T, \end{aligned} \tag{4.1}$$

respectively, where L_1, L_2, and L_3 denote the corresponding channel memory lengths.

In [25], Lindskog and Paulraj introduced the TR-STBC scheme as an extension of Alamouti's method for frequency selective fading channels. In this chapter, we generalize the TR-STBC scheme for a distributed single-relay network. To perform distributed TR-STBC encoding, data symbols are transmitted by S in blocks. During *Time slot 1* of the k-th transmitted block, where k is even, S transmits N

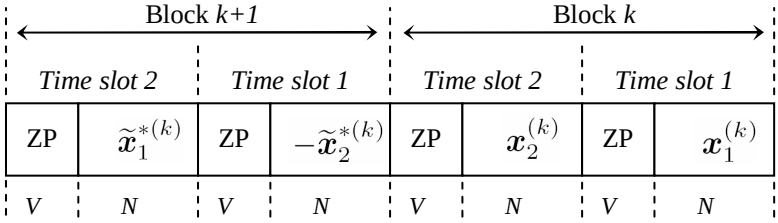

Figure 4.2: Source terminal transmission block format.

symbols

$$\boldsymbol{x}_1^{(k)} = [x_1^{(k)}(0), ..., x_1^{(k)}(N-1)]^T \tag{4.2}$$

and during *Time slot 2* of the k-th transmitted block, S transmits another N symbols

$$\boldsymbol{x}_2^{(k)} = [x_2^{(k)}(0), ..., x_2^{(k)}(N-1)]^T. \tag{4.3}$$

During *Time slot 1* of the $k+1$-th transmission block, $\boldsymbol{x}_2^{(k)}$ is time reversed, complex conjugated, and negated to create

$$\boldsymbol{x}_1^{(k+1)} = -\widetilde{\boldsymbol{x}}_2^{*(k)} = [-x_2^{*(k)}(N-1), ..., -x_2^{*(k)}(0)]^T \tag{4.4}$$

which is transmitted by S, and finally $\boldsymbol{x}_1^{(k)}$ is time reversed and complex conjugated to create

$$\boldsymbol{x}_2^{(k+1)} = \widetilde{\boldsymbol{x}}_1^{*(k)} = [x_1^{*(k)}(N-1), ..., x_1^{*(k)}(0)]^T \tag{4.5}$$

which is transmitted by S during *Time slot 2* of the $k+1$-th transmission block. After each N symbols, zero-padding (ZP) of length $V = \max(L_1 + L_3, L_2)$ is inserted to overcome the inter-block interference. The transmission procedure at S is depicted in Fig. 4.2. Here, a ZP-only scheme is used as it can be used for both the time-domain equalizer (TDE) [62] and the frequency-domain equalizer (FDE) [58]. Compared to the traditional CP method for FDE [26], the ZP scheme yields slightly more receiver complexity due to an increase in the discrete Fourier transform (DFT) size by the length of the ZP. On the other hand, this ZP scheme requires less transmission power [63].

4.2 Distributed TR-STBC Time-Domain MMSE Receivers

In this section we describe the time-domain distributed TR-STBC decoder and the corresponding MMSE equalizer for P3. Then, the MMSE receiver for P1 is derived by combining the P3 MMSE equalizer with an equalizer based only on the observations received during *Time slot 1* (TS1 Equalizer). For P1, two options (optimal and suboptimal) are presented for combining the P3 MMSE equalizer with the TS1 Equalizer.

4.2.1 Protocol III MMSE Receiver

Consider the source terminal transmission block shown in Fig. 4.2. The received signal at R during *Time slot 1* of the k-th transmitted block is

$$\boldsymbol{y}_{R\text{ext}}^{(k)} = \sqrt{E_{SR}}\,\boldsymbol{H}_{1\text{ext}}^{(k)}\,\boldsymbol{x}_1^{(k)} + \boldsymbol{n}_{R\text{ext}}^{(k)} \tag{4.6}$$

where E_{SR} is the average energy available at R, taking into account the path loss and shadowing effects over the $S\rightarrow R$ link, $\boldsymbol{n}_{R\text{ext}}^{(k)}$ is an additive white complex Gaussian noise vector with each component having zero-mean and variance σ_{nR}^2, and $\boldsymbol{H}_{1\text{ext}}^{(k)}$ is the channel convolution matrix for the $S\rightarrow R$ link. Matrix $\boldsymbol{H}_{1\text{ext}}^{(k)}$ has dimension $(N+V)\times N$ and the form

$$\boldsymbol{H}_{1\text{ext}}^{(k)} = \begin{bmatrix} \boldsymbol{h}_{1\text{ext}}^{(k)} & 0 & \dots & 0 \\ 0 & \boldsymbol{h}_{1\text{ext}}^{(k)} & \dots & 0 \\ \vdots & \vdots & \ddots & \vdots \\ 0 & 0 & \dots & \boldsymbol{h}_{1\text{ext}}^{(k)} \end{bmatrix} \tag{4.7}$$

where $\boldsymbol{h}_{1\text{ext}}^{(k)} = [(\boldsymbol{h}_1^{(k)})^T, \boldsymbol{0}_{1\times(V-L_1)}]^T$. The relay terminal first removes the last $V-L_1$ noise-only terms in $\boldsymbol{y}_{R\text{ext}}^{(k)}$. Then it scales each entry of the resulting vector by a factor $\sqrt{E_{SR}+\sigma_{nR}^2}$ to give an average unit energy.

The truncated and scaled received signal $\overline{\boldsymbol{y}}_R^{(k)}$ can now be written as

$$\overline{\boldsymbol{y}}_R^{(k)} = \sqrt{\frac{E_{SR}}{E_{SR}+\sigma_{nR}^2}}\,\boldsymbol{H}_1^{(k)}\,\boldsymbol{x}_1^{(k)} + \frac{1}{\sqrt{E_{SR}+\sigma_{nR}^2}}\,\boldsymbol{n}_R^{(k)} \tag{4.8}$$

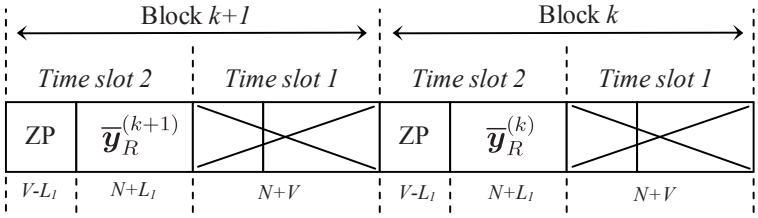

Figure 4.3: Relay terminal transmission block format for TDE.

where $\boldsymbol{n}_R^{(k)}$ is the truncated noise vector, and matrix $\boldsymbol{H}_1^{(k)}$ has the same form as (4.7) with $\boldsymbol{h}_{1\text{ext}}^{(k)}$ replaced by $\boldsymbol{h}_1^{(k)}$ and has dimension $(N + L_1) \times N$. The relay terminal transmits the signal $\overline{\boldsymbol{y}}_R^{(k)}$ during *Time slot 2*. This simple scaling without any decoding is known as *amplify-and-forward* processing and is depicted in Fig. 4.3. In the figure $\overline{\boldsymbol{y}}_R^{(k)}$ and $\overline{\boldsymbol{y}}_R^{(k+1)}$ represent the truncated and scaled relay terminal received vectors during blocks k and $k+1$, respectively. As seen from the figure, there is no transmission from R during *Time slot 1*, and a ZP of length $V - L_1$ is inserted by the relay terminal.

During *Time slot 2*, the destination terminal receives signals from both the relay and source terminals. The received signal at D for the k-th transmitted block is given by

$$\boldsymbol{y}_{Dt2}^{(k)} = \sqrt{E_{RD}}\, \boldsymbol{H}_3^{(k)}\, \overline{\boldsymbol{y}}_R^{(k)} + \sqrt{E_{SD}}\, \boldsymbol{H}_2^{(k)}\, \boldsymbol{x}_2^{(k)} + \boldsymbol{n}_{Dt2}^{(k)} \tag{4.9}$$

where E_{RD} and E_{SD} are the average energies available at D, taking into account the different path loss and shadowing effects over the $R \rightarrow D$ and $S \rightarrow D$ links, and $\boldsymbol{n}_{Dt2}^{(k)}$ is the additive white complex Gaussian noise vector with each entry having zero-mean and variance σ_{nD}^2. Finally, $\boldsymbol{H}_2^{(k)}$ and $\boldsymbol{H}_3^{(k)}$ are the channel convolution matrices for the $S \rightarrow D$ and $R \rightarrow D$ links. Again, matrices $\boldsymbol{H}_2^{(k)}$ and $\boldsymbol{H}_3^{(k)}$ have the same form as (4.7) with $\boldsymbol{h}_{1\text{ext}}^{(k)}$ replaced by $\boldsymbol{h}_{2\text{ext}}^{(k)} = [(\boldsymbol{h}_2^{(k)})^T, \boldsymbol{0}_{1\times(V-L_2)}]^T$ and $\boldsymbol{h}_{3\text{ext}}^{(k)} = [(\boldsymbol{h}_3^{(k)})^T, \boldsymbol{0}_{1\times(V-L_1-L_3)}]^T$, respectively, yielding matrices with dimensions $(N+V)\times N$ and $(N + V) \times (N + L_1)$. Combining and scaling (4.6) and (4.9), and by defining $\gamma_1 = \sqrt{\frac{E_{RD}E_{SR}}{E_{SR}+\sigma_{nR}^2}}$, $\gamma_2 = \sqrt{E_{SD}}$, and $\gamma_3 = \sqrt{\frac{E_{RD}}{E_{SR}+\sigma_{nR}^2}}$, we have

$$\boldsymbol{y}_{Dt2}^{(k)} = \gamma_1 \boldsymbol{H}_3^{(k)} \boldsymbol{H}_1^{(k)} \boldsymbol{x}_1^{(k)} + \gamma_2 \boldsymbol{H}_2^{(k)} \boldsymbol{x}_2^{(k)} + \boldsymbol{n}_{Dt2}^{(k)} + \gamma_3 \boldsymbol{H}_3^{(k)} \boldsymbol{n}_R^{(k)}. \tag{4.10}$$

Assuming that the channels' coefficients remain constant over two consecutive

blocks, the received signal at D during *Time slot 2* of the $k+1$-th transmitted block is given by

$$\boldsymbol{y}_{Dt2}^{(k+1)} = -\gamma_1 \boldsymbol{H}_3^{(k)} \boldsymbol{H}_1^{(k)} \widetilde{\boldsymbol{x}}_2^{*(k)} + \gamma_2 \boldsymbol{H}_2^{(k)} \widetilde{\boldsymbol{x}}_1^{*(k)} + \boldsymbol{n}_{Dt2}^{(k+1)} + \gamma_3 \boldsymbol{H}_3^{(k)} \boldsymbol{n}_R^{(k+1)} . \tag{4.11}$$

Now using the encoding rule given in (4.4) and (4.5) and stacking the observation vectors, gives

$$\begin{aligned} \boldsymbol{y}_{Dt2} &\triangleq \begin{bmatrix} \boldsymbol{y}_{Dt2}^{(k)} \\ \widetilde{\boldsymbol{y}}_{Dt2}^{*(k+1)} \end{bmatrix} \\ &= \begin{bmatrix} \gamma_1 \boldsymbol{H}_3^{(k)} \boldsymbol{H}_1^{(k)} & \gamma_2 \boldsymbol{H}_2^{(k)} \\ \gamma_2 \widetilde{\boldsymbol{H}}_2^{*(k)} & -\gamma_1 \widetilde{\boldsymbol{H}}_3^{*(k)} \widetilde{\boldsymbol{H}}_1^{*(k)} \end{bmatrix} \begin{bmatrix} \boldsymbol{x}_1^{(k)} \\ \boldsymbol{x}_2^{(k)} \end{bmatrix} + \begin{bmatrix} \boldsymbol{n}_{Dt2}^{(k)} + \gamma_3 \boldsymbol{H}_3^{(k)} \boldsymbol{n}_R^{(k)} \\ \widetilde{\boldsymbol{n}}_{Dt2}^{*(k+1)} + \gamma_3 \widetilde{\boldsymbol{H}}_3^{*(k)} \widetilde{\boldsymbol{n}}_R^{*(k+1)} \end{bmatrix} \\ &\triangleq \boldsymbol{H}\boldsymbol{x} + \boldsymbol{n} \end{aligned} \tag{4.12}$$

where $\widetilde{\boldsymbol{A}}^*$ denotes the complex conjugation and time reversal of matrix $\boldsymbol{A}$.

Matrix $\boldsymbol{H}$ has the property that the transmitted blocks $\boldsymbol{x}_1^{(k)}$ and $\boldsymbol{x}_2^{(k)}$ become decoupled by multiplying both sides of (4.12) by the matrix

$$\boldsymbol{H}_d = \begin{bmatrix} \gamma_1 \widetilde{\boldsymbol{H}}_{3d}^{*(k)} \widetilde{\boldsymbol{H}}_{1d}^{*(k)} & \gamma_2 \boldsymbol{H}_{2d}^{(k)} \\ \gamma_2 \widetilde{\boldsymbol{H}}_{2d}^{*(k)} & -\gamma_1 \boldsymbol{H}_{3d}^{(k)} \boldsymbol{H}_{1d}^{(k)} \end{bmatrix} \tag{4.13}$$

where $\boldsymbol{H}_{1d}^{(k)}$ has the same form as $\boldsymbol{H}_1^{(k)}$ but with dimensions $(N+V+L_1)\times(N+V)$, $\boldsymbol{H}_{2d}^{(k)}$ has the same form as $\boldsymbol{H}_2^{(k)}$ but with dimensions $(N+2V)\times(N+V)$, and $\boldsymbol{H}_{3d}^{(k)}$ has the same form as $\boldsymbol{H}_3^{(k)}$ but with dimensions $(N+2V)\times(N+V+L_1)$. Thus, the resulting output from the TR-STBC decoder is

$$\begin{aligned} \boldsymbol{z} &= \begin{bmatrix} \boldsymbol{z}_1^{(k)} \\ \boldsymbol{z}_2^{(k)} \end{bmatrix} \triangleq \boldsymbol{H}_d \, \boldsymbol{y}_{Dt2} \\ &= \begin{bmatrix} \boldsymbol{G}^{(k)} & \boldsymbol{0} \\ \boldsymbol{0} & \boldsymbol{G}^{(k)} \end{bmatrix} \begin{bmatrix} \boldsymbol{x}_1^{(k)} \\ \boldsymbol{x}_2^{(k)} \end{bmatrix} + \boldsymbol{H}_d \begin{bmatrix} \boldsymbol{n}_{Dt2}^{(k)} + \gamma_3 \boldsymbol{H}_3^{(k)} \boldsymbol{n}_R^{(k)} \\ \widetilde{\boldsymbol{n}}_{Dt2}^{*(k+1)} + \gamma_3 \widetilde{\boldsymbol{H}}_3^{*(k)} \widetilde{\boldsymbol{n}}_R^{*(k+1)} \end{bmatrix} \end{aligned} \tag{4.14}$$

where

$$\boldsymbol{G}^{(k)} = \gamma_1^2 \, \widetilde{\boldsymbol{H}}_{3d}^{*(k)} \widetilde{\boldsymbol{H}}_{1d}^{*(k)} \boldsymbol{H}_3^{(k)} \boldsymbol{H}_1^{(k)} + \gamma_2^2 \, \boldsymbol{H}_{2d}^{(k)} \widetilde{\boldsymbol{H}}_2^{*(k)} . \tag{4.15}$$

Equation (4.14) demonstrates that the decoder outputs $\boldsymbol{z}_1$ and $\boldsymbol{z}_2$ are decoupled in terms of $\boldsymbol{x}_1$ and $\boldsymbol{x}_2$. We also see that the decoupled signals $\boldsymbol{z}_1$ and $\boldsymbol{z}_2$ have equal

channel gain matrices and can show that the statistics of the noise terms in $\boldsymbol{z}_1$ and $\boldsymbol{z}_2$ are identical and uncorrelated, leading to independence since they are jointly Gaussian. Therefore, the same MMSE tap weights can be applied to both blocks $\boldsymbol{z}_1$ and $\boldsymbol{z}_2$ to remove the inter-symbol interference (ISI). Thus, we consider a block of only one decoder's outputs, $\boldsymbol{z}_1 = [z_1(0), \ldots, z_1(N+2V-1)]^T$, when deriving the MMSE solution for the equalizer taps.

We assume that the q-tap equalizer is symbol spaced with tap weight vector $\boldsymbol{w}$. And for convenience, we let q be an odd integer. The output of the block equalizer is written $\widehat{\boldsymbol{x}}_1 = \boldsymbol{Z}_1\,\boldsymbol{w}$, where $\boldsymbol{Z}_1$ has dimensions $(N+2V+q-1)\times q$ and the form shown in (4.7) with $\boldsymbol{h}_{1\text{ext}}^{(k)}$ replaced by $\boldsymbol{z}_1$. The estimation error at the output of the equalizer is $\boldsymbol{e}_1 = \boldsymbol{x}_{1\text{ext}} - \boldsymbol{Z}_1\,\boldsymbol{w}$ where $\boldsymbol{x}_{1\text{ext}} = \left[\boldsymbol{0}_{1\times[(2V+q-1)/2]}, \boldsymbol{x}_1^T, \boldsymbol{0}_{1\times[(2V+q-1)/2]}\right]^T$.

It can be shown that the optimum MMSE equalizer tap weight vector is then

$$\boldsymbol{w}_o = \left[\mathrm{E}\{\boldsymbol{Z}_1^\dagger\,\boldsymbol{Z}_1\}\right]^{-1}\mathrm{E}\{\boldsymbol{Z}_1^\dagger\,\boldsymbol{x}_{1\text{ext}}\}\,. \tag{4.16}$$

It can also be shown that $(q\times q)$-dimensional autocorrelation matrix $E\{\boldsymbol{Z}_1^\dagger\,\boldsymbol{Z}_1\}$ has the form

$$E\{\boldsymbol{Z}_1^\dagger\,\boldsymbol{Z}_1\} = \begin{bmatrix} \mathrm{Tr}_0(\boldsymbol{R}_z) & \mathrm{Tr}_1(\boldsymbol{R}_z) & \ldots & \mathrm{Tr}_{(q-1)}(\boldsymbol{R}_z) \\ \mathrm{Tr}_{-1}(\boldsymbol{R}_z) & \mathrm{Tr}_0(\boldsymbol{R}_z) & \ldots & \mathrm{Tr}_{(q-2)}(\boldsymbol{R}_z) \\ \vdots & \vdots & \ddots & \vdots \\ \mathrm{Tr}_{-(q-1)}(\boldsymbol{R}_z) & \mathrm{Tr}_{-(q-2)}(\boldsymbol{R}_z) & \ldots & \mathrm{Tr}_0(\boldsymbol{R}_z) \end{bmatrix} \tag{4.17}$$

where the vector autocorrelation matrix

$$\begin{aligned}\boldsymbol{R}_z &= \mathrm{E}\{\boldsymbol{z}_1\,\boldsymbol{z}_1^\dagger\} \\ &= \sigma_x^2\boldsymbol{G}\,\boldsymbol{G}^\dagger + \sigma_{nD}^2\gamma_1^2\widetilde{\boldsymbol{H}}_{3d}^*\widetilde{\boldsymbol{H}}_{1d}^*(\widetilde{\boldsymbol{H}}_{3d}^*\widetilde{\boldsymbol{H}}_{1d}^*)^\dagger + \sigma_{nD}^2\gamma_2^2\boldsymbol{H}_{2d}\boldsymbol{H}_{2d}^H \\ &\quad + \sigma_{nR}^2\gamma_3^2\gamma_2^2\boldsymbol{H}_{2d}\widetilde{\boldsymbol{H}}_3^*(\boldsymbol{H}_{2d}\widetilde{\boldsymbol{H}}_3^*)^\dagger + \sigma_{nR}^2\gamma_3^2\gamma_1^2\widetilde{\boldsymbol{H}}_{3d}^*\widetilde{\boldsymbol{H}}_{1d}^*\boldsymbol{H}_3(\widetilde{\boldsymbol{H}}_{3d}^*\widetilde{\boldsymbol{H}}_{1d}^*\boldsymbol{H}_3)^\dagger,\end{aligned} \tag{4.18}$$

$\mathrm{Tr}_j(\boldsymbol{A})$ is the j-th off-diagonal trace of matrix $\boldsymbol{A}$ and the (k) superscripts are dropped from the notation. Similarly, by defining q-dimensional cross-correlation vector $\boldsymbol{p} \triangleq E\{\boldsymbol{Z}_1^\dagger\,\boldsymbol{x}_{1\text{ext}}\}$, it can be shown that

$$\boldsymbol{p} = [\mathrm{Tr}_{(-V-\nu)}(\boldsymbol{G}), \mathrm{Tr}_{(-V-\nu+1)}(\boldsymbol{G}), \ldots, \mathrm{Tr}_{(-V+\nu)}(\boldsymbol{G})]^\dagger \tag{4.19}$$

where $\nu = (q-1)/2$. The optimum MMSE equalizer tap weights can be obtained by substituting (4.17) and (4.19) into (4.16).

4.2.2 Protocol I MMSE Receiver

In this section we propose optimal and suboptimal MMSE receivers for P1 by combining the P3 MMSE receiver with the TS1 equalizer. In the optimal case, the taps of the P3 MMSE equalizer and the TS1 equalizer are jointly optimized using the MMSE criterion, and in the suboptimal case, the taps of the P3 MMSE equalizer and the TS1 equalizer are independently derived and combined using the MSE at the output of the equalizers.

Optimal Protocol I MMSE Receiver

The difference between protocols P1 and P3 is that for P1 the destination terminal utilizes the additional observations of the direct $S \rightarrow D$ link during *Time slot 1*. Assuming that the channel coefficients remain constant over two consecutive blocks, the received signals at D during *Time slot 1* of the k-th and $k+1$-th blocks are:

$$\begin{aligned} \boldsymbol{y}_{Dt1}^{(k)} &= \gamma_2 \, \boldsymbol{H}_2^{(k)} \boldsymbol{x}_1^{(k)} + \boldsymbol{n}_{Dt1}^{(k)} \\ \boldsymbol{y}_{Dt1}^{(k+1)} &= -\gamma_2 \, \boldsymbol{H}_2^{(k)} \widetilde{\boldsymbol{x}}_2^{*(k)} + \boldsymbol{n}_{Dt1}^{(k+1)} . \end{aligned} \tag{4.20}$$

The information received during *Time slot 1* does not require an orthogonalizing decoder, as the symbols $\boldsymbol{x}_1$ and $\boldsymbol{x}_2$ are not coupled. However, the TR-STBC decoder is again required for the *Time slot 2* observations. A block diagram of the MMSE equalizer for P1 is shown in Fig. 4.4.

As before, it is assumed the *Time slot 2* (TS2) equalizer shown in Fig. 4.4 has q-length tap weight vectors $\boldsymbol{w}_{01}$ and $\boldsymbol{w}_{02}$, where q is an odd integer. Similarly, for the *Time slot 1* (TS1) equalizer, the tap weight vectors $\boldsymbol{w}_{11}$ and $\boldsymbol{w}_{12}$ have length $q_2 = V + l$, where l is an odd integer for convenience.

First, consider the equalizer output estimates of the symbols $\boldsymbol{x}_1$,

$$\widehat{\boldsymbol{x}}_1 = \boldsymbol{Z}_{01} \, \boldsymbol{w}_{01} + \boldsymbol{Y}_{11} \, \boldsymbol{w}_{11} \tag{4.21}$$

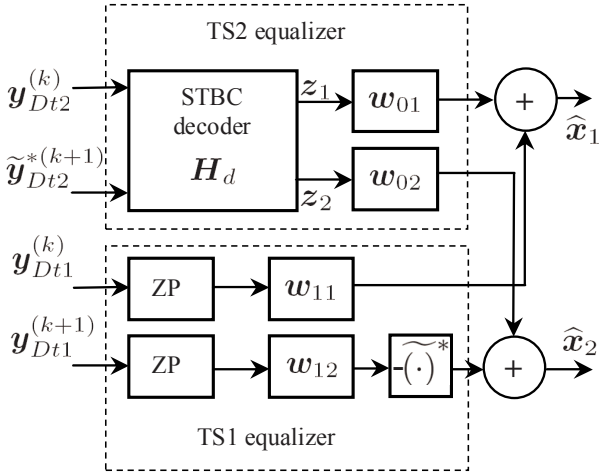

Figure 4.4: Jointly optimized (optimal) MMSE equalizer for P1.

where $\boldsymbol{Z}_{01}$ has dimension $(N+2V+q-1)\times q$ and the form shown in (4.7) with $\boldsymbol{h}_{1\text{ext}}^{(k)}$ replaced by $\boldsymbol{z}_1$ and $\boldsymbol{Y}_{11}$ has dimension $(N+V+q+q_2-l-1)\times q_2$ and the form shown in (4.7) with $\boldsymbol{h}_{1\text{ext}}^{(k)}$ replaced by $\boldsymbol{y}_{11}=\left[\boldsymbol{0}_{1\times[(q-l)/2]},(\boldsymbol{y}_{Dt1}^{(k)})^T,\boldsymbol{0}_{1\times[(q-l)/2]}\right]^T$. The received signal $\boldsymbol{y}_{Dt1}^{(k)}$ is zero-padded both in front and behind with $(q-1)/2$ zeros to align the output of the TS1 equalizer with that of the TS2 one. The output error of the equalizer is $\boldsymbol{e}_1=\boldsymbol{x}_{1\text{ext}}-\widehat{\boldsymbol{x}}_1$, where $\boldsymbol{x}_{1\text{ext}}=\left[\boldsymbol{0}_{1\times[(2V+q-1)/2]},\boldsymbol{x}_1^T,\boldsymbol{0}_{1\times[(2V+q-1)/2]}\right]^T$.

Defining $\boldsymbol{C}_{ZZ}=\mathrm{E}\{\boldsymbol{Z}_{01}^\dagger\ \boldsymbol{Z}_{01}\}$, $\boldsymbol{C}_{YY}=\mathrm{E}\{\boldsymbol{Y}_{11}^\dagger\boldsymbol{Y}_{11}\}$, $\boldsymbol{C}_{ZY}=\mathrm{E}\{\boldsymbol{Z}_{01}^\dagger\boldsymbol{Y}_{11}\}$, $\boldsymbol{c}_{Zx}=\mathrm{E}\{\boldsymbol{Z}_{01}^\dagger\ \boldsymbol{x}_{1\text{ext}}\}$, and $\boldsymbol{c}_{Yx}=\mathrm{E}\{\boldsymbol{Y}_{11}^\dagger\ \boldsymbol{x}_{1\text{ext}}\}$, the optimum MMSE equalizer tap weight vector is

$$\begin{bmatrix}\boldsymbol{w}_{01}\\ \boldsymbol{w}_{11}\end{bmatrix}=\begin{bmatrix}\boldsymbol{C}_{ZZ} & \boldsymbol{C}_{ZY}\\ \boldsymbol{C}_{ZY}^\dagger & \boldsymbol{C}_{YY}\end{bmatrix}^{-1}\begin{bmatrix}\boldsymbol{c}_{Zx}\\ \boldsymbol{c}_{Yx}\end{bmatrix}. \tag{4.22}$$

Clearly, $\boldsymbol{C}_{ZZ}$ and $\boldsymbol{c}_{Zx}$ are given in (4.17) and (4.19), respectively, and $q_2\times q_2$ matrix $\boldsymbol{C}_{YY}$ has the same form as (4.17) but with q and $\boldsymbol{R}_z$ replaced by q_2 and $\boldsymbol{R}_y=\mathrm{E}\{\boldsymbol{y}_{Dt1}^{(k)}(\boldsymbol{y}_{Dt1}^{(k)})^\dagger\}=\sigma_x^2\gamma_2^2\boldsymbol{H}_2\boldsymbol{H}_2^\dagger+\sigma_{nD}^2\boldsymbol{I}_{N+V}$, respectively. In addition, $\boldsymbol{C}_{ZY}$ has the form

$$\boldsymbol{C}_{ZY}=\begin{bmatrix}\mathrm{Tr}_m(\boldsymbol{R}_{yz}) & \mathrm{Tr}_{(m+1)}(\boldsymbol{R}_{yz}) & \dots & \mathrm{Tr}_{(m+q_2-1)}(\boldsymbol{R}_{yz})\\ \mathrm{Tr}_{(m-1)}(\boldsymbol{R}_{yz}) & \mathrm{Tr}_m(\boldsymbol{R}_{yz}) & \dots & \mathrm{Tr}_{(m+q_2-2)}(\boldsymbol{R}_{yz})\\ \vdots & \vdots & \ddots & \vdots\\ \mathrm{Tr}_{(m-q+1)}(\boldsymbol{R}_{yz}) & \mathrm{Tr}_{(m-q+2)}(\boldsymbol{R}_{yz}) & \dots & \mathrm{Tr}_{(m+q_2-q)}(\boldsymbol{R}_{yz})\end{bmatrix} \tag{4.23}$$

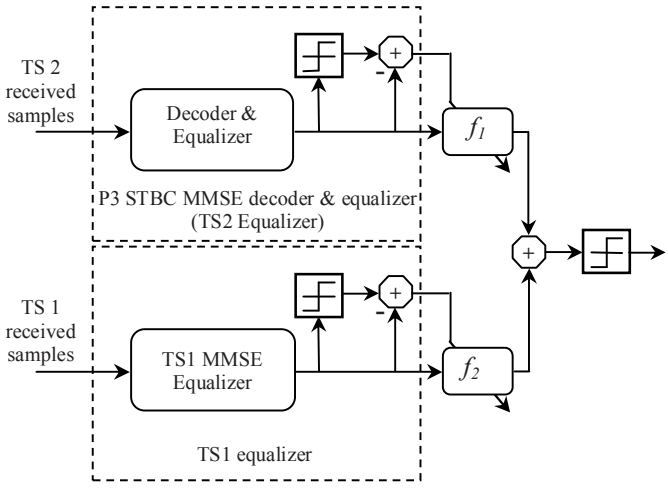

Figure 4.5: Sub-optimal MMSE equalizer for P1.

where $m = (q-l)/2$, the vector cross-correlation matrix $\boldsymbol{R}_{yz} = \mathrm{E}\{\boldsymbol{y}_{Dt1}^{(k)}\,\boldsymbol{z}_1^{\dagger}\} = \sigma_x^2\,\gamma_2\,\boldsymbol{H}_2\,\boldsymbol{G}^{\dagger}$, and finally, $\boldsymbol{c}_{Yx} = [\boldsymbol{0}_{1\times[(l-1)/2]}, (\widetilde{\boldsymbol{h}}_{2\mathrm{ext}}^{*(k)})^T, \boldsymbol{0}_{1\times[(l-1)/2]}]^T$.

Similarly, the equalizer output estimating the symbols $\boldsymbol{x}_2$ is

$$\widehat{\boldsymbol{x}}_2 = \boldsymbol{Z}_{02}\,\boldsymbol{w}_{02} - \widetilde{\boldsymbol{Y}}_{12}^{*}\,\widetilde{\boldsymbol{w}}_{12}^{*} \tag{4.24}$$

where $\boldsymbol{Z}_{02}$ has the same size and the form as $\boldsymbol{Z}_{01}$ in (4.21) with $\boldsymbol{z}_1$ replaced by $\boldsymbol{z}_2$ and $\boldsymbol{Y}_{12}$ has the same size and the form as $\boldsymbol{Y}_{11}$ in (4.21) with $\boldsymbol{y}_{Dt1}^{(k)}$ replaced by $\boldsymbol{y}_{Dt1}^{(k+1)}$. Analogously, it can be shown that the optimum MMSE equalizer tap weight vector for estimating the symbols $\boldsymbol{x}_2$ is

$$\begin{bmatrix} \boldsymbol{w}_{02} \\ \widetilde{\boldsymbol{w}}_{12}^{*} \end{bmatrix} = \begin{bmatrix} \boldsymbol{C}_{ZZ} & \widetilde{\boldsymbol{C}}_{ZY}^{*} \\ (\widetilde{\boldsymbol{C}}_{ZY}^{*})^{\dagger} & \widetilde{\boldsymbol{C}}_{YY}^{*} \end{bmatrix}^{-1} \begin{bmatrix} \boldsymbol{c}_{Zx} \\ \widetilde{\boldsymbol{c}}_{Yx}^{*} \end{bmatrix}. \tag{4.25}$$

Sub-Optimal Protocol I MMSE Receiver

The suboptimal P1 MMSE equalizer is derived here using independently-optimized P3 MMSE and TS1 equalizers. The block diagram of the suboptimal P1 equalizer is shown in Fig. 4.5. In the figure, the 'TS2 Equalizer' is the P3 STBC MMSE decoder/equalizer given in Sec. 4.2.1 and the 'TS1 Equalizer' is the non-STBC equalizer that only depends on the information received at the destination during TS1 given by (4.20).

To derive the MMSE solution for the 'TS1 Equalizer', we define the tap weight vector $\boldsymbol{w}_1$ of length $q_2 = V + l$, where l is an odd integer for convenience. First, we consider the equalizer output estimating the symbols $\boldsymbol{x}_1$,

$$\widehat{\boldsymbol{x}}_1 = \boldsymbol{Y}_{11}\,\boldsymbol{w}_1 \tag{4.26}$$

where $\boldsymbol{Y}_{11}$ is given in (4.21). The optimum MMSE equalizer tap weight vector is then

$$\boldsymbol{w}_1 = \boldsymbol{C}_{YY}^{-1}\boldsymbol{c}_{Yx} \tag{4.27}$$

where $\boldsymbol{C}_{YY}$ and $\boldsymbol{c}_{Yx}$ are given in (4.22). The two equations given in (4.20) have the same channel gain and noise statistics. Hence, the same optimal equalizer tap weight vector, $\boldsymbol{w}_1$, can be used to estimate the symbols $\boldsymbol{x}_2$ as

$$\widehat{\boldsymbol{x}}_2 = -\widetilde{\boldsymbol{Y}}_{12}^{*}\,\widetilde{\boldsymbol{w}}_1^{*} \tag{4.28}$$

where $\boldsymbol{Y}_{12}$ is given in (4.24).

To reduce the computational complexity of the equalizer, we propose a suboptimal P1 MMSE equalizer which combines the 'TS1 Equalizer' and 'TS2 Equalizer' outputs scaled by factors f_2 and f_1, respectively. The factors f_2 and f_1 depend on the average sliced MSE of the equalizer outputs. To calculate these factors, we define $\widehat{\boldsymbol{x}}_{TS1}$ and $\widehat{\boldsymbol{x}}_{TS2}$ as the 'TS1' and 'TS2' equalizer outputs and $\check{\boldsymbol{x}}_{TS1}$ and $\check{\boldsymbol{x}}_{TS2}$ as the corresponding slicer outputs. Then the average sliced MSEs $a1_{\mathrm{MSE}}$ and $a2_{\mathrm{MSE}}$ of the 'TS2 Equalizer' and 'TS1 Equalizer' outputs can be estimated using

$$\begin{aligned} a1_{\mathrm{MSE}} &= \frac{1}{2N}\|\check{\boldsymbol{x}}_{TS2} - \widehat{\boldsymbol{x}}_{TS2}\|^2, \\ a2_{\mathrm{MSE}} &= \frac{1}{2N}\|\check{\boldsymbol{x}}_{TS1} - \widehat{\boldsymbol{x}}_{TS1}\|^2 . \end{aligned} \tag{4.29}$$

Finally, the scale factors are

$$f_1 = \frac{a1_{\mathrm{MSE}}}{a1_{\mathrm{MSE}} + a2_{\mathrm{MSE}}}, \qquad f_2 = \frac{a2_{\mathrm{MSE}}}{a1_{\mathrm{MSE}} + a2_{\mathrm{MSE}}} . \tag{4.30}$$

By updating the 'TS1' and 'TS2' equalizer tap weights independently, this suboptimal equalizer has reduced complexity relative to the optimal one. In Sec. 4.6, the complexity versus performance tradeoff of the two P1 equalizers are discussed.

4.3 Distributed TR-STBC Time-Domain Adaptive Receivers

Next, we develop adaptive receiver structures for both protocols P1 and P3 by exploiting the structure of the TR-STBC decoder. The adaptive algorithms eliminate the need for explicit CIR estimation at the receiver and allow the receiver to track a time-varying channel.

4.3.1 Protocol III Adaptive Receiver

By defining $\boldsymbol{H}_{1D}^{(k)} = \gamma_1 \boldsymbol{H}_{3d}^{(k)} \boldsymbol{H}_{1d}^{(k)}$ and letting $\boldsymbol{H}_{2D}^{(k)} = \gamma_2 \boldsymbol{H}_{2d}^{(k)}$, (4.13) can be written as

$$\boldsymbol{H}_d = \begin{bmatrix} \widetilde{\boldsymbol{H}}_{1D}^{*(k)} & \boldsymbol{H}_{2D}^{(k)} \\ \widetilde{\boldsymbol{H}}_{2D}^{*(k)} & -\boldsymbol{H}_{1D}^{(k)} \end{bmatrix}. \tag{4.31}$$

Using the property that the Wiener tap weight vector $\boldsymbol{w}_o$ is the same for both outputs $\boldsymbol{z}_1$ and $\boldsymbol{z}_2$, the equalizer outputs for the two streams can written as

$$\begin{aligned} \begin{bmatrix} \widehat{\boldsymbol{x}}_1 \\ \widehat{\boldsymbol{x}}_2 \end{bmatrix} &= \begin{bmatrix} \boldsymbol{W} & \boldsymbol{0} \\ \boldsymbol{0} & \boldsymbol{W} \end{bmatrix} \begin{bmatrix} \boldsymbol{z}_1 \\ \boldsymbol{z}_2 \end{bmatrix} \\ &= \begin{bmatrix} \boldsymbol{W}\, \widetilde{\boldsymbol{H}}_{1\mathrm{D}}^{*(k)} & \boldsymbol{W}\, \boldsymbol{H}_{2\mathrm{D}}^{(k)} \\ \boldsymbol{W}\, \widetilde{\boldsymbol{H}}_{2\mathrm{D}}^{*(k)} & -\boldsymbol{W}\, \boldsymbol{H}_{1\mathrm{D}}^{(k)} \end{bmatrix} \begin{bmatrix} \boldsymbol{y}_{Dt2}^{(k)} \\ \widetilde{\boldsymbol{y}}_{Dt2}^{*(k+1)} \end{bmatrix} \end{aligned} \tag{4.32}$$

where the equalizer matrix $\boldsymbol{W}$ has dimension $(N + 2V + q - 1) \times (N + 2V)$ and has the form shown in (4.7) with $\boldsymbol{h}_{1\mathrm{ext}}^{(k)}$ replaced by $\boldsymbol{w}_o$. Using the analysis of Sec. 4.2.1, it can be shown that the optimal tap weight vector $\boldsymbol{w}_o$ has the conjugate time-reversal symmetry property $\boldsymbol{w}_o = \widetilde{\boldsymbol{w}}_o^*$. Based on this property,

$$\begin{bmatrix} \widehat{\boldsymbol{x}}_1 \\ \widehat{\boldsymbol{x}}_2 \end{bmatrix} \triangleq \begin{bmatrix} \widetilde{\boldsymbol{A}}_1^* & \boldsymbol{A}_2 \\ \widetilde{\boldsymbol{A}}_2^* & -\boldsymbol{A}_1 \end{bmatrix} \begin{bmatrix} \boldsymbol{y}_{Dt2}^{(k)} \\ \widetilde{\boldsymbol{y}}_{Dt2}^{*(k+1)} \end{bmatrix} \tag{4.33}$$

where joint equalizer-channel matrixes $\boldsymbol{A}_1 = \boldsymbol{W}\, \boldsymbol{H}_{1\mathrm{D}}^{(k)}$ and $\boldsymbol{A}_2 = \boldsymbol{W}\, \boldsymbol{H}_{2\mathrm{D}}^{(k)}$. Time reversing and conjugating $\widehat{\boldsymbol{x}}_2$, we can write

$$\begin{bmatrix} \widehat{\boldsymbol{x}}_1 \\ \widetilde{\widehat{\boldsymbol{x}}}_2^* \end{bmatrix} = \begin{bmatrix} \widetilde{\boldsymbol{A}}_1^*\, \boldsymbol{y}_{Dt2}^{(k)} + \boldsymbol{A}_2\, \widetilde{\boldsymbol{y}}_{Dt2}^{*(k+1)} \\ \boldsymbol{A}_2\, \widetilde{\boldsymbol{y}}_{Dt2}^{*(k)} - \widetilde{\boldsymbol{A}}_1^*\, \boldsymbol{y}_{Dt2}^{(k+1)} \end{bmatrix}. \tag{4.34}$$

If we define the combined equalizer and decoder vectors

$$\boldsymbol{w}_1 = \gamma_1 \,\mathrm{conv}(\mathrm{conv}(\widetilde{\boldsymbol{h}}_1^*, \widetilde{\boldsymbol{h}}_{3\mathrm{ext}}^*), \widetilde{\boldsymbol{w}}_o^*) \tag{4.35}$$

and

$$\boldsymbol{w}_2 = \gamma_2 \,\mathrm{conv}(\boldsymbol{w}_o, \boldsymbol{h}_{2\mathrm{ext}}), \tag{4.36}$$

both of length $q_a = q+V$, the combined decoder and equalizer output can be written as

$$\begin{bmatrix} \widehat{\boldsymbol{x}}_1 \\ \widetilde{\widehat{\boldsymbol{x}}}_2^* \end{bmatrix} = \begin{bmatrix} \boldsymbol{Y}^{(k)} & \widetilde{\boldsymbol{Y}}^{*(k+1)} \\ -\boldsymbol{Y}^{(k+1)} & \widetilde{\boldsymbol{Y}}^{*(k)} \end{bmatrix} \begin{bmatrix} \boldsymbol{w}_1 \\ \boldsymbol{w}_2 \end{bmatrix} \triangleq \boldsymbol{U}_{Dt2}\, \boldsymbol{w}^{(k)} \tag{4.37}$$

where matrix $\boldsymbol{Y}^{(i)}$ has dimension $(N+2V+q-1)\times(q+V)$ and has the form shown in (4.7) with $\boldsymbol{h}_{1\mathrm{ext}}^{(k)}$ replaced by $\boldsymbol{y}_{Dt2}^{(i)}$. The equalizer tap weights $\boldsymbol{w}^{(k)}$ are now isolated in (4.37), and they can be easily adapted using block versions of, for example, the well-known NLMS and RLS algorithms [44].

4.3.2 Protocol I Optimal Adaptive Receiver

Using the analysis of Sec. 4.2.2, it can be shown that the optimal tap weight vectors of the optimal P1 MMSE equalizer satisfy $\boldsymbol{w}_{01} = \widetilde{\boldsymbol{w}}_{02}^*$ and $\boldsymbol{w}_{11} = \boldsymbol{w}_{12}$. Applying these relations and using similar arguments used in deriving equations (4.31)–(4.37), the optimal P1 MMSE equalizer output can be rewritten as

$$\begin{aligned} \begin{bmatrix} \widehat{\boldsymbol{x}}_1 \\ \widetilde{\widehat{\boldsymbol{x}}}_2^* \end{bmatrix} &= \boldsymbol{U}_{Dt2} \begin{bmatrix} \boldsymbol{w}_{1p1} \\ \boldsymbol{w}_{2p1} \end{bmatrix} + \begin{bmatrix} \boldsymbol{Y}_{11} \\ -\boldsymbol{Y}_{12} \end{bmatrix} \boldsymbol{w}_{11} \\ &= \left[\begin{array}{c|c} \boldsymbol{U}_{Dt2} & \begin{matrix} \boldsymbol{Y}_{11} \\ -\boldsymbol{Y}_{12} \end{matrix} \end{array}\right] \begin{bmatrix} \boldsymbol{w}_{1p1} \\ \boldsymbol{w}_{2p1} \\ \boldsymbol{w}_{11} \end{bmatrix} \triangleq \boldsymbol{U}\boldsymbol{w}^{(k)} \end{aligned} \tag{4.38}$$

where combined equalizer and decoder vectors $\boldsymbol{w}_{1p1} = \gamma_1 \,\mathrm{conv}(\mathrm{conv}(\widetilde{\boldsymbol{h}}_1^*, \widetilde{\boldsymbol{h}}_{3\mathrm{ext}}^*), \boldsymbol{w}_{01})$ and $\boldsymbol{w}_{2p1} = \gamma_2 \,\mathrm{conv}(\boldsymbol{w}_{01}, \boldsymbol{h}_{2\mathrm{ext}})$ have length $q_a = q+V$, and $\boldsymbol{w}_{11}$ is given in (4.22). As in (4.37), the equalizer tap weights $\boldsymbol{w}^{(k)}$ are isolated in (4.38), and traditional block adaptive algorithms can be used to construct the adaptive P1 receiver.

4.3.3 Protocol I Suboptimal Adaptive Receiver

The suboptimal P1 adaptive equalizer consists of independently adapting the 'TS1' and 'TS2' equalizers as in the case of the suboptimal P1 MMSE equalizer. The 'TS2' adaptive equalizer is just the same as the adaptive equalizer for P3 given in Sec. 4.3.1. The 'TS1' adaptive equalizer can be easily put into block adaptive form by considering the MMSE solutions given in (4.26) and (4.28). These two equations can be combined and the output of the adaptive 'TS1' equalizer is then

$$\begin{bmatrix} \widehat{\boldsymbol{x}}_1 \\ \widetilde{\widehat{\boldsymbol{x}}}_2^* \end{bmatrix} = \begin{bmatrix} \boldsymbol{Y}_{11} \\ -\boldsymbol{Y}_{12} \end{bmatrix} \boldsymbol{w}_1 \triangleq \boldsymbol{U}_{Dt1}\, \boldsymbol{w}^{(k)}. \tag{4.39}$$

To obtain the suboptimal P1 adaptive equalizer output, the 'TS1' and 'TS2' adaptive equalizer outputs are scaled and combined as explained for the suboptimal P1 MMSE equalizer in (4.29) and (4.30).

4.3.4 Block RLS Algorithms

To compare the performances of the adaptive receivers for P1 and P3, we have derived three block versions of the RLS algorithm which are summarized in Tables 4.2 and 4.3. These versions use equations (4.37) for the P3 receiver, (4.38) for the P1 optimal receiver, and (4.37) and (4.39) for the P1 suboptimal receiver. The estimation error vector $\boldsymbol{e}^{(k)}$ is

$$\boldsymbol{e}^{(k)} = \begin{bmatrix} \boldsymbol{x}_{1\text{ext}}^{(k)} \\ \widetilde{\boldsymbol{x}}_{2\text{ext}}^{*(k)} \end{bmatrix} - \begin{bmatrix} \widehat{\boldsymbol{x}}_1^{(k)} \\ \widetilde{\widehat{\boldsymbol{x}}}_2^{*(k)} \end{bmatrix} \tag{4.40}$$

where $\boldsymbol{x}_{\ell\text{ext}}^{(k)} = \left[\boldsymbol{0}_{1\times[(2V+q-1)/2]}, (\boldsymbol{x}_\ell^{(k)})^T, \boldsymbol{0}_{1\times[(2V+q-1)/2]}\right]^T$. Note also that in both block RLS algorithms, the Matrix Inversion Lemma is not applied, as it increases the dimensionality of the required matrix inversions. The adaptive receivers operate in training mode for the training blocks within a frame and switch to decision directed mode for the data blocks.

Table 4.2: Block RLS Algorithm for Distributed TR-STBC Systems

Protocol III	**Protocol I Optimal**
Initial conditions: $\boldsymbol{w}^{(0)} = \mathbf{0}_{2q_a \times 1}$ $\boldsymbol{\Phi}^{(0)} = \boldsymbol{I}_{2q_a \times 2q_a}$	Initial conditions: $\boldsymbol{w}^{(0)} = \mathbf{0}_{(2q_a+q_2)\times 1}$ $\boldsymbol{\Phi}^{(0)} = \boldsymbol{I}_{(2q_a+q_2)\times(2q_a+q_2)}$
Update taps at each iteration using: $\boldsymbol{\Phi}^{(k+2)} = \lambda\boldsymbol{\Phi}^{(k)} + \boldsymbol{U}_{Dt2}^{\dagger}\boldsymbol{U}_{Dt2}$ $\boldsymbol{w}^{(k+2)} = \boldsymbol{w}^{(k)} + (\boldsymbol{\Phi}^{(k+2)})^{-1}\boldsymbol{U}_{Dt2}^{\dagger}\boldsymbol{e}^{(k)}$ where λ is small positive close to 1	Update taps at each iteration using: $\boldsymbol{\Phi}^{(k+2)} = \lambda\boldsymbol{\Phi}^{(k)} + \boldsymbol{U}^{\dagger}\boldsymbol{U}$ $\boldsymbol{w}^{(k+2)} = \boldsymbol{w}^{(k)} + (\boldsymbol{\Phi}^{(k+2)})^{-1}\boldsymbol{U}^{\dagger}\boldsymbol{e}^{(k)}$ where λ is small positive close to 1

Table 4.3: Block RLS Algorithm for P1 Sub-Optimal Distributed TR-STBC System

P1 Sub-Optimal	
TS2 Initial conditions: $\boldsymbol{w}^{(0)} = \mathbf{0}_{2q_a \times 1}$ $\boldsymbol{\Phi}^{(0)} = \boldsymbol{I}_{2q_a \times 2q_a}$	TS1 Initial conditions: $\boldsymbol{w}^{(0)} = \mathbf{0}_{q_2 \times 1}$ $\boldsymbol{\Phi}^{(0)} = \boldsymbol{I}_{q_2 \times q_2}$
Equalizer output: $\widehat{\boldsymbol{x}}_{TS2} = \boldsymbol{U}_{Dt2}\,\boldsymbol{w}^{(k)}$	Equalizer output: $\widehat{\boldsymbol{x}}_{TS1} = \boldsymbol{U}_{Dt1}\,\boldsymbol{w}^{(k)}$
Update taps at each iteration using: $\boldsymbol{\Phi}^{(k+2)} = \lambda\boldsymbol{\Phi}^{(k)} + \boldsymbol{U}_{Dt2}^{\dagger}\boldsymbol{U}_{Dt2}$ $\boldsymbol{w}^{(k+2)} = \boldsymbol{w}^{(k)} + (\boldsymbol{\Phi}^{(k+2)})^{-1}\boldsymbol{U}_{Dt2}^{\dagger}\boldsymbol{e}^{(k)}$ where λ is small positive close to 1	Update taps at each iteration using: $\boldsymbol{\Phi}^{(k+2)} = \lambda\boldsymbol{\Phi}^{(k)} + \boldsymbol{U}_{Dt1}^{\dagger}\boldsymbol{U}_{Dt1}$ $\boldsymbol{w}^{(k+2)} = \boldsymbol{w}^{(k)} + (\boldsymbol{\Phi}^{(k+2)})^{-1}\boldsymbol{U}_{Dt1}^{\dagger}\boldsymbol{e}^{(k)}$ where λ is small positive close to 1
Combined output: $\widehat{\boldsymbol{x}} = f_1\widehat{\boldsymbol{x}}_{TS2} + f_2\widehat{\boldsymbol{x}}_{TS1}$	

4.4 Distributed TR-STBC Frequency-Domain MMSE Receivers

In the context of the previous research into SC FDE-STBC systems [26, 28, 29, 22], in this section we derive frequency-domain MMSE equalization schemes for distributed TR-STBC systems to compare with the time-domain MMSE equalization schemes derived in Sec. 4.2.

4.4.1 Protocol III MMSE Receiver

Considering the same distributed TR-STBC transmission scheme described in Sec. 4.1, the received signal at R during *Time slot 1* of the k-th transmitted block is

$$\boldsymbol{y}_{R\text{ext}}^{(k)} = \sqrt{E_{SR}}\,\boldsymbol{H}_1^{(k)}\,\boldsymbol{x}_{1\text{ext}}^{(k)} + \boldsymbol{n}_{R\text{ext}}^{(k)} \tag{4.41}$$

where $\boldsymbol{H}_1^{(k)}$ is a $(N+V)\times(N+V)$ circulant channel matrix for the $S\rightarrow R$ link with first column of the form $[(\boldsymbol{h}_1^{(k)})^T, \boldsymbol{0}_{1\times(N+V-L_1-1)}]^T$ and $\boldsymbol{x}_{1\text{ext}}^{(k)} = [(\boldsymbol{x}_1^{(k)})^T, \boldsymbol{0}_{1\times V}]^T$.

The relay terminal first removes the last $V-L_1$ noise-only terms in $\boldsymbol{y}_{R\text{ext}}^{(k)}$ and scales each entry of the resulting vector by a factor $\sqrt{E_{SR}+\sigma_{nR}^2}$ to give an average unit energy. Then a ZP of length $V-L_1$ is appended. The modified and scaled observations $\overline{\boldsymbol{y}}_{RF}^{(k)}$ can now be written as

$$\overline{\boldsymbol{y}}_{RF}^{(k)} = \sqrt{\frac{E_{SR}}{E_{SR}+\sigma_{nR}^2}}\,\boldsymbol{H}_1^{(k)}\,\boldsymbol{x}_{1\text{ext}}^{(k)} + \frac{1}{\sqrt{E_{SR}+\sigma_{nR}^2}}\,\boldsymbol{n}_{RF}^{(k)} \tag{4.42}$$

where $\boldsymbol{n}_{RF}^{(k)} = [(\boldsymbol{n}_R^{(k)})^T, \boldsymbol{0}_{1\times(V-L_1)}]^T$ with $\boldsymbol{n}_R^{(k)}$ containing the first $N+V-L_1-1$ samples of $\boldsymbol{n}_{R\text{ext}}^{(k)}$. The relay terminal transmits $\overline{\boldsymbol{y}}_{RF}^{(k)}$ during *Time slot 2* as depicted in Fig. 4.6. In the figure $\overline{\boldsymbol{y}}_{RF}^{(k)}$ and $\overline{\boldsymbol{y}}_{RF}^{(k+1)}$ represent the modified and scaled relay observation vectors during blocks k and $k+1$, respectively. As seen from the figure, there is no transmission from R during *Time slot 1*, and a ZP of length $V-L_1$ is inserted by the relay terminal. Note that Fig. 4.6 is the same as Fig. 4.3 only differing in notation.

During *Time slot 2*, the destination terminal receives signals from both the relay and source terminals. The received signal at D for the k-th transmitted block is

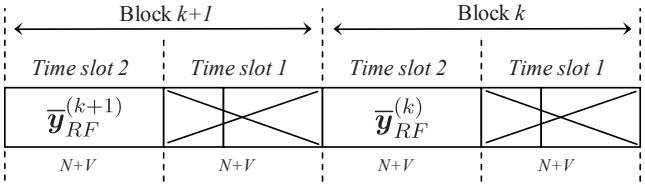

Figure 4.6: Relay terminal transmission block format for FDE.

given by

$$\boldsymbol{y}_{Dt2}^{(k)} = \sqrt{E_{RD}}\,\boldsymbol{H}_3^{(k)}\,\overline{\boldsymbol{y}}_{RF}^{(k)} + \sqrt{E_{SD}}\,\boldsymbol{H}_2^{(k)}\,\boldsymbol{x}_{2\text{ext}}^{(k)} + \boldsymbol{n}_{Dt2}^{(k)} \tag{4.43}$$

where $\boldsymbol{H}_2^{(k)}$ is a $(N+V)\times(N+V)$ circulant channel matrix for the $S{\rightarrow}D$ link with the first column of the form $[(\boldsymbol{h}_2^{(k)})^T, \boldsymbol{0}_{1\times(N+V-L_2-1)}]^T$, $\boldsymbol{H}_3^{(k)}$ is a $(N+V)\times(N+V)$ circulant channel matrix for the $R{\rightarrow}D$ link with the first column of the form $[(\boldsymbol{h}_3^{(k)})^T, \boldsymbol{0}_{1\times(N+V-L_3-1)}]^T$, and finally $\boldsymbol{x}_{2\text{ext}}^{(k)} = [(\boldsymbol{x}_2^{(k)})^T, \boldsymbol{0}_{1\times V}]^T$. Combining and scaling (4.42) and (4.43), we find

$$\boldsymbol{y}_{Dt2}^{(k)} = \gamma_1\boldsymbol{H}_3^{(k)}\boldsymbol{H}_1^{(k)}\boldsymbol{x}_{1\text{ext}}^{(k)} + \gamma_2\boldsymbol{H}_2^{(k)}\boldsymbol{x}_{2\text{ext}}^{(k)} + \boldsymbol{n}_{Dt2}^{(k)} + \gamma_3\boldsymbol{H}_3^{(k)}\boldsymbol{n}_{RF}^{(k)}\,. \tag{4.44}$$

Assuming that the channels' coefficients remain constant over two consecutive blocks, and defining a permutation matrix $\boldsymbol{P}$ as in [58],

$$\boldsymbol{P} = \begin{bmatrix} \boldsymbol{E}_N & \boldsymbol{0}_{N\times V} \\ \boldsymbol{0}_{V\times N} & \boldsymbol{E}_V \end{bmatrix} \tag{4.45}$$

the received signal at D during *Time slot 2* of the $k+1$-th transmitted block is given by

$$\boldsymbol{y}_{Dt2}^{(k+1)} = -\gamma_1\boldsymbol{H}_3^{(k)}\boldsymbol{H}_1^{(k)}\boldsymbol{P}\boldsymbol{x}_{2\text{ext}}^{*(k)} + \gamma_2\boldsymbol{H}_2^{(k)}\boldsymbol{P}\boldsymbol{x}_{1\text{ext}}^{*(k)} + \boldsymbol{n}_{Dt2}^{(k+1)} + \gamma_3\boldsymbol{H}_3^{(k)}\boldsymbol{n}_{RF}^{(k+1)}\,. \tag{4.46}$$

Left-multiplying (4.46) by $\boldsymbol{P}$, conjugating, and using the property from [58] that $\boldsymbol{P}\boldsymbol{H}_\ell^{(k)}\boldsymbol{P} = \boldsymbol{H}_\ell^{T(k)}$, we have

$$\begin{aligned}\boldsymbol{P}\boldsymbol{y}_{Dt2}^{*(k+1)} = &-\gamma_1(\boldsymbol{H}_3^{(k)})^\dagger(\boldsymbol{H}_1^{(k)})^\dagger\boldsymbol{x}_{2\text{ext}}^{(k)} + \gamma_2(\boldsymbol{H}_2^{(k)})^\dagger\boldsymbol{x}_{1\text{ext}}^{(k)} \\ &+ \boldsymbol{P}\boldsymbol{n}_{Dt2}^{*(k+1)} + \gamma_3(\boldsymbol{H}_3^{(k)})^\dagger\boldsymbol{P}\boldsymbol{n}_{RF}^{*(k+1)}\,.\end{aligned} \tag{4.47}$$

Now taking the discrete Fourier transform (DFT) of (4.44) and (4.47) and stacking

the resulting vectors, we can write

$$\begin{aligned}\underline{\boldsymbol{y}}_{Dt2} &\triangleq \begin{bmatrix} \boldsymbol{Q}\boldsymbol{y}_{Dt2}^{(k)} \\ \boldsymbol{Q}\boldsymbol{P}\boldsymbol{y}_{Dt2}^{*(k+1)} \end{bmatrix} \triangleq \begin{bmatrix} \underline{\boldsymbol{y}}_{Dt2}^{(k)} \\ \overline{\underline{\boldsymbol{y}}}_{Dt2}^{*(k+1)} \end{bmatrix} \triangleq \boldsymbol{\Lambda}\underline{\boldsymbol{x}} + \underline{\boldsymbol{n}} \\ &= \begin{bmatrix} \gamma_1 \boldsymbol{\Lambda}_3^{(k)} \boldsymbol{\Lambda}_1^{(k)} & \gamma_2 \boldsymbol{\Lambda}_2^{(k)} \\ \gamma_2 \boldsymbol{\Lambda}_2^{*(k)} & -\gamma_1 \boldsymbol{\Lambda}_3^{*(k)} \boldsymbol{\Lambda}_1^{*(k)} \end{bmatrix} \begin{bmatrix} \underline{\boldsymbol{x}}_1^{(k)} \\ \underline{\boldsymbol{x}}_2^{(k)} \end{bmatrix} + \begin{bmatrix} \underline{\boldsymbol{n}}_{Dt2}^{(k)} + \gamma_3 \boldsymbol{\Lambda}_3^{(k)} \underline{\boldsymbol{n}}_R^{(k)} \\ \overline{\underline{\boldsymbol{n}}}_{Dt2}^{*(k+1)} + \gamma_3 \boldsymbol{\Lambda}_3^{*(k)} \overline{\underline{\boldsymbol{n}}}_R^{*(k+1)} \end{bmatrix}\end{aligned} \tag{4.48}$$

where $\boldsymbol{Q}$ is the orthonormal DFT matrix, diagonal matrix $\boldsymbol{\Lambda}_i^{(j)} = \boldsymbol{Q}\boldsymbol{H}_i^{(j)}\boldsymbol{Q}^*$ with (n,n)-th entry equal to the n-th DFT coefficient of the CIR $\boldsymbol{h}_i^{(j)}$, $\underline{\boldsymbol{x}}_i^{(k)} = \boldsymbol{Q}\,\boldsymbol{x}_{i\text{ext}}^{(k)}$, $\underline{\boldsymbol{n}}_i^{(j)} = \boldsymbol{Q}\,\boldsymbol{n}_i^{(j)}$, and finally $\overline{\underline{\boldsymbol{n}}}_i^{*(j)} = \boldsymbol{Q}\boldsymbol{P}\boldsymbol{n}_i^{*(j)}$.

Matrix $\boldsymbol{\Lambda}$ has the property that the transmitted blocks $\underline{\boldsymbol{x}}_1^{(k)}$ and $\underline{\boldsymbol{x}}_2^{(k)}$ become decoupled by multiplying both sides of the equation (4.48) by matrix $\boldsymbol{\Lambda}^\dagger$. Thus, the resulting output from the decoder is

$$\begin{aligned}\boldsymbol{\psi} &\triangleq \begin{bmatrix} \boldsymbol{\psi}^{(k)} \\ \boldsymbol{\psi}^{(k+1)} \end{bmatrix} = \boldsymbol{\Lambda}^\dagger \underline{\boldsymbol{y}}_{Dt2} = \boldsymbol{\Lambda}^\dagger \boldsymbol{\Lambda}\underline{\boldsymbol{x}} + \boldsymbol{\Lambda}^\dagger \boldsymbol{n} \\ &= \begin{bmatrix} \widetilde{\boldsymbol{\Lambda}} & \boldsymbol{0} \\ \boldsymbol{0} & \widetilde{\boldsymbol{\Lambda}} \end{bmatrix} \begin{bmatrix} \underline{\boldsymbol{x}}_1^{(k)} \\ \underline{\boldsymbol{x}}_2^{(k)} \end{bmatrix} + \boldsymbol{\Lambda}^\dagger \begin{bmatrix} \underline{\boldsymbol{n}}_{Dt2}^{(k)} + \gamma_3 \boldsymbol{\Lambda}_3^{(k)} \underline{\boldsymbol{n}}_R^{(k)} \\ \overline{\underline{\boldsymbol{n}}}_{Dt2}^{*(k+1)} + \gamma_3 \boldsymbol{\Lambda}_3^{*(k)} \overline{\underline{\boldsymbol{n}}}_R^{*(k+1)} \end{bmatrix}\end{aligned} \tag{4.49}$$

where

$$\widetilde{\boldsymbol{\Lambda}} \triangleq \gamma_1^2 \boldsymbol{\Lambda}_3^{(k)} \boldsymbol{\Lambda}_3^{*(k)} \boldsymbol{\Lambda}_1^{(k)} \boldsymbol{\Lambda}_1^{*(k)} + \gamma_2^2 \boldsymbol{\Lambda}_2^{(k)} \boldsymbol{\Lambda}_2^{*(k)} \,. \tag{4.50}$$

Along with being decoupled in terms of the symbols $\underline{\boldsymbol{x}}_1^{(k)}$ and $\underline{\boldsymbol{x}}_2^{(k)}$, we see that the decoder outputs $\boldsymbol{\psi}^{(k)}$ and $\boldsymbol{\psi}^{(k+1)}$ have equal channel gain matrices and can show for each protocol that the statistics of the noise terms in $\boldsymbol{\psi}^{(k)}$ and $\boldsymbol{\psi}^{(k+1)}$ are identical and uncorrelated, leading to independence since they are jointly Gaussian. Therefore, the same MMSE tap weights can be applied to both blocks $\boldsymbol{\psi}^{(k)}$ and $\boldsymbol{\psi}^{(k+1)}$ to remove the ISI. Thus, a block of only one decoder's outputs, $\boldsymbol{\psi}^{(k)}$ is considered when deriving the MMSE solution for the equalizer taps.

As we are performing FDE, the distributed TR-STBC MMSE-FDE equalizer must have $N + V$ taps, equal to the length of the block. Minimizing the MSE

$J = \mathrm{E}\{\|\underline{\boldsymbol{x}}_1^{(k)} - \boldsymbol{W}\boldsymbol{\psi}^{(k)}\|^2\}$ as a function of the $(N+V)\times(N+V)$ diagonal matrix $\boldsymbol{W}$, it can be shown that the optimum distributed TR-STBC MMSE-FDE equalizer tap weight vector is

$$\boldsymbol{W}_0 = \sigma_x^2(\sigma_x^2\widetilde{\boldsymbol{\Lambda}} + \sigma_{nD}^2\boldsymbol{I}_N + \sigma_{nR}^2\gamma_3^2\boldsymbol{\Lambda}_3^{(k)}\boldsymbol{\Lambda}_3^{*(k)})^{-1}\,. \tag{4.51}$$

In deriving the solution (4.51), we use the fact that after the orthonormal transformation by $\boldsymbol{Q}$, the noise vectors, $\underline{\boldsymbol{n}}_i^{(j)}$, and symbol vectors, $\underline{\boldsymbol{x}}_i^{(k)}$, remain white with correlation matrices $\boldsymbol{R}_{ni} = \sigma_{ni}^2\boldsymbol{I}_{(N+V)}$ and $\boldsymbol{R}_x = \sigma_x^2\boldsymbol{I}_{(N+V)}$, respectively. Thus, the outputs of the distributed TR-STBC MMSE-FDE equalizer for both blocks are

$$\widehat{\underline{\boldsymbol{x}}}_1^{(k)} = \boldsymbol{W}_0\boldsymbol{\psi}^{(k)} \text{ and } \widehat{\underline{\boldsymbol{x}}}_2^{(k)} = \boldsymbol{W}_0\boldsymbol{\psi}^{(k+1)}. \tag{4.52}$$

4.4.2 Protocol I MMSE FDE Receivers

In this section we propose analogous optimal and suboptimal frequency-domain MMSE receivers for P1 by combining the frequency-domain P3 MMSE receiver with a frequency-domain version of the TS1 equalizer. In the optimal case, the taps of the P3 equalizer and the TS1 equalizer are jointly optimized using the MMSE criterion, and in the suboptimal case, the taps of the P3 equalizer and the TS1 equalizer are independently derived and linearly combined at the outputs of the equalizers.

Optimal Protocol I MMSE FDE Receiver

As in the time-domain case, assuming that the channel coefficients remain constant over two consecutive blocks, the received signals at D during *Time slot 1* of the k-th and $k+1$-th blocks are

$$\begin{aligned}\boldsymbol{y}_{Dt1}^{(k)} &= \gamma_2\,\boldsymbol{H}_2^{(k)}\boldsymbol{x}_{1\text{ext}}^{(k)} + \boldsymbol{n}_{Dt1}^{(k)}\\ \boldsymbol{y}_{Dt1}^{(k+1)} &= -\gamma_2\,\boldsymbol{H}_2^{(k)}\boldsymbol{P}\boldsymbol{x}_{1\text{ext}}^{*(k)} + \boldsymbol{n}_{Dt1}^{(k+1)}\end{aligned} \tag{4.53}$$

where $\boldsymbol{H}_2^{(k)}$ is a $(N+V)\times(N+V)$ circulant channel matrix for the $S\rightarrow D$ link with first column of the form $[(\boldsymbol{h}_2^{(k)})^T, \boldsymbol{0}_{1\times(N+V-L_2-1)}]^T$ and $\boldsymbol{n}_{Dt1}^{(j)}$ is the additive

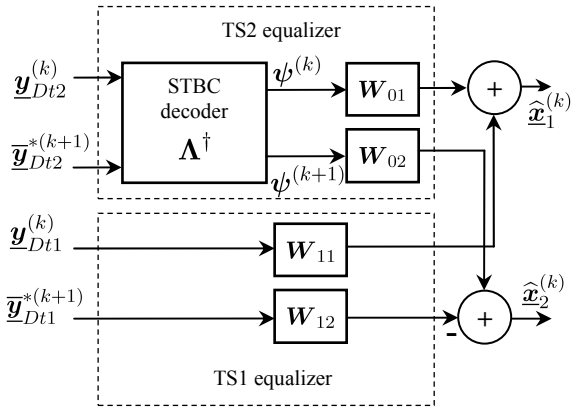

Figure 4.7: Optimal frequency domain MMSE equalizer for P1.

white complex Gaussian noise vector. The information received during *Time slot 1* does not require an orthogonalizing decoder, as the symbols $\boldsymbol{x}_{1\text{ext}}$ and $\boldsymbol{x}_{2\text{ext}}$ are not coupled. However, the TR-STBC frequency domain decoder is again required for the *Time slot 2* observations. A block diagram of the optimal frequency-domain MMSE equalizer for P1 is shown in Fig. 4.7.

We assume that the TS2 equalizer shown in Fig. 4.7 requires $(N+V)\times(N+V)$ diagonal tap weight matrices $\boldsymbol{W}_{01}$ and $\boldsymbol{W}_{02}$. Similarly, the TS1 equalizer also requires $(N+V)\times(N+V)$ diagonal tap weight matrices $\boldsymbol{W}_{11}$ and $\boldsymbol{W}_{12}$. First, consider the equalizer output estimates of the symbols $\underline{\boldsymbol{x}}_1^{(k)}$,

$$\begin{aligned}\widehat{\underline{\boldsymbol{x}}}_1^{(k)} &= \boldsymbol{W}_{01}\boldsymbol{\psi}^{(k)} + \boldsymbol{W}_{11}\boldsymbol{Q}\boldsymbol{y}_{Dt1}^{(k)} \\ &\triangleq \boldsymbol{W}_{01}\boldsymbol{\psi}^{(k)} + \boldsymbol{W}_{11}\underline{\boldsymbol{y}}_{Dt1}^{(k)}\,. \end{aligned} \tag{4.54}$$

After minimizing the MSE based on the output error vector, $\underline{\boldsymbol{e}}_1 = \underline{\boldsymbol{x}}_1^{(k)} - \widehat{\underline{\boldsymbol{x}}}_1^{(k)}$, the optimum MMSE equalizer tap weight vector is then

$$\left[\begin{array}{cc} \boldsymbol{W}_{01} & \boldsymbol{W}_{11} \end{array}\right] = \left[\begin{array}{cc} \boldsymbol{R}_{X\widetilde{Y}} & \boldsymbol{R}_{XY} \end{array}\right] \left[\begin{array}{cc} \boldsymbol{R}_{\widetilde{Y}\widetilde{Y}} & \boldsymbol{R}_{\widetilde{Y}Y} \\ \boldsymbol{R}_{\widetilde{Y}Y}^{\dagger} & \boldsymbol{R}_{YY} \end{array}\right]^{-1} \tag{4.55}$$

with correlation matrices

$$\begin{aligned}
\boldsymbol{R}_{\widetilde{Y}\widetilde{Y}} &\triangleq \sigma_x^2\widetilde{\boldsymbol{\Lambda}}\widetilde{\boldsymbol{\Lambda}} + \sigma_{nD}^2\widetilde{\boldsymbol{\Lambda}} + \sigma_{nR}^2\gamma_3^2\boldsymbol{\Lambda}_3\boldsymbol{\Lambda}_3^*\widetilde{\boldsymbol{\Lambda}} \\
\boldsymbol{R}_{\widetilde{Y}Y} &\triangleq \sigma_x^2\gamma_2\widetilde{\boldsymbol{\Lambda}}\boldsymbol{\Lambda}_2^* \\
\boldsymbol{R}_{YY} &\triangleq \sigma_x^2\gamma_2^2\boldsymbol{\Lambda}_2\boldsymbol{\Lambda}_2^* + \sigma_{nD}^2\boldsymbol{I}_{(N+V)} \\
\boldsymbol{R}_{X\widetilde{Y}} &\triangleq \sigma_x^2\widetilde{\boldsymbol{\Lambda}} \\
\boldsymbol{R}_{XY} &\triangleq \sigma_x^2\gamma_2\boldsymbol{\Lambda}_2^*\,.
\end{aligned} \tag{4.56}$$

Again, we have used the property that the orthonormally-transformed noise vectors, $\underline{\boldsymbol{n}}_i^{(j)}$, and signal vectors, $\underline{\boldsymbol{x}}_i^{(k)}$, remain white. Analogously, by setting

$$\begin{aligned}
\underline{\widehat{\boldsymbol{x}}}_2^{(k)} &= \boldsymbol{W}_{02}\boldsymbol{\psi}^{(k+1)} - \boldsymbol{W}_{12}\boldsymbol{Q}\boldsymbol{P}\boldsymbol{y}_{Dt1}^{*(k+1)} \\
&\triangleq \boldsymbol{W}_{02}\boldsymbol{\psi}^{(k+1)} - \boldsymbol{W}_{12}\overline{\underline{\boldsymbol{y}}}_{Dt1}^{*(k+1)}
\end{aligned} \tag{4.57}$$

the optimum MMSE equalizer tap weight vector for estimating the symbols $\underline{\boldsymbol{x}}_2^{(k)}$ is

$$\begin{bmatrix} \boldsymbol{W}_{02} & \boldsymbol{W}_{12} \end{bmatrix} = \begin{bmatrix} \boldsymbol{R}_{X\widetilde{Y}} & \boldsymbol{R}_{XY}^{\dagger} \end{bmatrix} \begin{bmatrix} \boldsymbol{R}_{\widetilde{Y}\widetilde{Y}} & \boldsymbol{R}_{\widetilde{Y}Y}^{\dagger} \\ \boldsymbol{R}_{\widetilde{Y}Y} & \boldsymbol{R}_{YY} \end{bmatrix}^{-1}. \tag{4.58}$$

Sub-Optimal Protocol I MMSE FDE Receiver

The suboptimal frequency-domain P1 MMSE equalizer is derived here by using the independently-optimized frequency-domain P3 MMSE and TS1 equalizers. The block diagram for the suboptimal P1 equalizer is again shown in Fig. 4.5. In the figure, the 'TS2 Equalizer' is the frequency-domain P3 STBC MMSE decoder and equalizer given in Sec. 4.4.1 and the 'TS1 Equalizer' is the frequency-domain TS1 equalizer described below.

To derive the MMSE solution for the 'TS1 Equalizer', we consider a $(N+V)\times(N+V)$ diagonal tap weight matrix $\boldsymbol{W}_1$. First, we examine the equalizer output estimates of the symbols $\underline{\boldsymbol{x}}_1^{(k)}$,

$$\underline{\widehat{\boldsymbol{x}}}_1^{(k)} = \boldsymbol{W}_1\boldsymbol{Q}\boldsymbol{y}_{Dt1}^{(k)} \triangleq \boldsymbol{W}_1\underline{\boldsymbol{y}}_{Dt1}^{(k)}. \tag{4.59}$$

The optimum MMSE equalizer tap weight matrix $\boldsymbol{W}_1$ is

$$\boldsymbol{W}_1 = \boldsymbol{R}_{XY}\boldsymbol{R}_{YY}^{-1} \tag{4.60}$$

where $\boldsymbol{R}_{XY}$ and $\boldsymbol{R}_{YY}$ are given in (4.56). Because the two equations given in (4.53) have the same channel gain and noise statistics, the same tap weight matrix $\boldsymbol{W}_1$ can be used to estimate the symbols $\underline{\boldsymbol{x}}_2^{(k)}$ with

$$\underline{\widehat{\boldsymbol{x}}}_2^{(k)} = -\boldsymbol{W}_1^* \boldsymbol{Q} \boldsymbol{P} \boldsymbol{y}_{Dt1}^{*(k+1)} \triangleq -\boldsymbol{W}_1^* \, \underline{\overline{\boldsymbol{y}}}_{Dt1}^{*(k+1)}. \tag{4.61}$$

The suboptimal frequency-domain P1 MMSE equalizer combines the frequency-domain 'TS1 Equalizer' and 'TS2 Equalizer' outputs after scaling by the factors f_2 and f_1, as shown before in (4.29) and (4.30). Again, the suboptimal P1 MMSE equalizer has low complexity compared to the optimal equalizer.

4.5 Distributed TR-STBC Frequency-Domain Adaptive Receivers

In this section we describe frequency-domain adaptive receiver structures for both protocols P1 and P3 which exploit the structure of the TR-STBC decoder. The adaptive algorithms once again eliminate the need for explicit CIR estimation at the receiver and allow the receiver to track a time-varying channel.

4.5.1 Protocol III Frequency-Domain Adaptive Receiver

By defining $\boldsymbol{\Lambda}_{1D}^{(k)} \triangleq \gamma_1 \boldsymbol{\Lambda}_3^{(k)} \boldsymbol{\Lambda}_1^{(k)}$ and $\boldsymbol{\Lambda}_{2D}^{(k)} \triangleq \gamma_2 \boldsymbol{\Lambda}_2^{(k)}$, decoder matrix $\boldsymbol{\Lambda}^{\dagger}$ in (4.49) can be rewritten as

$$\boldsymbol{\Lambda}^{\dagger} = \begin{bmatrix} \boldsymbol{\Lambda}_{1D}^{*(k)} & \boldsymbol{\Lambda}_{2D}^{(k)} \\ \boldsymbol{\Lambda}_{2D}^{*(k)} & -\boldsymbol{\Lambda}_{1D}^{(k)} \end{bmatrix}. \tag{4.62}$$

From equation (4.51), we see that the TR-STBC MMSE FDE tap weight matrix, $\boldsymbol{W}_0$, is real and diagonal, and $\boldsymbol{\Lambda}_{1D}^{(k)}$ and $\boldsymbol{\Lambda}_{2D}^{(k)}$ are diagonal matrices. Using these properties, the TR-STBC MMSE FDE outputs for the two streams can be written

as

$$\begin{aligned}\begin{bmatrix} \widehat{\underline{\boldsymbol{x}}}_1^{(k)} \\ \widehat{\underline{\boldsymbol{x}}}_2^{(k)} \end{bmatrix} &= \begin{bmatrix} \boldsymbol{W}_0 & \boldsymbol{0} \\ \boldsymbol{0} & \boldsymbol{W}_0 \end{bmatrix} \begin{bmatrix} \boldsymbol{\psi}^{(k)} \\ \boldsymbol{\psi}^{(k+1)} \end{bmatrix} \\ &= \begin{bmatrix} \boldsymbol{W}_0 \boldsymbol{\Lambda}_{1D}^{*(k)} & \boldsymbol{W}_0 \boldsymbol{\Lambda}_{2D}^{(k)} \\ \boldsymbol{W}_0 \boldsymbol{\Lambda}_{2D}^{*(k)} & -\boldsymbol{W}_0 \boldsymbol{\Lambda}_{1D}^{(k)} \end{bmatrix} \begin{bmatrix} \underline{\boldsymbol{y}}_{Dt2}^{(k)} \\ \overline{\underline{\boldsymbol{y}}}_{Dt2}^{*(k+1)} \end{bmatrix} \\ &\triangleq \begin{bmatrix} \boldsymbol{A}_1 & \boldsymbol{A}_2 \\ \boldsymbol{A}_2^* & -\boldsymbol{A}_1^* \end{bmatrix} \begin{bmatrix} \underline{\boldsymbol{y}}_{Dt2}^{(k)} \\ \overline{\underline{\boldsymbol{y}}}_{Dt2}^{*(k+1)} \end{bmatrix} \end{aligned} \tag{4.63}$$

where $\boldsymbol{A}_1 = \boldsymbol{W}_0 \boldsymbol{\Lambda}_{1D}^{*(k)}$ and $\boldsymbol{A}_2 = \boldsymbol{W}_0 \boldsymbol{\Lambda}_{2D}^{(k)}$ are diagonal matrices. Thus, equation (4.63) can be rewritten as

$$\begin{aligned}\begin{bmatrix} \widehat{\underline{\boldsymbol{x}}}_1^{(k)} \\ \widehat{\underline{\boldsymbol{x}}}_2^{*(k)} \end{bmatrix} &= \begin{bmatrix} \mathrm{diag}(\underline{\boldsymbol{y}}_{Dt2}^{(k)}) & \mathrm{diag}(\overline{\underline{\boldsymbol{y}}}_{Dt2}^{*(k+1)}) \\ -\mathrm{diag}(\overline{\underline{\boldsymbol{y}}}_{Dt2}^{(k+1)}) & \mathrm{diag}(\underline{\boldsymbol{y}}_{Dt2}^{*(k)}) \end{bmatrix} \begin{bmatrix} \boldsymbol{w}_{1F} \\ \boldsymbol{w}_{2F} \end{bmatrix} \\ &\triangleq \boldsymbol{U}_{Dt2F}\, \boldsymbol{w}^{(k)} \end{aligned} \tag{4.64}$$

where $\mathrm{diag}(\boldsymbol{c})$ is a diagonal matrix containing the vector $\boldsymbol{c}$ as its diagonal elements, and $\boldsymbol{w}_{1F}$ and $\boldsymbol{w}_{2F}$ are the vectors containing the diagonal elements of $\boldsymbol{A}_1$ and $\boldsymbol{A}_2$, respectively. Because now the equalizer tap weights $\boldsymbol{w}^{(k)}$ are isolated in (4.64), they can be easily adapted using block versions of the NLMS and RLS algorithms [44].

4.5.2 Protocol I Optimal Frequency-Domain Adaptive Receiver

Using the analysis of Sec. 4.4.2, it can also be shown that the optimal tap weight vectors of the optimal frequency-domain P1 MMSE equalizer satisfy $\boldsymbol{W}_{01} = \boldsymbol{W}_{02}$ and $\boldsymbol{W}_{11} = \boldsymbol{W}_{12}^*$. Applying these relations and similar arguments used in deriving equations (4.62)–(4.64), the optimal frequency-domain P1 MMSE equalizer outputs

(4.54) and (4.57) can be rewritten as

$$\begin{aligned}\begin{bmatrix} \widehat{\underline{\boldsymbol{x}}}_1^{(k)} \\ \widehat{\underline{\boldsymbol{x}}}_2^{*(k)} \end{bmatrix} &= \boldsymbol{U}_{Dt2F} \begin{bmatrix} \boldsymbol{w}_{1Fp1} \\ \boldsymbol{w}_{2Fp1} \end{bmatrix} + \begin{bmatrix} \mathrm{diag}(\underline{\boldsymbol{y}}_{Dt1}^{(k)}) \\ -\mathrm{diag}(\overline{\underline{\boldsymbol{y}}}_{Dt1}^{(k+1)}) \end{bmatrix} \boldsymbol{w}_{11F} \\ &= \left[\begin{array}{c|c} \boldsymbol{U}_{Dt2F} & \begin{array}{c} \mathrm{diag}(\underline{\boldsymbol{y}}_{Dt1}^{(k)}) \\ -\mathrm{diag}(\overline{\underline{\boldsymbol{y}}}_{Dt1}^{(k+1)}) \end{array} \end{array}\right] \begin{bmatrix} \boldsymbol{w}_{1Fp1} \\ \boldsymbol{w}_{2Fp1} \\ \boldsymbol{w}_{11F} \end{bmatrix} \\ &\triangleq \boldsymbol{U}_F \, \boldsymbol{w}^{(k)} \end{aligned} \tag{4.65}$$

where $\boldsymbol{U}_{Dt2F}$ is given in (4.64) and combined equalizer and decoder vectors $\boldsymbol{w}_{1Fp1}$, $\boldsymbol{w}_{2Fp1}$, and $\boldsymbol{w}_{11F}$ contain the diagonal elements of $\gamma_1 \boldsymbol{W}_{01} \boldsymbol{\Lambda}_3^{*(k)} \boldsymbol{\Lambda}_1^{*(k)}$, $\gamma_2 \boldsymbol{W}_{01} \boldsymbol{\Lambda}_2^{(k)}$, and $\boldsymbol{W}_{11}$, respectively. As in (4.64), the equalizer tap weights $\boldsymbol{w}^{(k)}$ in (4.65) are isolated, and again traditional block adaptive algorithms can be used to construct the adaptive optimal frequency-domain P1 receiver.

4.5.3 Protocol I Suboptimal Frequency-Domain Adaptive Receiver

The suboptimal frequency-domain P1 adaptive equalizer consists of independently-adapted 'TS1' and 'TS2' equalizers as in the case of the suboptimal P1 MMSE equalizer. The 'TS2' adaptive equalizer is just the adaptive FDE for P3 given in Sec. 4.5.1. The 'TS1' adaptive equalizer can be easily put into block adaptive form by considering the MMSE solutions given in (4.59) and (4.61). These two equations can be combined, yielding

$$\begin{aligned}\begin{bmatrix} \widehat{\underline{\boldsymbol{x}}}_1^{(k)} \\ \widehat{\underline{\boldsymbol{x}}}_2^{*(k)} \end{bmatrix} &= \begin{bmatrix} \boldsymbol{W}_1 \underline{\boldsymbol{y}}_{Dt1}^{(k)} \\ -\boldsymbol{W}_1 \overline{\underline{\boldsymbol{y}}}_{Dt1}^{(k+1)} \end{bmatrix} \\ &= \begin{bmatrix} \mathrm{diag}(\underline{\boldsymbol{y}}_{Dt1}^{(k)}) \\ -\mathrm{diag}(\overline{\underline{\boldsymbol{y}}}_{Dt1}^{(k+1)}) \end{bmatrix} \boldsymbol{w}_{1F} \triangleq \boldsymbol{U}_{Dt1F} \, \boldsymbol{w}^{(k)} \end{aligned} \tag{4.66}$$

where the equalizer tap vector $\boldsymbol{w}_{1F}$ contains the diagonal elements of $\boldsymbol{W}_1$. To obtain the suboptimal frequency-domain P1 adaptive equalizer output, the 'TS1' and 'TS2'

Table 4.4: Frequency-Domain Block RLS Algorithm for Distributed TR-STBC Systems

Protocol III	**Protocol I Optimal**
Initial conditions: $\boldsymbol{w}^{(0)} = \mathbf{0}_{2(N+V)\times 1}$ $\boldsymbol{\Phi}^{(0)} = \boldsymbol{I}_{2(N+V)\times 2(N+V)}$	Initial conditions: $\boldsymbol{w}^{(0)} = \mathbf{0}_{3(N+V)\times 1}$ $\boldsymbol{\Phi}^{(0)} = \boldsymbol{I}_{3(N+V)\times 3(N+V)}$
Update taps at each iteration using: $\boldsymbol{\Phi}^{(k+2)} = \lambda\boldsymbol{\Phi}^{(k)} + \boldsymbol{U}_{Dt2F}^{\dagger}\boldsymbol{U}_{Dt2F}$ $\boldsymbol{w}^{(k+2)} = \boldsymbol{w}^{(k)} + (\boldsymbol{\Phi}^{(k+2)})^{-1}\boldsymbol{U}_{Dt2F}^{\dagger}\boldsymbol{e}^{(k)}$ where λ is small positive close to 1	Update taps at each iteration using: $\boldsymbol{\Phi}^{(k+2)} = \lambda\boldsymbol{\Phi}^{(k)} + \boldsymbol{U}_{F}^{\dagger}\boldsymbol{U}_{F}$ $\boldsymbol{w}^{(k+2)} = \boldsymbol{w}^{(k)} + (\boldsymbol{\Phi}^{(k+2)})^{-1}\boldsymbol{U}_{F}^{\dagger}\boldsymbol{e}^{(k)}$ where λ is small positive close to 1

adaptive equalizer outputs are scaled and combined as explained for the suboptimal frequency-domain P1 MMSE equalizer.

4.5.4 Frequency-Domain Block RLS Algorithms

To compare the performances of the adaptive frequency-domain receivers for P1 and P3, we have derived three frequency-domain versions of the block RLS algorithm which are summarized in Tables 4.4 and 4.5. These versions use equations (4.64) for the P3 receiver, (4.65) for the P1 optimal receiver and (4.64) and (4.66) for the P1 suboptimal receivers. Here the estimation error vector $\boldsymbol{e}^{(k)}$ is

$$\boldsymbol{e}^{(k)} = \begin{bmatrix} \underline{\boldsymbol{x}}_1^{(k)} \\ \underline{\boldsymbol{x}}_2^{(k)} \end{bmatrix} - \begin{bmatrix} \underline{\widehat{\boldsymbol{x}}}_1^{(k)} \\ \underline{\widehat{\boldsymbol{x}}}_2^{(k)} \end{bmatrix}. \tag{4.67}$$

The equalizer operates in training mode for the training blocks within a frame and switches to decision directed mode for the data blocks.

4.6 Simulation Results

To simulate the distributed TR-STBC system, we use a QPSK system with a symbol rate of 271 kSymbols/s. We consider Rayleigh fading channels with normalized exponential power delay profiles. Although in the analysis we assume that the channel is constant for two consecutive data blocks, in the simulations the channel

Table 4.5: Frequency-Domain Block RLS Algorithm for Sub-Optimal P1 Distributed TR-STBC System

P1 Sub-Optimal	
TS2 Initial conditions: $\boldsymbol{w}^{(0)} = \mathbf{0}_{2(N+V)\times 1}$ $\boldsymbol{\Phi}^{(0)} = \boldsymbol{I}_{2(N+V)\times 2(N+V)}$	TS1 Initial conditions: $\boldsymbol{w}^{(0)} = \mathbf{0}_{(N+V)\times 1}$ $\boldsymbol{\Phi}^{(0)} = \boldsymbol{I}_{(N+V)\times(N+V)}$
Equalizer output: $\underline{\widehat{\boldsymbol{x}}}_{TS2} = \boldsymbol{U}_{Dt2F}\,\boldsymbol{w}^{(k)}$	Equalizer output: $\underline{\widehat{\boldsymbol{x}}}_{TS1} = \boldsymbol{U}_{Dt1F}\,\boldsymbol{w}^{(k)}$
Update taps at each iteration using: $\boldsymbol{\Phi}^{(k+2)} = \lambda\boldsymbol{\Phi}^{(k)} + \boldsymbol{U}^{\dagger}_{Dt2F}\,\boldsymbol{U}_{Dt2F}$ $\boldsymbol{w}^{(k+2)} = \boldsymbol{w}^{(k)} + (\boldsymbol{\Phi}^{(k+2)})^{-1}\,\boldsymbol{U}^{\dagger}_{Dt2F}\,\boldsymbol{e}^{(k)}$ where λ is small positive close to 1	Update taps at each iteration using: $\boldsymbol{\Phi}^{(k+2)} = \lambda\boldsymbol{\Phi}^{(k)} + \boldsymbol{U}^{\dagger}_{Dt1F}\,\boldsymbol{U}_{Dt1F}$ $\boldsymbol{w}^{(k+2)} = \boldsymbol{w}^{(k)} + (\boldsymbol{\Phi}^{(k+2)})^{-1}\,\boldsymbol{U}^{\dagger}_{Dt1F}\,\boldsymbol{e}^{(k)}$ where λ is small positive close to 1
Combined output: $\underline{\widehat{\boldsymbol{x}}} = f_1\underline{\widehat{\boldsymbol{x}}}_{TS2} + f_2\underline{\widehat{\boldsymbol{x}}}_{TS1}$	

is allowed to vary from symbol to symbol to more realistically model a real world fading environment. We also assume perfect power control so that the $S\rightarrow D$ and $R\rightarrow D$ links have equal power. We use CIR lengths $L_1 = 1$, $L_2 = 3$ and $L_3 = 3$. We compare the time- and frequency-domain equalizers using protocols P1 and P3. Unless otherwise noted, we use a data block size of $N = 124$ symbols with a ZP length of $V = \max(L_1 + L_3, L_2) = 4$ symbols, leading to a total block size of $N + V = 128$.

As the number of taps in the TDE system is independent of the block size, we use simulations to find a suitable number of taps for the TDE operating over the channel specified. In this case we compare P3-based TDE and FDE systems. Figure 4.8 shows the MMSE as a function of the number of TDE taps for different signal-to-noise ratio (SNR) values. The figure also includes the MMSE for the FDE system. Because the FDE is forced to have as many equalizer taps as the block size, the length of the FDE is kept constant at 128. It is observed that the MMSE values decrease with increasing TDE tap length, and the TDE reaches the optimum MMSE values with far fewer taps compared to the FDE. Experimentally, we have found that the TDE adaptive equalizer tap length is independent of the block size,

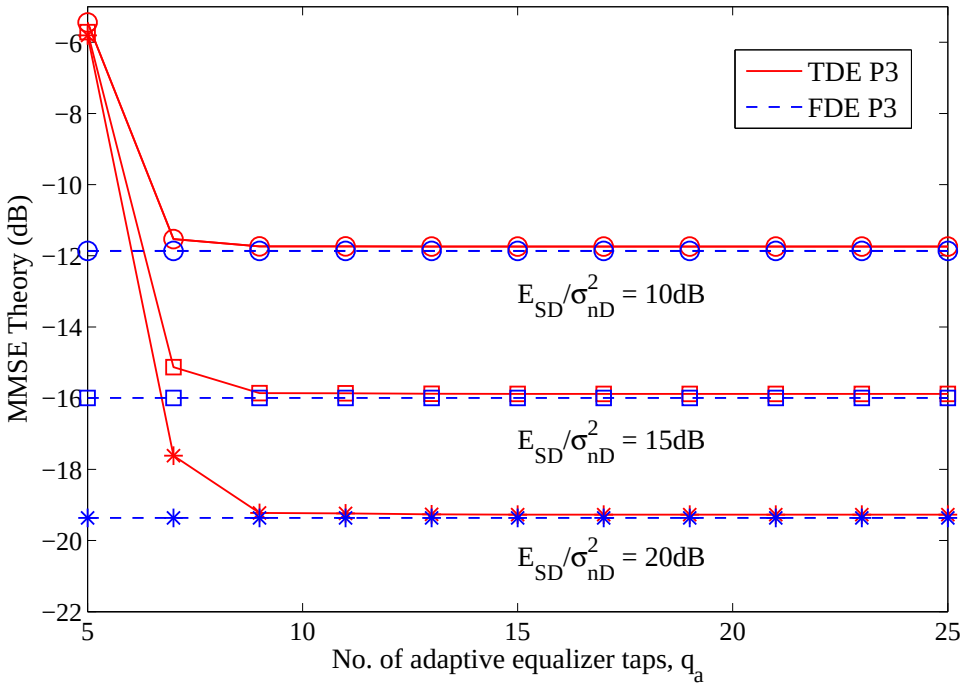

Figure 4.8: MMSE vs. adaptive equalizer tap length ($E_{SD}/\sigma^2_{nD} = E_{RD}/\sigma^2_{nD}$, $E_{SR}/\sigma^2_{nR} = 20$dB and $N = 124$).

but note that it is dependent on the type of channel involved. As a conservative value which works well for all of the SNR values considered, we set the adaptive equalizer length for P3 to $q_a = 15$ for the remaining simulations in this chapter. The required TS1 equalizer tap length, q_2, would usually be less than that of the adaptive P3 equalizer as the TS1 equalizer only has information received over the direct $S \rightarrow D$ link. Therefore, for a conservative value of q_2, we let $q_2 = q_a$ is chosen in the TS1 TDE.

The symbol error rate (SER) of the adaptive equalizers is an important steady-state parameter measuring how well the adaptive receivers perform during different environmental conditions. In all of the SER results given in this chapter, unless otherwise mentioned, we use the frame format shown in Fig. 4.9. In the figure, D_{x} and D_{xT} represent actual and training data, respectively, so an 8-block data frame includes 2 training blocks. Each block D_{x} or D_{xT} has the transmission data block format shown in Fig. 4.2. We assume that the links $S \rightarrow D$ and $R \rightarrow D$ are changing with the same Doppler frequency but the $S \rightarrow R$ link has a significantly lower Doppler

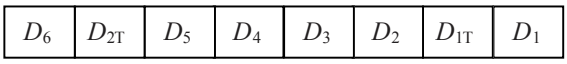

Figure 4.9: Frame Structure

frequency compared to the other links. This scenario would correspond, for example, to the case of two mobile users approaching the same base station from similar directions at similar velocities.

First, we examine the effects of the Doppler frequencies on the performance of the systems. Figures 4.10 and 4.11 show the performances of the TDE and FDE adaptive algorithms for P3 systems at Doppler frequencies of 10 and 30 Hz, respectively. To show the diversity benefit of using STBC techniques, the performances of the analogous TS1 equalizers operating without space-time coding and a relay node are also included. The $S \rightarrow R$ link has a fixed Doppler frequency of 1Hz in all of these simulations. From both figures, it is clear that the SER increases with Doppler frequency as a result of the inability of the adaptive algorithms to track the faster channel variations. As a reference the figures also include the MMSE SER values where the receiver has perfect knowledge of the CIR at the middle of each individual transmission block. The MMSE SER also increases with Doppler frequency due to the increase in CIR variation across each data frame.

Figures 4.12 and 4.13 show the performances of the optimal P1, suboptimal P1, P3 and TS1 equalizers in the time and frequency domains, respectively. The simulations are performed at a 10Hz Doppler frequency with a very good $S \rightarrow R$ link ($E_{SR}/\sigma_{nR}^2 = 30$dB, 1Hz Doppler). Figure 4.12 reveals that the optimal P1 TDE performs better than the other TDE schemes in both the adaptive and non-adaptive (MMSE) environments. In Fig. 4.13 we see that all three FDE adaptive schemes have very similar performances with the optimal P1 FDE outperforming for the benchmark MMSE case.

In Figs. 4.14 and 4.15 we also examine the behaviors of the equalization schemes for P1 and P3 when the $S \rightarrow R$ link has very low signal strength. In both the time- and frequency-domain scenarios, the performance of the P3 receiver is extremely poor due to noise amplification at the relay terminal which is passed on to the

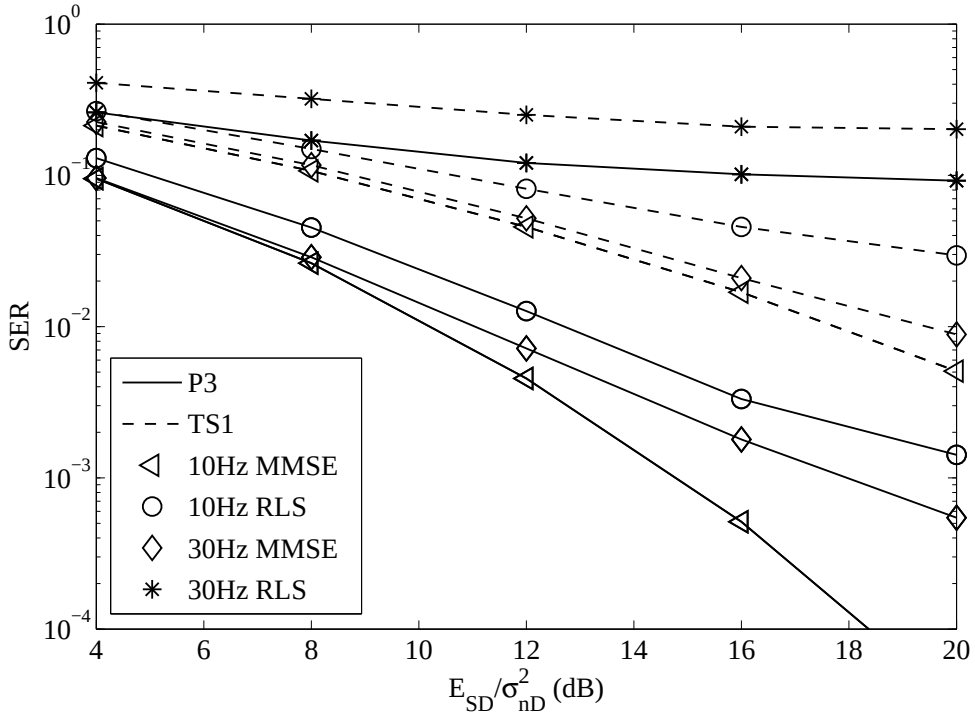

Figure 4.10: Effect of Doppler frequency (10Hz and 30Hz) on the performance of time-domain adaptive algorithms ($E_{SD}/\sigma^2_{nD} = E_{RD}/\sigma^2_{nD}$, $E_{SR}/\sigma^2_{nR} = 30$dB and $S \rightarrow R$ link with 1Hz Doppler frequency).

Table 4.6: Complexity of the Adaptive Algorithms

Adaptive Algorithm	**Number of Real Multiplications**
TDE RLS P3	$26M \log_2 M + 40M + 18q_a^2 - 21q_a + 14$
TDE RLS P1 suboptimal	$26M \log_2 M + 40M + 18q_a^2 - 21q_a + 20M_1 \log_2 M_1 + 24M_1 + 14q_2^2 - 21q_2 + 16N + 30$
TDE RLS P1 optimal	$46M \log_2 M + 80M + 2(2q_a + q_2)^3/3 + 4(2q_a + q_2)^2 + 6q_a + 6q_2 - 4$
FDE RLS P3	$12M_2 \log_2 M_2 + 41M_2$
FDE RLS P1 suboptimal	$24M_2 \log_2 M_2 + 64M_2 + 16N + 2$
FDE RLS P1 optimal	$16M_2 \log_2 M_2 + 207M_2$
Definitions: $M = N + V + q_a - 1$, $M_1 = N + V + q_2 - 1$ and $M_2 = N + V$	

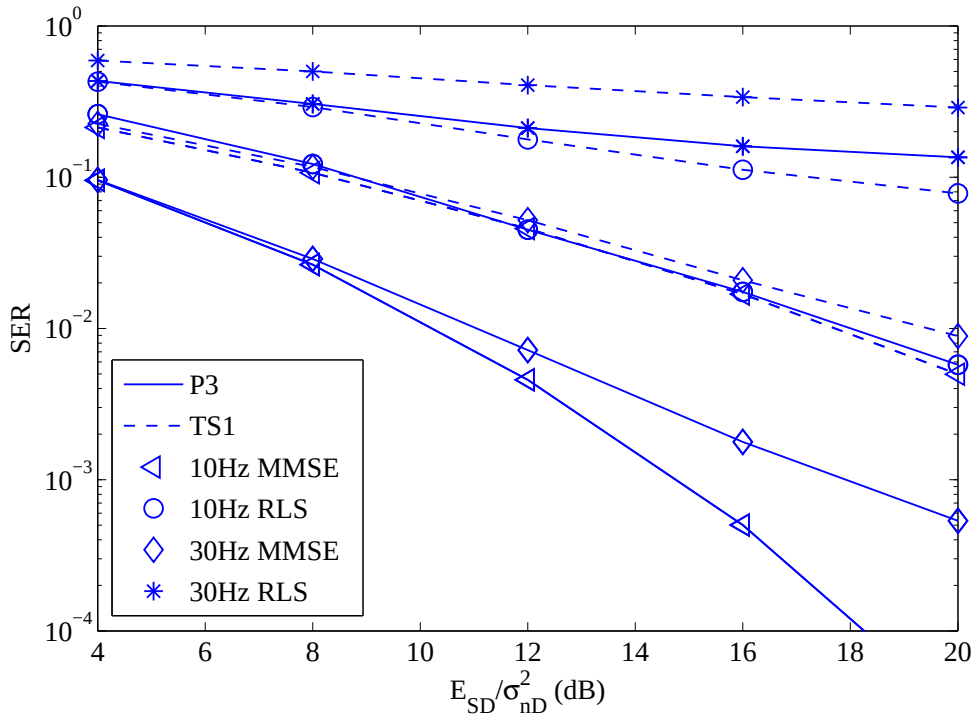

Figure 4.11: Effect of Doppler frequency (10Hz and 30Hz) on the performance of frequency-domain adaptive algorithms ($E_{SD}/\sigma^2_{nD} = E_{RD}/\sigma^2_{nD}$, $E_{SR}/\sigma^2_{nR} = 30$dB and $S \rightarrow R$ link with 1Hz Doppler frequency).

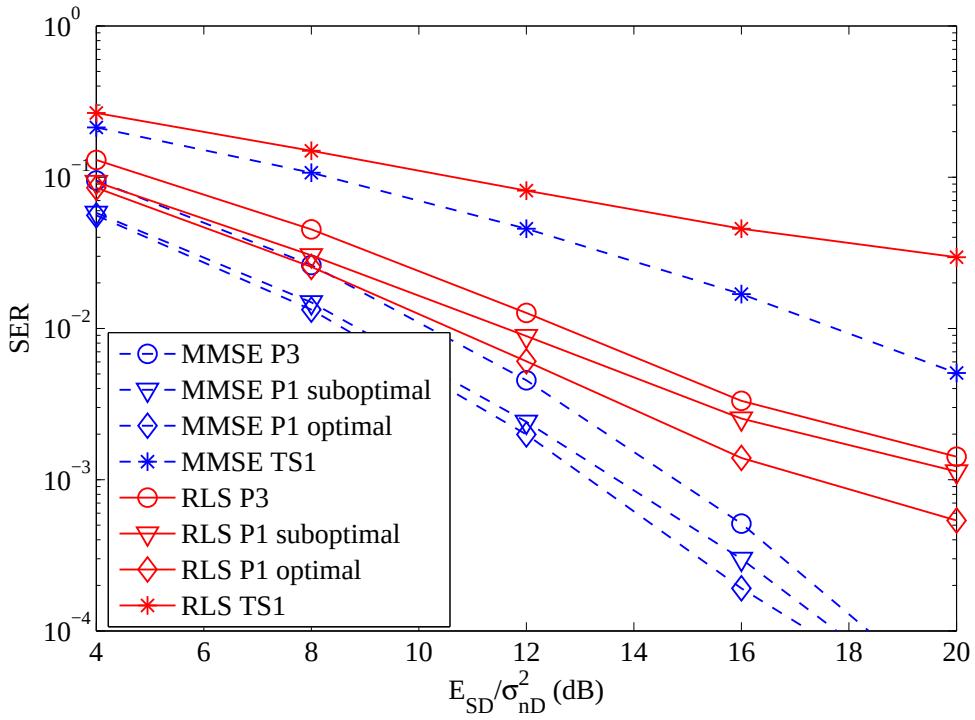

Figure 4.12: SER curves for P1- and P3-based TDEs with 10Hz Doppler frequency ($E_{SD}/\sigma^2_{nD} = E_{RD}/\sigma^2_{nD}$, $E_{SR}/\sigma^2_{nR} = 30$dB and $S \rightarrow R$ link with 1Hz Doppler frequency).

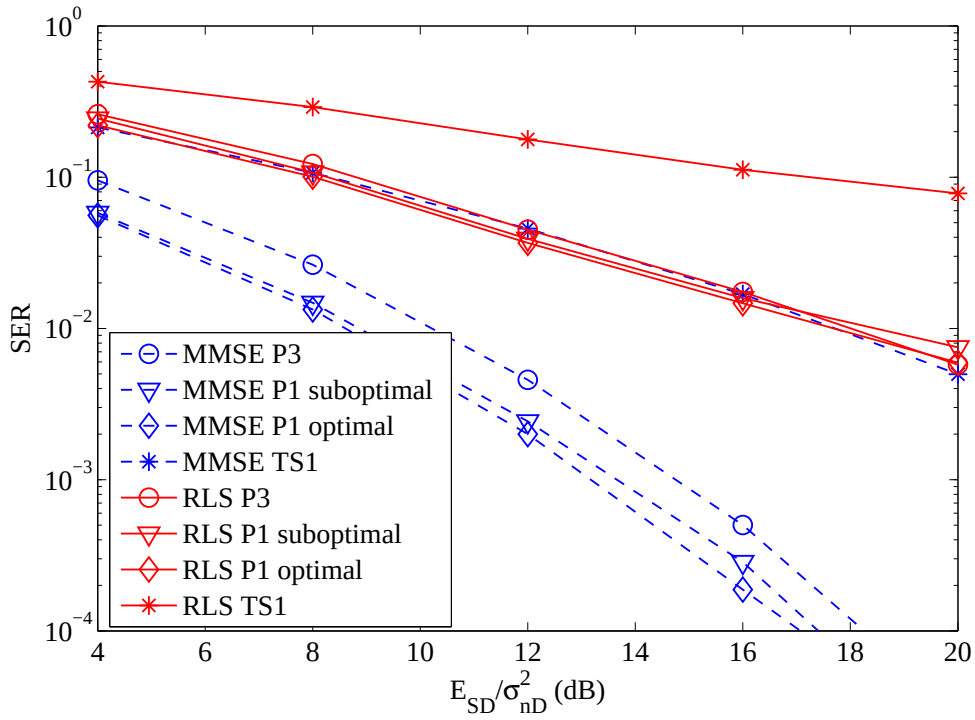

Figure 4.13: SER curves for P1- and P3-based FDEs with 10Hz Doppler frequency ($E_{SD}/\sigma^2_{nD} = E_{RD}/\sigma^2_{nD}$, $E_{SR}/\sigma^2_{nR} = 30$dB and $S \rightarrow R$ link with 1Hz Doppler frequency).

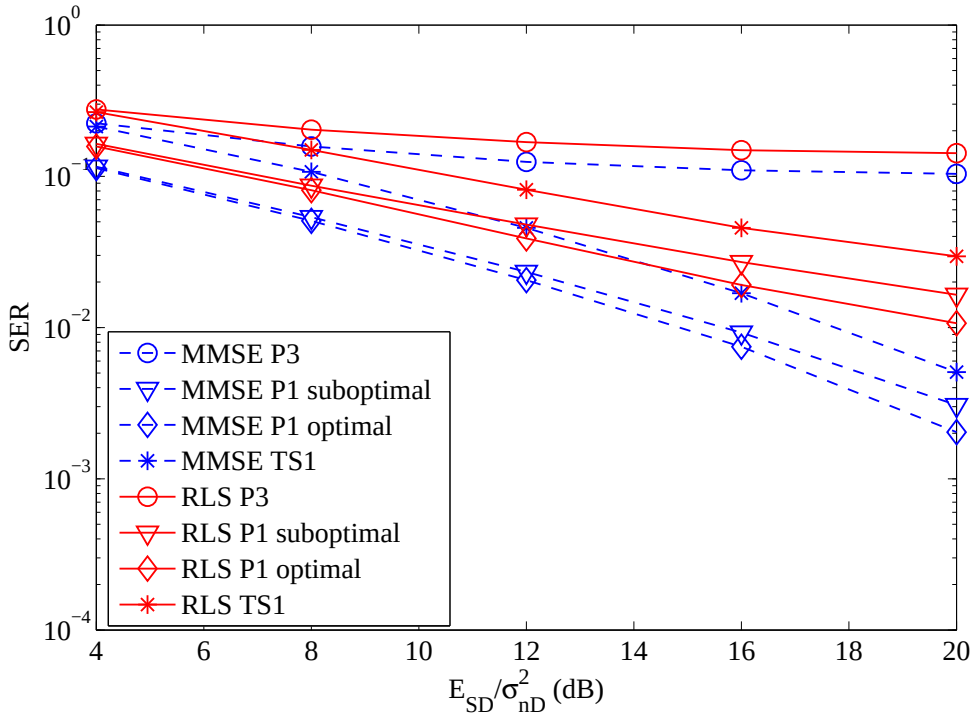

Figure 4.14: SER curves for P1- and P3-based TDEs with 10Hz Doppler frequency ($E_{SD}/\sigma^2_{nD} = E_{RD}/\sigma^2_{nD}$, $E_{SR}/\sigma^2_{nR} = 0$dB and $S \rightarrow R$ link with 1Hz Doppler frequency).

destination, overwhelming any advantage of the STBC scheme. On the other hand, the P1 receivers have much better performance compared to P3. The superiority of the P1 receivers in this case is due to the diversity combining of the TS1 and TS2 information, with the TS1 observations received directly through the $S \rightarrow D$ link.

We compare the adaptive (RLS) time- and frequency-domain equalizers in Fig. 4.16. The TDE adaptive RLS algorithms outperform all of the FDE algorithms. The main reason is that the TDEs require far fewer equalizer taps than the FDEs for the considered channel, and therefore, the TDE algorithms adapt much faster to the changing channel than the FDE algorithms.

From the above figures we can see that overall the P1 and P3 equalizers have better performance compared to TS1 equalizers. The main reason is that the TS1 equalizers do not used the extra information received through the relaying terminal. Thus, the TS1 equalizers have lower diversity gain compared to the P1 and P3 equalizers.

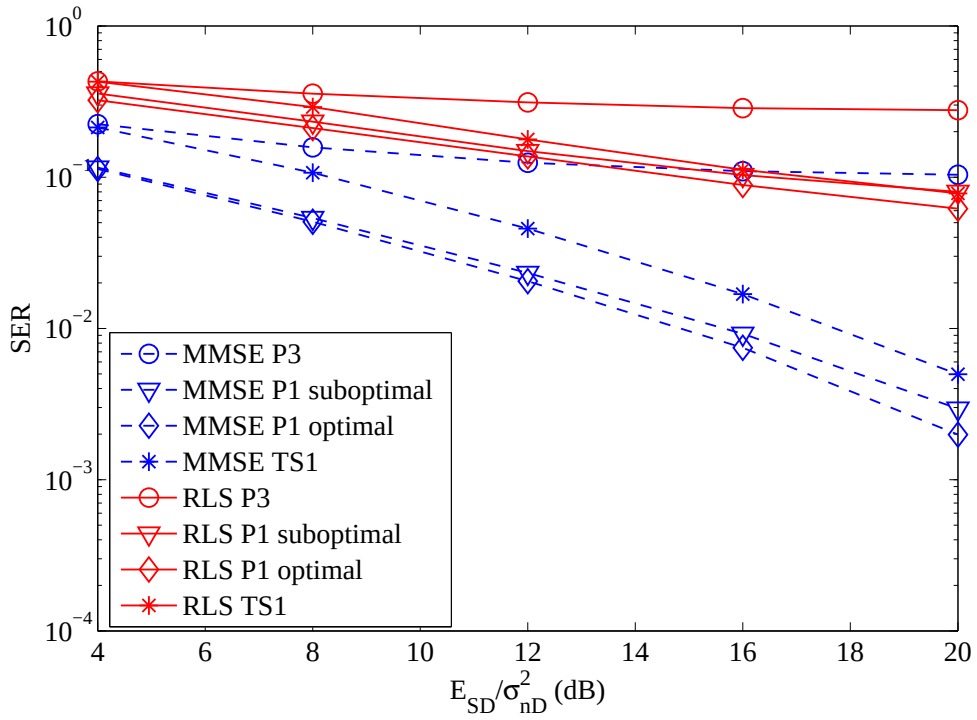

Figure 4.15: SER curves for P1- and P3-based FDEs with 10Hz Doppler frequency ($E_{SD}/\sigma^2_{nD} = E_{RD}/\sigma^2_{nD}$, $E_{SR}/\sigma^2_{nR} = 0$dB and $S \rightarrow R$ link with 1Hz Doppler frequency).

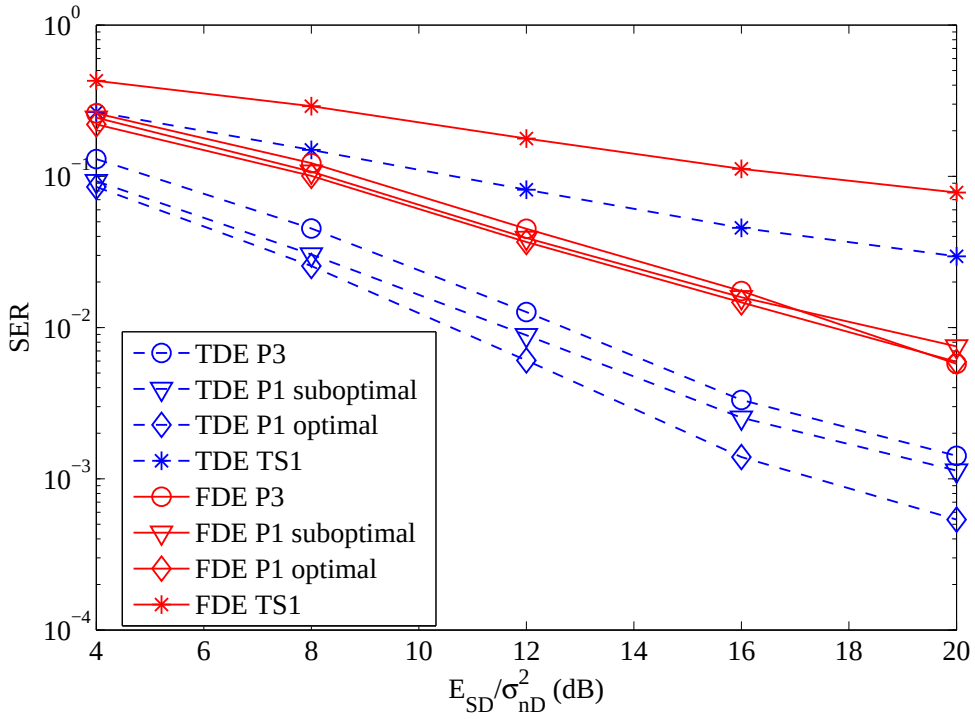

Figure 4.16: SER comparison of TDEs and FDEs adaptive (RLS) algorithms with 10Hz Doppler frequency ($E_{SD}/\sigma^2_{nD} = E_{RD}/\sigma^2_{nD}$, $E_{SR}/\sigma^2_{nR} = 30$dB and $S \rightarrow R$ link with 1Hz Doppler frequency).

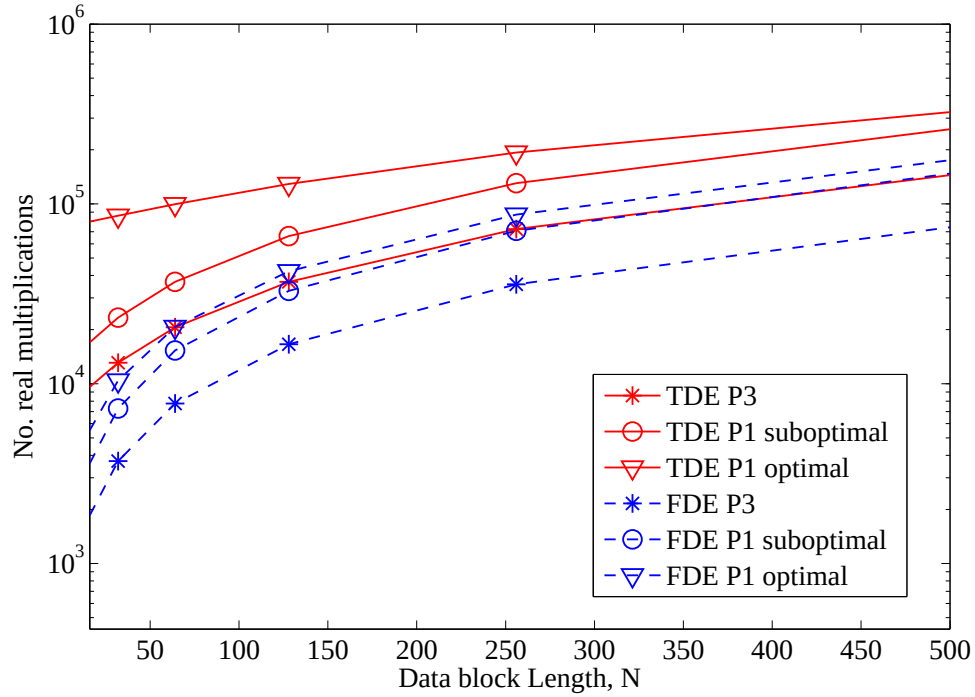

Figure 4.17: Number of real multiplications required for adaptive algorithms.

Finally, we examine the complexity of the adaptive algorithms. Table 4.6 gives the complexity of each adaptive algorithm in terms of the number of real multiplications required for each data block. The time-domain algorithms include linear convolutions and correlations. Utilizing previous research on fast convolutions and correlations for large sample sizes [52, 53, 54], the Fast Fourier Transform (FFT) is used as an efficient method for computing the time-domain convolutions and correlations in the time-domain algorithms as in Chapter 3. Furthermore, the P3 and suboptimal P1 TDE RLS algorithms involve Hermitian Toeplitz matrix inversion. To perform this operation, the Trench algorithm [55] is used.

To make the complexity comparison clearer, in Fig. 4.17 the number of real multiplications involved in computing each of the adaptive algorithms is plotted. The channel parameters are fixed to those used in the simulations and we vary the data block length, N. We see that the time-domain systems have higher complexity than the frequency-domain systems with around twice the complexity at large values of N. In each domain the P3 adaptive system has the lowest complexity and the P1 optimal system has the highest complexity. Thus, the time-domain adaptive algorithms have better system performances but at the cost of increased complexity compared to the frequency-domain adaptive systems. In both the time and frequency domains a complexity reduction can be achieved by using the suboptimal P1 equalizer without a significant performance reduction relative to the optimal P1 equalizer.

4.7 Summary

In this chapter we have developed time- and frequency-domain adaptive equalizers for distributed TR-STBC systems based on the two protocols proposed in [1]. The adaptive equalizers eliminate the need for explicit CIR estimation at the receiver. The simulations show that the adaptive algorithms work well for both protocols, and, at the cost of increased complexity, time-domain adaptive algorithms perform better than frequency-domain algorithms. In both the time and frequency domains

the Protocol I receivers outperform the Protocol III receivers, particularly in the case of a weak $S \rightarrow R$ link.

We have also found that overall the P1 and P3 equalizers have better performance compared to the TS1 equalizers. The main reason is that TS1 equalizers do not use the extra information received through the relaying terminal. Thus, the TS1 equalizers have lower diversity gains compared to the P1 and P3 equalizers. Hence, the amplifying and forward relaying system can be used to increase the performance by improving the diversity of the system.

Chapter 5

MIMO Two-Hop One-Relay Relaying Systems

In the previous chapter, we have developed an adaptive equalization scheme for an AF relaying system. We showed that the relaying system improves error performance by increasing the diversity of the system. In this chapter we analyze the ergodic capacity of an AF MIMO two-hop system including the direct link.

Wireless relaying networks have recently been given considerable attention due to their many advantages. Apart from increasing the range, relaying networks can also achieve better diversity by using cooperative transmission from the source and several relays [1, 21]. The relaying terminals forward the information from the source to the destination mainly using the two well known methods: AF and DF. Since MIMO systems can provide better system capacity than SISO systems, relaying has recently been extended to MIMO scenarios [23, 24]. MIMO relays aim to provide improved system capacity, increases in range, and better diversity.

In this chapter we analyze the ergodic capacity of an AF MIMO two-hop system including the direct link. Most of the capacity results on two-hop MIMO relays have been derived by employing asymptotic methods [64, 65, 66]. Furthermore, the random matrix results required for the MIMO relay capacity analysis are usually presented for two separate cases [67, 68], depending on whether the system is defined

by a Wishart or a Pseudo-Wishart [50] distribution. However, a unified expression for the capacity of the AF MIMO two-hop system, without the source to destination link, was derived in [69].

The main contribution of this chapter is to derive an exact expression for the capacity of an AF MIMO two-hop system including the source to destination link as shown in Fig. 5.1. The expression derived in this chapter is unified, and it can be used for arbitrary numbers of antennas at the source, relay and destination. In the chapter we also present simulation results to validate the analysis and use the results to quantify the capacity improvement due to the direct link.

5.1 System Model

We use the relay network topology shown in Fig. 5.1. The source (S), relay (R), and destination (D) terminals are equipped with n_s, n_r and n_d antennas respectively, which we represent by the 3-tuple (n_s, n_r, n_d). During the first hop, S transmits (broadcasts) to R and D and in the second hop R transmits the amplified signal from the first hop to D. We assume that the normalized channel matrices for the source-to-relay ($S \rightarrow R$), source-to-destination ($S \rightarrow D$), and relay-to-destination ($R \rightarrow D$) links are given by $\boldsymbol{H}_1 \in \mathcal{C}^{n_r \times n_s}$, $\boldsymbol{H}_3 \in \mathcal{C}^{n_d \times n_s}$, and $\boldsymbol{H}_2 \in \mathcal{C}^{n_d \times n_r}$, respectively. We also assume that S and R have no CSI, that D has perfect knowledge of all the channels, and the channels are frequency-flat and the entries of the channel matrices are ZMCSCG random variables of unit variance. Furthermore, it is assumed that R assists in the communication with D using AF mode. Hence, R amplifies the received observation corresponding to the signal from S by a factor, b, and retransmits it to D. The received signal at the destination after the two hops is then given by

$$\boldsymbol{y} = \begin{bmatrix} \sqrt{P_3}\boldsymbol{H}_3 \\ \sqrt{P_2}\sqrt{P_1}b\boldsymbol{H}_2\boldsymbol{H}_1 \end{bmatrix} \boldsymbol{x} + \begin{bmatrix} \boldsymbol{n}_3 \\ \sqrt{P_2}b\boldsymbol{H}_2\boldsymbol{n}_1 + \boldsymbol{n}_2 \end{bmatrix}. \tag{5.1}$$

In (5.1), the parameters P_1, P_2 and P_3 are the average powers of the $S \rightarrow R$, $R \rightarrow D$ and $S \rightarrow D$ links, respectively, taking into account the different path loss and shad-

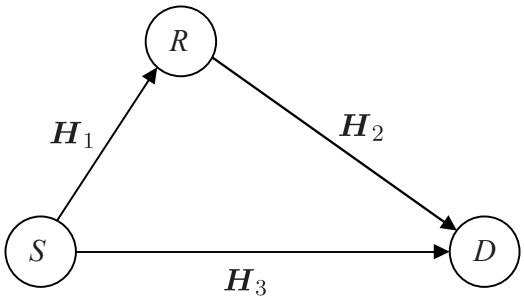

Figure 5.1: MIMO relay network topology.

owing effects over the links. The variables $\boldsymbol{n}_1$, $\boldsymbol{n}_2$ and $\boldsymbol{n}_3$ are the noise vectors at R, D (second-hop) and D (first-hop) respectively, and $\boldsymbol{x}$ is the vector of transmit symbols. The transmit symbols are assumed i.i.d. with $E\{\boldsymbol{x}\boldsymbol{x}^\dagger\} = \rho \boldsymbol{I}_{n_s}$. The noise at R and D is modeled as ZMCSCG with $E\{\boldsymbol{n}_1\boldsymbol{n}_1^\dagger\} = \sigma_1^2 \boldsymbol{I}_{n_r}$, $E\{\boldsymbol{n}_2\boldsymbol{n}_2^\dagger\} = \sigma_2^2 \boldsymbol{I}_{n_d}$, and $E\{\boldsymbol{n}_3\boldsymbol{n}_3^\dagger\} = \sigma_3^2 \boldsymbol{I}_{n_d}$. With this information, and defining $F_1 = \sqrt{P_2}\sqrt{P_1}b$, $F_2 = \sqrt{P_2}b$, $F_3 = \sqrt{P_3}$, the received signal at the destination can also be written as

$$\boldsymbol{y} = \boldsymbol{H}\boldsymbol{x} + \boldsymbol{B}\boldsymbol{v} \tag{5.2}$$

where

$$\boldsymbol{H} = \begin{bmatrix} F_3\boldsymbol{H}_3 \\ F_1\boldsymbol{H}_2\boldsymbol{H}_1 \end{bmatrix}, \tag{5.3}$$

$$\boldsymbol{B} = \begin{bmatrix} \sigma_3^2\boldsymbol{I}_{n_d} & \boldsymbol{0} \\ \boldsymbol{0} & \sigma_1^2 F_2^2 \boldsymbol{H}_2\boldsymbol{H}_2^\dagger + \sigma_2^2\boldsymbol{I}_{n_d} \end{bmatrix}^{1/2}, \tag{5.4}$$

and $\boldsymbol{v}$ is a normalized zero mean Gaussian noise vector, which has $\boldsymbol{I}_{2n_d}$ as its covariance matrix.

5.2 Capacity Analysis

The ergodic capacity of the system is given by [23] as below, (the factor $1/2$ accounts for the fact that information is conveyed to the destination terminal over two time slots [1])

$$C = \frac{1}{2} E\left\{\log_2\left|\boldsymbol{I}_{2n_d} + \rho\boldsymbol{H}\boldsymbol{H}^\dagger(\boldsymbol{B}\boldsymbol{B}^\dagger)^{-1}\right|\right\}. \tag{5.5}$$

The singular value decomposition of $\boldsymbol{H}_2$ can be defined as $\boldsymbol{H}_2 = \boldsymbol{U}\boldsymbol{D}\boldsymbol{V}^\dagger$, where $\boldsymbol{D}$ is an $n_d \times n_r$ diagonal matrix with $\{\sqrt{\nu_1}, \ldots, \sqrt{\nu_l}\}$ as the main diagonal elements in decreasing order and where $l = \min(n_d, n_r)$. Then, using the identity $\det(\boldsymbol{I}+\boldsymbol{A}\boldsymbol{B}) = \det(\boldsymbol{I}+\boldsymbol{B}\boldsymbol{A})$ and defining $\boldsymbol{\Phi} = \sigma_1^2 F_2^2 \boldsymbol{H}_2 \boldsymbol{H}_2^\dagger + \sigma_2^2 \boldsymbol{I}_{n_d}$, the ergodic capacity can also be written as

$$\begin{aligned} C &= \frac{1}{2} E\left\{\log_2\left|\boldsymbol{I}_{n_s} + \rho \boldsymbol{H}^\dagger (\boldsymbol{B}\boldsymbol{B}^\dagger)^{-1} \boldsymbol{H}\right|\right\} \\ &= \frac{1}{2} E\left\{\log_2\left|\boldsymbol{I}_{n_s} + \rho \begin{pmatrix} F_3\boldsymbol{H}_3 \\ F_1\boldsymbol{H}_2\boldsymbol{H}_1 \end{pmatrix}^\dagger \begin{pmatrix} \sigma_3^2 \boldsymbol{I}_{n_d} & \boldsymbol{0} \\ \boldsymbol{0} & \boldsymbol{\Phi} \end{pmatrix}^{-1} \begin{pmatrix} F_3\boldsymbol{H}_3 \\ F_1\boldsymbol{H}_2\boldsymbol{H}_1 \end{pmatrix}\right|\right\} \\ &= \frac{1}{2} E\left\{\log_2\left|\boldsymbol{I}_{n_s} + \rho\left(\sigma_3^{-2} F_3^2 \boldsymbol{H}_3^\dagger \boldsymbol{H}_3 + F_1 \boldsymbol{H}_1^\dagger \boldsymbol{H}_2^\dagger \boldsymbol{\Phi}^{-1} F_1 \boldsymbol{H}_2 \boldsymbol{H}_1\right)\right|\right\} \\ &= \frac{1}{2} E\left\{\log_2\left|\boldsymbol{I}_{n_s} + \rho \begin{pmatrix} \boldsymbol{H}_3^\dagger & \boldsymbol{H}_1^\dagger \end{pmatrix} \begin{pmatrix} \sigma_3^{-2} F_3^2 \boldsymbol{I}_{n_d} & \boldsymbol{0} \\ \boldsymbol{0} & F_1^2 \boldsymbol{H}_2^\dagger \boldsymbol{\Phi}^{-1} \boldsymbol{H}_2 \end{pmatrix} \begin{pmatrix} \boldsymbol{H}_3 \\ \boldsymbol{H}_1 \end{pmatrix}\right|\right\}. \end{aligned} \tag{5.6}$$

Substituting $\boldsymbol{H}_2 = \boldsymbol{U}\boldsymbol{D}\boldsymbol{V}^\dagger$ into (5.6) gives

$$C = \frac{1}{2} E\left\{\log_2\left|\boldsymbol{I}_{n_s} + \rho \boldsymbol{U}_t^\dagger \boldsymbol{A} \boldsymbol{U}_t\right|\right\} \tag{5.7}$$

where

$$\boldsymbol{A} = \begin{pmatrix} \sigma_3^{-2} F_3^2 \boldsymbol{I}_{n_d} & \boldsymbol{0} \\ \boldsymbol{0} & \boldsymbol{\Omega} \end{pmatrix}, \; \boldsymbol{U}_t = \begin{pmatrix} \boldsymbol{U}^\dagger \boldsymbol{H}_3 \\ \boldsymbol{V}^\dagger \boldsymbol{H}_1 \end{pmatrix}. \tag{5.8}$$

In (5.8), $\boldsymbol{\Omega} = F_1^2 \boldsymbol{D}^\dagger \left(\sigma_1^2 F_2^2 \boldsymbol{D}\boldsymbol{D}^\dagger + \sigma_2^2 \boldsymbol{I}\right)^{-1} \boldsymbol{D}$. Note that $\boldsymbol{U}_t$ contains i.i.d ZMCSCG entries since the unitary matrices $\boldsymbol{U}^\dagger$ and $\boldsymbol{V}^\dagger$ do not change the statistics of $\boldsymbol{H}_3$ and $\boldsymbol{H}_1$. After defining $c = \sigma_3^{-2} F_3^2$, $c_1 = (F_1^2 - \sigma_3^{-2} F_3^2 \sigma_1^2 F_2^2)$, $c_2 = \sigma_3^{-2} F_3^2 \sigma_2^2$, $c_3 = F_1^2$, $c_4 = \sigma_1^2 F_2^2$, and $c_5 = \sigma_2^2$, $\boldsymbol{\Omega}$ can be given as

$$\boldsymbol{\Omega} = \begin{cases} \operatorname{diag}\left\{\frac{c_3\nu_1}{c_4\nu_1+c_5}, \ldots, \frac{c_3\nu_l}{c_4\nu_l+c_5}\right\}, & \text{for } n_r \leqslant n_d \\ \operatorname{diag}\left\{\frac{c_3\nu_1}{c_4\nu_1+c_5}, \ldots, \frac{c_3\nu_l}{c_4\nu_l+c_5}, \underbrace{0, \ldots, 0}_{n_r - n_d}\right\}, & \text{for } n_r > n_d \end{cases}. \tag{5.9}$$

Further, by defining $m = \max(n_d, n_r)$, $q = n_d + l$ and $s = \min(n_s, q)$, the ergodic capacity can also be expressed as

$$C = \frac{1}{2} E\left\{\log_2\left|\boldsymbol{I}_{n_s} + \rho \widetilde{\boldsymbol{U}}_t^\dagger \widetilde{\boldsymbol{A}} \widetilde{\boldsymbol{U}}_t\right|\right\} \tag{5.10}$$

where $\widetilde{\boldsymbol{U}}_t \in \mathcal{C}^{n_s \times q}$ has i.i.d ZMCSCG entries with unit variance and

$$\widetilde{\boldsymbol{A}} = \begin{pmatrix} c\boldsymbol{I}_{n_d} & \boldsymbol{0} \\ \boldsymbol{0} & \operatorname{diag}\left\{ \frac{c_3\nu_1}{c_4\nu_1+c_5}, \ldots, \frac{c_3\nu_l}{c_4\nu_l+c_5} \right\} \end{pmatrix}. \tag{5.11}$$

Note that $\widetilde{\boldsymbol{A}}$ and $\widetilde{\boldsymbol{U}}_t$ are simply re-sized versions of $\boldsymbol{A}$ and $\boldsymbol{U}_t$ according to $n_r \leqslant n_d$ or $n_r > n_d$. Since $l = \min(n_d, n_r)$ in (5.11), $\widetilde{\boldsymbol{A}}$ is an $(n_d + n_r) \times (n_d + n_r)$ diagonal matrix and $\widetilde{\boldsymbol{U}}_t \in \mathcal{C}^{n_s \times (n_d+n_r)}$ when $n_r \leqslant n_d$, and $\widetilde{\boldsymbol{A}}$ is an $(n_d + n_d) \times (n_d + n_d)$ diagonal matrix and $\widetilde{\boldsymbol{U}}_t \in \mathcal{C}^{n_s \times (n_d+n_d)}$ when $n_r > n_d$. Now using the procedure explained in Sec. 2.5 for MIMO system capacity analysis, the ergodic capacity can be written as

$$C = \frac{s}{2\ln(2)} \int_0^\infty \ln(1+\rho\lambda)\, f(\lambda)\, d\lambda, \tag{5.12}$$

where λ denotes an arbitrary eigenvalue of $\widetilde{\boldsymbol{U}}_t^\dagger \widetilde{\boldsymbol{A}} \widetilde{\boldsymbol{U}}_t$ and $f(\lambda)$ is the PDF of λ. Hence, to find the ergodic capacity of the system, we need to find the arbitrary eigenvalue density, $f(\lambda)$, of the random matrix $\widetilde{\boldsymbol{U}}_t^\dagger \widetilde{\boldsymbol{A}} \widetilde{\boldsymbol{U}}_t$. The derivation of $f(\lambda)$ is given below. The derivation of $f(\lambda)$ and the capacity expressions for the different cases given below involves a complex series of steps. This is given in a fairly dense form. However an overview of the results is given in Sec. 5.3 to clarify the application of the relevant formulae.

5.2.1 Derivation of the Arbitrary Eigenvalue Density, $f(\lambda)$

Assuming the random diagonal matrix $\widetilde{\boldsymbol{A}}$ has all distinct eigenvalues $\boldsymbol{\mu} = \{\mu_1, \ldots, \mu_q\}$, then the conditional unordered eigenvalue PDF $f(\lambda|\boldsymbol{\mu})$ for arbitrary numbers of antennas at the source, relay and destination can be obtained from [69] as

$$f(\lambda|\boldsymbol{\mu}) = \frac{1}{s\prod_{k<p}^{q}(\mu_p - \mu_k)} \sum_{k=q-s+1}^{q} \frac{\lambda^{n_s-q+k-1}}{\Gamma(n_s-q+k)} \left|\boldsymbol{G}\right|, \tag{5.13}$$

where $\boldsymbol{G}$ is a $q \times q$ matrix with entries

$$\boldsymbol{G}_{i,j} = \begin{cases} \mu_j^{i-1}, & \text{for } i \neq k \\ \mu_j^{q-n_s-1} e^{-\frac{\lambda}{\mu_j}}, & \text{for } i = k \end{cases}. \tag{5.14}$$

However, the eigenvalues of $\widetilde{\boldsymbol{A}}$ are not all distinct but can be given as $\{c, \ldots, c, \mu_1, \ldots, \mu_l\}$, where c is a constant which has multiplicity n_d and $\mu_k = \frac{c_3\nu_k}{c_4\nu_k + c_5}$ are random variables, which are unequal with probability 1. When $\widetilde{\boldsymbol{A}}$ does not have all distinct values, the conditional PDF $f(\lambda|\boldsymbol{\mu})$ can be obtained by using the following identities on multiple derivatives,

1. If $y = x^n$, then the k^{th} derivative of y, $y^{(k)} = (n-k+1)_k \; x^{n-k}$, where $(n)_k$ is the Pochhammer symbol.

2. If $y = x^n e^{-s/x}$, then the k^{th} derivative of y, $y^{(k)} = e^{-s/x} \sum_{i=0}^{k} \frac{k!}{i!(k-i)!}(n-k+1)_{k-i} \; s^i \; x^{n-k-i}$.

These derivatives are then used to derive an alternative version of (5.13) using the method given in *Lemma 2* of [48]. The lemma basically explains the derivation of $f(\lambda|\boldsymbol{\mu})$ for the general case when not all the μ_k values are necessarily distinct. With this approach $f(\lambda|\boldsymbol{\mu})$ can be calculated as

$$\begin{aligned} f(\lambda|\boldsymbol{\mu}) = & \frac{1}{s\prod_{k<p}^{l}(\mu_k - \mu_p)\prod_{k=1}^{l}(c-\mu_k)^{n_d}\prod_{k=1}^{n_d-1}k!} \\ & \times \frac{1}{(-1)^{q(q-1)/2}} \sum_{k=q-s+1}^{q} \frac{\lambda^{n_s-q+k-1}}{\Gamma(n_s-q+k)} \left|\boldsymbol{G}\right|, \end{aligned} \tag{5.15}$$

where $\Gamma_m(n) = \prod_{i=1}^{m}\Gamma(n-i+1)$ and $\boldsymbol{G}$ is a $q \times q$ matrix with entries given as

$$\boldsymbol{G}_{i,j} = \begin{cases} (i-n_d+j)_{n_d-j} \; c^{i-n_d+j-1}, & \text{for } i \neq k,\; j = 1, \ldots, n_d \\ \sum_{t=0}^{n_d-j} e^{-\frac{\lambda}{c}} \frac{(n_d-j)!}{t!(n_d-j-t)!} & \\ \quad \times (q-n_s-n_d+j)_{n_d-j-t}\lambda^t c^{q-n_s-n_d+j-1-t}, & \text{for } i = k,\; j = 1, \ldots, n_d \\ \mu_{j-n_d}^{i-1}, & \text{for } i \neq k,\; j = n_d+1, \ldots, q \\ \mu_{j-n_d}^{q-n_s-1} e^{-\frac{\lambda}{\mu_{j-n_d}}}, & \text{for } i = k,\; j = n_d+1, \ldots, q \end{cases} . \tag{5.16}$$

Then, using the results in (5.15)-(5.16) the arbitrary eigenvalue PDF, $f(\lambda)$, can be derived as given below. Here, the main case considered is $P_1 \neq P_3$, ($c_1 \neq 0$) which is of more physical interest. The special case, $P_1 = P_3$, ($c_1 = 0$) has to be considered separately and yields a simpler result.

The PDF of λ, $f(\lambda)$, can be calculated by using the result in (5.15). The eigenvalues of $\widetilde{\boldsymbol{A}}$, $\boldsymbol{\mu} = \{c, \ldots, c, \mu_1, \ldots, \mu_l\}$, are related to the eigenvalues of $\boldsymbol{H}_2\boldsymbol{H}_2^\dagger$, $\boldsymbol{\nu} = \{\nu_1, \ldots, \nu_l\}$ via, $\mu_k = \frac{c_3\nu_k}{c_4\nu_k + c_5}$. Then, using the result for $f(\lambda|\boldsymbol{\mu})$ in (5.15), $f(\lambda|\boldsymbol{\nu})$ can be obtained by substituting $\mu_k = \frac{c_3\nu_k}{c_4\nu_k + c_5}$ in $f(\lambda|\boldsymbol{\mu})$, as fixing the value of $\boldsymbol{\mu}$ is equivalent to fixing the value of $\boldsymbol{\nu}$. Then using $f(\lambda|\boldsymbol{\nu})$ and $f(\boldsymbol{\nu})$, the eigenvalue p.d.f $f(\lambda)$ can be derived as shown below.

The matrix $\boldsymbol{H}_2\boldsymbol{H}_2^\dagger$ is Wishart or pseudo-Wishart [50] depending on the dimension, $n_d \times n_r$, of $\boldsymbol{H}_2$. However, the non-zero eigenvalues of $\boldsymbol{H}_2\boldsymbol{H}_2^\dagger$ are the same irrespective of whether the matrix is Wishart or pseudo-Wishart. Hence, the non-zero unordered eigenvalue p.d.f of $\boldsymbol{H}_2\boldsymbol{H}_2^\dagger$ can be given as [49]

$$f(\boldsymbol{\nu}) = \frac{\pi^{l(l-1)}}{l!\mathcal{C}\Gamma_l(l)\mathcal{C}\Gamma_l(m)} \prod_{k=1}^{l} \nu_k^{m-l} e^{-\nu_k} \prod_{k<p}^{l} (\nu_k - \nu_p)^2, \tag{5.17}$$

where $\mathcal{C}\Gamma_l(m)$ denotes the complex multivariate gamma function,

$$\mathcal{C}\Gamma_l(m) = \pi^{l(l-1)/2} \prod_{k=1}^{l} \Gamma(m-k+1). \tag{5.18}$$

Using the result in (5.15), the conditional PDF, $f(\lambda|\boldsymbol{\nu})$, can be obtained by substituting $\mu_k = \frac{c_3\nu_k}{c_4\nu_k + c_5}$ in (5.15) as

$$\begin{aligned} f(\lambda|\boldsymbol{\nu}) = & \frac{1}{s\prod_{k=1}^{n_d-1} k!(-1)^{q(q-1)/2}(c_3c_5)^{l(l-1)/2}} \\ & \times \frac{1}{\prod_{k<p}^{l}(\nu_k - \nu_p)\prod_{k=1}^{l} \frac{((cc_4-c_3)\nu_k + cc_5)^{n_d}}{(c_4\nu_k + c_5)^{n_d+l-1}}} \\ & \times \sum_{k=q-s+1}^{q} \frac{\lambda^{n_s-q+k-1}}{\Gamma(n_s-q+k)} |\boldsymbol{G}|. \end{aligned} \tag{5.19}$$

Then, using the relation $f(\lambda, \boldsymbol{\nu}) = f(\boldsymbol{\nu})f(\lambda|\boldsymbol{\nu})$, $f(\lambda, \boldsymbol{\nu})$ can be given as

$$\begin{aligned} f(\lambda, \boldsymbol{\nu}) = & \frac{\pi^{l(l-1)}}{l!\,\mathcal{C}\Gamma_l(l)\,\mathcal{C}\Gamma_l(m)} \frac{(-1)^{-n_d l}}{s\prod_{k=1}^{n_d-1} k!(-1)^{q(q-1)/2}(c_3c_5)^{l(l-1)/2}} \\ & \times \prod_{k=1}^{l} \nu_k^{m-l} e^{-\nu_k} \frac{(c_4\nu_k + c_5)^{q-1}}{(c_1\nu_k - cc_5)^{n_d}} \prod_{k<p}^{l} (\nu_k - \nu_p) \sum_{k=q-s+1}^{q} \frac{\lambda^{n_s-q+k-1}}{\Gamma(n_s-q+k)} |\boldsymbol{G}| \\ \triangleq & C_0 \sum_{k=q-s+1}^{q} \frac{\lambda^{n_s-q+k-1}}{\Gamma(n_s-q+k)} \prod_{k=1}^{l} \xi(\nu_k) |\Phi_i(\nu_j)| |\boldsymbol{G}|. \end{aligned} \tag{5.20}$$

In (5.20), $\prod_{k<p}^{l}(\nu_k - \nu_p) = (-1)^{l(l-1)/2}\,|\Phi_j(\nu_i)|$, $\Phi_i(\nu_j) = \nu_j^{i-1}$,

$$C_0 = \frac{\pi^{l(l-1)}}{l!\mathcal{C}\Gamma_l(l)\mathcal{C}\Gamma_l(m)}\frac{(-1)^{-n_d l}(-1)^{l(l-1)/2}}{s\prod_{k=1}^{n_d-1}k!(-1)^{q(q-1)/2}(c_3c_5)^{l(l-1)/2}}, \tag{5.21}$$

$$\xi(\nu_k) = \nu_k^{m-l}e^{-\nu_k}\frac{(c_4\nu_k + c_5)^{q-1}}{(c_1\nu_k - cc_5)^{n_d}}, \tag{5.22}$$

and $\boldsymbol{G}$ is a $q \times q$ matrix with entries given as

$$\boldsymbol{G}_{i,j} = \begin{cases} (i-n_d+j)_{n_d-j}\; c^{i-n_d+j-1}, & \text{for } i \neq k,\ j = 1,\ldots,n_d \\ \sum_{t=0}^{n_d-j} e^{-\frac{\lambda}{c}}\frac{(n_d-j)!}{t!(n_d-j-t)!} & \\ \quad\times(q-n_s-n_d+j)_{n_d-j-t}\lambda^t c^{q-n_s-n_d+j-1-t}, & \text{for } i = k,\ j = 1,\ldots,n_d \\ \left(\frac{c_3\nu_{j-n_d}}{c_4\nu_{j-n_d}+c_5}\right)^{i-1}, & \text{for } i \neq k,\ j = n_d+1,\ldots,q \\ \left(\frac{c_3\nu_{j-n_d}}{c_4\nu_{j-n_d}+c_5}\right)^{q-n_s-1} e^{-\frac{\lambda(c_4\nu_{j-n_d}+c_5)}{c_3\nu_{j-n_d}}}, & \text{for } i = k,\ j = n_d+1,\ldots,q \end{cases}. \tag{5.23}$$

Now $f(\lambda)$ can be obtained by integrating (5.20) over all ν_j as,

$$\begin{aligned} f(\lambda) &= \int_0^\infty \ldots \int_0^\infty f(\lambda, \boldsymbol{\nu})\, d\nu_1 \ldots d\nu_l \\ &= C_0 \sum_{k=q-s+1}^{q} \frac{\lambda^{n_s-q+k-1}}{\Gamma(n_s-q+k)} \\ &\quad\times \int_0^\infty \ldots \int_0^\infty \prod_{k=1}^{l} \xi(\nu_k)\,|\Phi_i(\nu_j)|\,|\boldsymbol{G}|\, d\nu_1 \ldots d\nu_l. \end{aligned} \tag{5.24}$$

Note that the form of the integration in (5.24) is exactly the same as the integrals defined in *Lemma 2* of [32]. In particular the structure of ξ, $\Phi_i(\nu_j)$ and $\boldsymbol{G}$ given in (5.22), (5.20) and (5.23), respectively, is identical to the required structure in [32]. Hence, the integration is obtained by an immediate application of [32] as,

$$\int_0^\infty \ldots \int_0^\infty \prod_{k=1}^{l} \xi(\nu_k)\,|\Phi_i(\nu_j)|\,|\boldsymbol{G}|\, d\nu_1 \ldots d\nu_l = l!\,|\boldsymbol{\Psi}|\,, \tag{5.25}$$

where $\boldsymbol{\Psi}$ is a $q \times q$ matrix with entries given as

$$\boldsymbol{\Psi}_{i,j} = \begin{cases} (i-n_d+j)_{n_d-j}\, c^{i-n_d+j-1}, & \text{for } i \neq k,\ j = 1,\ldots,n_d \\ \sum_{t=0}^{n_d-j} e^{-\frac{\lambda}{c}} \frac{(n_d-j)!}{t!(n_d-j-t)!} & \\ \quad \times (q-n_s-n_d+j)_{n_d-j-t} \lambda^t c^{q-n_s-n_d+j-1-t}, & \text{for } i = k,\ j = 1,\ldots,n_d \\ \int x^{j-n_d-1} \left(\frac{c_3 x}{c_4 x + c_5}\right)^{i-1} \xi(x) dx \triangleq I_A(i,j), & \text{for } i \neq k,\ j = n_d+1,\ldots,q \\ \int x^{j-n_d-1} \left(\frac{c_3 x}{c_4 x + c_5}\right)^{q-n_s-1} e^{-\frac{\lambda(c_4 x + c_5)}{c_3 x}} \xi(x) dx, & \text{for } i = k,\ j = n_d+1,\ldots,q \end{cases} . \tag{5.26}$$

Hence, $f(\lambda)$ can be obtained by integrating (5.20) over all ν_j by using the method described in *Lemma 2* of [32] as,

$$\begin{aligned} f(\lambda) &= C_0 \sum_{k=q-s+1}^{q} \frac{\lambda^{n_s-q+k-1}}{\Gamma(n_s-q+k)} \\ &\quad \times \int_0^\infty \ldots \int_0^\infty \prod_{k=1}^{l} \xi(\nu_k) \left|\Phi_i(\nu_j)\right| |\boldsymbol{G}|\, d\nu_1 \ldots d\nu_l \\ &\triangleq \underbrace{C_0 l!}_{C_1} \sum_{k=q-s+1}^{q} \frac{\lambda^{n_s-q+k-1}}{\Gamma(n_s-q+k)} |\boldsymbol{\Psi}| . \end{aligned} \tag{5.27}$$

In (5.26), $I_A(i,j)$ is defined to be

$$\begin{aligned} I_A(i,j) = \sum_{v=0}^{q-i} \binom{q-i}{v} \left(\frac{c_4}{c_1}\right)^v \left(\frac{c_4 c_2}{c_1} + c_5\right)^{q-i-v} \\ \times \sum_{w=0}^{j+i+m-q-2} \binom{j+i+m-q-2}{w} \frac{c_3^{i-1} e^{-c_2/c_1}}{c_1^{w+1}} \left(\frac{c_2}{c_1}\right)^{j+i+m-q-2-w} I_{A1}, \end{aligned} \tag{5.28}$$

where I_{A1} is calculated below for the different system parameters. Finally, the PDF of an arbitrary eigenvalue, λ, of $\widetilde{\boldsymbol{U}}_t^\dagger \widetilde{\boldsymbol{A}} \widetilde{\boldsymbol{U}}_t$ can be obtained by using the Laplace expansion of (5.27) as

$$f(\lambda) = C_1 \sum_{i=q-s+1}^{q} \sum_{j=1}^{q} (-1)^{i+j} \frac{\lambda^{n_s-q+i-1}}{\Gamma(n_s-q+i)} |\boldsymbol{K}_{i,j}|\, A_\lambda(i,j), \tag{5.29}$$

where

$$C_1 = \frac{\pi^{l(l-1)}}{\mathcal{C}\Gamma_l(l)\, \mathcal{C}\Gamma_l(m)} \frac{(-1)^{-n_d l} (-1)^{l(l-1)/2}}{s \prod_{k=1}^{n_d-1} k! (-1)^{q(q-1)/2} (c_3 c_5)^{l(l-1)/2}}, \tag{5.30}$$

and $A_\lambda(i,j)$ is given as

$$A_\lambda(i,j) = \begin{cases} \sum_{t=0}^{n_d-j} e^{-\frac{\lambda}{c}} \frac{(n_d-j)!}{t!(n_d-j-t)!} \\ \quad \times (q-n_s-n_d+j)_{n_d-j-t} \\ \quad \times \lambda^t c^{q-n_s-n_d+j-1-t}, & \text{for } i=1,\ldots,q,\ j=1,\ldots,n_d \\ \int_0^\infty x^{j-n_d-1} \left(\frac{c_3 x}{c_4 x+c_5}\right)^{q-n_s-1} \\ \quad \times e^{-\frac{\lambda}{\left(\frac{c_3 x}{c_4 x+c_5}\right)}} \xi(x)\, dx, & \text{for } i=1,\ldots,q,\ j=n_d+1,\ldots,q \end{cases} . \tag{5.31}$$

In (5.31), $\xi(x)$ is obtained by replacing ν_k by x in (5.22) as

$$\xi(x) = x^{m-l} e^{-x} \frac{(c_4 x + c_5)^{q-1}}{(c_1 x - c_2)^{n_d}}, \tag{5.32}$$

and in (5.29), $\boldsymbol{K}_{i,j}$ denotes the $(i,j)^{\text{th}}$ minor of $\boldsymbol{K}$ with elements given by

$$\boldsymbol{K}_{i,j} = \begin{cases} (i-n_d+j)_{n_d-j}\, c^{i-n_d+j-1}, & \text{for } i=1,\ldots,q,\ j=1,\ldots,n_d \\ \int_0^\infty x^{j-n_d-1} \left(\frac{c_3 x}{c_4 x+c_5}\right)^{i-1} \xi(x)\, dx \\ \quad \triangleq I_A(i,j), & \text{for } i=1,\ldots,q,\ j=n_d+1,\ldots,q \end{cases} . \tag{5.33}$$

In (5.28), if $c_1 > 0$, ($P_1 > P_3$) then $I_{A1} = \int_{-c_2}^\infty y^{v+w-n_d} e^{-\frac{y}{c_1}} dy$. Since $c_2 > 0$ the integral includes the point $y = 0$ where a singularity occurs when $v+w-n_d < 0$. In this case the individual integral diverges but the sum of integrals implicit in (5.29) must remain finite. Hence, the integral is computed as

$$I_{A1} = \underbrace{\int_{-c_2}^{-\epsilon} y^{v+w-n_d} e^{-\frac{y}{c_1}} dy}_{I_{A11}} + \underbrace{\int_{\epsilon}^{\infty} y^{v+w-n_d} e^{-\frac{y}{c_1}} dy}_{I_{A12}} . \tag{5.34}$$

where ϵ is a very small positive number close to zero. With this approach the divergent integrals cancel out in (5.29) and the resulting computations prove to be robust and stable. In (5.34) the two integrals can be evaluated as

$$I_{A12} = \begin{cases} -e^{\frac{-\epsilon}{c_1}} \sum_{k=0}^{v+w-n_d} \frac{(-1)^{v+w-n_d-k}(v+w-n_d)!(\epsilon)^k}{k!(-1/c_1)^{v+w-n_d-k+1}}, & \text{for } v+w-n_d \geq 0 \\ \frac{(-1)^{n_d-w-v}(1/c_1)^{n_d-w-v-1}\text{Ei}(-\epsilon/c_1)}{(n_d-w-v-1)!} \\ + \sum_{k=0}^{n_d-w-v-2} \frac{e^{-\epsilon/c_1}}{(\epsilon)^{n_d-w-v-1}} \\ \quad \times \frac{(-1)^k (1/c_1)^k (\epsilon)^k}{(n_d-w-v-1)(n_d-w-v-2)\ldots(n_d-w-v-1-k)}, & \text{for } v+w-n_d < 0 \end{cases} . \tag{5.35}$$

$$I_{A11} = \begin{cases} e^{\frac{\epsilon}{c_1}} \sum_{k=0}^{v+w-n_d} \frac{(-1)^{v+w-n_d-k}(v+w-n_d)!(-\epsilon)^k}{k!(-1/c_1)^{v+w-n_d-k+1}} \\ -e^{\frac{c_2}{c_1}} \sum_{k=0}^{v+w-n_d} \frac{(-1)^{v+w-n_d-k}(v+w-n_d)!(-c_2)^k}{k!(-1/c_1)^{v+w-n_d-k+1}}, & \text{for } v+w-n_d \geq 0 \\ \frac{(-1)^{n_d-w-v-1}(1/c_1)^{n_d-w-v-1}\mathrm{Ei}(\epsilon/c_1)}{(n_d-w-v-1)!} \\ +\frac{(-1)^{n_d-w-v}(1/c_1)^{n_d-w-v-1}\mathrm{Ei}(c_2/c_1)}{(n_d-w-v-1)!} \\ -\sum_{k=0}^{n_d-w-v-2} \frac{e^{\epsilon/c_1}}{(-\epsilon)^{n_d-w-v-1}} \\ \quad \times \frac{(-1)^k(1/c_1)^k(-\epsilon)^k}{(n_d-w-v-1)(n_d-w-v-2)...(n_d-w-v-1-k)} \\ +\sum_{k=0}^{n_d-w-v-2} \frac{e^{c_2/c_1}}{(-c_2)^{n_d-w-v-1}} \\ \quad \times \frac{(-1)^k(1/c_1)^k(-c_2)^k}{(n_d-w-v-1)(n_d-w-v-2)...(n_d-w-v-1-k)}, & \text{for } v+w-n_d < 0 \end{cases} . \quad (5.36)$$

In (5.35) and (5.36), $\mathrm{Ei}(x)$ is the exponential integral. Note also that when $c_1 > 0$, the integral in (5.31) has a singular point at $x = c_2/c_1$. That integral also has to be approximated as in (5.34), and to be consistent, the region of integration has to be $(0, c_2/c_1 - \epsilon/c_1)$ and $(c_2/c_1 + \epsilon/c_1, \infty)$.

If $c_1 < 0$, $(P_1 < P_3)$ then $I_{A1} = \int_{c_2}^{\infty} -(-y)^{v+w-n_d} e^{\frac{y}{c_1}} dy$ in (5.28) and is given by

$$I_{A1} = (c_1)^{v+w-n_d+1} \Gamma(v+w-n_d+1, -c_2/c_1), \quad (5.37)$$

where $\Gamma(a,z) = \int_z^{\infty} e^{-x} x^{a-1} dx$ is the complementary incomplete gamma function.

Then, using the above result and (5.12), the ergodic capacity can be calculated as

$$C = \sum_{i=q-s+1}^{q} \sum_{j=1}^{q} \frac{s}{2\ln(2)} C_1 (-1)^{i+j} |\boldsymbol{K}_{i,j}| \cdot \underbrace{\int_0^{\infty} \ln(1+\rho\lambda) \frac{\lambda^{n_s-q+i-1}}{\Gamma(n_s-q+i)} A_{\lambda}(i,j)\, d\lambda}_{I_B} \quad (5.38)$$

where I_B is given as

$$I_B = \begin{cases} \sum_{t=0}^{n_d-j} \sum_{r=1}^{n_s+t-q+i} \frac{(n_d-j)!}{t!(n_d-j-t)!} \\ \times \frac{(q-n_s-n_d+j)_{n_d-j-t}}{\Gamma(n_s-q+i)} C^{q-n_s-n_d+j-1-t} \\ \times (1/\rho)^{n_s+t-q+i} (n_s+t-q+i-1)! e^{\frac{1}{\rho c}} \\ \times \Gamma\left(-(n_s+t-q+i)+r, 1/(\rho c)\right) (\rho c)^r, & i = 1,\ldots,q,\ j = 1,\ldots,n_d \\ I_C, & i = 1,\ldots,q,\ j = n_d+1,\ldots,q \end{cases} , \quad (5.39)$$

and

$$I_C = \int_0^\infty \frac{x^{j-n_d-1}(n_s-q+i-1)!}{\Gamma(n_s-q+i)} \left(\frac{c_3 x}{c_4 x + c_5}\right)^{q-n_s-1} (1/\rho)^{n_s-q+i} \times e^{\frac{c_4 x + c_5}{\rho c_3 x}} \sum_{k=1}^{n_s-q+i} \frac{\Gamma(-(n_s-q+i)+k, (c_4 x + c_5)/(\rho c_3 x))}{((c_4 x + c_5)/(\rho c_3 x))^k} \xi(x)\, dx. \quad (5.40)$$

A closed-form expression for the integral, I_C, in (5.39) is difficult to find but it can be evaluated numerically. Again, note that when $c_1 > 0$, the integral, I_C, has a singular point at $x = c_2/c_1$. The same approximation is used as in (5.34), and the region of integration is $(0, c_2/c_1 - \epsilon/c_1)$ to $(c_2/c_1 + \epsilon/c_1, \infty)$.

Special Case: Ergodic Capacity of a (1,1,1) System

For the special case of a (1,1,1) system, the capacity expression given in (5.38) reduces to

$$\begin{aligned} C = &-\frac{c e^{\frac{1}{\rho c}} \Gamma\left(0, 1/(\rho c)\right)}{2\,\ln(2)} \left(\frac{c_4 c_2}{c_1} + c_5\right) \frac{e^{-c_2/c_1}}{c_1} \left(\mathrm{Ei}(\epsilon/c_1) - \mathrm{Ei}(c_2/c_1) - \mathrm{Ei}(-\epsilon/c_1)\right) \\ &- \frac{c e^{\frac{1}{\rho c}} \Gamma\left(0, 1/(\rho c)\right)}{2\,\ln(2)} \left(\frac{c_4}{c_1}\right) e^{-c_2/c_1} (e^{c2/c_1} + e^{-\epsilon/c_1} - e^{\epsilon/c_1}) \\ &+ \frac{1}{2\,\ln(2)} \int_0^\infty c_3\, x\, e^{-x} e^{\frac{c_4 x + c_5}{\rho c_3 x}} \Gamma(0, (c_4 x + c_5)/(\rho c_3 x)) \frac{1}{(c_1 x - c_2)}\, dx, \end{aligned} \quad (5.41)$$

when $P_1 > P_3$, and

$$\begin{aligned} C = &-\frac{c e^{\frac{1}{\rho c}} \Gamma\left(0, 1/(\rho c)\right)}{2\,\ln(2)} \left(\frac{c_4 c_2}{c_1} + c_5\right) \frac{e^{-c_2/c_1}}{c_1} \Gamma(0, -c_2/c_1) \\ &- \frac{c e^{\frac{1}{\rho c}} \Gamma\left(0, 1/(\rho c)\right)}{2\,\ln(2)} \left(\frac{c_4}{c_1}\right) e^{-c_2/c_1} \Gamma(1, -c_2/c_1) \\ &+ \frac{1}{2\,\ln(2)} \int_0^\infty c_3\, x\, e^{-x} e^{\frac{c_4 x + c_5}{\rho c_3 x}} \Gamma(0, (c_4 x + c_5)/(\rho c_3 x)) \frac{1}{(c_1 x - c_2)}\, dx, \end{aligned} \quad (5.42)$$

when $P_1 < P_3$. Note that the integral in (5.41) has a singular point at $x = c_2/c_1$. The same approximation is used as in (5.34), and the region of integration is $(0, c_2/c_1 - \epsilon/c_1)$ to $(c_2/c_1 + \epsilon/c_1, \infty)$.

The result in (5.38) is for the case where $P_1 \neq P_3$, ($c_1 \neq 0$). The special case, $P_1 = P_3$, ($c_1 = 0$) occurs with probability zero in a random fading environment. Furthermore, in practical systems this scenario is not very interesting as the relay link is usually much stronger. However, results for the case where $P_1 = P_3$ are given below for completeness.

5.2.2 Ergodic Capacity when $P_1 = P_3$

In this special case, when $P_1 = P_3$, the ergodic capacity of the system can be obtained by using (5.38). However, $\boldsymbol{K}_{i,j}$ and I_B in (5.38) have to be re-evaluated by substituting $c_1 = 0$. Then, denoting $\boldsymbol{K}'_{i,j}$ and I'_B as the re-evaluated version of $\boldsymbol{K}_{i,j}$ and I_B, respectively, by substituting $c_1 = 0$ in (5.38), $\boldsymbol{K}'_{i,j}$ can be evaluated as

$$\boldsymbol{K}'_{i,j} = \begin{cases} (i - n_d + j)_{n_d - j}\, c^{i-n_d+j-1}, & \text{for } i = 1, \ldots, q,\ j = 1, \ldots, n_d \\ \int_0^\infty x^{j-n_d-1} \left(\frac{c_3 x}{c_4 x + c_5}\right)^{i-1} \xi(x) dx & \\ \quad \triangleq I'_A(i,j), & \text{for } i = 1, \ldots, q,\ j = n_d + 1, \ldots, n_d + l \end{cases}, \tag{5.43}$$

where $I'_A(i,j) = c_3^{i-1}(-c_2)^{-n_d} \sum_{v=0}^{q-i} \begin{pmatrix} q-i \\ v \end{pmatrix} (c_4)^v\, (c_5)^{q-i-v}\, \Gamma(v+j+i+m-q-1)$, and I'_B can be calculated as

$$I'_B = \begin{cases} \sum_{t=0}^{n_d-j} \frac{(n_d-j)!}{t!(n_d-j-t)!} \frac{(q-n_s-n_d+j)_{n_d-j-t}}{\Gamma(n_s-q+i)} & \\ \times \sum_{r=1}^{n_s+t-q+i} c^{q-n_s-n_d+j-1-t} (1/\rho)^{n_s+t-q+i} & \\ \quad \times (n_s + t - q + i - 1)! e^{\frac{1}{\rho c}} & \\ \quad \times \Gamma(-(n_s + t - q + i) + r, 1/(\rho c))(\rho c)^r, & ; i = 1, \ldots, q,\ j = 1, \ldots, n_d \\ I'_C, & i = 1, \ldots, q,\ j = n_d + 1, \ldots, q \end{cases}, \tag{5.44}$$

where

$$I_C' = \frac{2c_3^{q-n_s-1}}{(-c_2)^{n_d}} \sum_{v=0}^{n_s} \binom{n_s}{v} c_4^v c_5^{n_s-v} \times \int_0^\infty \frac{\ln(1+\rho\lambda)\lambda^{n_s-q+i-1}}{\Gamma(n_s-q+i)} e^{-\frac{\lambda c_4}{c_3}} \left(\frac{\lambda c_5}{c_3}\right)^{\frac{v+j+m-n_s-1}{2}} K_{v+j+m-n_s-1}\left(2\sqrt{\frac{\lambda c_5}{c_3}}\right) d\lambda. \tag{5.45}$$

Then, substituting (5.43) and (5.44) in (5.38), the ergodic capacity of the system when $P_1 = P_3$ can be obtained. By using the result in (5.38), the ergodic capacity of the system without the direct link can also be obtained as a special case. The derivation is given below.

5.2.3 Ergodic Capacity without the Direct Link

When the direct link is removed, $P_3 = 0$, $\sigma_3^2 = 0$ and $P_3/\sigma_3^2 = 0$. This implies that $c = 0$, $c_1 = F_1^2$ and $c_2 = 0$. Substituting these values in (5.38), the ergodic capacity without the direct link can be obtained. In this case, the terms $\boldsymbol{K}_{i,j}$ and I_B in (5.38) are simpler than before. Then, denoting $\boldsymbol{K}_{i,j}^{''}$ and $I_B^{''}$ as the re-evaluated version of $\boldsymbol{K}_{i,j}$ and I_B, respectively, for this case, $\boldsymbol{K}_{i,j}^{''}$ can be evaluated as

$$\boldsymbol{K}_{i,j}^{''} = \begin{cases} 0, & i = 1,\ldots,q,\ j = 1,\ldots,n_d, i \neq n_d - j + 1 \\ (i - n_d + j)_{n_d - j}, & i = 1,\ldots,q,\ j = 1,\ldots,n_d, i = n_d - j + 1 \\ \int_0^\infty x^{j-n_d-1}\left(\frac{c_3 x}{c_4 x + c_5}\right)^{i-1} \xi(x) dx & \\ \quad \triangleq I_A''(i,j), & i = 1,\ldots,q,\ j = n_d+1,\ldots,n_d+l \end{cases}, \tag{5.46}$$

where

$$I_A''(i,j) = c_1^{-n_d} c_3^{i-1} \sum_{v=0}^{q-i} \binom{q-i}{v} (c_4)^v (c_5)^{q-i-v} \underbrace{\int_0^\infty x^{j+i+m+v-n_d-2-q} e^{-x} dx}_{I_{A1}''}. \tag{5.47}$$

The integral, $I_{A1}^{''}$, in (5.47) includes the point $x = 0$ where a singularity occurs when $j+i+m+v-n_d-2-q < 0$. In this case, as before, the individual integral diverges

but the sum of integrals implicit in (5.38) must remain finite. Hence, the integral is computed as

$$\begin{aligned} I_{A1}^{''} &= \int_{\epsilon}^{\infty} x^{j+i+m+v-n_d-2-q} e^{-x} dx \\ &= \Gamma(j+i+m+v-n_d-1-q, \epsilon), \end{aligned} \tag{5.48}$$

where ϵ is a very small positive number close to zero. Also, $I_B^{''}$ can be calculated as,

$$I_B^{''} = \begin{cases} 0, & \text{for } i = 1, \ldots, q,\ j = 1, \ldots, n_d \\ I_C, & \text{for } i = 1, \ldots, q,\ j = n_d + 1, \ldots, q \end{cases}, \tag{5.49}$$

where I_C is given in (5.40) with $c_2 = 0$. Note that the integral, I_C, in (5.49) may have a singular point at $x = 0$. Hence, the same approximation is used as in (5.48), and the region of integration is ϵ to ∞. Then substituting (5.46) and (5.49) into (5.38), the ergodic capacity of the system without the direct link can be obtained.

5.3 Overview of Analysis

The results derived above involve a complex series of steps. Hence, in this subsection we briefly outline what we have done and the results derived in the previous sections. The main objective of this chapter has been to analyze the ergodic capacity of an AF MIMO two-hop system including the direct link. We have derived the ergodic capacity expressions for different situations from the PDF of the arbitrary eigenvalue. Our derived results are summarized in Fig. 5.2.

5.4 Results and Discussion

We now validate our results by using Monte Carlo simulations. In all the results given, the following conditions are used:

- the total transmitted power from the source is equal to one, $\rho = 1/n_s$;
- on average, the total transmitted power from the relay is equal to one, $b = \sqrt{1/(n_r P_1 + n_r \sigma_1^2)}$.

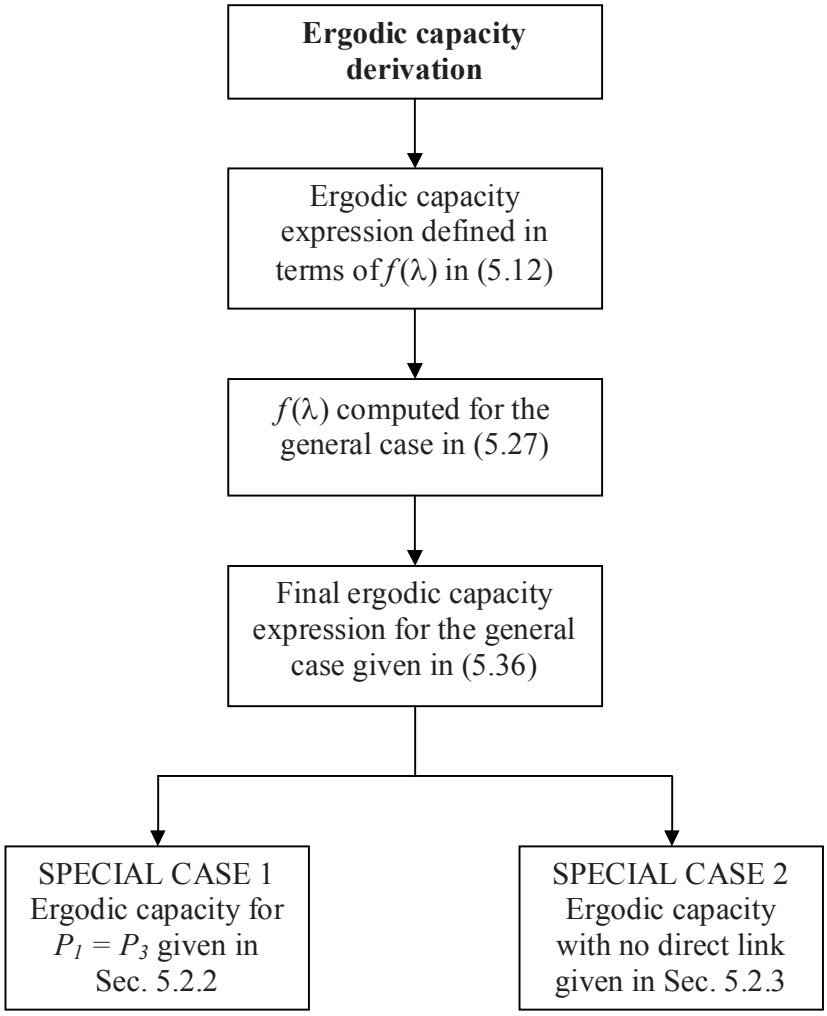

Figure 5.2: Overview of the results derived in Chapter 5.

Furthermore, we set $\sigma_1^2 = \sigma_2^2 = \sigma_3^2 = 1$, implying that the SNR of the links $(S \rightarrow D)$, $(S \rightarrow R)$ and $(R \rightarrow D)$ are P_3, P_1 and P_2, respectively. First, in Fig. 5.3, the result in (5.29) for the PDF of the arbitrary eigenvalue λ is validated via simulation. The plot shows the PDF of the arbitrary eigenvalue λ for system configuration $(3, 2, 3)$. Figure 5.3 shows that the analytical results are in agreement with the simulations.

In Figure 5.4 we plot the analytical and simulated ergodic capacity of the AF MIMO system given in Fig. 5.1. The analytical results are based on (5.38) and the results are given for the system configurations: $(2, 2, 2)$, $(2, 2, 3)$ and $(3, 2, 3)$. The results are given as a function of the SNR in the links as $P_1 = P_2 = 1.5P_3$. We see that the analytical results exactly match the simulations.

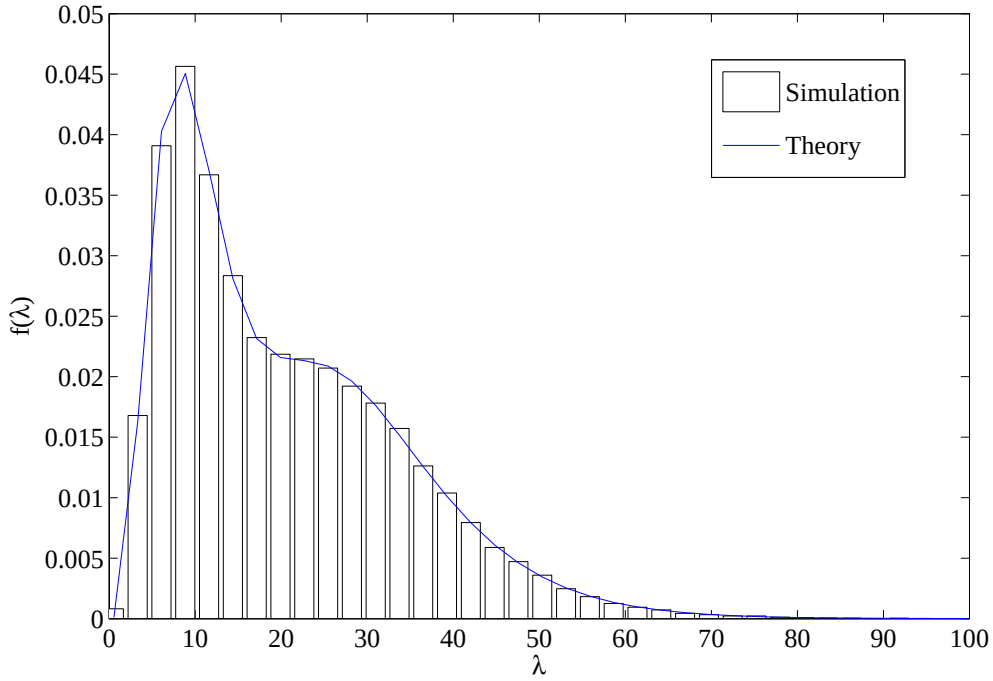

Figure 5.3: Analytical and simulated PDFs of the arbitrary eigenvalue of $\widetilde{\boldsymbol{U}}_t^{\dagger}\widetilde{\boldsymbol{A}}\widetilde{\boldsymbol{U}}_t$, with system parameters: $(3, 2, 3)$, $P_1 = P_2 = 10$dB, and $P_3 = 5$dB.

In Figure 5.5 we show the performance of the analytical and simulated ergodic capacity of the system with configuration $(3, 2, 3)$, when the $S \rightarrow D$ link strength varies. The results show that the capacity of the system improves with increases in the $S \rightarrow D$ signal strength due to diversity improvement. Note that when $P_3 = P_1$, the results in Sec. 5.2.2 are used to generate the analytical results. We also include the performance of the system without the direct link, obtained using the results in Sec. 5.2.3. Hence, Fig. 5.5 shows the performance gains of the system due to the inclusion of the direct link. Again the analytical results exactly match with the simulations.

Finally, Fig. 5.6 illustrates the performance of a $(3, 2, 3)$ system with a varying $R \rightarrow D$ link SNR. The SNRs have the relationship $P_1 = \alpha P_2 = 10$dB. The results show that when P_3 (the SNR of the $S \rightarrow D$ link) is high there is not much improvement in capacity even though P_2 is increased. Also, when P_3 is weak, the capacity improvement due to increases in P_2 is more obvious. As expected, this implies that when there is a good $S \rightarrow D$ link, there is less advantage in having an amplify-and-

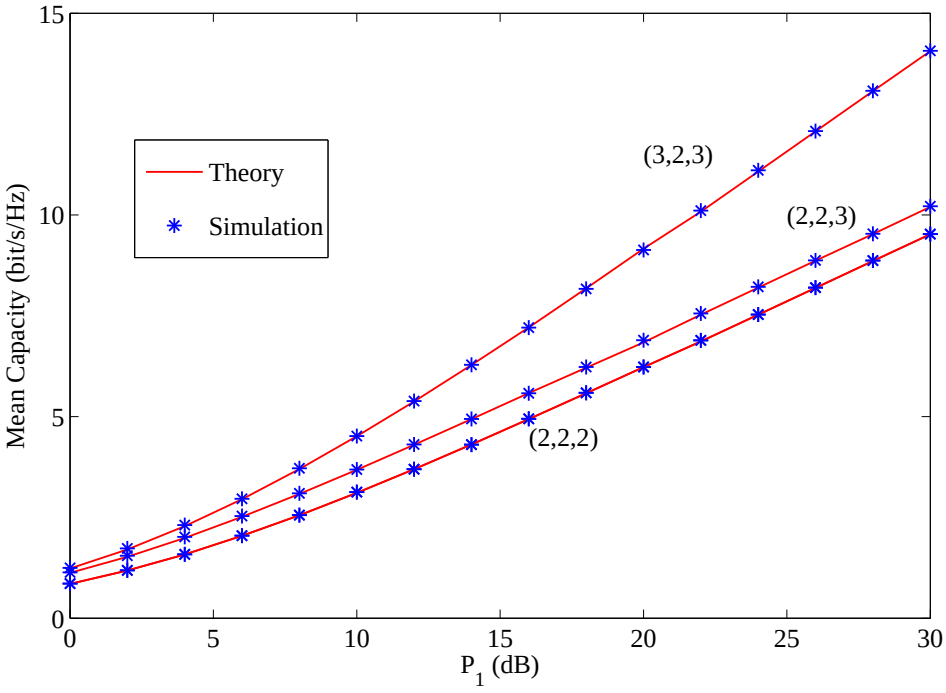

Figure 5.4: Analytical and simulated ergodic capacity values of the system with parameters: $P_1 = P_2 = 1.5P_3$.

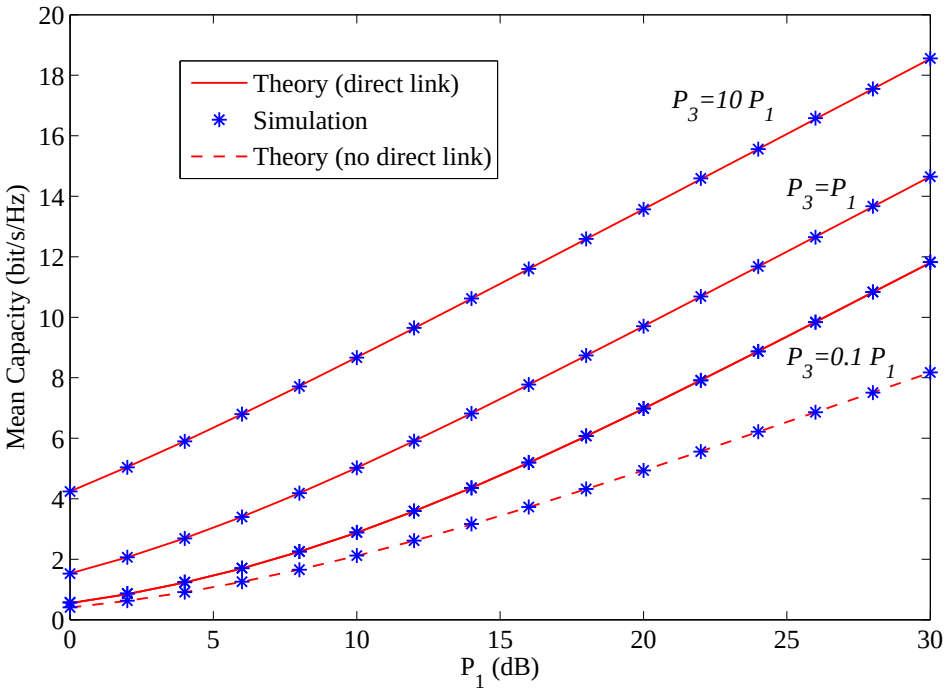

Figure 5.5: Analytical and simulated ergodic capacity values of the system with parameters: $(3, 2, 3)$ and $P_1 = P_2$.

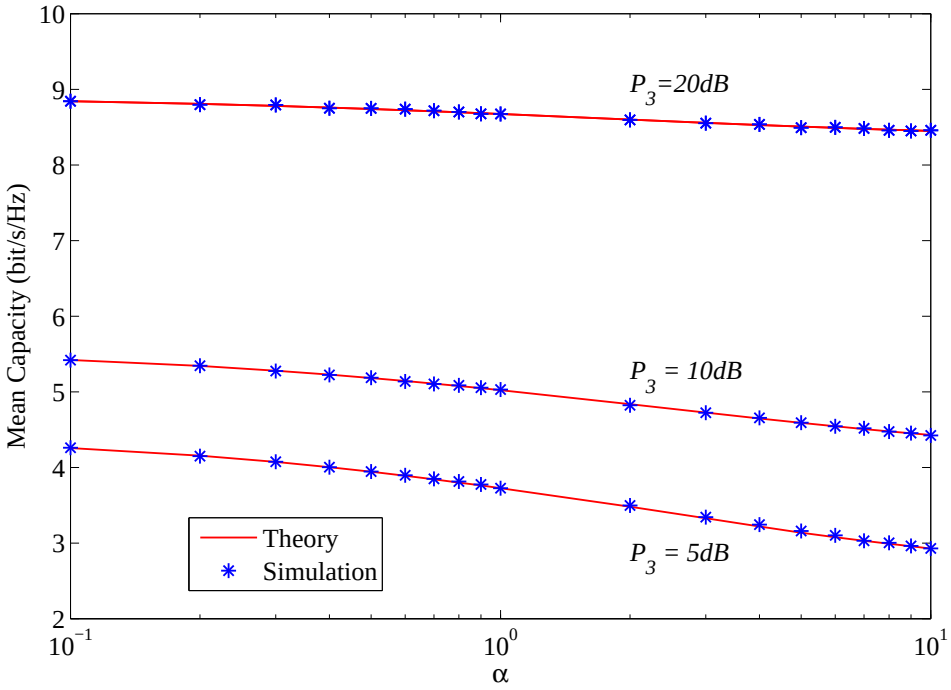

Figure 5.6: Analytical and simulated ergodic capacity values of a $(3, 2, 3)$ system vs. α, where $P_1 = \alpha P_2 = 10$dB. Also shown is the $S \rightarrow D$ link power, P_3.

forward relay. However, the relay is useful when the $S \rightarrow D$ link is weak.

5.5 Summary

In this chapter we have given an ergodic capacity analysis of an AF MIMO two-hop system including the source to destination link. We first derived an expression for the probability density function of the unordered eigenvalue of the system and from that, derived a closed-form expression for the ergodic capacity of the system. Note that the final capacity result requires a single numerical integral. This is undesirable, but is to be expected as capacity results for simpler MIMO relays [69] also involve one numerical integral. The analysis is validated by using simulations, and both results match exactly. We show that having the direct link improves the capacity due to diversity and quantify this improvement. Furthermore, we demonstrate that when there is a good $S \rightarrow D$ link, there is limited advantage in having an amplify-and-forward relay from a capacity vantage point. However, the relay is useful when

the $S \rightarrow D$ link is weak.

Chapter 6

MIMO Two-Hop Two-Relay Relaying Systems

In the previous chapter we analyzed an ergodic capacity of an AF MIMO two-hop one relay system including the source to destination link. Our main contribution in this chapter is to derive an exact expression for the capacity of an AF MIMO two-hop two relay system as shown in Fig. 6.1. We first develop an expression for the probability density function of an arbitrary eigenvalue of the system. Then, using this result, we derive an exact expression for the ergodic capacity of the system. We also present simulation results to validate the analysis. Further, we show that the ergodic capacity for a single relaying system without the direct link can be derived from the results in this chapter as a special case. These expressions are useful for gaining further insights into the effects of various system parameters on the performance of the wireless relaying system.

6.1 System Model

The source (S), relay (R_x), and destination (D) terminals are equipped with n_s, n_r and n_d antennas, respectively. We represent the number of antennas used in the system by the 3-tuple (n_s, n_r, n_d). For simplicity, it is assumed that both the relays have an equal numbers of antennas although this is not necessary for the

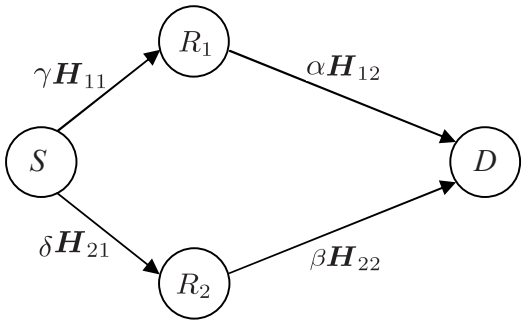

Figure 6.1: MIMO relay network topology.

analytical approach. In this model we assume that there is no direct link between the source and destination. This will be the case when the $S \rightarrow D$ distance is large and the relays are used to make communication possible, rather than to improve performance. During the first hop, the source terminal transmits (broadcasts) to the relays and in the second hop, the relay terminals transmit the amplified signal from the first hop to the destination. We assume that the normalized channel matrices for the source-to-relay ($S \rightarrow R_1$, $S \rightarrow R_2$), and relay-to-destination ($R_1 \rightarrow D$, $R_2 \rightarrow D$) links are given by $\boldsymbol{H}_{11}, \boldsymbol{H}_{21} \in \mathcal{C}^{n_r \times n_s}$, and $\boldsymbol{H}_{12}, \boldsymbol{H}_{22} \in \mathcal{C}^{n_d \times n_r}$, respectively. We also assume that the channels are frequency-flat and the entries of the channel matrices are ZMCSCG random variables of unit variance. Furthermore, we let that the relay terminal assist in the communication with the destination terminal using AF mode. In this mode, without decoding or demodulation the relay terminal, R_x amplifies the received observation corresponding to the signal from the source by a factor, a_x and retransmits it to the destination. In this analysis, a_x is chosen so that on average the total transmitted power from R_x is P_r. The received signal at the destination

after the two hops is then given by

$$\begin{aligned}\boldsymbol{y} &= \overbrace{\begin{bmatrix} \boldsymbol{H}_{12} & \boldsymbol{H}_{22} \end{bmatrix}}^{\boldsymbol{U}_1} \boldsymbol{\Gamma} \overbrace{\begin{bmatrix} \boldsymbol{H}_{11} \\ \boldsymbol{H}_{21} \end{bmatrix}}^{\boldsymbol{U}_2} \boldsymbol{x} \\ &\quad + \begin{bmatrix} \boldsymbol{H}_{12} & \boldsymbol{H}_{22} \end{bmatrix} \underbrace{\begin{bmatrix} \sigma\frac{\alpha}{a_1}\boldsymbol{I}_{n_r} & \boldsymbol{0} \\ \boldsymbol{0} & \sigma\frac{\beta}{a_2}\boldsymbol{I}_{n_r} \end{bmatrix}}_{\boldsymbol{D}} \underbrace{\begin{bmatrix} \boldsymbol{n}_1 \\ \boldsymbol{n}_2 \end{bmatrix}}_{\boldsymbol{w}} + \sigma\boldsymbol{n} \\ &\triangleq \boldsymbol{U}_1\boldsymbol{\Gamma}\boldsymbol{U}_2\boldsymbol{x} + \boldsymbol{U}_1\boldsymbol{D}\boldsymbol{w} + \sigma\boldsymbol{n} \end{aligned} \tag{6.1}$$

where

$$\boldsymbol{\Gamma} = \begin{bmatrix} \gamma\sqrt{\frac{P_t}{n_s}}\frac{\alpha}{a_1}\boldsymbol{I}_{n_r} & \boldsymbol{0} \\ \boldsymbol{0} & \delta\sqrt{\frac{P_t}{n_s}}\frac{\beta}{a_2}\boldsymbol{I}_{n_r} \end{bmatrix}.$$

In (6.1), the parameters γ^2, δ^2, α^2 and β^2 are the average powers of the $S\rightarrow R_1$, $S\rightarrow R_2$, $R_1\rightarrow D$ and $R_2\rightarrow D$ links, respectively, taking into account the different path loss and shadowing effects over the links. The variables $\sigma\boldsymbol{n}_1$, $\sigma\boldsymbol{n}_2$ and $\sigma\boldsymbol{n}$ are the noise vectors at R_1, R_2 and D, respectively, and $\sqrt{\frac{P_t}{n_s}}\boldsymbol{x}$ is the vector of transmit symbols. The transmit symbols are i.i.d. with $E\{\frac{P_t}{n_s}\boldsymbol{x}\boldsymbol{x}^\dagger\} = \frac{P_t}{n_s}\boldsymbol{I}_{n_s}$. Hence, the total transmit power is P_t. The noise at the relays and destination is modeled as ZMCSCG with $E\{\sigma^2\boldsymbol{n}_1\boldsymbol{n}_1^\dagger\} = \sigma^2\boldsymbol{I}_{n_r}$, $E\{\sigma^2\boldsymbol{n}_2\boldsymbol{n}_2^\dagger\} = \sigma^2\boldsymbol{I}_{n_r}$, and $E\{\sigma^2\boldsymbol{n}\boldsymbol{n}^\dagger\} = \sigma^2\boldsymbol{I}_{n_d}$. With this information, and defining $\boldsymbol{B} = (\sigma^2\boldsymbol{I}_{n_d} + \boldsymbol{U}_1\boldsymbol{D}^2\boldsymbol{U}_1^\dagger)^{1/2}$, the received signal at the destination can also be written as

$$\boldsymbol{y} = \boldsymbol{A}\boldsymbol{x} + \boldsymbol{B}\boldsymbol{v} \tag{6.2}$$

where $\boldsymbol{A} = \boldsymbol{U}_1\boldsymbol{\Gamma}\boldsymbol{U}_2$ and $\boldsymbol{v}$ is a normalized noise vector which has $\boldsymbol{I}_{n_d}$ as its covariance matrix.

6.2 Capacity Analysis

The ergodic capacity of the system can be calculated following [23] as below, (the factor 1/2 accounts for the fact that information is conveyed to the destination

terminal over two time slots [1]):

$$C = \frac{1}{2} E\left\{\log_2 \left| \boldsymbol{I}_{n_d} + \boldsymbol{A}\boldsymbol{A}^\dagger (\boldsymbol{B}\boldsymbol{B}^\dagger)^{-1} \right| \right\}. \tag{6.3}$$

To make the analysis possible, we have to assume that both relays receive the signal with the same SNR, i.e. $\gamma^2 = \delta^2$. This is reasonable when the link distances are similar and is the scenario which tends to maximize the relay capacity. When $\gamma^2 \neq \delta^2$ bounds and approximations are also developed later in the section.

Using the identity $\det(\boldsymbol{I} + \boldsymbol{A}\boldsymbol{B}) = \det(\boldsymbol{I} + \boldsymbol{B}\boldsymbol{A})$, and defining $\widetilde{\boldsymbol{U}}_1 \triangleq \boldsymbol{U}_1\boldsymbol{D}$, the capacity can be rewritten as

$$C = \frac{1}{2} E\left\{\log_2 \left| \boldsymbol{I}_{n_s} + \rho\, \boldsymbol{U}_2^\dagger \widetilde{\boldsymbol{U}}_1^\dagger (\sigma^2 \boldsymbol{I}_{n_d} + \widetilde{\boldsymbol{U}}_1 \widetilde{\boldsymbol{U}}_1^\dagger)^{-1} \widetilde{\boldsymbol{U}}_1 \boldsymbol{U}_2 \right| \right\} \tag{6.4}$$

where $\rho = \frac{\gamma^2 P_t}{\sigma^2 n_s}$. Assuming that $n_d < 2n_r$, and using the singular value decomposition $\widetilde{\boldsymbol{U}}_1 = \boldsymbol{E}_1 \boldsymbol{V} \boldsymbol{E}_2^\dagger$, the capacity can also be written as

$$\begin{aligned} C &= \frac{1}{2} E\left\{\log_2 \left| \boldsymbol{I}_{n_s} + \rho\, \widetilde{\boldsymbol{U}}_2^\dagger \boldsymbol{V}^\dagger (\sigma^2 \boldsymbol{I}_{n_d} + \boldsymbol{V}\boldsymbol{V}^\dagger)^{-1} \boldsymbol{V} \widetilde{\boldsymbol{U}}_2 \right| \right\} \\ &= \frac{\min(n_d, n_s)}{2\,\ln(2)} \int_0^\infty \ln(1+\rho\lambda)\, f(\lambda)\, d\lambda \end{aligned} \tag{6.5}$$

where $\widetilde{\boldsymbol{U}}_2 = \boldsymbol{E}_2^\dagger \boldsymbol{U}_2$, λ denotes the non-zero arbitrary eigenvalue of $\widetilde{\boldsymbol{U}}_2^\dagger \boldsymbol{V}^\dagger (\sigma^2 \boldsymbol{I}_{n_d} + \boldsymbol{V}\boldsymbol{V}^\dagger)^{-1}\ \boldsymbol{V}\widetilde{\boldsymbol{U}}_2$ and $f(\lambda)$ is the PDF of λ. For this case, $n_d < 2n_r$, the matrix $\widetilde{\boldsymbol{U}}_1^\dagger \widetilde{\boldsymbol{U}}_1$ is pseudo-Wishart [70]. Let $\widetilde{\boldsymbol{U}}_1^\dagger \widetilde{\boldsymbol{U}}_1$ have ordered non-zero eigenvalues, $\nu_1 > \ldots > \nu_{n_d} > 0$. The density of the unordered nonzero eigenvalues of $\widetilde{\boldsymbol{U}}_1^\dagger \widetilde{\boldsymbol{U}}_1$ for the pseudo-Wishart case is given in [67] for the case when all of the diagonal elements of matrix, $\boldsymbol{D}^2$, are distinct. However, in this situation the diagonal elements of the matrix $\boldsymbol{D}^2$ in (6.1) are not all distinct. When $\boldsymbol{D}^2$ does not have all distinct values, the PDF, $f(\boldsymbol{\nu})$, of the unordered nonzero eigenvalues of $\widetilde{\boldsymbol{U}}_1^\dagger \widetilde{\boldsymbol{U}}_1$ can be obtained by using the identities on multiple derivatives given in Sec. 5.2.1. These derivatives are then used to derive $f(\boldsymbol{\nu})$ using the method given in *Lemma 2* of [48]. The lemma basically explains a derivation of $f(\boldsymbol{\nu})$ for the general case when $\boldsymbol{D}^2$ does not have all distinct values. With this approach, $f(\boldsymbol{\nu})$ can be calculated as

$$f(\boldsymbol{\nu}) = \frac{\prod_{k<p}^{n_d} (\nu_p - \nu_k)\, |\boldsymbol{K}|}{n_d!\, \Gamma_{n_d}(n_d) \Gamma_{n_r}(n_r) \Gamma_{n_r}(n_r) (w_2 - w_1)^{n_r{}^2}}. \tag{6.6}$$

In (6.6), $\Gamma_{n_s}(n_d) = \prod_{k=1}^{n_s} \Gamma(n_d - k + 1)$ and $\boldsymbol{K}$ is a $2n_r \times 2n_r$ matrix with entries given as

$$\boldsymbol{K}_{i,j} = \begin{cases} (j - n_r + i)_{n_r - i}\, w_1^{j-n_r+i-1}, & i = 1, \ldots, n_r,\ j = 1, \ldots, 2n_r - n_d \\ e^{-\nu_{j-2n_r+n_d}/w_1} & \\ \times \sum_{k=0}^{n_r-i} \frac{(n_r-i)!}{k!(n_r-i-k)!} (n_r - n_d + i)_{n_r-i-k} & i = 1, \ldots, n_r, \\ \quad \times \nu_{j-2n_r+n_d}^{k} w_1^{n_r-n_d+i-k-1}, & j = 2n_r - n_d + 1, \ldots, 2n_r \\ (j - 2n_r + i)_{2n_r - i}\, w_2^{j-2n_r+i-1}, & i = n_r + 1, \ldots, 2n_r, \\ & j = 1, \ldots, 2n_r - n_d \\ e^{-\nu_{j-2n_r+n_d}/w_2} & \\ \times \sum_{k=0}^{2n_r-i} \frac{(2n_r-i)!}{k!(2n_r-i-k)!} (-n_d + i)_{2n_r-i-k} & i = n_r + 1, \ldots, 2n_r, \\ \quad \times \nu_{j-2n_r+n_d}^{k} w_2^{-n_d+i-k-1}, & j = 2n_r - n_d + 1, \ldots, 2n_r \end{cases}, \tag{6.7}$$

where $w_1 = \sigma^2\alpha^2/a_1^2$ and $w_2 = \sigma^2\beta^2/a_2^2$. Let $\boldsymbol{P} = \boldsymbol{V}^\dagger(\sigma^2 \boldsymbol{I}_{n_d} + \boldsymbol{V}\boldsymbol{V}^\dagger)^{-1}\boldsymbol{V}$, where $\boldsymbol{V}$ is defined in (6.5). Then for $n_d < 2n_r$, $\boldsymbol{P}$ can be given as

$$\boldsymbol{P} = \text{diag}\left\{\mu_1, \ldots, \mu_{n_d}, \underbrace{0, \ldots, 0}_{2n_r - n_d}\right\}, \tag{6.8}$$

where $\mu_k = \frac{\nu_k}{\nu_k + \sigma^2}$. Then, the capacity can also be expressed as

$$C = \frac{1}{2} E\left\{\log_2 \left| \boldsymbol{I}_{n_s} + \rho \widehat{\boldsymbol{U}}_2^\dagger \widehat{\boldsymbol{P}} \widehat{\boldsymbol{U}}_2 \right| \right\}, \tag{6.9}$$

where $\widehat{\boldsymbol{U}}_2 \in \mathcal{C}^{n_d \times n_s}$ has i.i.d ZMCSCG entries with unit variance and $\widehat{\boldsymbol{P}} = \text{diag}\{\mu_1, \ldots, \mu_{n_d}\}$. Note that $\widehat{\boldsymbol{P}}$ and $\widehat{\boldsymbol{U}}_2$ are simply re-sized versions of $\boldsymbol{P}$ and $\widetilde{\boldsymbol{U}}_2$. The matrix $\widehat{\boldsymbol{P}}^{1/2}\widehat{\boldsymbol{U}}_2\widehat{\boldsymbol{U}}_2^\dagger\widehat{\boldsymbol{P}}^{1/2}$ is central complex Wishart when $n_d \leqslant n_s$ and central complex pseudo-Wishart when $n_d > n_s$ [50]. Hence, the density function, $f(\lambda)$ in (6.5) will be different for the cases $n_d \leqslant n_s$ and $n_d > n_s$. Therefore, the ergodic capacity for the system needs to be evaluated separately for those cases, and they are given below. The derivation of $f(\lambda)$ and the capacity expressions for the different cases given below involves a complex series of steps. This is given in a fairly dense form.

However an overview of the results is given in Sec. 6.4 to clarify the application of the relevant formulae.

6.2.1 Capacity Analysis for the Case $n_d \leqslant n_s$

For the case $n_d \leqslant n_s$, the matrix $\widehat{\boldsymbol{P}}^{1/2}\widehat{\boldsymbol{U}}_2\widehat{\boldsymbol{U}}_2^{\dagger}\widehat{\boldsymbol{P}}^{1/2}$ is central complex Wishart [50]. Then, using the result in [67] for the PDF of the non-zero arbitrary eigenvalue for the Wishart case, the conditional PDF of a non-zero arbitrary eigenvalue of $\widehat{\boldsymbol{P}}^{1/2}\widehat{\boldsymbol{U}}_2\widehat{\boldsymbol{U}}_2^{\dagger}\widehat{\boldsymbol{P}}^{1/2}$ can be obtained as

$$f(\lambda|\boldsymbol{\mu}) = \frac{\sum_{r=1}^{n_d}\left|\boldsymbol{G}^1\right|}{n_d\,\Gamma_{n_d}(n_s)\prod_{k=1}^{n_d}\mu_k^{n_s-n_d+1}\prod_{k<p}^{n_d}(\mu_p-\mu_k)}. \tag{6.10}$$

In (6.10), $\boldsymbol{G}^1$ is a $n_d \times n_d$ matrix with entries

$$\boldsymbol{G}^1_{i,j} = \begin{cases} \lambda^{n_s-n_d+i-1}e^{-\lambda/\mu_j}, & \text{for } i=r,\ j=1,\ldots,n_d \\ \frac{\Gamma(n_s-n_d+i)}{\mu_j^{n_d-n_s-i}}, & \text{for } i\neq r,\ j=1,\ldots,n_d \end{cases}. \tag{6.11}$$

Then the conditional PDF $f(\lambda|\boldsymbol{\nu})$ can be obtained by substituting $\mu_k = \left(\frac{\nu_k}{\sigma^2+\nu_k}\right)$ in (6.10). Thus the joint PDF $f(\lambda,\boldsymbol{\nu}) = f(\boldsymbol{\nu})f(\lambda|\boldsymbol{\nu})$ can be written as

$$\begin{aligned} f(\lambda,\boldsymbol{\nu}) &= \frac{1}{n_d\,n_d!\,\sigma^{n_d(n_d-1)}\,\Gamma_{n_d}(n_s)\,\Gamma_{n_d}(n_d)\,\Gamma_{n_r}(n_r)\,\Gamma_{n_r}(n_r)\,(w_2-w_1)^{n_r^2}} \\ &\quad\times\sum_{r=1}^{n_d}\prod_{k=1}^{n_d}\frac{(\sigma^2+\nu_k)^{n_s}}{\nu_k^{n_s-n_d+1}}\left|\boldsymbol{K}\right|\left|\boldsymbol{G}^1\right| \\ &\triangleq C_0\sum_{r=1}^{n_d}\prod_{k=1}^{n_d}\xi(\nu_k)\left|\boldsymbol{K}\right|\left|\boldsymbol{G}^1\right|. \end{aligned} \tag{6.12}$$

Density $f(\lambda)$ can then be found by integrating over all ν_k by using the method described in *Lemma 2* of [32] as,

$$\begin{aligned} f(\lambda) &= C_0\sum_{r=1}^{n_d}\int_0^{\infty}\cdots\int_0^{\infty}\prod_{k=1}^{n_d}\xi(\nu_k)\left|\boldsymbol{K}\right|\left|\boldsymbol{G}^1\right|d\nu_1\ldots d\nu_{n_d} \\ &= \underbrace{C_0\,n_d!}_{C_1}\sum_{r=1}^{n_d}|\boldsymbol{\Psi}| \end{aligned} \tag{6.13}$$

where

$$C_1 = \frac{1}{n_d\,\sigma^{n_d(n_d-1)}\,\Gamma_{n_d}(n_s)\,\Gamma_{n_d}(n_d)\,\Gamma_{n_r}(n_r)\,\Gamma_{n_r}(n_r)\,(w_2-w_1)^{n_r^2}}. \tag{6.14}$$

In (6.13), $\mathbf{\Psi}$ is a $2n_r \times 2n_r$ matrix with entries given as

$$\mathbf{\Psi}_{i,j} = \begin{cases} (j-n_r+i)_{n_r-i}\, w_1^{j-n_r+i-1}, & i=1,\ldots,n_r,\ j=1,\ldots,2n_r-n_d \\ (j-2n_r+i)_{2n_r-i}\, w_2^{j-2n_r+i-1}, & i=n_r+1,\ldots,2n_r, \\ & j=1,\ldots,2n_r-n_d \\ \sum_{k=0}^{n_r-i} \frac{(n_r-i)!}{k!(n_r-i-k)!}(n_r-n_d+i)_{n_r-i-k} & i=1,\ldots,n_r, \\ \quad \times w_1^{n_r-n_d+i-k-1}\Gamma(n_s+j-2n_r) & j=2n_r-n_d+1,\ldots,2n_r \text{ and} \\ \quad \times I_A(j,k,w_1), & j \neq r+2n_r-n_d \\ \sum_{k=0}^{2n_r-i} \frac{(2n_r-i)!}{k!(2n_r-i-k)!}(-n_d+i)_{2n_r-i-k} & i=n_r+1,\ldots,2n_r, \\ \quad \times w_2^{-n_d+i-k-1}\Gamma(n_s+j-2n_r) & j=2n_r-n_d+1,\ldots,2n_r \text{ and} \\ \quad \times I_A(j,k,w_2), & j \neq r+2n_r-n_d \\ \sum_{k=0}^{n_r-i} \frac{(n_r-i)!}{k!(n_r-i-k)!}(n_r-n_d+i)_{n_r-i-k} & i=1,\ldots,n_r, \\ \quad \times w_1^{n_r-n_d+i-k-1}\lambda^{n_s+j-2n_r-1} & j=2n_r-n_d+1,\ldots,2n_r \text{ and} \\ \quad \times I_B(k,w_1), & j=r+2n_r-n_d \\ \sum_{k=0}^{2n_r-i} \frac{(2n_r-i)!}{k!(2n_r-i-k)!}(-n_d+i)_{2n_r-i-k} & i=n_r+1,\ldots,2n_r, \\ \quad \times w_2^{-n_d+i-k-1}\lambda^{n_s+j-2n_r-1} & j=2n_r-n_d+1,\ldots,2n_r \text{ and} \\ \quad \times I_B(k,w_2), & j=r+2n_r-n_d \end{cases}, \tag{6.15}$$

where

$$I_A(j,k,w) = \sum_{p=0}^{2n_r-j} \frac{(2n_r-j)!}{p!(2n_r-j-p)!}\sigma^{2(2n_r-j-p)} w^{n_d+j+k+p-2n_r}\Gamma(n_d+j+k+p-2n_r), \tag{6.16}$$

$$I_B(k,w) = \sum_{p=0}^{n_s} \frac{n_s!}{p!(n_s-p)!}\sigma^{2(n_s-p)} e^{-\lambda} 2(\lambda\sigma^2 w)^{(n_d+p-n_s+k)/2} K_{n_d+p-n_s+k}(2\sqrt{\lambda\sigma^2/w}), \tag{6.17}$$

and K_x is the modified Bessel function of the second kind. Finally, using the Laplace expansion of (6.13), the density function of the non-zero arbitrary eigenvalue of $\widetilde{\boldsymbol{U}}_2^{\dagger}\boldsymbol{V}^{\dagger}(\sigma^2\boldsymbol{I}_{n_d}+\boldsymbol{V}\boldsymbol{V}^{\dagger})^{-1}\boldsymbol{V}\widetilde{\boldsymbol{U}}_2$ is calculated as

$$f(\lambda) = C_1 \sum_{i=1}^{2n_r}\sum_{j=1}^{n_d}(-1)^{i+j+2n_r-n_d}\left|\boldsymbol{Q}_{i,j+2n_r-n_d}\right| A_\lambda(i,j). \tag{6.18}$$

In (6.18), $\boldsymbol{Q}_{k,l}$ denotes the $(k,l)^{\text{th}}$ minor of $\boldsymbol{Q}$ with elements given as

$$\boldsymbol{Q}_{i,j} = \begin{cases} (j-n_r+i)_{n_r-i}\, w_1^{j-n_r+i-1}, & i=1,\ldots,n_r, \\ & j=1,\ldots,2n_r-n_d \\ (j-2n_r+i)_{2n_r-i}\, w_2^{j-2n_r+i-1}, & i=n_r+1,\ldots,2n_r, \\ & j=1,\ldots,2n_r-n_d \\ \sum_{k=0}^{n_r-i}\frac{(n_r-i)!}{k!(n_r-i-k)!}(n_r-n_d+i)_{n_r-i-k} & i=1,\ldots,n_r, \\ \quad w_1^{n_r-n_d+i-k-1}\Gamma(n_s+j-2n_r)I_A(j,k,w_1), & j=2n_r-n_d+1,\ldots,2n_r \\ \sum_{k=0}^{2n_r-i}\frac{(2n_r-i)!}{k!(2n_r-i-k)!}(-n_d+i)_{2n_r-i-k} & i=n_r+1,\ldots,2n_r, \\ \quad w_2^{-n_d+i-k-1}\Gamma(n_s+j-2n_r)I_A(j,k,w_2), & j=2n_r-n_d+1,\ldots,2n_r \end{cases}, \tag{6.19}$$

and $A_\lambda(i,j)$ is given as

$$A_\lambda(i,j) = \begin{cases} \sum_{k=0}^{n_r-i}\frac{(n_r-i)!}{k!(n_r-i-k)!}(n_r-n_d+i)_{n_r-i-k} & \\ \quad w_1^{n_r-n_d+i-k-1}\lambda^{n_s+j-n_d-1}I_B(k,w_1), & \text{for } i=1,\ldots,n_r \\ \sum_{k=0}^{2n_r-i}\frac{(2n_r-i)!}{k!(2n_r-i-k)!}(-n_d+i)_{2n_r-i-k} & \\ \quad w_2^{-n_d+i-k-1}\lambda^{n_s+j-n_d-1}I_B(k,w_2), & \text{for } i=n_r+1,\ldots,2n_r \end{cases}. \tag{6.20}$$

Now, substituting (6.18) into (6.5), the ergodic capacity of the system for the case $n_d \leqslant n_s$ can be finally written as

$$C = \frac{n_d\, C_1}{2\,\ln(2)}\sum_{i=1}^{2n_r}\sum_{j=1}^{n_d}(-1)^{i+j+2n_r-n_d}\left|\boldsymbol{Q}_{i,j+2n_r-n_d}\right|\int_0^\infty \ln(1+\rho\lambda)\, A_\lambda(i,j)\, d\lambda, \tag{6.21}$$

where C_1, $\boldsymbol{Q}$ and $A_\lambda(i,j)$ are given in (6.14), (6.19) and (6.20), respectively.

6.2.2 Capacity Analysis for the Case $n_d > n_s$

For the case $n_d < n_s$, the matrix $\widehat{\boldsymbol{P}}^{1/2}\widehat{\boldsymbol{U}}_2\widehat{\boldsymbol{U}}_2^{\dagger}\widehat{\boldsymbol{P}}^{1/2}$ is central complex pseudo-Wishart [50]. Then using the result in [67] for the PDF of the non-zero arbitrary eigenvalue for the pseudo-Wishart case, the conditional PDF of a non-zero arbitrary eigenvalue of $\widehat{\boldsymbol{P}}^{1/2}\widehat{\boldsymbol{U}}_2\widehat{\boldsymbol{U}}_2^{\dagger}\widehat{\boldsymbol{P}}^{1/2}$ can be obtained as

$$\begin{aligned} f(\lambda|\boldsymbol{\mu}) &= \frac{1}{n_s\Gamma_{n_s}(n_s)\prod_{k=1}^{n_d}\mu_k^{n_s-n_d+1}\left|\mu_i^{j-1}\right|}\sum_{r=1}^{n_s}\left|\widetilde{\boldsymbol{G}}\right| \\ &= \frac{1}{n_s\Gamma_{n_s}(n_s)\prod_{k=1}^{n_d}\mu_k^{n_s-n_d+1}\prod_{k<p}^{n_d}(\mu_p-\mu_k)}\sum_{r=1}^{n_s}\left|\widetilde{\boldsymbol{G}}\right|. \end{aligned} \tag{6.22}$$

In (6.22), $\widetilde{\boldsymbol{G}}$ is a $n_d \times n_d$ matrix with entries

$$\widetilde{\boldsymbol{G}}_{i,j} = \begin{cases} \mu_j^{n_s-n_d+i}, & \text{for } i = 1,\ldots,n_d-n_s,\ j=1,\ldots,n_d \\ \lambda^{n_s-n_d+i-1}e^{-\lambda/\mu_j}, & \text{for } i > n_d-n_s, \text{ and } i = n_d-n_s+r,\ j=1,\ldots,n_d \\ \frac{\Gamma(i-n_d+n_s)}{\mu_j^{n_d-n_s-i}}, & \text{for } i > n_d-n_s, \text{ and } i \neq n_d-n_s+r,\ j=1,\ldots,n_d \end{cases}. \tag{6.23}$$

Then, the conditional PDF $f(\lambda|\boldsymbol{\nu})$ can be obtained by substituting $\mu_k = \left(\frac{\nu_k}{\sigma^2+\nu_k}\right)$ into (6.22). Thus the joint PDF $f(\lambda,\boldsymbol{\nu}) = f(\boldsymbol{\nu})f(\lambda|\boldsymbol{\nu})$ can be written as

$$\begin{aligned} f(\lambda,\boldsymbol{\nu}) &= \frac{1}{n_s\, n_d!\,\sigma^{n_d(n_d-1)}\,\Gamma_{n_s}(n_s)\,\Gamma_{n_d}(n_d)\,\prod_{k=1}^{n_r}k!\prod_{k=1}^{n_r}k!\,(w_2-w_1)^{n_r^2}} \\ &\quad\times\sum_{r=1}^{n_s}\prod_{k=1}^{n_d}\frac{(\sigma^2+\nu_k)^{n_s}}{\nu_k^{n_s-n_d+1}}\left|\boldsymbol{K}\right|\left|\widetilde{\boldsymbol{G}}\right| \\ &\triangleq C_{01}\sum_{r=1}^{n_s}\prod_{k=1}^{n_d}\xi(\nu_k)\left|\boldsymbol{K}\right|\left|\widetilde{\boldsymbol{G}}\right|. \end{aligned} \tag{6.24}$$

By integrating over all ν_k, $f(\lambda)$ can be found by using the method described in *Lemma 2* of [32] as,

$$f(\lambda) = C_{01}\sum_{r=1}^{n_s}\int_0^{\infty}\cdots\int_0^{\infty}\prod_{k=1}^{n_d}\xi(\nu_k)\left|\boldsymbol{K}\right|\left|\widetilde{\boldsymbol{G}}\right|d\nu_1\ldots d\nu_{n_d} = \underbrace{C_{01}n_d!}_{C_2}\sum_{r=1}^{n_s}\left|\widetilde{\boldsymbol{\Psi}}\right| \tag{6.25}$$

where

$$C_2 = \frac{1}{n_s\,\sigma^{n_d(n_d-1)}\,\Gamma_{n_s}(n_s)\,\Gamma_{n_d}(n_d)\,\prod_{k=1}^{n_r}k!\prod_{k=1}^{n_r}k!\,(w_2-w_1)^{n_r^2}}. \tag{6.26}$$

In (6.25), $\widetilde{\mathbf{\Psi}}$ is a $2n_r \times 2n_r$ matrix with entries given as

$$\widetilde{\mathbf{\Psi}}_{i,j} = \begin{cases} (j-n_r+i)_{n_r-i}\, w_1^{j-n_r+i-1}, & i=1,\ldots,n_r,\ j=1,\ldots,2n_r-n_d \\ (j-2n_r+i)_{2n_r-i}\, w_2^{j-2n_r+i-1}, & i=n_r+1,\ldots,2n_r, \\ & j=1,\ldots,2n_r-n_d \\ \sum_{k=0}^{n_r-i} \frac{(n_r-i)!}{k!(n_r-i-k)!}(n_r-n_d+i)_{n_r-i-k} & i=1,\ldots,n_r, \\ \quad \times w_1^{n_r-n_d+i-k-1} I_A(j,k,w_1), & j=2n_r-n_d+1,\ldots,2n_r-n_s \\ \sum_{k=0}^{2n_r-i} \frac{(2n_r-i)!}{k!(2n_r-i-k)!}(-n_d+i)_{2n_r-i-k} & i=n_r+1,\ldots,2n_r, \\ \quad \times w_2^{-n_d+i-k-1} I_A(j,k,w_2), & j=2n_r-n_d+1,\ldots,2n_r-n_s \\ \sum_{k=0}^{n_r-i} \frac{(n_r-i)!}{k!(n_r-i-k)!}(n_r-n_d+i)_{n_r-i-k} & i=1,\ldots,n_r, \\ \quad \times w_1^{n_r-n_d+i-k-1}\Gamma(n_s+j-2n_r) & j>2n_r-n_s, \\ \quad \times I_A(j,k,w_1), & \text{and } j\neq 2n_r-n_s+r \\ \sum_{k=0}^{2n_r-i} \frac{(2n_r-i)!}{k!(2n_r-i-k)!}(-n_d+i)_{2n_r-i-k} & i=n_r+1,\ldots,2n_r, \\ \quad \times w_2^{-n_d+i-k-1}\Gamma(n_s+j-2n_r) & j>2n_r-n_s, \\ \quad \times I_A(j,k,w_2), & \text{and } j\neq 2n_r-n_s+r \\ \sum_{k=0}^{n_r-i} \frac{(n_r-i)!}{k!(n_r-i-k)!}(n_r-n_d+i)_{n_r-i-k} & i=1,\ldots,n_r, \\ \quad \times w_1^{n_r-n_d+i-k-1}\lambda^{n_s+j-2n_r-1} & j>2n_r-n_s, \\ \quad \times I_B(k,w_1), & \text{and } j=2n_r-n_s+r \\ \sum_{k=0}^{2n_r-i} \frac{(2n_r-i)!}{k!(2n_r-i-k)!}(-n_d+i)_{2n_r-i-k} & i=n_r+1,\ldots,2n_r, \\ \quad \times w_2^{-n_d+i-k-1}\lambda^{n_s+j-2n_r-1} & j>2n_r-n_s, \\ \quad \times I_B(k,w_2), & \text{and } j=2n_r-n_s+r \end{cases}, \tag{6.27}$$

where $I_A(j,k,w)$ and $I_B(k,w)$ are given in (6.16) and (6.17), respectively. Then, using the Laplace expansion of (6.25), the density function of the non-zero arbitrary

eigenvalue of $\widetilde{\boldsymbol{U}}_2^{\dagger}\boldsymbol{V}^{\dagger}(\sigma^2\boldsymbol{I}_{n_d}+\boldsymbol{V}\boldsymbol{V}^{\dagger})^{-1}\boldsymbol{V}\widetilde{\boldsymbol{U}}_2$ for the case $n_d > n_s$ is calculated as

$$f(\lambda) = C_2 \sum_{i=1}^{2n_r}\sum_{j=1}^{n_s}(-1)^{i+j+2n_r-n_s}\left|\widetilde{\boldsymbol{Q}}_{i,j+2n_r-n_s}\right|\widetilde{A}_{\lambda}(i,j). \tag{6.28}$$

In (6.28), $\widetilde{\boldsymbol{Q}}_{x,y}$ denotes the $(x,y)^{\text{th}}$ minor of $\widetilde{\boldsymbol{Q}}$ with elements given in (6.29) and

$$\widetilde{\boldsymbol{Q}}_{i,j} = \begin{cases} (j-n_r+i)_{n_r-i}\, w_1^{j-n_r+i-1}, & i=1,\ldots,n_r,\ j=1,\ldots,2n_r-n_d \\ (j-2n_r+i)_{2n_r-i} \times w_2^{j-2n_r+i-1}, & i=n_r+1,\ldots,2n_r, \\ & j=1,\ldots,2n_r-n_d \\ \sum_{k=0}^{n_r-i}\frac{(n_r-i)!}{k!(n_r-i-k)!}(n_r-n_d+i)_{n_r-i-k} \times w_1^{n_r-n_d+i-k-1} \times I_A(j,k,w_1), & i=1,\ldots,n_r, \\ & j=2n_r-n_d+1,\ldots,2n_r-n_s \\ \sum_{k=0}^{2n_r-i}\frac{(2n_r-i)!}{k!(2n_r-i-k)!}(-n_d+i)_{2n_r-i-k} \times w_2^{-n_d+i-k-1} \times I_A(j,k,w_2), & i=n_r+1,\ldots,2n_r, \\ & j=2n_r-n_d+1,\ldots,2n_r-n_s \\ \sum_{k=0}^{n_r-i}\frac{(n_r-i)!}{k!(n_r-i-k)!}(n_r-n_d+i)_{n_r-i-k} \times w_1^{n_r-n_d+i-k-1} \times \Gamma(n_s+j-2n_r) I_A(j,k,w_1), & i=1,\ldots,n_r, \\ & j>2n_r-n_s \\ \sum_{k=0}^{2n_r-i}\frac{(2n_r-i)!}{k!(2n_r-i-k)!}(-n_d+i)_{2n_r-i-k} \times w_2^{-n_d+i-k-1} \times \Gamma(n_s+j-2n_r), I_A(j,k,w_2) & i=n_r+1,\ldots,2n_r, \\ & j>2n_r-n_s \end{cases}, \tag{6.29}$$

$\widetilde{A}_{\lambda}(i,j)$ is defined as

$$\widetilde{A}_{\lambda}(i,j) = \begin{cases} \sum_{k=0}^{n_r-i}\frac{(n_r-i)!}{k!(n_r-i-k)!}(n_r-n_d+i)_{n_r-i-k} \times w_1^{n_r-n_d+i-k-1}\lambda^{j-1} I_B(k,w_1), & \text{for } i=1,\ldots,n_r \\ \sum_{k=0}^{2n_r-i}\frac{(2n_r-i)!}{k!(2n_r-i-k)!}(-n_d+i)_{2n_r-i-k} \times w_2^{-n_d+i-k-1}\lambda^{j-1} I_B(k,w_2), & \text{for } i=n_r+1,\ldots,2n_r \end{cases}. \tag{6.30}$$

Now, substituting (6.28) in (6.5), the ergodic capacity of the system for the case $n_d > n_s$ can be finally written as

$$C = \frac{n_s\, C_2}{2\,\ln(2)} \sum_{i=1}^{2n_r} \sum_{j=1}^{n_s} (-1)^{i+j+2n_r-n_s} \left| \widetilde{\boldsymbol{Q}}_{i,j+2n_r-n_s} \right| \times \int_0^\infty \ln(1+\rho\lambda)\, \widetilde{A}_\lambda(i,j)\, d\lambda, \tag{6.31}$$

where C_2, $\widetilde{\boldsymbol{Q}}$ and $\widetilde{A}_\lambda(i,j)$ are given in (6.26), (6.29) and (6.30), respectively.

Note that the final capacity result requires a single numerical integral as in Chapter 5. This is undesirable, but is to be expected as capacity results for simpler MIMO relays also involve one numerical integral.

Special Case: Ergodic Capacity of a (1,1,1) System

For the special case of a (1,1,1) system, the capacity expression given in (6.21) reduces to

$$\begin{aligned} C = &\int_0^\infty \frac{-\ln(1+\rho\lambda)e^{-\lambda}}{\ln(2)(w_2-w_1)} \left(\sigma^2 K_0(2\sqrt{\lambda\sigma^2/w_1}) + (\lambda\sigma^2 w_1)^{1/2} K_1(2\sqrt{\lambda\sigma^2/w_1})\right) d\lambda \\ &+ \int_0^\infty \frac{\ln(1+\rho\lambda)e^{-\lambda}}{\ln(2)(w_2-w_1)} \left(\sigma^2 K_0(2\sqrt{\lambda\sigma^2/w_2}) + (\lambda\sigma^2 w_2)^{1/2} K_1(2\sqrt{\lambda\sigma^2/w_2})\right) d\lambda. \end{aligned} \tag{6.32}$$

Note that even for this special case, a closed form expression is difficult to obtain and so the capacity result requires numerical integration.

The ergodic capacity analysis we have just derived is only valid when $\gamma^2 = \delta^2$, but when $\gamma^2 \neq \delta^2$, an approximation, a lower bound and an upper bound for the capacity can be obtained by replacing γ and δ by $\frac{\gamma+\delta}{2}$, $\min(\gamma,\delta)$ and $\max(\gamma,\delta)$, respectively. These approximations and bounds are quite accurate unless $\gamma^2 \gg \delta^2$ or $\gamma^2 \ll \delta^2$. However, in these cases it is usually preferable to use a single relay system. Hence the analysis is useful for most cases of interest. This is shown in more detail in Sec. 6.5.

Using the results given in (6.21) and (6.31), the ergodic capacity for a single MIMO relaying system can be obtained as a special case of this more general result. The results for the single MIMO relaying system are given in the following section.

6.3 Ergodic Capacity for a Single Relaying System

The ergodic capacity for a single MIMO relaying system can be obtained from the results given in (6.21) and (6.31). By letting $\beta^2 = 0$ (removing the link between the source and destination through R_2) in (6.21) and (6.31), the capacity for a single relaying system can be calculated. For the case $n_d \leqslant n_s < 2n_r$, setting $\beta^2 = 0$ in (6.21) gives the capacity of a single relaying system as

$$C = \frac{n_d C_1}{2\,\ln(2)} \sum_{i=1}^{2n_r} \sum_{j=1}^{n_d} (-1)^{i+j+2n_r-n_d} \left| \boldsymbol{Q}_{i,j+2n_r-n_d} \right| \times \int_0^\infty \ln(1+\rho\lambda)\, A_\lambda(i,j)\, d\lambda. \tag{6.33}$$

In (6.33), $\boldsymbol{Q}$ and $A_\lambda(i,j)$ have much simpler results than (6.19), (6.20) and they are given in (6.34) and (6.35), respectively. Similarly, the capacity for a single relaying system for the case $n_d > n_s$ can be calculated using (6.31).

6.4 Overview of Analysis

The results derived above involve a complex series of steps. Hence, this subsection briefly outlines what we have done and the results derived in this chapter. The main objective of this chapter is to analyze the ergodic capacity of an AF MIMO two-hop two-relay system without the direct link. We have derived the ergodic capacity expressions for different situations from the PDF of the arbitrary eigenvalue. Our derived results are summarized in Fig. 6.2.

6.5 Results and Discussion

We now validate these results by using Monte Carlo simulations. Here we set $P_t = P_r = \sigma^2 = 1$, and thus the relays' amplification factors are given by $a_1 = \sqrt{n_r(\gamma^2+1)}$ and $a_2 = \sqrt{n_r(\delta^2+1)}$. We choose the value of a_x so that on average

$$\boldsymbol{Q}_{i,j} = \begin{cases} (j-n_r+i)_{n_r-i}\, w_1^{j-n_r+i-1}, & i=1,\ldots,n_r,\ j=1,\ldots,2n_r-n_d \\ 0, & i=n_r+1,\ldots,2n_r, \\ & j=1,\ldots,2n_r-n_d, \\ & \text{and } i \neq 2n_r+1-j \\ (j-2n_r+i)_{2n_r-i}, & i=n_r+1,\ldots,2n_r, \\ & j=1,\ldots,2n_r-n_d, \\ & \text{and } i=2n_r+1-j \\ \sum_{k=0}^{n_r-i} \frac{(n_r-i)!}{k!(n_r-i-k)!}(n_r-n_d+i)_{n_r-i-k} & \\ \quad \times w_1^{n_r-n_d+i-k-1}\Gamma(n_s+j-2n_r) & i=1,\ldots,n_r, \\ \quad \times I_A(j,k,w_1), & j=2n_r-n_d+1,\ldots,2n_r \\ 0, & i=n_r+1,\ldots,2n_r, \\ & j=2n_r-n_d+1,\ldots,2n_r \end{cases} \tag{6.34}$$

where $I_A(j,k,w)$ is given in (6.16).

$$A_\lambda(i,j) = \begin{cases} \sum_{k=0}^{n_r-i} \frac{(n_r-i)!}{k!(n_r-i-k)!}(n_r-n_d+i)_{n_r-i-k} & \\ \quad \times w_1^{n_r-n_d+i-k-1}\lambda^{n_s+j-n_d-1} I_B(k,w_1), & \text{for } i=1,\ldots,n_r \\ 0, & \text{for } i=n_r+1,\ldots,2n_r \end{cases} \tag{6.35}$$

where $I_B(k,w)$ is given in (6.17).

the total transmitted power from a relay is 1 ($P_r = 1$). First, the ergodic capacity of the system shown in Fig. 6.1 is given for different system variables in Fig. 6.3. The analytical results for $n_d \geqslant n_s$ are based on (6.21) and for $n_d > n_s$ are based on (6.31). The analytical results show a perfect agreement with the simulation results.

As mentioned before, the capacity expressions derived in this chapter can also be used for a single relay system by the simple expedient of setting $\beta = 0$. Derivations for this case were given in Sec. 6.3. The results are shown in Fig. 6.4 for both two relay and single relay systems. The results are given for $\gamma^2{=}\delta^2{=}\alpha^2{\approx}\ \beta^2$. The reason that results are not reported for exactly $\alpha^2{=}\ \beta^2$ is that these results have a

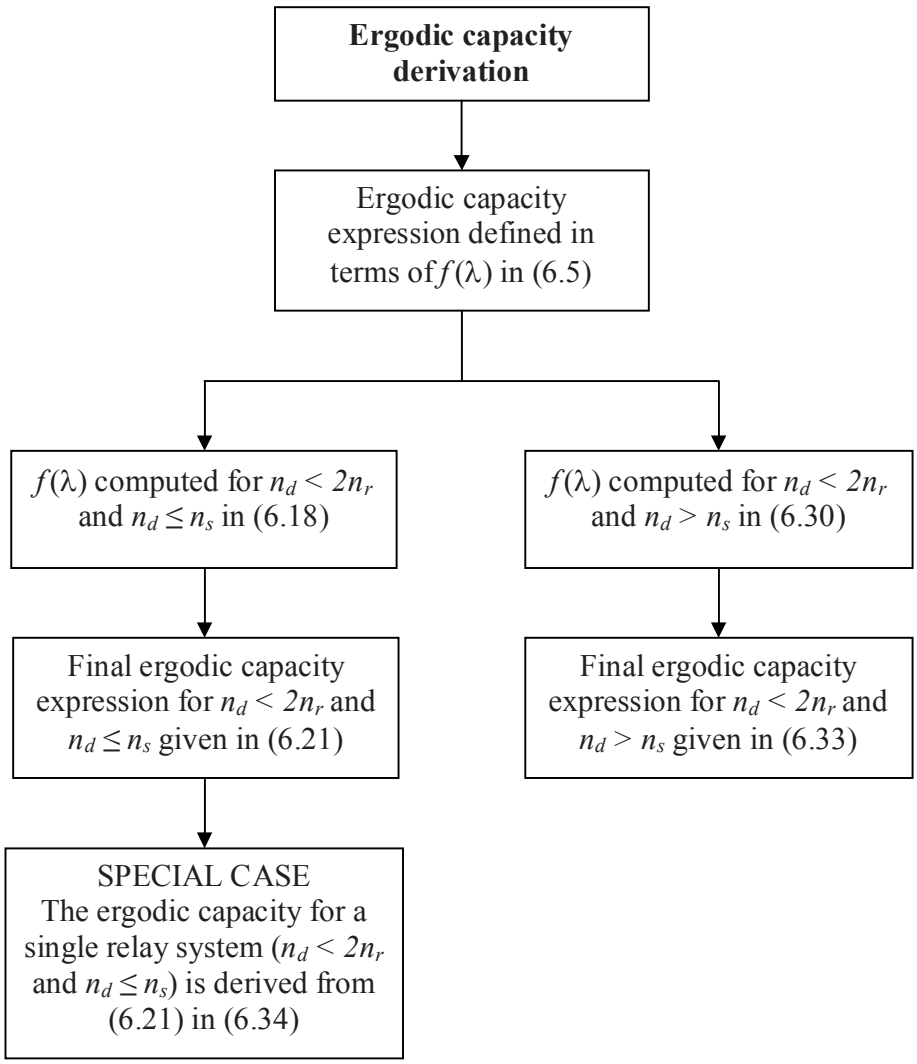

Figure 6.2: Overview of the results derived in Chapter 6.

numerical problem at the point $\alpha^2 = \beta^2$. If $\alpha^2 = \beta^2$ was an important special case then a simpler result could be derived for the case $\alpha^2 = \beta^2$ by setting $\alpha = \beta + \varepsilon$ and letting $\varepsilon \to 0$. However, $\alpha \neq \beta$ with probability 1, so the case where $\alpha = \beta$ does not seem to merit closer attention. We observe excellent agreement between the simulations and analysis of the single relay system. We see that the system with two relays provides better capacity compared to a single relay system, due to extra diversity.

The results derived in this chapter assume $\gamma^2 = \delta^2$. However, when $\gamma^2 \neq \delta^2$, an approximation, a lower bound and an upper bound for the capacity can be obtained

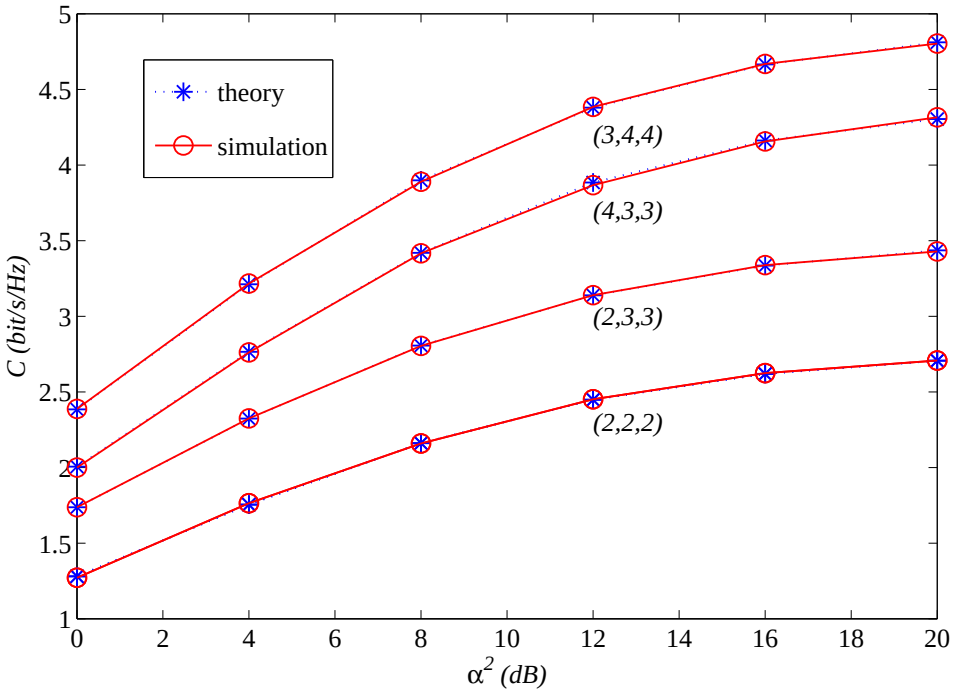

Figure 6.3: Mean capacity for different system sizes and link gains (γ^2=δ^2=10dB, α^2=β^2 - 4 dB and $P_t = P_r = \sigma^2 = 1$).

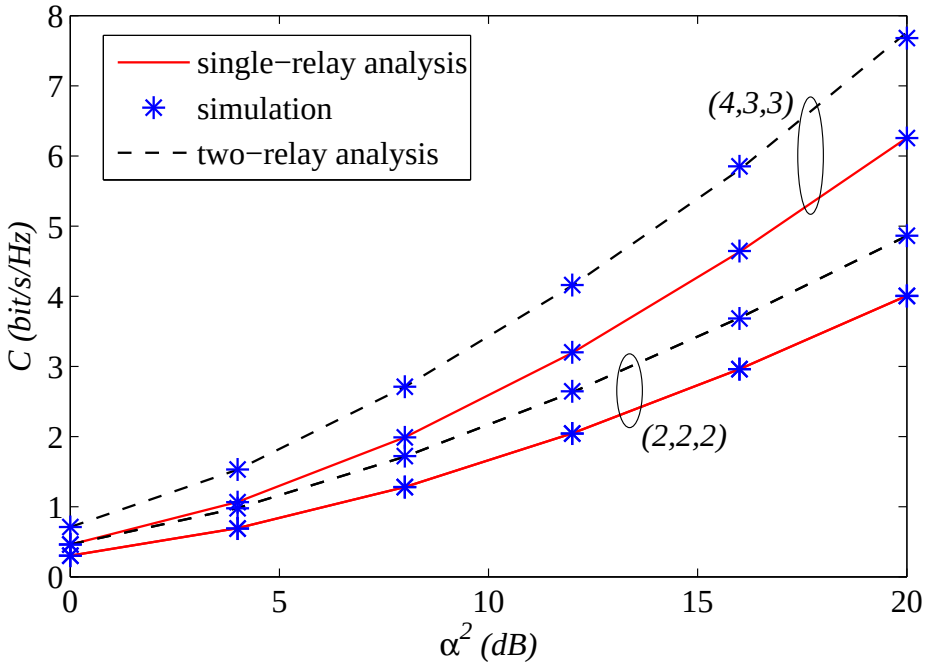

Figure 6.4: Relay system capacity with one and two relays (γ^2=δ^2=α^2≈ β^2 and $P_t = P_r = \sigma^2 = 1$).

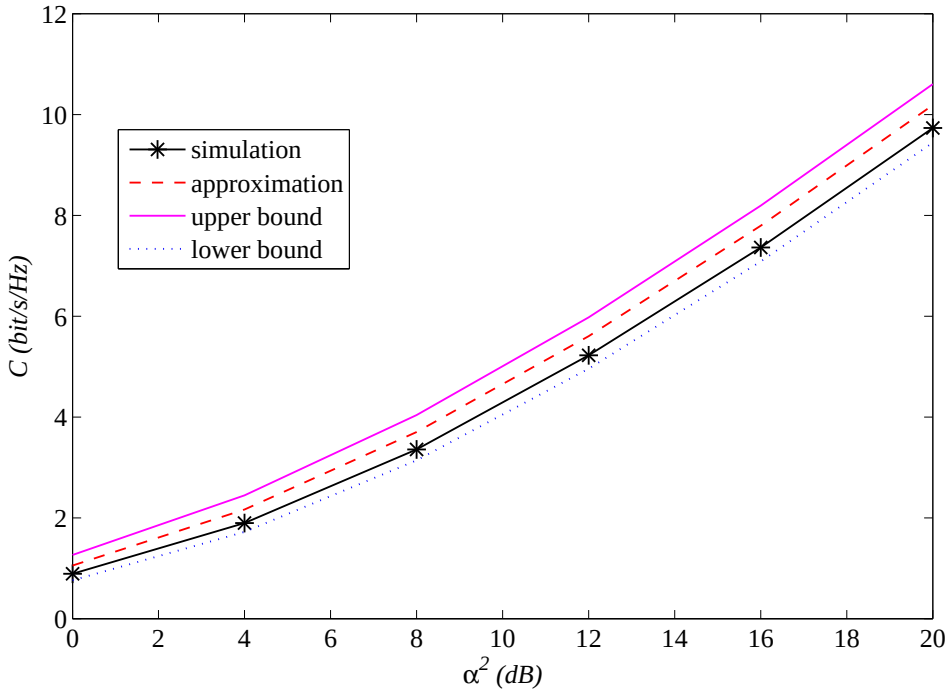

Figure 6.5: Capacity bounds and approximations for a relaying system with two relays (γ^2=α^2, β^2=$\alpha^2 - 5$ dB, δ^2=$\gamma^2 + 5$ dB, $P_t = P_r = \sigma^2 = 1$ and $(5, 4, 4)$).

as mentioned before. Figure 6.5 shows the capacity and bounds for the relaying system with two relays when $\gamma^2 \neq \delta^2$. The results show that the approximation, lower bound and upper bound for the capacity are in good agreement with the simulated results.

To show that these approximations and bounds are quite accurate unless $\gamma^2 \gg \delta^2$ or $\gamma^2 \ll \delta^2$. Consider the results given in Figs. 6.6 and 6.7. Figures 6.6 and 6.7 show the capacity and bounds for the relaying system with two relays when $\gamma^2 = \delta^2 - 5$dB and $\gamma^2 = \delta^2 - 10$dB, respectively. In both figures the results of a single relaying system are shown as a reference. When γ^2 is close to δ^2 (Fig. 6.6), the approximation, lower bound and upper bound for the capacity are in good agreement with the simulated results and the performance of a single relaying system is weaker than the two relay relaying system. However, when γ^2 is some distance away from δ^2 (Fig. 6.7), the approximation and the bounds are loose and the performance of a single relaying system is better than the two relay relaying system. This shows that the two relay based relaying system has higher performance when $\gamma^2 \approx \delta^2$ and when

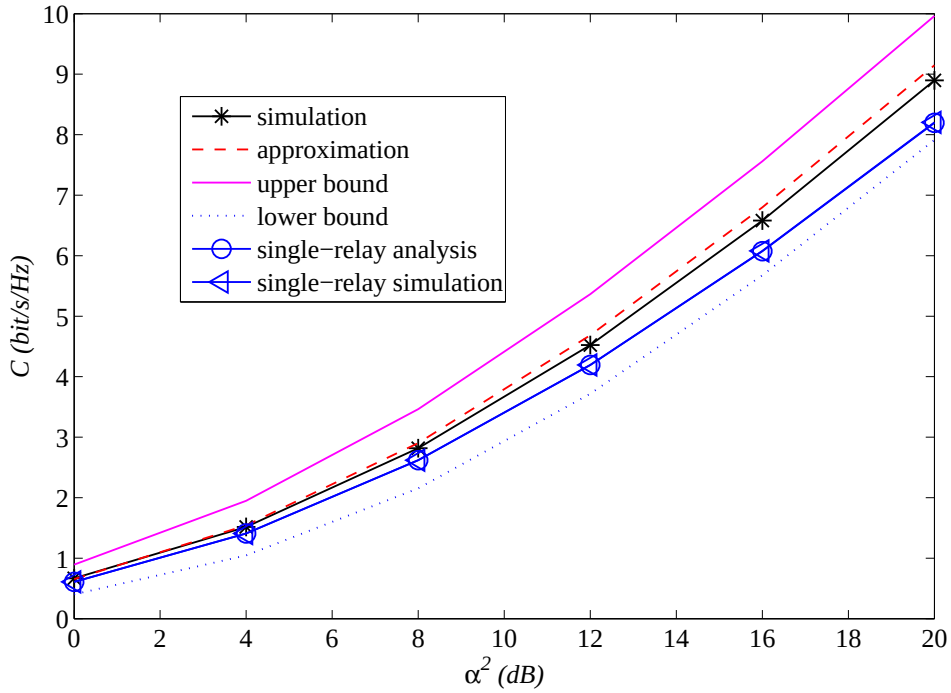

Figure 6.6: Capacity bounds and approximations for a relaying system with two relays (γ^2=α^2, β^2=$\alpha^2 - 1$ dB, δ^2=$\gamma^2 - 5$ dB, $P_t = P_r = \sigma^2 = 1$ and $(5, 4, 4)$). Note: results of a single relay system ($\beta^2 = 0$) are given as a reference

$\gamma^2 \gg \delta^2$ or $\gamma^2 \ll \delta^2$ a single relay system is preferred. Furthermore, this also shows that the approximation and bounds given are valid unless $\gamma^2 \gg \delta^2$ or $\gamma^2 \ll \delta^2$. Hence the analytical results are useful when a two relay system is preferred, and when a single relay is preferred the corresponding analysis can be used.

The ergodic capacity for a single relaying system without the direct link was derived in Secs. 6.3 and 5.2.3 by using different approaches. The analytical results for single relaying systems produced in both the chapters are given in Fig. 6.8. The SNR values P_1 and P_2 in Chapter 5 correspond to γ^2 and α^2, respectively. The results from both the chapters agree well implying that both approaches give the same results as expected.

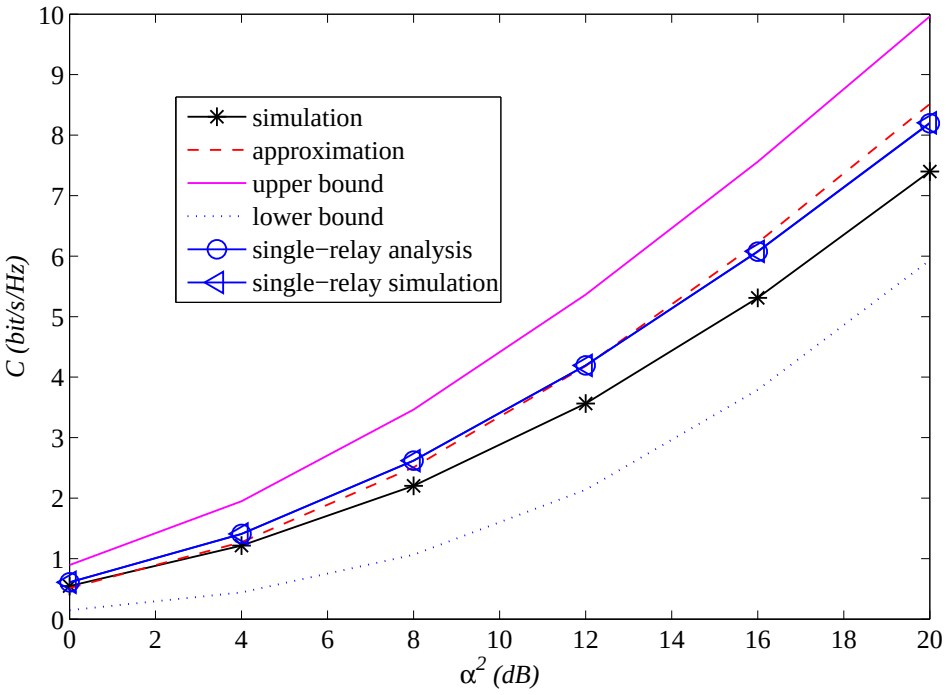

Figure 6.7: Capacity bounds and approximations for a relaying system with two relays (γ^2=α^2, β^2=$\alpha^2 - 1$ dB, δ^2=$\gamma^2 - 10$ dB, $P_t = P_r = \sigma^2 = 1$ and $(5, 4, 4)$). Note: results of a single relay system ($\beta^2 = 0$) are given as a reference

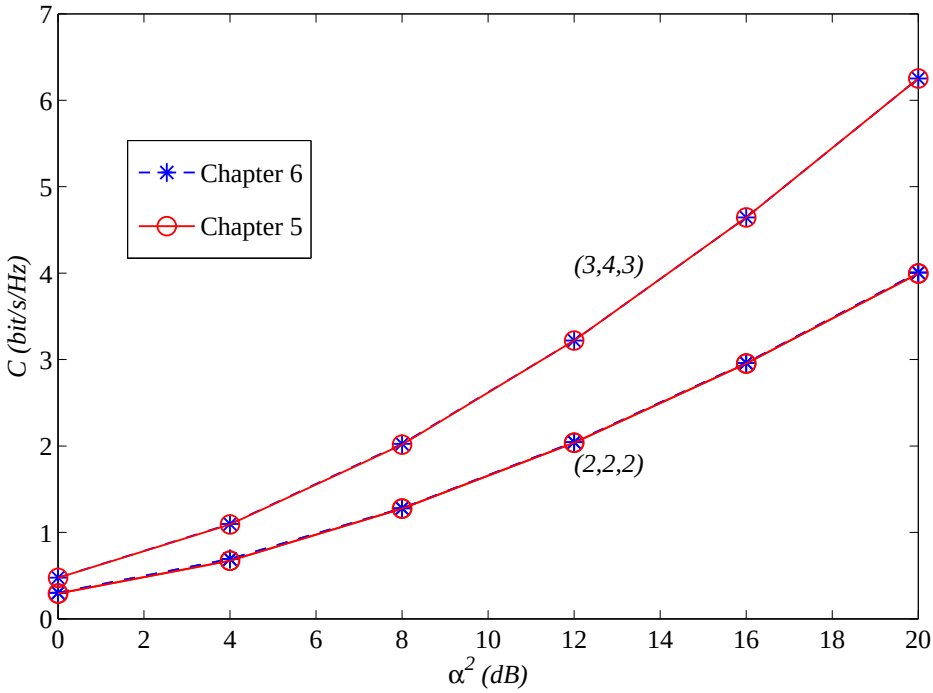

Figure 6.8: Ergodic capacity results for single relaying system using results from Chapters 5 and 6 (γ^2=α^2, and $P_t = P_r = \sigma^2 = 1$).

6.6 Summary

In this chapter we have derived an exact expression for the capacity of the AF MIMO two-hop two relay system shown in Fig. 6.1. We first developed an expression for the probability density function of the arbitrary eigenvalue of the system. Then, using this result, we found a closed-form expression for the ergodic capacity of the system. We verified the analysis using Monte Carlo simulation and demonstrated perfect agreement between our analysis and simulations. We have also shown that these results can be used to obtain the capacity for a single relay system by setting appropriate parameters.

We also compared relaying systems using one and two relays. Our results verify the capacity gain of relaying systems with two relays due to the extra diversity compared to a single relaying system.

To derive our equations, we assumed $\gamma^2 = \delta^2$. However, we have found that when $\gamma^2 \neq \delta^2$, an approximation, a lower bound and an upper bound for the capacity can be obtained by replacing γ and δ by $\frac{\gamma+\delta}{2}$, $\min(\gamma, \delta)$ and $\max(\gamma, \delta)$, respectively. These approximations and bounds are quite accurate unless $\gamma^2 \gg \delta^2$ or $\gamma^2 \ll \delta^2$, and in these cases a single relay system is preferred.

As a special case, we have derived the ergodic capacity for a single relaying system without the direct link as we did in Chapter 5 using a different approach. We have compared the results from both chapters and have shown that both approaches generate the same results as expected.

Chapter 7

Relay Amplification in MIMO Two-Hop Relaying Systems

In this chapter we compare three types of relay amplification methods in MIMO amplify-and-forward (AF) relaying systems. We compare these methods in terms of system capacity performance for three different types of AF MIMO two-hop relaying systems. Furthermore, we explain the capacity behavior using the cumulative distribution functions of the signal-to-noise ratios of the amplification methods.

In most of the literature on wireless relaying, the relay terminal amplifies the received signal from the source by using the second order statistics of the source to relay channel [1, 29] or by using instantaneous knowledge of the source to relay channel [71]. In other work, the relay terminal amplifies the received signal using an optimized gain matrix [23, 24, 30]. However, there seems to be very little work that compares different amplification methods in a common framework. In this chapter we compare three types of relay amplification methods:

- amplification using the second order statistics of the source to relay channel (average amplification);

- amplification using instantaneous knowledge of the source to relay channel (instantaneous channel amplification); and

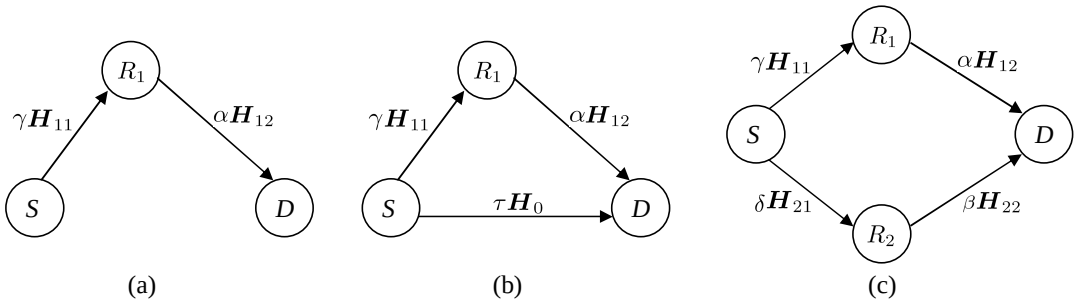

Figure 7.1: MIMO relay network topologies. (a) Topology 1. (b) Topology 2. (c) Topology 3

- amplification using the instantaneous received signal power at the relay (instantaneous power amplification).

In these comparisons, the mean capacity of three different AF MIMO two-hop relaying systems are evaluated based on the above amplification methods. Note that the results are simulation-based due to the difficulty in obtaining capacity results for the two instantaneous methods. For the average amplification case, capacity results are available [69, 72, 73].

7.1 System Model

The three relay network topologies we consider are shown in Fig. 7.1. The source (S), relay (R_x), and destination (D) terminals are equipped with n_s, n_r and n_d antennas respectively. For simplicity, we assume that all the relaying terminals have equal number of antennas. During the first hop, the source terminal transmits (broadcasts) to the relay(s) or to the relay(s) and destination. In the second hop, the relay terminal(s) transmit the amplified signal from the first hop to the destination. We assume that the normalized channel matrices for the source-to-destination ($S \rightarrow D$), source-to-relay ($S \rightarrow R_1$, $S \rightarrow R_2$), and relay-to-destination ($R_1 \rightarrow D$, $R_2 \rightarrow D$) links are given by $\boldsymbol{H}_0 \in \mathcal{C}^{n_d \times n_s}$, $\boldsymbol{H}_{11}, \boldsymbol{H}_{21} \in \mathcal{C}^{n_r \times n_s}$, and $\boldsymbol{H}_{12}, \boldsymbol{H}_{22} \in \mathcal{C}^{n_d \times n_r}$, respectively. We also assume that the channels are frequency-flat and the entries of the channel matrices are ZMCSCG random variables of unit variance. Furthermore, we assume that the relay terminal assists in the communication with the destination terminal

using AF mode. In this mode, without decoding or demodulation, the relay terminal, R_x, amplifies the received observation corresponding to the signal from the source by a factor, a_x, and retransmits it to the destination.

Firstly, we consider topology 1 in Fig. 7.1. In this scenario no signal is received by the destination during the first hop. The received signal at the destination after the two hops is given by:

$$\boldsymbol{y}_{\text{Top 1}} = \alpha\,\gamma\,a_1\,\boldsymbol{H}_{12}\boldsymbol{H}_{11}\boldsymbol{x} + \alpha\,a_1\,\boldsymbol{H}_{12}\boldsymbol{n}_1 + \boldsymbol{n}_3. \tag{7.1}$$

Then, defining $\boldsymbol{A}_1 = \alpha\,\gamma a_1\,\boldsymbol{H}_{12}\boldsymbol{H}_{11}$ and $\boldsymbol{B}_1 = (\sigma_3^2\,\boldsymbol{I}_{n_d} + \alpha^2\,a_1^2\,\sigma_1^2\,\boldsymbol{H}_{12}\boldsymbol{H}_{12}^{\dagger})^{1/2}$, (7.1) can be written as

$$\boldsymbol{y}_{\text{Top 1}} = \boldsymbol{A}_1\boldsymbol{x} + \boldsymbol{B}_1\boldsymbol{v}_1, \tag{7.2}$$

where $\boldsymbol{v}_1$ is a Gaussian noise vector and will be explained later.

In topology 2, the destination receives information during the first hop as well. In this case the received signal at the destination after the two hops is given by:

$$\boldsymbol{y}_{\text{Top 2}} = \begin{bmatrix} \tau\boldsymbol{H}_0 \\ \alpha\gamma a_1\boldsymbol{H}_{12}\boldsymbol{H}_{11} \end{bmatrix}\boldsymbol{x} + \begin{bmatrix} \boldsymbol{n}_0 \\ \alpha a_1\boldsymbol{H}_{12}\boldsymbol{n}_1 + \boldsymbol{n}_3 \end{bmatrix}. \tag{7.3}$$

Again, (7.3) can also be written in the same form as (7.2):

$$\boldsymbol{y}_{\text{Top 2}} = \boldsymbol{A}_2\boldsymbol{x} + \boldsymbol{B}_2\boldsymbol{v}_2, \tag{7.4}$$

where

$$\boldsymbol{A}_2 = \begin{bmatrix} \tau\boldsymbol{H}_0 \\ \alpha\gamma a_1\boldsymbol{H}_{12}\boldsymbol{H}_{11} \end{bmatrix}, \tag{7.5}$$

and

$$\boldsymbol{B}_2 = \begin{bmatrix} \sigma_0^2\boldsymbol{I}_{n_d} & \boldsymbol{0} \\ \boldsymbol{0} & \sigma_1^2\alpha^2 a_1^2\boldsymbol{H}_{12}\boldsymbol{H}_{12}^{\dagger} + \sigma_3^2\boldsymbol{I}_{n_d} \end{bmatrix}^{1/2}. \tag{7.6}$$

Similarly, the received signal at the destination after the two hops in topology 3 is given by

$$\begin{aligned}\boldsymbol{y}_{\text{Top 3}} =& (\alpha\,\gamma\,a_1\,\boldsymbol{H}_{12}\boldsymbol{H}_{11} + \beta\,\delta\,a_2\,\boldsymbol{H}_{22}\boldsymbol{H}_{21})\boldsymbol{x} \\ &+ \alpha\,a_1\,\boldsymbol{H}_{12}\boldsymbol{n}_1 + \beta\,a_2\,\boldsymbol{H}_{22}\boldsymbol{n}_2 + \boldsymbol{n}_3.\end{aligned} \tag{7.7}$$

Then, defining

$$\boldsymbol{A}_3 = \alpha\,\gamma\,a_1\,\boldsymbol{H}_{12}\boldsymbol{H}_{11} + \beta\,\delta\,a_2\,\boldsymbol{H}_{22}\boldsymbol{H}_{21}, \tag{7.8}$$

and

$$\boldsymbol{B}_3 = (\sigma_3^2\,\boldsymbol{I}_{n_d} + \alpha^2\,a_1^2\,\sigma_1^2\,\boldsymbol{H}_{12}\boldsymbol{H}_{12}^{\dagger} + \beta^2\,a_2^2\,\sigma_2^2\,\boldsymbol{H}_{22}\boldsymbol{H}_{22}^{\dagger})^{\frac{1}{2}}, \tag{7.9}$$

equation (7.7) can also be given as:

$$\boldsymbol{y}_{\text{Top }3} = \boldsymbol{A}_3\boldsymbol{x} + \boldsymbol{B}_3\boldsymbol{v}_3. \tag{7.10}$$

In (7.1) - (7.10), the parameters τ^2, γ^2, δ^2, α^2 and β^2 are the average powers of the $S\rightarrow D$, $S\rightarrow R_1$, $S\rightarrow R_2$, $R_1\rightarrow D$ and $R_2\rightarrow D$ links, respectively, taking into account the different path loss and shadowing effects over the links. The variables $\boldsymbol{n}_1$, $\boldsymbol{n}_2$, $\boldsymbol{n}_3$ and $\boldsymbol{n}_0$ are the noise vectors at R_1, R_2, D (second-hop) and D (first-hop) respectively, and $\boldsymbol{x}$ is the vector of transmit symbols. The transmit symbols are assumed to be i.i.d. with $E\{\boldsymbol{x}\boldsymbol{x}^{\dagger}\} = \rho\boldsymbol{I}_{n_s}$. The noise at the relays and destination is modeled as ZMCSCG with $E\{\boldsymbol{n}_0\boldsymbol{n}_0^{\dagger}\} = \sigma_0^2\boldsymbol{I}_{n_d}$, $E\{\boldsymbol{n}_1\boldsymbol{n}_1^{\dagger}\} = \sigma_1^2\boldsymbol{I}_{n_r}$, $E\{\boldsymbol{n}_2\boldsymbol{n}_2^{\dagger}\} = \sigma_2^2\boldsymbol{I}_{n_r}$, and $E\{\boldsymbol{n}_3\boldsymbol{n}_3^{\dagger}\} = \sigma_3^2\boldsymbol{I}_{n_d}$. Finally, $\boldsymbol{v}_1$, $\boldsymbol{v}_2$ and $\boldsymbol{v}_3$ are normalized complex Gaussian noise vectors, which have $\boldsymbol{I}_{n_d}$, $\boldsymbol{I}_{2n_d}$ and $\boldsymbol{I}_{n_d}$, respectively, as their covariance matrices.

The instantaneous capacity expressions for the system topologies are given following [23] as below, (the factor 1/2 accounts for the fact that the information is conveyed to the destination terminal over two time slots [1]). For topology 1 the instantaneous capacity is

$$C_1 = \frac{1}{2}\log_2\left|\boldsymbol{I}_{n_d} + \rho\boldsymbol{A}_1\boldsymbol{A}_1^{\dagger}(\boldsymbol{B}_1\boldsymbol{B}_1^{\dagger})^{-1}\right|. \tag{7.11}$$

For topology 2 we have

$$C_2 = \frac{1}{2}\log_2\left|\boldsymbol{I}_{2n_d} + \rho\boldsymbol{A}_2\boldsymbol{A}_2^{\dagger}(\boldsymbol{B}_2\boldsymbol{B}_2^{\dagger})^{-1}\right|, \tag{7.12}$$

and for topology 3

$$C_3 = \frac{1}{2}\log_2\left|\boldsymbol{I}_{n_d} + \rho\boldsymbol{A}_3\boldsymbol{A}_3^{\dagger}(\boldsymbol{B}_3\boldsymbol{B}_3^{\dagger})^{-1}\right|. \tag{7.13}$$

In order to evaluate the means and variances of the capacities of the system topologies under different amplification methods, we restrict the total power from each relay to be P_r. Under this condition, evaluation of the amplification factor of the relays, a_x, is given below.

7.1.1 Average Amplification

The signal received by the relay, R_1, during the first hop can be given as:

$$\boldsymbol{y}_{R_1} = \gamma \boldsymbol{H}_{11}\boldsymbol{x} + \boldsymbol{n}_1. \tag{7.14}$$

Then, using the power constraint, $\mathrm{E}\{\|a_1\boldsymbol{y}_{R_1}\|^2\} = P_r$, and assuming only second order statistics are known, the amplification factor a_1 can be calculated as

$$a_1 = \sqrt{\frac{P_r}{n_r(\rho\,\gamma^2\,n_s + \sigma_1^2)}}, \tag{7.15}$$

where the expectation is taken over $\boldsymbol{H}_{11}$, $\boldsymbol{x}$ and $\boldsymbol{n}_1$. Then, using a similar procedure, the amplification factor a_2 can be calculated as

$$a_2 = \sqrt{\frac{P_r}{n_r(\rho\,\delta^2\,n_s + \sigma_2^2)}}. \tag{7.16}$$

7.1.2 Instantaneous Channel Amplification

As before, using (7.14) and the power constraint, $\mathrm{E}\{\|a_1\boldsymbol{y}_{R_1}\|^2\} = P_r$, and assuming that instantaneous knowledge of the source to relay link, ($S \rightarrow R_1$), is known at R_1, the amplification factor a_1 can be calculated as

$$a_1 = \sqrt{\frac{P_r}{\rho\,\gamma^2\ \mathrm{tr}\{\boldsymbol{H}_{11}^\dagger\boldsymbol{H}_{11}\} + n_r\,\sigma_1^2}}, \tag{7.17}$$

where the expectation is only taken over $\boldsymbol{x}$ and $\boldsymbol{n}_1$. Again, using a similar procedure, the amplification factor a_2 can be calculated as

$$a_2 = \sqrt{\frac{P_r}{\rho\,\delta^2\ \mathrm{tr}\{\boldsymbol{H}_{21}^\dagger\boldsymbol{H}_{21}\} + n_r\,\sigma_2^2}}. \tag{7.18}$$

7.1.3 Instantaneous Power Amplification

In this method, the relays use the instantaneous power of the received signal at the relay for amplification. Using (7.14) and the power constraint, the amplification factor a_1 in this case can be calculated as

$$a_1 = \sqrt{\frac{P_r}{\|\gamma \boldsymbol{H}_{11}\boldsymbol{x} + \boldsymbol{n}_1\|^2}}. \tag{7.19}$$

The amplification factor, a_2, can be determined using a similar procedure as

$$a_2 = \sqrt{\frac{P_r}{\|\delta \boldsymbol{H}_{21}\boldsymbol{x} + \boldsymbol{n}_2\|^2}}. \tag{7.20}$$

Looking at the amplification methods given above, the average amplification method seems to be the simplest method to implement for the relaying terminal, as it only requires the second order statistics of the source to relay link. In the instantaneous channel amplification method, the relay terminal is required to estimate the source to relay link. This would add extra complexity to the relaying terminal compared to the average amplification method. The instantaneous power amplification method may be simple for the relaying terminal but it has some inherent problems. The instantaneous power amplification method would lead to exactly the same relay transmission power, P_r. Hence, although the received signal at the relaying terminal has different power levels depending on the modulation type used, the transmitting signal from the relay has the same power level. This would cause a problem at the destination terminal for non-constant amplitude modulation types such as 4PAM and 16QAM. Hence, if this scheme is to be implemented, the relay terminal should send the amplification factor used to the destination terminal with each symbol. This additional information needed at the destination would create enormous overhead in the instantaneous power amplification method compared to the other methods. Hence, this approach is not feasible for non-constant amplitude constellations and is mainly of interest as a type of upper bound.

7.2 Simulation Results and Discussion

Using Monte Carlo simulations we now compared the instantaneous capacity of the system topologies given in Fig. 7.1 for the three amplification methods. We set $\rho = 1/n_s$ and $P_r = 1$. Furthermore, we let $\sigma_0^2 = \sigma_1^2 = \sigma_2^2 = \sigma_3^2 = 1$, implying that the average signal-to-noise ratio (SNR) of the links $(S \rightarrow D)$, $(S \rightarrow R_1)$, $(S \rightarrow R_2)$, $(R_1 \rightarrow D)$ and $(R_2 \rightarrow D)$ are τ^2, γ^2, δ^2, α^2 and β^2, respectively. We represent the number of antennas used in the system by the 3-tuple (n_s, n_r, n_d).

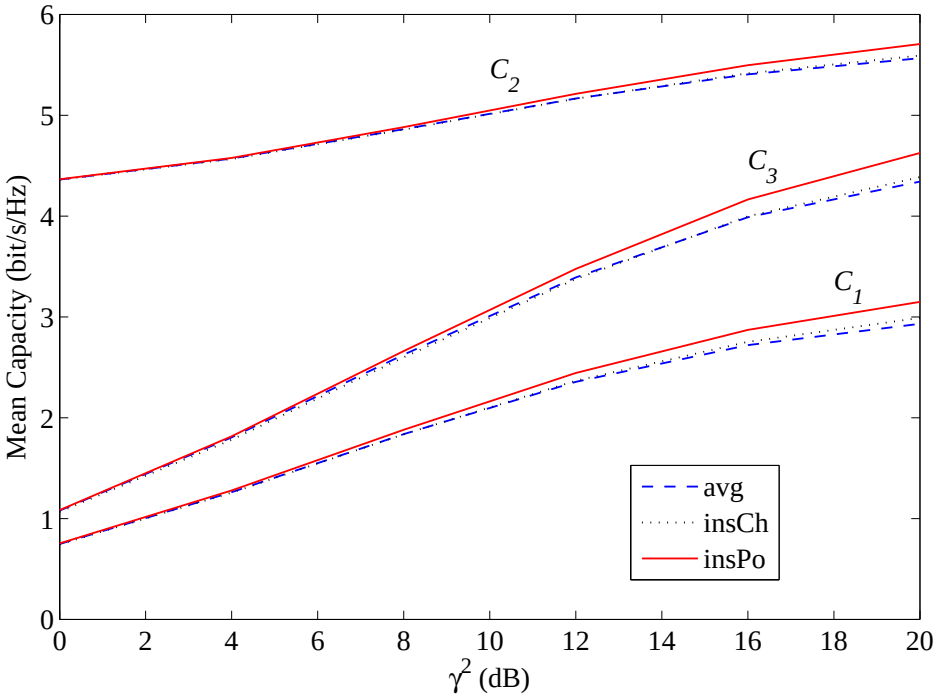

Figure 7.2: Mean capacity of the system topologies under different amplification methods for the system parameters: $(3, 2, 3)$, $\tau^2 = \alpha^2 = \beta^2 = 10$dB and $\gamma^2 = \delta^2$.

Figures 7.2 and 7.3 show the mean capacity of the system topologies under the three amplification methods. In Figure 7.2 we plot the mean capacity when the source and relays have the same propagation conditions to the destination. Likewise, in Fig. 7.3 we show the mean capacity when the relays have better propagation conditions to the destination than the source to destination link. In the figures, 'avg', 'insCh' and 'insPo' stand for the average, instantaneous channel and instantaneous power amplification methods, respectively. The results from both fig-

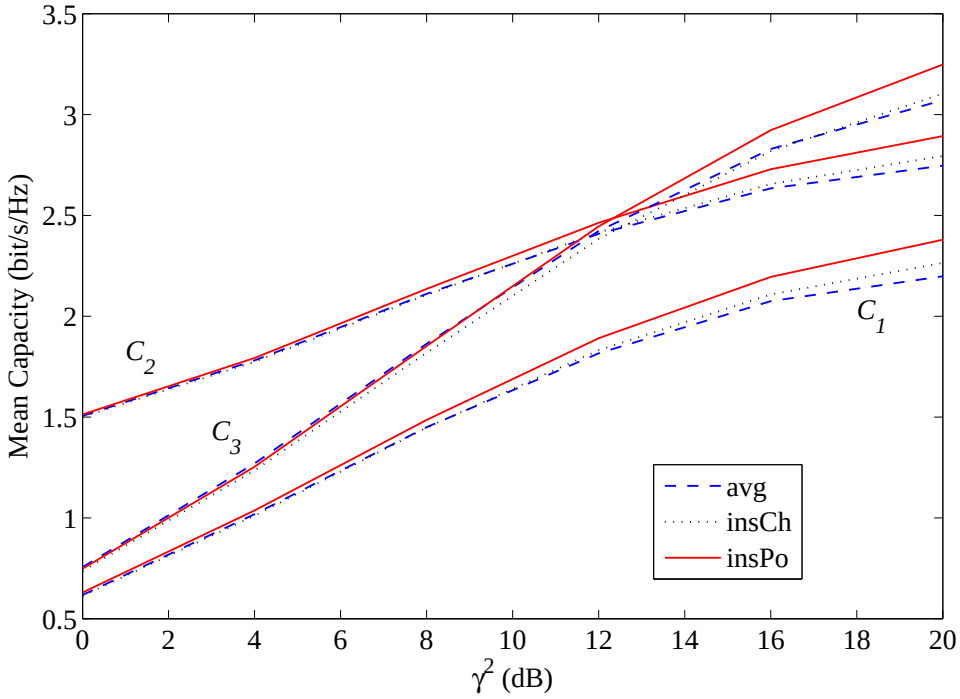

Figure 7.3: Mean capacity of the system topologies under different amplification methods for the system parameters: $(2, 2, 2)$, $\alpha^2 = \beta^2 = \tau^2 + 8\text{dB} = 10\text{dB}$ and $\gamma^2 = \delta^2$.

ures show that for larger SNRs the instantaneous power amplification method has a higher mean capacity in all the system topologies compared to the other two amplification methods. For smaller SNRs, the mean capacity of all the amplification methods converges to the same level in all the system topologies. Also, for larger SNRs the instantaneous channel amplification method is slightly better than the average amplification method. Thus, a better system capacity can be obtained by using the instantaneous power amplification method. However, as explained before, to implement the instantaneous power amplification method requires additional information at the destination and would create enormous overhead compared to the other methods.

To explain the mean capacity behaviors of the amplification methods, we consider system topology 1 with dimension $(n_s, 1, 1)$. The mean capacity for this scenario is given in Fig. 7.4. Again, the same mean capacity behavior is seen as in Figs. 7.2 and 7.3. As in (7.11), the capacity of the system depends on the SNR of the system,

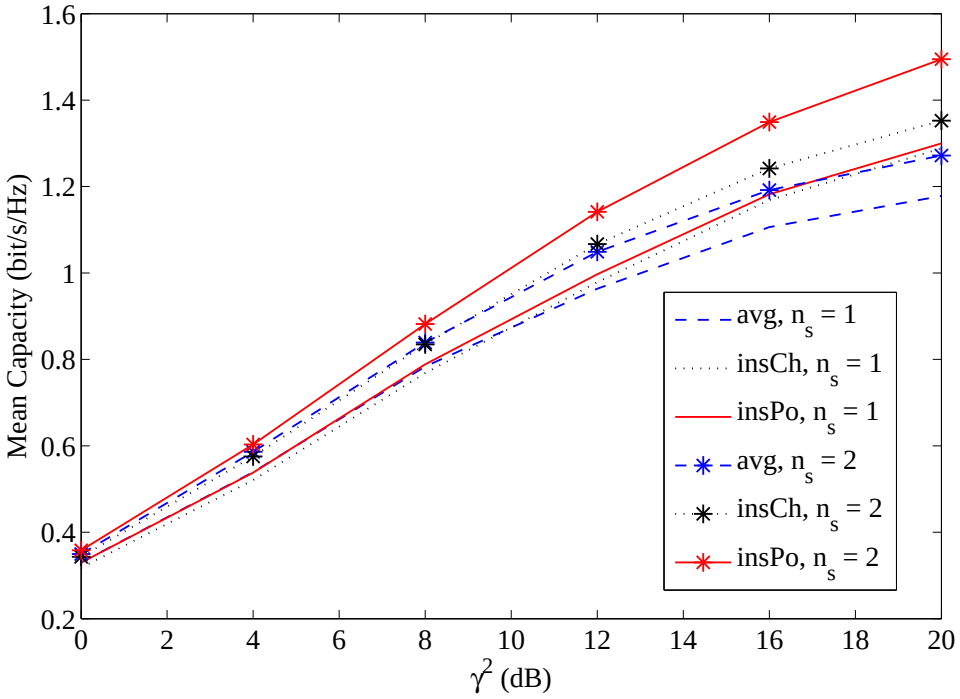

Figure 7.4: Mean capacity of system topology 1 under different amplification methods for the system parameters: $(n_s, 1, 1)$, $\alpha^2 = 10$dB.

the scalar $\rho \boldsymbol{A}_1 \boldsymbol{A}_1^\dagger (\boldsymbol{B}_1 \boldsymbol{B}_1^\dagger)^{-1}$. The cumulative distribution functions (CDFs) of the SNRs for the three amplification methods are calculated using the analysis in Sec. 7.3 for this system configuration. The analytical CDFs of the SNRs given in Sec. 7.3 are plotted in Fig. 7.5 with their simulated values for $\alpha^2 = 10$dB, and $\gamma^2 = 20$dB. The simulated values agree well with the analytical values.

The results show that the average amplification method has a higher probability of low SNR values compared to the other amplification methods, hence, the mean capacity of the average amplification method is lower compared to the other methods. Note that the average amplification method also has higher SNRs for $n_s = 1$, but the gains of the higher SNR region are overshadowed by the losses in the low SNR region due to the logarithmic relationship between capacity and SNR. Furthermore, the instantaneous power amplification method has slightly higher SNR values at the top end when $n_s = 1$ and much higher SNR values at the top end when $n_s = 2$ compared to the instantaneous channel amplification method. Hence, the mean capacity of the instantaneous power amplification method is slightly higher

than that of the instantaneous channel amplification method. Thus, the CDFs of the SNRs can be used to explain the mean capacity behaviors of the systems.

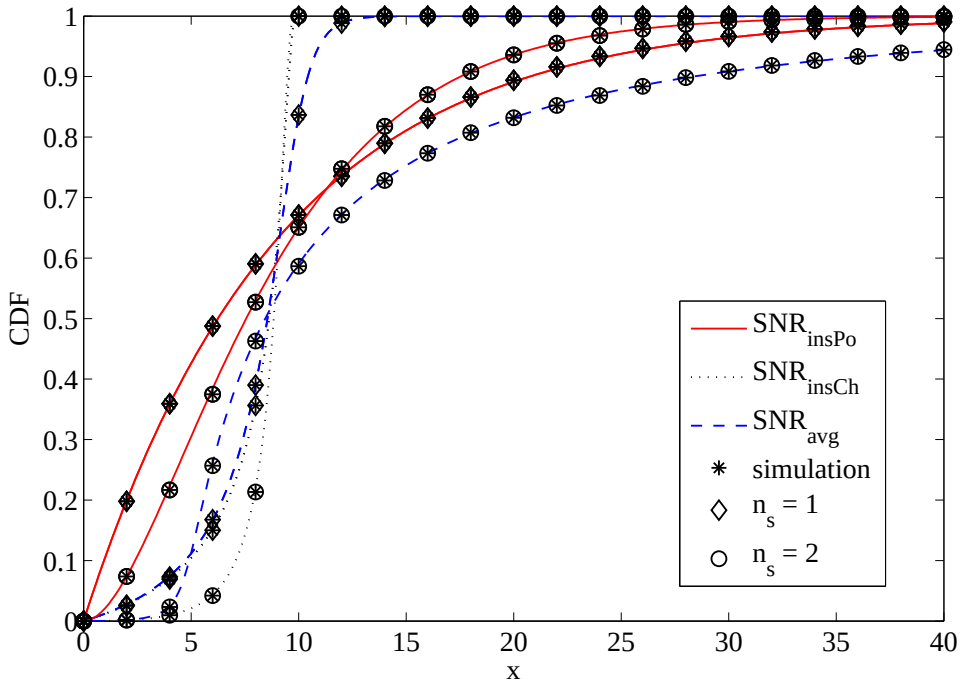

Figure 7.5: CDFs of the SNRs of system topology 1 under different amplification methods for the system parameters: $(n_s, 1, 1)$, $\alpha^2 = 10$dB, and $\gamma^2 = 20$dB.

The mean capacity results follow a simple pattern with the instantaneous power amplification giving the highest values as supported by our SNR analysis. The capacity variance has two types of behavior. For the $(1, 1, 1)$ system the average amplification method has the highest variance as shown in Figs. 7.5 - 7.6. This may be unexpected as the amplification factors are constant for the average amplification and hence there are fewer random variables involved in the capacity. However, in the $(1, 1, 1)$ case the extra random variables in the amplification factors for the instantaneous power amplification are scalars in the denominator of (7.19) - (7.20). These act to control the variability in the strength of the $S \rightarrow R$ link resulting in lower variability. However, when there are multiple antennas at the source or relay then the denominators in (7.19) - (7.20) have cross-product terms between the elements of $\boldsymbol{H}_{11}$ or $\boldsymbol{H}_{21}$. The variation caused by these extra variables exceeds any stabilizing effect and so the capacity variance is higher for the instantaneous

power amplification whenever $n_s > 1$ or $n_r > 1$. This is shown in Fig. 7.7 and the conclusion is verified by the SNR CDFs in Fig. 7.5.

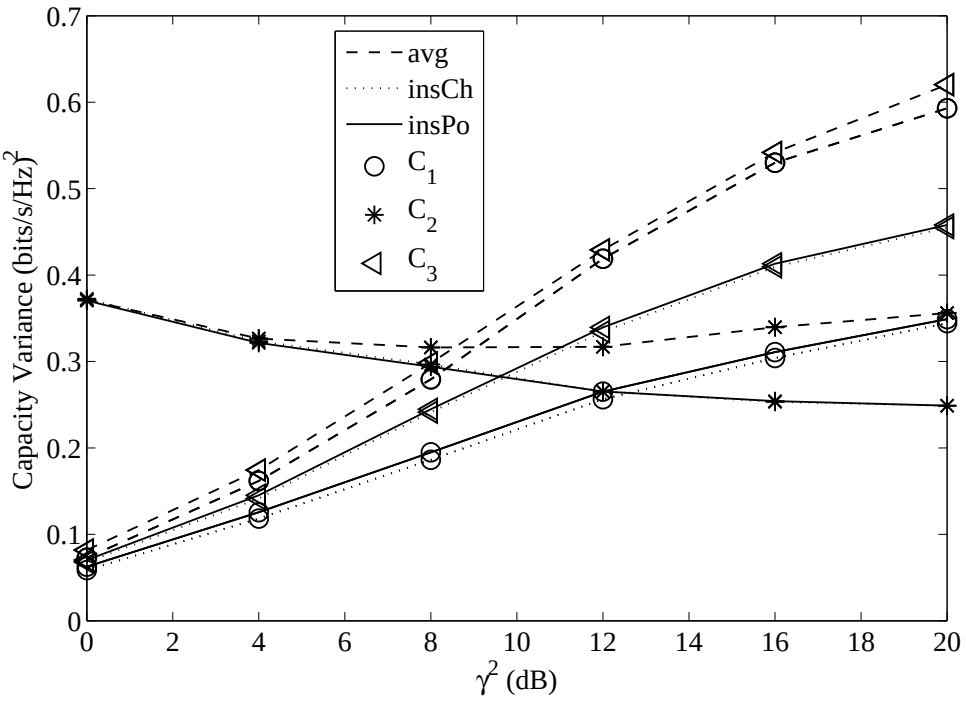

Figure 7.6: Capacity variance of the system topologies under different amplification methods for the system parameters: $(1, 1, 1)$, $\tau^2 = \alpha^2 = \beta^2 = 10$dB and $\gamma^2 = \delta^2$.

For high SNRs, we have shown that the instantaneous power amplification method has a slightly higher mean capacity in all the system topologies compared to the other two amplification methods. However, we also have seen that the instantaneous power amplification method is more unstable compared to the other amplification methods when the number of antennas in the relay and/or the source is more than one. In addition, the instantaneous power amplification method has other problems as explained before. Therefore, it is more important to look in detail at the average and instantaneous channel amplification methods.

Figures 7.8 and 7.9 show the percentage difference between the instantaneous channel amplification method compared to the average amplification in terms of the mean capacity of the systems for different link gains. The results show a small difference in mean capacity for the two amplification methods. The average am-

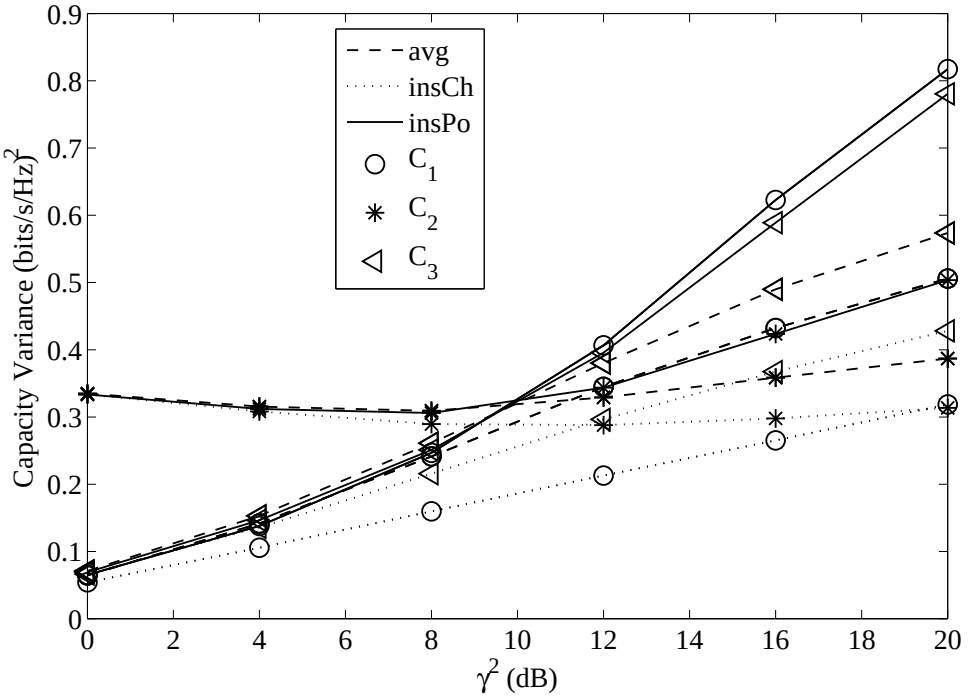

Figure 7.7: Capacity variance of the system topologies under different amplification methods for the system parameters: $(4, 4, 4)$, $\tau^2 = \alpha^2 = \beta^2 = 10$dB and $\gamma^2 = \delta^2$.

plification has a higher mean capacity at lower SNRs and a lower mean capacity at high SNRs compared to the instantaneous channel amplification method. Thus, the instantaneous channel amplification method has almost no advantage in terms of mean capacity but its capacity is less variable compared to the average amplification method. On the other hand, the average amplification method is simpler to implement as it does not require channel estimation at the relaying terminal.

7.3 CDFs of the SNRs of Topology 1 for the Three Amplification Methods

The mean capacity results presented in Figs. 7.2 and 7.3 are only simulation based due to the difficulty in obtaining capacity results for the two instantaneous methods. To gain some understanding and analytical verification of these results, in this section we look at the end-to-end SNRs of topology 1 for the three different am-

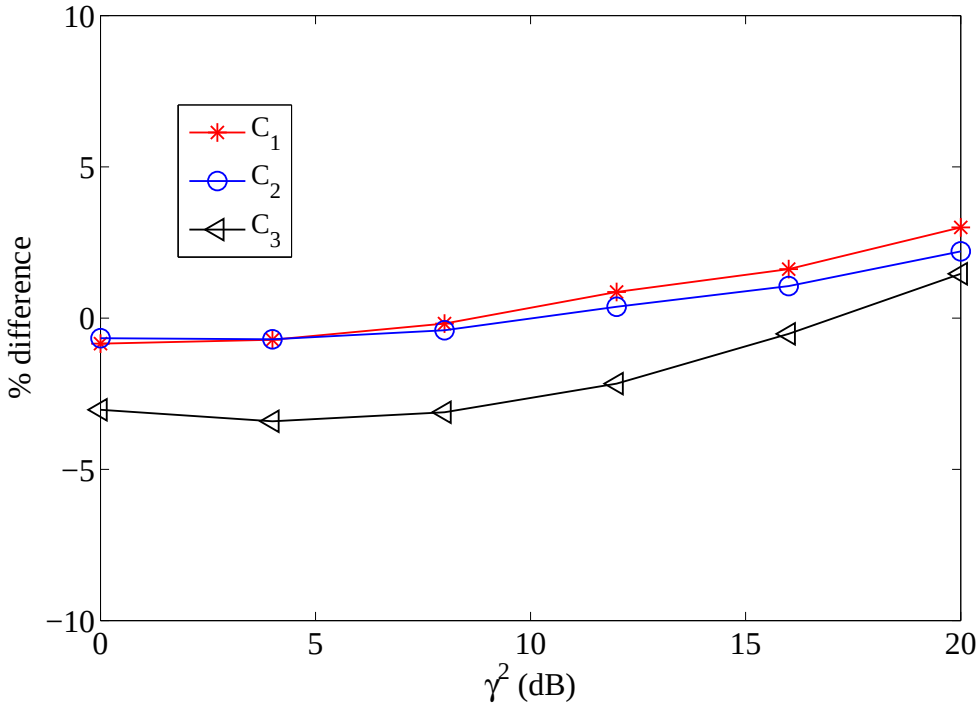

Figure 7.8: Percentage difference of the instantaneous channel amplification method compared to the average amplification in mean capacity for the system parameters: $(2, 2, 2)$, $\alpha^2 = \beta^2 = \tau^2 + 8\text{dB} = 10\text{dB}$ and $\gamma^2 = \delta^2$.

plification methods. This is still a complex task for the general case. Hence, some major simplifications are made to make the analysis tractable. With these approximations, the CDFs of the SNRs of topology 1 for the three amplification methods are derived. The SNR for system topology 1 with $(n_s, 1, 1)$ is $\rho \boldsymbol{A}_1 \boldsymbol{A}_1^\dagger (\boldsymbol{B}_1 \boldsymbol{B}_1^\dagger)^{-1}$. For the three amplification methods, the SNRs of the system can be written as

$$\text{SNR}_{\text{avg}} = \frac{\rho\alpha^2\gamma^2 \boldsymbol{H}_{12}\boldsymbol{H}_{11}\boldsymbol{H}_{11}^\dagger\boldsymbol{H}_{12}^\dagger}{\sigma^2(\rho\gamma^2 n_s + \sigma^2 + \alpha^2\|\boldsymbol{H}_{12}\|^2)}, \tag{7.21}$$

$$\text{SNR}_{\text{insCh}} = \frac{\rho\alpha^2\gamma^2 \boldsymbol{H}_{12}\boldsymbol{H}_{11}\boldsymbol{H}_{11}^\dagger\boldsymbol{H}_{12}^\dagger}{\sigma^2(\rho\gamma^2\ \text{tr}\{\boldsymbol{H}_{11}^\dagger\boldsymbol{H}_{11}\} + \sigma^2 + \alpha^2\|\boldsymbol{H}_{12}\|^2)}, \tag{7.22}$$

and

$$\text{SNR}_{\text{insPo}} = \frac{\rho\alpha^2\gamma^2 \boldsymbol{H}_{12}\boldsymbol{H}_{11}\boldsymbol{H}_{11}^\dagger\boldsymbol{H}_{12}^\dagger}{\sigma^2(\|\gamma\boldsymbol{H}_{11}\boldsymbol{x} + \boldsymbol{n}_1\|^2 + \alpha^2\|\boldsymbol{H}_{12}\|^2)}. \tag{7.23}$$

For the system with $(n_s, 1, 1)$, $\boldsymbol{H}_{12}$ and $\boldsymbol{n}_1$ are complex scalar quantities. Then, to make the analysis possible, $\|\boldsymbol{H}_{12}\|^2$ is fixed at its mean value, $E[\|\boldsymbol{H}_{12}\|^2] = 1$,

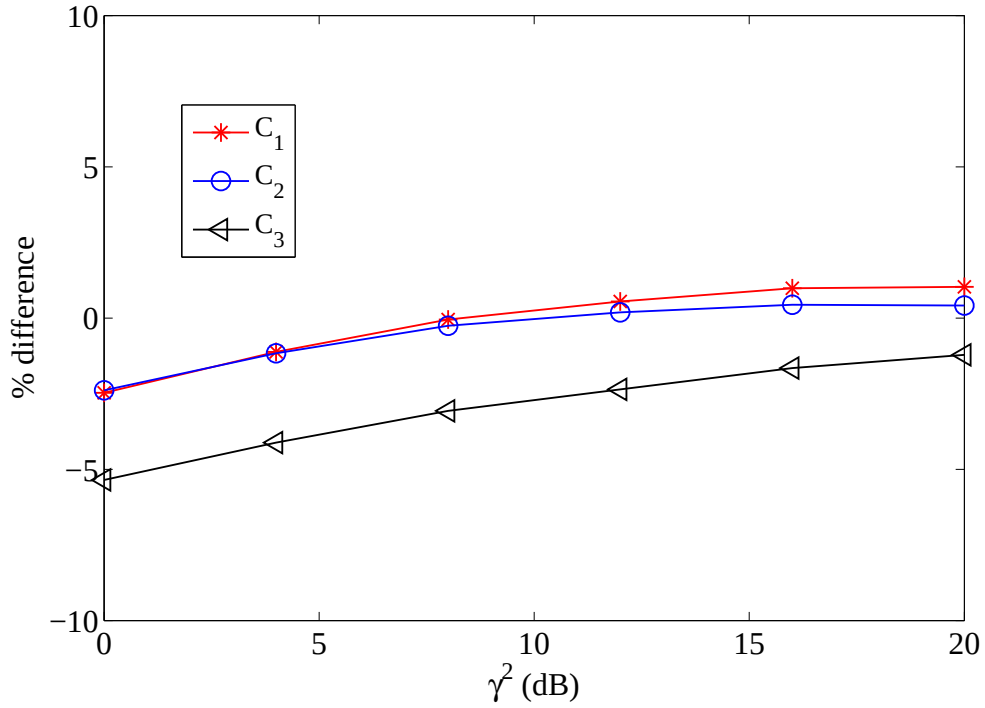

Figure 7.9: Percentage difference of the instantaneous channel amplification method compared to the average amplification in mean capacity for the system parameters: $(2, 2, 2)$, $\alpha^2 = \beta^2 = \gamma^2 = \delta^2 = \tau^2 + 10$dB.

and BPSK modulation is assumed. Making the relay-destination link a constant simplifies the analysis while preserving the effect of the relay amplification on the random source-relay link. The aim is to capture the fundamental behavior of the relay without any unnecessary complexity. Let the entries of the matrix $\boldsymbol{H}_{11}$ be $\boldsymbol{H}_{11} = [h_1, \ldots, h_{n_s}]$. As defined before, the entries are ZMCSCG random variables of unit variance. Then, the derivation of the CDFs of the SNRs of the amplification methods are as follows.

7.3.1 CDF of the SNR of the Average Amplification Method

The SNR in (7.21) can now be written as

$$\begin{aligned}\mathrm{SNR}_{\mathrm{avg}} &= \frac{\rho\,\alpha^2\,\gamma^2 \boldsymbol{H}_{12}\boldsymbol{H}_{11}\boldsymbol{H}_{11}^{\dagger}\boldsymbol{H}_{12}^{\dagger}}{\sigma^2(\rho\,\gamma^2\,n_s+\sigma^2+\alpha^2\|\boldsymbol{H}_{12}\|^2)}\\ &= \frac{\rho\,\alpha^2\,\gamma^2(|h_1|^2+\ldots+|h_{n_s}|^2)}{\sigma^2(\rho\,\gamma^2\,n_s+\sigma^2+\alpha^2)}\\ &\triangleq \frac{\rho\alpha^2\gamma^2 Q}{\sigma^2(\rho\,\gamma^2\,n_s+\sigma^2+\alpha^2)},\end{aligned} \tag{7.24}$$

where $Q = |h_1|^2+\ldots+|h_{n_s}|^2$. The random variable, Q, has a complex Chi-squared distribution with n_s degrees of freedom, i.e. $Q \sim \chi^2_{n_s}$. Then, the CDF of the SNR of the average amplification can be calculated as

$$\begin{aligned}F_{\mathrm{SNR}_{\mathrm{avg}}}(x) &= \Pr\left[\mathrm{SNR}_{\mathrm{avg}} < \mathrm{x}\right]\\ &= \Pr\left[\frac{\rho\,\alpha^2\,\gamma^2 Q}{\sigma^2(\rho\,\gamma^2\,n_s+\sigma^2+\alpha^2)} < x\right]\\ &= \Pr\left[Q < \frac{x[\sigma^2(\rho\,\gamma^2\,n_s+\sigma^2+\alpha^2)]}{\rho\,\alpha^2\,\gamma^2}\right].\end{aligned} \tag{7.25}$$

Now, the CDF can be given using a Chi-square (χ^2) distribution [74, 75] as:

$$F_{\mathrm{SNR}_{\mathrm{avg}}}(x) = \frac{1}{\Gamma(n_s)}\gamma\left(\frac{x[\sigma^2(\rho\gamma^2 n_s+\sigma^2+\alpha^2)]}{\rho\alpha^2\gamma^2}, n_s\right), \tag{7.26}$$

where $\gamma(x,m) = \int_0^x e^{-t}t^{m-1}dt$ is the incomplete gamma function and $\Gamma(m) = (m-1)!$.

7.3.2 CDF of the SNR of the Instantaneous Channel Amplification Method

The SNR in (7.22) can be rewritten as

$$\begin{aligned}\mathrm{SNR}_{\mathrm{insCh}} &= \frac{\rho\,\alpha^2\,\gamma^2 \boldsymbol{H}_{12}\boldsymbol{H}_{11}\boldsymbol{H}_{11}^{\dagger}\boldsymbol{H}_{12}^{\dagger}}{\sigma^2(\rho\,\gamma^2\ \mathrm{tr}\{\boldsymbol{H}_{11}^{\dagger}\boldsymbol{H}_{11}\}+\sigma^2+\alpha^2\|\boldsymbol{H}_{12}\|^2)}\\ &= \frac{\rho\,\alpha^2\,\gamma^2(|h_1|^2+\ldots+|h_{n_s}|^2)}{\sigma^2(\rho\,\gamma^2(|h_1|^2+\ldots+|h_{n_s}|^2)+\sigma^2+\alpha^2)}\\ &= \frac{\rho\,\alpha^2\,\gamma^2\,Q}{\sigma^2(\rho\,\gamma^2\,Q+\sigma^2+\alpha^2)}.\end{aligned} \tag{7.27}$$

As before, $Q \sim \chi^2_{n_s}$. Then, the CDF of the SNR of the instantaneous channel amplification method can be calculated as

$$\begin{aligned} F_{\mathrm{SNR}_{\mathrm{insCh}}}(x) &= \Pr\left[\mathrm{SNR}_{\mathrm{insCh}} < \mathrm{x}\right] \\ &= \Pr\left[\frac{\rho\,\alpha^2\,\gamma^2\,Q}{\sigma^2(\rho\,\gamma^2\,Q + \sigma^2 + \alpha^2)} < x\right] \\ &= \Pr\left[\rho\,\alpha^2\,\gamma^2\,Q < x\sigma^2(\rho\,\gamma^2 Q + \sigma^2 + \alpha^2)\right] \\ &= \Pr\left[\rho\,\alpha^2\,\gamma^2\,Q < x\sigma^2(\rho\,\gamma^2\,Q + \sigma^2 + \alpha^2)\right] \\ &= \Pr\left[Q < \frac{x(\sigma^2(\sigma^2+\alpha^2))}{\rho\,\alpha^2\,\gamma^2 - x\,\rho\,\sigma^2\,\gamma^2}\right]. \end{aligned} \tag{7.28}$$

Then, the CDF can be given using results on the Chi-square (χ^2) distribution as:

$$F_{\mathrm{SNR}_{\mathrm{insCh}}}(x) = \frac{1}{\Gamma(n_s)}\gamma\left(\frac{x(\sigma^2(\sigma^2+\alpha^2))}{\rho\,\alpha^2\,\gamma^2 - x\,\rho\,\sigma^2\,\gamma^2}, n_s\right). \tag{7.29}$$

7.3.3 CDF of the SNR of the Instantaneous Power Amplification Method

Let the entries of the symbol vector $\boldsymbol{x}$ be $\boldsymbol{x} = [x_1, \ldots, x_{n_s}]^T$. Then, the SNR in (7.23) can be rewritten as

$$\begin{aligned} \mathrm{SNR}_{\mathrm{insPo}} &= \frac{\rho\,\alpha^2\,\gamma^2 \boldsymbol{H}_{12}\boldsymbol{H}_{11}\boldsymbol{H}_{11}^{\dagger}\boldsymbol{H}_{12}^{\dagger}}{\sigma^2(\|\gamma\,\boldsymbol{H}_{11}\boldsymbol{x} + \boldsymbol{n}_1\|^2 + \alpha^2\|\boldsymbol{H}_{12}\|^2)} \\ &= \frac{\rho\,\alpha^2\,\gamma^2(|h_1|^2 + \ldots + |h_{n_s}|^2)}{\sigma^2(\|\gamma(h_1x_1 + \ldots + h_{n_s}x_{n_s}) + \boldsymbol{n}_1\|^2 + \alpha^2)} \\ &= \frac{\rho\,\alpha^2\,\gamma^2(|h_1|^2 + \ldots + |h_{n_s}|^2)}{\sigma^2(\|\gamma(h_1x_1 + \ldots + h_{n_s}x_{n_s}) + n_1\|^2 + \alpha^2)}, \end{aligned} \tag{7.30}$$

where $\boldsymbol{n}_1$ is a scalar random variable and is written as n_1. Then, the CDF of the SNR of the instantaneous power amplification can be calculated as

$$\begin{aligned} F_{\mathrm{SNR}_{\mathrm{insPo}}}(x) &= \Pr\left[\mathrm{SNR}_{\mathrm{insPo}} < \mathrm{x}\right] \\ &= \Pr\left[\frac{\rho\,\alpha^2\,\gamma^2(|h_1|^2 + \ldots + |h_{n_s}|^2)}{\sigma^2(\|\gamma(h_1x_1 + \ldots + h_{n_s}x_{n_s}) + n_1\|^2 + \alpha^2)} < x\right]. \end{aligned} \tag{7.31}$$

Note that each $x_i \in \pm\sqrt{\rho}$, and hence h_ix_i is ZMCSCG random variable with a variance of ρ. Then, defining $\boldsymbol{s} = (s_1, \ldots, s_{n_s}) \triangleq (h_1x_1/\sqrt{\rho}, \ldots, h_{n_s}x_{n_s}/\sqrt{\rho})$ and

letting $\sigma^2 = 1$ as in the simulations, (7.31) can be calculated as

$$\begin{aligned} F_{\mathrm{SNR}_{\mathrm{insPo}}}(x) &= \Pr\left[\frac{\rho\,\alpha^2\,\gamma^2(|s_1|^2+\ldots+|s_{n_s}|^2)}{(\|\gamma\sqrt{\rho}(s_1+\ldots+s_{n_s})+n_1\|^2+\alpha^2)} < x\right] \\ &= \Pr\left[\frac{\sum_{i=1}^{n_s}\rho\,\alpha^2\,\gamma^2|s_i|^2}{\begin{array}{c}\sum_{i=1}^{n_s}\gamma^2\,\rho\,|s_i|^2+\sum_{i=1}^{n_s}\sum_{j=1,j\neq i}^{n_s}\gamma^2\,\rho s_i s_j^* \\ +\sum_{i=1}^{n_s}\gamma\,\sqrt{\rho}\,s_i n_1^*+\sum_{i=1}^{n_s}\gamma\,\sqrt{\rho}s_i^* n_1+|n_1|^2+\alpha^2\end{array}} < x\right] \\ &= \Pr\left[\begin{array}{c}\sum_{i=1}^{n_s}\gamma^2\,\rho|s_i|^2 \\ -\sum_{i=1}^{n_s}\frac{\gamma^2\rho}{\alpha^2}|s_i|^2x-\sum_{i=1}^{n_s}\sum_{j=1,j\neq i}^{n_s}\frac{\gamma^2\rho}{\alpha^2}s_i s_j^* x \\ -\sum_{i=1}^{n_s}\frac{\gamma\sqrt{\rho}}{\alpha^2}s_i n_1^* x-\sum_{i=1}^{n_s}\frac{\gamma\sqrt{\rho}}{\alpha^2}s_i^* n_1 x+\frac{1}{\alpha^2}|n_1|^2x\end{array} < x\right]. \end{aligned} \quad (7.32)$$

Now, defining $\boldsymbol{q} = (s_1,\ldots,s_{n_s},n_1)^T$, the CDF can be written in a quadratic form and we obtain

$$F_{\mathrm{SNR}_{\mathrm{insPo}}}(x) = \Pr\left[\boldsymbol{q}^\dagger\boldsymbol{A}\boldsymbol{q} < x\right]. \quad (7.33)$$

In (7.33), $\boldsymbol{A}$ is an $(n_s+1)\times(n_s+1)$ matrix given as

$$\boldsymbol{A} = \begin{bmatrix} \frac{\rho\alpha^2\gamma^2-x\rho\gamma^2}{\alpha^2} & \frac{-x\rho\gamma^2}{\alpha^2} & \cdots & \frac{-x\rho\gamma^2}{\alpha^2} & \frac{-x\sqrt{\rho}\gamma}{\alpha^2} \\ \frac{-x\rho\gamma^2}{\alpha^2} & \frac{\rho\alpha^2\gamma^2-x\rho\gamma^2}{\alpha^2} & \cdots & \frac{-x\rho\gamma^2}{\alpha^2} & \frac{-x\sqrt{\rho}\gamma}{\alpha^2} \\ \vdots & \vdots & \ddots & \vdots & \vdots \\ \frac{-x\rho\gamma^2}{\alpha^2} & \frac{-x\rho\gamma^2}{\alpha^2} & \cdots & \frac{\rho\alpha^2\gamma^2-x\rho\gamma^2}{\alpha^2} & \frac{-x\sqrt{\rho}\gamma}{\alpha^2} \\ \frac{-x\sqrt{\rho}\gamma}{\alpha^2} & \frac{-x\sqrt{\rho}\gamma}{\alpha^2} & \cdots & \frac{-x\sqrt{\rho}\gamma}{\alpha^2} & \frac{-x}{\alpha^2} \end{bmatrix}. \quad (7.34)$$

It can be shown that the eigenvalues of the matrix $\boldsymbol{A}$, $\lambda_1,\lambda_2,\ldots,\lambda_{n_s+1}$, have the relationship $\lambda_1 < \lambda_2 < \lambda_3 = \ldots = \lambda_{n_s+1}$ and only λ_1 is negative.

The random variable, $y = \boldsymbol{q}^\dagger\boldsymbol{A}\boldsymbol{q}$ is a quadratic form. Using the results in [76, 77], the PDF of y can be given as

$$p(y) = -\frac{1}{\lambda_1(1-\frac{\lambda_3}{\lambda_1})^{n_s-1}(1-\frac{\lambda_2}{\lambda_1})}e^{-\frac{y}{\lambda_1}} \qquad (y<0), \quad (7.35)$$

and

$$p(y) = \frac{1}{\lambda_2(1-\frac{\lambda_3}{\lambda_2})^{n_s-1}(1-\frac{\lambda_1}{\lambda_2})}e^{-\frac{y}{\lambda_2}} + \sum_{j=1}^{n_s-1}\frac{B_{n_s-1-j}}{\lambda_3^j\Gamma(j)}y^{j-1}e^{-\frac{y}{\lambda_3}} \qquad (y>0). \quad (7.36)$$

In (7.36), the B_k's are constants given by

$$B_k = \sum_{j=0}^{k} \frac{(-1)^k (k-j)! j! \lambda_2^j \lambda_1^{k-j}}{k! \lambda_3^k (1-\frac{\lambda_2}{\lambda_3})^{j+1} (1-\frac{\lambda_1}{\lambda_3})^{k+1-j}}. \tag{7.37}$$

Now, using (7.35) and (7.36), the CDF, $F_{\mathrm{SNR}_{\mathrm{insPo}}}(x)$, can be calculated as

$$\begin{aligned} F_{\mathrm{SNR}_{\mathrm{insPo}}}(x) =& \frac{1}{(1-\frac{\lambda_3}{\lambda_1})^{n_s-1}(1-\frac{\lambda_2}{\lambda_1})} \\ &+ \frac{1}{(1-\frac{\lambda_3}{\lambda_2})^{n_s-1}(1-\frac{\lambda_1}{\lambda_2})} \left(1-e^{-\frac{x}{\lambda_2}}\right) + \sum_{j=1}^{n_s-1} \frac{B_{n_s-1-j}}{\Gamma(j)} \gamma\left(\frac{x}{\lambda_3}, j\right). \end{aligned} \tag{7.38}$$

7.4 Summary

In this chapter we have compared three types of relay amplification methods in terms of system capacity performance. For the comparison, we used three different types of AF MIMO two-hop relaying systems. Using Monte Carlo simulations, we showed that the instantaneous power amplification has a higher mean capacity compared to the other methods. However, the instantaneous power amplification method has a higher variance than the other amplification methods when the number of antennas in the relay and/or the source is greater than one. In addition, the instantaneous power amplification method requires additional information at the destination and would create enormous overhead compared to the other methods. Therefore, the instantaneous power amplification method does not seem to be very attractive and practical compared to the other two amplification methods.

Using the simulations, we also showed that the instantaneous channel amplification method has almost no advantage in terms of the mean capacity, but its capacity is less variable than the average amplification method. On the other hand, the average amplification method is simpler to implement, as it does not require channel estimation at the relaying terminal.

Further, we explained the capacity behaviors using the cumulative distribution functions of the signal-to-noise ratios of the amplification methods. The CDFs support our observations made using the simulations and show that instantaneous

power amplification has a higher mean capacity compared to the other methods. However, the instantaneous power amplification method has a higher capacity variance compared to the other methods when the number of antennas in the source or in the relay is more than one.

Chapter 8

Conclusions and Future Work

In this chapter we summarize the main findings and conclusions that have been presented in the thesis. The chapter also includes a discussion of some open problems and possible research directions for the future.

8.1 Conclusions

The thesis considers the design and analysis of cooperative diversity systems and MIMO amplify-and-forward relaying systems. In particular we investigate cooperative diversity systems using space-time block codes with adaptive equalization in the time and frequency domains. For MIMO relaying systems, we analyzed the ergodic capacity of various systems and compared different amplify-and-forward methods in terms of system capacity performance.

Transmit diversity using STBC has proven to be effective at mitigating multipath fading and it has been shown that transmit diversity can have similar performance to receive diversity [10, 25]. However, the optimal maximum likelihood sequence estimation techniques for transmit diversity systems have exponentially increasing complexity with the signal constellation size and channel impulse response length. Also the optimal maximum likelihood sequence estimation techniques require perfect CSI to be known at the receiver. In Chapter 3 we have proposed a new block time-domain adaptive equalization structure for TR-STBC systems, which elimi-

nates the separate decoder and also the need for explicit CSI estimation at the receiver. Using simulations, we found that for short delay spread channels a time-domain block equalizer requires significantly less equalizer taps than the analogous frequency-domain equalizer for SC FDE-STBC systems. As a result, the TDE RLS algorithms converge faster and have better SER steady-state performance than the analogous adaptive FDE algorithms. Furthermore, the equalizer length of the block TDE we have developed is independent of the block size. Thus, new alternative frame structures are possible for the block TDE which allow the system to perform better in fast time-varying channels. Finally, we analyzed the complexity of the TDE and FDE RLS algorithms. We found that the TDE system has a slightly higher complexity than the FDE system. Overall the TDE adaptive algorithm has better system performance but at the cost of increased complexity compared to the FDE adaptive system. In general, we conclude that a time-domain adaptive block equalizer is better to use for short delay spread channels due to its fast convergence. However, for long delay spread channels a time-domain adaptive block equalizer has much higher complexity, so a frequency-domain adaptive block equalizer should be used instead.

Cooperative diversity techniques have recently been proposed for the uplink in cellular systems to exploit the diversity gains afforded by transmitter diversity techniques [21, 1, 22]. Most researchers working on cooperative diversity assume a flat fading channel or explicit estimation of the CIR to be available at the receiver. In Chapter 4 we proposed both time- and frequency-domain adaptive block equalization schemes for an amplify-and-forward relay network based on Protocols I and III proposed by Nabar *et al.* [1]. By using simulations, we found that our adaptive algorithms work well for both protocols, and, at the cost of increased complexity, time-domain adaptive algorithms perform better than frequency-domain algorithms. In both the time and frequency domains the Protocol I receivers outperform the Protocol III receivers, particularly in the case of a weak source to relay link. We also found that overall both Protocol I and Protocol III equalizers have better performance compared to TS1 equalizers. The main reason is that TS1 equalizers do not

use the extra information received through relaying terminal. Thus, TS1 equalizers have lower diversity gain compared to the Protocol I and Protocol III equalizers. Therefore, we found that the amplifying-and-forward relaying system can be used to increase the performance by improving diversity of the system. In summary, again time-domain adaptive algorithms are more suitable for short delay spread channels compared to frequency-domain adaptive algorithms. In addition, optimal Protocol I equalizers are best to use if complexity is not an issue but suboptimal Protocol I equalizers yield reduced complexity without sacrificing too much performance. Note that the adaptive block equalizers we have proposed assume the channel very slowly, but in practical situations the channels may be varying faster than the adaptive equalizer can handle. In these situations, a training sequence needs to be sent more often or the block size needs to be decreased to handle the fast varying channels.

Combining wireless relaying systems with MIMO techniques, the system can achieve higher capacity, broader coverage, and better diversity. Many papers have been written on MIMO system analysis. However, relatively few address the issue of MIMO relay system analysis. In Chapter 5 and 6 we analyzed the ergodic capacity of two different MIMO two-hop relaying systems. In Chapter 5 we derived a closed-form expression for the ergodic capacity of an AF MIMO two-hop system including the source to destination link. We validated the analysis by using simulations. We showed that having the direct link improves the capacity due to diversity and quantified this improvement. Furthermore, we found that when there is a good $S \rightarrow D$ link, there is limited advantage in having an amplify-and-forward relay in terms spectral efficiency. However, when the $S \rightarrow D$ link is weak the relay is useful to provide better spectral efficiency.

In Chapter 6 we derived a closed-form expression for the capacity of the AF MIMO two-hop two relay system. Again, we verified the analysis by using simulations. We also showed that these results can be used to obtain the capacity for a single relay system by setting appropriate parameters. The results verified the capacity gain of relaying systems with two relays due to the extra diversity compared

to a single relaying system. However, the results also showed that when one of the source-to-relay links has relatively higher SNR compared to the other, a single relay system has better capacity than a two relay system. The reason is that the relay with the weak source-to-relay link amplifies the noise and passes it to the destination, corrupting the signal received through the other relay. As a results, the capacity of a two relay system becomes less than even a single relay system. Therefore, in more than two-relay based relaying systems, methods like relay selection should be used to choose the best relays to prevent signal corruption due to the relays with weak source-to-relay links.

There seems to be very little work that compares different amplification methods in AF MIMO systems. In Chapter 7 we compared three types of amplification methods: a) average amplification, b) instantaneous channel amplification, and c) instantaneous power amplification. We found that the instantaneous power amplification has a higher mean capacity compared to the other methods. However, the instantaneous power amplification method has a higher variance than the other amplification methods when the number of antennas in the relay and/or the source is greater than one. In addition, the instantaneous power amplification method requires additional information at the destination and would create enormous overhead compared to the other methods. Therefore, the instantaneous power amplification method does not seem to be very attractive compared to the other two amplification methods. We also found that the instantaneous channel amplification method has almost no advantage in terms of the mean capacity, but its capacity is less variable than the average amplification method. On the other hand, the average amplification method is simpler to implement as it does not require channel estimation at the relaying terminal.

Finally to recap the important points, time-domain block adaptive equalization has better performance compared to its frequency-domain counterpart for short delay spread channels due to its faster convergence behavior. Therefore, it is better to use a time-domain block adaptive equalizer for short delay spread channels. But, for long delay spread channels, a frequency-domain block adaptive equalizer needs

to be used to reduce the complexity. In cooperative diversity systems, again a time-domain block adaptive equalizer is better to use compared to a frequency-domain block adaptive equalizer for short delay spread channels. In addition, in cooperative diversity systems, the optimal Protocol I equalizer is better to use if complexity is not an issue.

In AF MIMO two-hop one-relay systems, it is always better to use the direct link signal if it is available to increase the capacity of the system. Note that in this system, the direct link signal and the signal from the relay arrive at the destination at two different time slots. Thus, the capacity increases due to the extra time diversity. However, in AF MIMO two-hop two-relay systems the signals from both the relays arrive at the destination at the same time. Therefore, the relay with the weaker source-to-relay link may corrupt the received from the other relay, resulting in a lower capacity than that even for a single relay system. Hence, in designing wireless networks, attention has to be given when using relays. This is because sometimes, depending on the signal strength of the channels, an amplify-and-forward relaying system can decrease the spectral efficiency as well as the error performance of the system. Therefore, in these situations, relay selection or another alternative method has to be used to achieve better system performance.

8.2 Suggested Future Work

In this thesis we studied the design of cooperative diversity systems by using space-time block codes with adaptive equalization in the time and frequency domains. We also analyzed the ergodic capacity of various AF MIMO systems and compared different amplify-and-forward methods in terms of system capacity performance. However, there still remain many open issues that require further exploration. Some of these open problems are enumerated below.

In this thesis we used STBCs that are only suitable for two transmitting antennas or one-relay based cooperative relaying systems. These systems achieve full rate and full diversity. It would be interesting in future research to expand this work on

adaptive equalization for more than one-relay based cooperative relaying systems. Earlier this was not possible as STBCs were designed primarily for two transmitting antennas. However, recently, quasi-orthogonal space-time block codes (QO-STBC) and rotated QO-STBC [78, 79, 80, 81] have been introduced for more than two transmit antenna based transmissions and also for more than one-relay based relaying systems, still achieving full rate and full diversity. With this advancement in this area of research, now it is possible to expand our work on equalization techniques for more than one-relay based cooperative relaying systems.

Very recently, cooperative diversity techniques have been proposed for the uplink in cellular systems to exploit the diversity gains afforded by transmitter diversity techniques. Hence, there are still many issues that need to be dealt with before implementing practical systems. One of the main issues is the timing synchronization between source and relaying terminals. In this thesis, specifically in Chapter 4, we assumed perfect timing synchronization. In practical systems, achieving perfect timing synchronization is a difficult task. Hence, to get a more realistic performance of a cooperative diversity system, it is important to reproduce the results by relaxing this assumption. In [82, 83] relaying systems have been studied by relaxing this assumption. Similar methods can be applied to the work in this thesis to gauge the performance of the adaptive equalization schemes in the case of imperfect synchronization.

Recently, superposition modulation [84, 85] has been introduced for cooperative diversity systems. The results show that the superposition modulation achieves better performance compared to "classical" cooperative diversity systems (cooperative diversity systems given in Chapter 4). Hence, it would be interesting to see the performance of adaptive equalization schemes for superposition modulation scenarios.

Throughout Chapters 5, 6 and 7 we have assumed i.i.d. Rayleigh channels, which are more suitable for urban or indoor environments. In practice, however, a LOS path or correlation may be present and in such scenarios a Ricean fading model and/or a correlated model may be preferable. Additionally, our assumption of the channels being frequency-flat may not be realistic. Therefore, the results derived

in these chapters need to be extended to frequency selective channels and also for other channel types such as Ricean and correlated Rayleigh.

The capacity results given in Chapter 7 are based on simulation results due to the difficulty in obtaining closed-form analytical expressions for the two instantaneous amplification methods. For example, the instantaneous channel amplification method analysis would require the eigenvalue distribution of matrices of the form

$$\boldsymbol{S} = \frac{\boldsymbol{H}\boldsymbol{H}^{\dagger}}{\mathrm{tr}\{\boldsymbol{H}^{\dagger}\boldsymbol{H}\}}, \tag{8.1}$$

where the entries of matrix $\boldsymbol{H}$ are ZMCSCG random variables with unit variance. However, these distributions are not available in the literature and their evaluation appears to be rather difficult. Nevertheless any progress on such a problem would be very useful.

All the work in this thesis assumes that the relays can not receive and transmit at the same time. However, with the help of new antenna technology it may be possible for wireless relays to receive and transmit at the same time (duplex) [86, 87]. This may improve the spectral efficiency and/or the systems' error performance. Thus, the work presented in the thesis could be extended to duplex relay scenarios.

The last and probably the most important issue is how the results in this thesis can be applied in practical systems. We have provided adaptive equalization techniques for cooperative diversity systems and also a MIMO relay system capacity analysis for two-hop relaying systems. Development of practical systems using the adaptive equalization techniques given in this work will still be challenging and a major research direction in the future. Furthermore, the capacity analysis results given for AF MIMO relay systems can be used as benchmarks for the throughput of real systems. However, approaching the optimal capacity with limited cost and complexity remains the ultimate challenge.

Bibliography

[1] R. U. Nabar, H. Bolcskei, and F. Kneubuhler, "Fading relay channels: Performance limits and space-time signal design," *IEEE J. Select. Areas Commun.*, vol. 22, no. 6, pp. 1099–1109, Aug. 2004.

[2] R. G. Gallager, *Low-Density Parity-Check Codes*. Cambridge, MA, USA: MIT Press, 1963.

[3] D. MacKay and R. Neal, "Near Shannon limit performance of low density parity check codes," *Electronics Letters*, vol. 32, no. 18, pp. 1645–1646, Aug. 1996.

[4] C. Berrou, A. Glavieux, and P. Thitimajshima, "Near Shannon limit error-correcting coding and decoding: Turbo-codes. 1," in *Proc. IEEE Int'l. Conf. on Communications*, vol. 2, Geneva, 23-26 May 1993, pp. 1064–1070.

[5] G. J. Foschini and M. J. Gans, "On the limits of wireless communication in a fading environment when using multiple antennas," *Wireless Personal Commun.*, vol. 6, no. 3, pp. 311–335, Mar. 1998.

[6] V. Tarokh, H. Jafarkhani, and A. Calderbank, "Space-time block codes from orthogonal designs," *IEEE Trans. Inform. Theory*, vol. 45, no. 5, pp. 1456–1467, Jul. 1999.

[7] B. Vucetic and J. Yuan, *Space-Time Coding*. New York, NY, USA: John Wiley & Sons, Inc., 2003.

[8] N. Seshadri and J. Winters, "Two signaling schemes for improving the error performance of frequency-division-duplex (FDD) transmission systems using

transmitter antenna diversity," in *Proc. IEEE Vehicular Technology Conf.*, Secausus, NJ, USA, 18-20 May 1993, pp. 508–511.

[9] V. Tarokh, N. Seshadri, and A. R. Calderbank, "Space-time codes for high data rate wireless communications : Performance criterion and code construction," *IEEE Trans. Inform. Theory*, vol. 44, no. 2, pp. 744–765, Mar. 1998.

[10] S. Alamouti, "A simple transmit diversity technique for wireless communications," *IEEE J. Select. Areas Commun.*, vol. 16, no. 8, pp. 1451–1458, Oct. 1998.

[11] E. Telatar, "Capacity of multi-antenna Gaussian channels," *Euro. Trans. Telecomm.*, vol. 10, pp. 585–595, Nov.-Dec. 1999.

[12] A. Lozano, F. Farrokhi, and R. Valenzuela, "Lifting the limits on high speed wireless data access using antenna arrays," *IEEE Commun. Mag.*, vol. 39, no. 9, pp. 156–162, Sep. 2001.

[13] S. Blostein and H. Leib, "Multiple antenna systems: their role and impact in future wireless access," *IEEE Commun. Mag.*, vol. 41, no. 7, pp. 94–101, Jul. 2003.

[14] M. Karaboikis, C. Soras, G. Tsachtsiris, and V. Makios, "Compact dual-printed inverted-f antenna diversity systems for portable wireless devices," *IEEE Antennas Wireless Propagat. Lett.*, vol. 3, pp. 9–14, 2004.

[15] C. Gomez-Calero, L. Gonzalez-Diaz, and R. Martinez-Rodriguez-Osorio, "Multi-band planar inverted-f antennas for MIMO mobile terminals," in *Proc. IEEE Int'l. Symp. on Antennas and Propagation*, Honolulu, HI, USA, 10-15 Jun. 2007, pp. 2413–2416.

[16] N. Honma, K. Nishimori, Y. Takatori, A. Ohta, and K. Tsunekawa, "Proposal of compact three-port MIMO antenna employing modified inverted f antenna and notch antennas," in *Proc. IEEE Int'l. Symp. on Antennas and Propagation*, Albuquerque, NM, USA, 9-14 Jul. 2006, pp. 2613–2616.

[17] H. Xiao, S. Ouyang, and Z. Nie, "The cross polarization discrimination of MIMO antennas at mobile station," in *Proc. Int'l. Conf. on Commun. Circuits and Systems*, Xiamen, China, 25-27 May 2008, pp. 203–206.

[18] E. C. V. D. Meulen, "Three-terminal communication channels," *Adv. Appl. Prob.*, vol. 3, no. 1, pp. 120–154, 1971.

[19] T. Cover and A. Gamal, "Capacity theorems for the relay channel," *IEEE Trans. Inform. Theory*, vol. 25, no. 5, pp. 572–584, Sep. 1979.

[20] J. Boyer, D. Falconer, and H. Yanikomeroglu, "A theoretical characterization of the multihop wireless communications channel with diversity," in *Proc. IEEE Global Telecommunications Conf.*, vol. 2, San Antonio, TX, USA, 25-29 Nov. 2001, pp. 841–845.

[21] A. Sendonaris, E. Erkip, and B. Aazhang, "User cooperation diversity – part 1: System description," *IEEE Trans. Commun.*, vol. 51, no. 11, pp. 1927–1938, Nov. 2003.

[22] H. Mheidat, M. Uysal, and N. Al-Dhahir, "Time-reversal space-time equalization for amplify-and-forward relaying," in *Proc. IEEE Int'l. Conf. on Communications*, Istanbul, Turkey, 11-15 Jun. 2006, pp. 1705 – 1711.

[23] M. Herdin, "MIMO amplify-and-forward relaying in correlated MIMO channels," in *Proc. Int'l. Conf. on Inform. Commun. and Signal Processing*, Bangkok, Thailand, 6-9 Dec. 2005, pp. 796–800.

[24] X. Tang and Y. Hua, "Optimal design of non-regenerative MIMO wireless relays," *IEEE Trans. Wireless Commun.*, vol. 6, no. 4, pp. 1398–1407, Apr. 2007.

[25] E. Lindskog and A. Paulraj, "A transmit diversity scheme for channels with intersymbol interference," in *Proc. IEEE Int'l. Conf. on Communications*, vol. 1, New Orleans, LA, USA, 18-22 Jun. 2000, pp. 307–311.

[26] N. Al-Dhahir, "Single-carrier frequency-domain equalization for space-time block-coded transmissions over frequency-selective fading channels," *IEEE Commun. Lett.*, vol. 7, pp. 304–306, Jul. 2001.

[27] Z. Liu, G. Giannakis, A. Scaglione, and S. Barbarossa, "Decoding and equalization of unknown multipath channels based on block precoding and transmit-antenna diversity," in *Proc. 33rd Asilomar Conf. on Signals, Systems, and Computers*, Pacific Grove, CA, USA, Oct. 1999, pp. 1557–1561.

[28] W. M. Younis, A. H. Sayed, and N. Al-Dhahir, "Efficient adaptive receivers for joint equalization and interference cancellation in multiuser space-time block-coded systems," *IEEE Trans. Signal Processing*, vol. 11, pp. 2849–2862, Nov. 2003.

[29] H. Mheidat, M. Uysal, and N. Al-Dhahir, "Equalization techniques for space-time coded cooperative systems," in *Proc. IEEE Vehicular Technology Conf.*, vol. 3, Los Angeles, CA, USA, 26-29 Sep. 2004, pp. 1708 – 1712.

[30] O. Munoz, J. Vidal, and A. Agustin, "Non-regenerative MIMO relaying with channel state information [cellular example]," in *Proc. IEEE Int'l. Conf. on Acoustics, Speech, and Signal Processing*, vol. 3, Philadelphia, PA, USA, 18-23 Mar. 2005, pp. iii/361–iii/364.

[31] M. Chiani, M. Win, and A. Zanella, "On the capacity of spatially correlated MIMO Rayleigh-fading channels," *IEEE Trans. Inform. Theory*, vol. 49, no. 10, pp. 2363–2371, Oct. 2003.

[32] H. Shin, M. Z. Win, J. H. Lee, and M. Chiani, "On the capacity of doubly correlated MIMO channels," *IEEE Trans. Wireless Commun.*, vol. 5, no. 8, pp. 2253–2265, Aug. 2006.

[33] P. J. Smith, S. Roy, and M. Shafi, "Capacity of MIMO systems with semicorrelated flat fading," *IEEE Trans. Inform. Theory*, vol. 49, no. 10, pp. 2781–2788, Oct. 2003.

[34] R. Blum, J. Winters, and N. Sollenberger, "On the capacity of cellular systems with MIMO," *IEEE Commun. Lett.*, vol. 6, no. 6, pp. 242–244, Jun. 2002.

[35] R. Blum, "MIMO capacity with interference," *IEEE J. Select. Areas Commun.*, vol. 21, no. 5, pp. 793–801, Jun. 2003.

[36] J. G. Proakis, *Digital Communications*. Boston, MA, USA: McGraw-Hill, 2001.

[37] D. Tse and P. Viswanath, *Fundamentals of Wireless Communication*. New York, NY, USA: Cambridge University Press, 2005.

[38] W. C. Jakes, *Microwave Mobile Communications*. New York, NY, USA: Wiley, 1974.

[39] T. S. Rappaport, Ed., *Wireless Communications: Principles and Practice*. Upper Saddle River, NJ, USA: Prentice-Hall, Inc., 1995.

[40] M. K. Simon and M. S. Alouini, *Digital Communications over Fading Channels: A Unified Approach to Performance Analysis*. New York, NY, USA: Wiley, 2000.

[41] A. Hiroike, F. Adachi, and N. Nakajima, "Combined effects of phase sweeping transmitter diversity and channel coding," *IEEE Trans. Veh. Technol.*, vol. 41, no. 2, pp. 170–176, May 1992.

[42] A. Hiroike and K. Hirade, "Multitransmitter simulcast digital signal transmission by using frequency offset strategy in land mobile radio telephone," *IEEE Trans. Veh. Technol.*, vol. 27, pp. 231–238, 1978.

[43] S. Haykin, *Communication Systems*, 3rd ed. New York, NY, USA: Wiley, 1994.

[44] ——, *Adaptive Filter Theory*, 4th ed. Upper Saddle River, NJ, USA: Prentice-Hall, 2002.

[45] J. Laneman and G. Wornell, "Energy-efficient antenna sharing and relaying for wireless networks," in *Proc. IEEE Wireless Communications and Networking Conf.*, vol. 1, Chicago, IL, USA, 23-28 Sep. 2000, pp. 7–12.

[46] A. Stefanov and E. Erkip, "Cooperative coding for wireless networks," *IEEE Trans. Commun.*, vol. 52, no. 9, pp. 1470–1476, Sep. 2004.

[47] J. Laneman and G. Wornell, "Distributed space-time-coded protocols for exploiting cooperative diversity in wireless networks," *IEEE Trans. Inform. Theory*, vol. 49, no. 10, pp. 2415–2425, Oct. 2003.

[48] M. Chiani, M. Z. Win, and H. Shin, "Capacity of MIMO systems in the presence of interference," in *Proc. IEEE Global Telecommunications Conf.*, San Francisco, California, USA, 30 Nov. -1 Dec. 2006, pp. 1–6.

[49] T. Ratnarajah, R. Vaillancourt, and M. Alvo, "Complex random matrices and Rayleigh channel capacity," *Commun. Inf. Syst.*, vol. 3, pp. 119–138, Oct. 2003.

[50] R. K. Mallik, "The pseudo-Wishart distribution and its application to MIMO systems," *IEEE Trans. Inform. Theory*, vol. 49, no. 10, pp. 2761–2769, Oct. 2003.

[51] "3rd generation partnership project; technical specification group GSM/EDGE radio access network; radio transmission and reception (release 1999)," 3GPP TS 05.05 V8.20.0, Annex C.3 Propagation models.

[52] R. E. Blahut, *Fast Algorithms for Digital Signal Processing.* Boston, MA, USA: Addison-Wesley Longman Publishing Co., Inc., 1985.

[53] J. S. Lim and A. V. Oppenheim, *Advanced Topics in Signal Processing.* Upper Saddle River, NJ, USA: Prentice-Hall, Inc., 1987.

[54] K. K. Parhi, *VLSI digital signal processing systems : design and implementation.* New York, NY, USA: Wiley, 1999.

[55] S. Zohar, "Toeplitz matrix inversion: The algorithm of W. F. Trench," *J. ACM*, vol. 16, no. 4, pp. 592–601, 1969.

[56] N. Al-Dhahir, M. Uysal, and C. N. Georghiades, "Three space-time block-coding schemes for frequency-selective fading channels with application to EDGE," in *Proc. IEEE Vehicular Technology Conf.*, Atlantic City, NJ, USA, 7-11 Oct. 2001, pp. 1834–1838.

[57] H. Mheidat, M. Uysal, and N. Al-Dhahir, "Comparative analysis of equalization techniques for STBC with application to EDGE," in *Proc. IEEE Vehicular Technology Conf.*, vol. 1, Milano, Italy, 17-19 May 2004, pp. 555 – 559.

[58] Y. Yang, Y. H. Chew, and T. T. Tjhung, "Single-carrier frequency-domain equalization for space-time coded systems over multipath channels," in *Proc. IEEE Vehicular Technology Conf.*, Melbourne, Australia, 7-10 May 2006, pp. 2193 – 2197.

[59] H. Mheidat, M. Uysal, and N. Al-Dhahir, "Equalization techniques for distributed space-time block codes with amplify-and-forward relaying," *IEEE Trans. Signal Processing*, vol. 55, no. 5, pp. 1839–1852, May 2007.

[60] X. Li, F. Ng, J.-T. Hwu, and M. Chen, "Channel equalization for STBC-encoded cooperative transmissions with asynchronous transmitters," in *Proc. Thirty-Ninth Asilomar Conf. on Signals, Systems, and Computers*, Pacific Grove, CA, USA, 28 Oct. – 1 Nov. 2005, pp. 457–461.

[61] F.-C. Zheng, A. Burr, and S. Olafsson, "A simple optimum detector for distributed space-time block coding under imperfect synchronisation," in *Proc. IEEE Eighth Workshop on Signal Processing Advances in Wireless Communications*, Helsinki, Finland, 17-20 Jun. 2007, pp. 1–5.

[62] A. Firag and L. M. Garth, "Joint time domain decoding and equalization for time reversal-space time block coded systems," in *Proc. IEEE Vehicular Technology Conf.*, Baltimore, MD, USA, 30 Sep. -3 Oct. 2007, pp. 506 – 510.

[63] Q. Guo, X. Yuan, and L. Ping, "Single- and multi-carrier IDMA schemes with cyclic prefixing and zero padding techniques," *Eur. Trans. Telecomm.*, vol. 19, pp. 537–547, Mar. 2008.

[64] H. Bölcskei, R. U. Nabar, O. Oyman, and A. Paulraj, "Capacity scaling laws in MIMO relay networks," *IEEE Trans. Wireless Commun.*, vol. 5, no. 6, pp. 1433–1444, Jun. 2006.

[65] J. Wagner, B. Rankov, and A. Wittneben, "On the asymptotic capacity of the Rayleigh fading amplify-and-forward MIMO relay channel," in *Proc. IEEE Int'l. Symp. Information Theory*, Nice, France, 24-29 Jun. 2007, pp. 2711–2715.

[66] V. Morgenshtern and H. Bolcskei, "Crystallization in large wireless networks," *IEEE Trans. Inform. Theory*, vol. 53, no. 10, pp. 3319–3349, Oct. 2007.

[67] A. Maaref and S. Aïssa, "Eigenvalue distributions of Wishart-type random matrices with application to the performance analysis of MIMO MRC systems," *IEEE Trans. Wireless Commun.*, vol. 6, no. 7, pp. 2678–2689, Jul. 2007.

[68] G. Alfano, A. Tulino, A. Lozano, and S. Verdu, "Capacity of MIMO channels with one-sided correlation," in *Proc. IEEE Int'l. Symp. on Spread Spectrum Techniques and Applications*, Sydney, Australia, 30 Aug. -2 Sep. 2004, pp. 515–519.

[69] S. Jin, M. R. McKay, C. Zhong, and K.-K. Wong, "Ergodic capacity analysis of amplify-and-forward MIMO dual-hop systems," in *Proc. IEEE Int'l. Symp. Information Theory*, Toronto, Canada, 6-11 Jul. 2008, pp. 1903–1907.

[70] J. A. Díaz-García, R. G. Jáimez, and K. V. Mardia, "Wishart and pseudo-Wishart distributions and some applications to shape theory," *J. Multivar. Anal.*, vol. 63, no. 1, pp. 73–87, 1997.

[71] S. Yang and J.-C. Belfiore, "Optimal space-time codes for the MIMO amplify-and-forward cooperative channel," *IEEE Trans. Inform. Theory*, vol. 53, no. 2, pp. 647–663, Feb. 2007.

[72] A. Firag, P. J. Smith, and M. R. McKay, "Capacity analysis for MIMO two-hop amplify-and-forward relaying systems with the source to destination link," submitted to *IEEE Int'l. Conf. on Communications*, 2009.

[73] A. Firag and P. J. Smith, "Capacity analysis for MIMO two-hop amplify-and-forward relaying systems," to appear in *Int'l. Symposium on Information Theory and its Applications (ISITA)*, Auckland, New Zealand, 2008.

[74] H. Stark and J. W. Woods, *Probability, Random Processes, and Estimation Theory for Engineers.* Upper Saddle River, NJ, USA: Prentice-Hall, Inc., 1986.

[75] A. Mathai and S. Provost, *Quadratic Forms in Normal Random Variables: Theory and Applications.* New York, NY, USA: Marcel Dekker, 1992.

[76] N. L. Johnson and S. Kotz, *Distributions in Statistics: Continuous Univariate Distributions.* New York, NY, USA: John Wiley and Sons, 1970, vol. 2.

[77] D. Raphaeli, "Distribution of noncentral indefinite quadratic forms in complex normal variables," *IEEE Trans. Inform. Theory*, vol. 42, no. 3, pp. 1002–1007, May 1996.

[78] H. Jafarkhani, "A quasi-orthogonal space-time block code," *IEEE Trans. Commun.*, vol. 49, no. 1, pp. 1–4, Jan. 2001.

[79] H. Mheidat, M. Uysal, and N. Al-Dhahir, "Quasi-orthogonal time-reversal spacetime block coding for frequency-selective fading channels," *IEEE Trans. Signal Processing*, vol. 55, no. 2, pp. 772–778, Jan. 2007.

[80] Y. Jing and H. Jafarkhani, "Using orthogonal and quasi-orthogonal designs in wireless relay networks," *IEEE Trans. Inform. Theory*, vol. 53, no. 11, pp. 4106–4118, Nov. 2007.

[81] F. Fazel and H. Jafarkhani, "Quasi-orthogonal space-frequency and space-time-frequency block codes for MIMO OFDM channels," *IEEE Trans. Wireless Commun.*, vol. 7, no. 1, pp. 184–192, Jan. 2008.

[82] Y. Mei, Y. Hua, A. Swami, and B. Daneshrad, "Combating synchronization errors in cooperative relays," in *Proc. IEEE Int'l. Conf. on Acoustics, Speech, and Signal Processing*, vol. 3, Philadelphia, PA, USA, 18-23 Mar. 2005, pp. iii/369–iii/372.

[83] F.-C. Zheng, A. Burr, and S. Olafsson, "Distributed space-time block coding for 3 and 4 relay nodes: Imperfect synchronisation and a solution," in *Proc. IEEE Int'l. Symp. on Personal, Indoor and Mobile Radio Communications*, Athens, Greece, 3-7 Sep. 2007, pp. 1–5.

[84] E. Larsson and B. Vojcic, "Cooperative transmit diversity based on superposition modulation," *IEEE Commun. Lett.*, vol. 9, no. 9, pp. 778–780, Sep. 2005.

[85] K. Ishii, "Coded cooperation protocol utilizing superposition modulation for half-duplex scenario," in *Proc. IEEE Int'l. Symp. on Personal, Indoor and Mobile Radio Communications*, Athens, Greece, Sep. 2007, pp. 1–5.

[86] H. Yang, M. Herben, I. Akkermans, and P. Smulders, "Impact analysis of directional antennas and multiantenna beamformers on radio transmission," *IEEE Trans. Veh. Technol.*, vol. 57, no. 3, pp. 1695–1707, May 2008.

[87] B. Alawieh, C. Assi, and W. Ajib, "Distributed correlative power control schemes for mobile ad hoc networks using directional antennas," *IEEE Trans. Veh. Technol.*, vol. 57, no. 3, pp. 1733–1744, May 2008.